INFLUENCE OF FABRIC ARCHITECTURE ON DAMAGE PROGRESSION AS EVIDENCED BY ACOUSTIC EMISSION

by

Austin James Lolatte

A thesis submitted in partial fulfillment
of the requirements for the degree

of

Master of Science

in

Mechanical Engineering

MONTANA STATE UNIVERSITY
Bozeman, Montana

July 2016

©COPYRIGHT

by

Austin James Lolatte

2016

All Rights Reserved

ACKNOWLEDGEMENTS

Thanks to Montana State University Composites Research Group members and faculty for their mentorship, composites manufacturing experience, and assistance for my education. My family, for always being supportive with each endeavor I undertake, educational or otherwise. And of course, Dr. Miller for guiding me on my research and laying the groundwork that sparked my initial interest in the subject. To these people and many others not named here, thank you for making this all possible.

TABLE OF CONTENTS

1. INTRODUCTION TO STUDY 1

2. BACKGROUND 8

Composite Materials 8
Fiber Reinforced Polymer Composite Materials 9
Fiber Reinforced Polymer Composite Manufacturing 13
VARTM 19
Pre-Preg 21
Assembly and Geometry of Different Fabric Types 22
Unidirectional Fabrics 23
Multiaxial Fabrics 24
Chopped Strand Mat 28
Woven Fabrics. 30
Plain Weave 30
Twill Weave 31
Satin Weave 31
Basket Weave 32
Leno Weave 33
Mock Leno Weave 34
Hybrid Fabrics 36
Carbon/Glass Hybrids 37
Aramid/Glass Hybrids 37
Carbon/Aramid 38
Other Fabric Types 38
Braided Fabrics 38
Tissues 39
Damage Progression for Composite Materials 40
Energy Released and Strain 45
Acoustic Emission 48
Elastic Wave Theory 51
Location Data 55
Absolute Energy Data 56
Frequency Data 58
Thesis Goals 64

3. EXPERIMENTAL PROCEDURES 65

Test Coupon Manufacture 65
Infusion 69

TABLE OF CONTENTS - CONTINUED

Stitching Removal....69
Cutting and Preparation....71
Mechanical Test Setup....72
Acoustic Emission Setup....73
Test Process....76

4. RESULTS....80

0° Coupons Results....80
Glass- A1 Results....82
Glass- A1*....88
Glass-C1....93
Summary of 0° Coupons....99
90° Coupons....100
Glass-A2....102
Glass-A2*....107
Glass-C2....113
Summary of 90° Coupons....118
Biaxial Coupons....119
Glass-A3....123
Glass- A3*....128
Glass- B1....133
Glass-B2....138
Glass- C3....143
Summary of Biaxial Coupons....149
Comparison Summary of All Samples....150

5. CONCLUSIONS....155

Future Work....165

REFERENCES CITED....168

APPENDICES....175

APPENDIX A: Coupon Data....176
APPENDIX B: Manufacturing Data....192
APPENDIX C: Coupon Test Data....208
APPENDIX D: MS Excel ANOVA Setup....279
APPENDIX E: AEWin Software Settings....282

LIST OF TABLES

Table Page

1: Advantages and Disadvantages of Different Manufacturing Processes 19

2: Comparison of Properties of Various Weave Patterns 35

3: Compilation of Various Independent Research on PFRQs Related to Various Mechanisms 62

4: Peak Frequency Bin Ranges 64

5: Fabric Types with Corresponding Architecture and Weights 66

6: Test Matrix for Each Coupon Type 68

7: $\bar{x}$ and σ of V_f, UTS, εf, N_{PFRQ}, and E_{abs} for Every 0° Coupon 100

8: $\bar{x}$ and σ of V_f, UTS, εf, N_{PFRQ}, and E_{abs} for Every 90° Coupon 119

9: $\bar{x}$ and σ of V_f, UTS, εf, N_{PFRQ}, and E_{abs} for Every Biaxial Coupon 150

10: $\bar{x}$ of V_f, UTS, εf, N_{PFRQ}, and E_{abs} for Every Coupon 151

11: Energy Released per Event Recorded for Each Sample 152

12: ANOVA for E_{abs} for each Sample Group 153

LIST OF FIGURES

Figure Page

1: Electricity Generation Mix by 2030 Implementing a National 30% RES Compared to Our Current Progression 1

2: Renewable Energy Development by 2030 Implementing a National 30% RES Compared to Our Current Progression 2

3: Various Commercial Wind Turbine Sizes Through Time 3

4: Levelized Cost of Various Forms of Energy 4

5: Examples of Unidirectional ($[0]_8$) and Quadriaxial ($[0/90/\pm45]_S$) Fiber Layups 10

6: SEM Cross Section of an FRPC 13

7: Diagram of a Hand Layup Process 14

8: Diagram of Pressure Molding Manufacturing Process 14

9: Diagram of Vacuum Bagging Manufacturing Process 15

10: Diagram of Filament Winding Manufacturing Process 15

11: Diagram of Poltrusion Manufacturing Process 16

12: Diagram of Spray Method Manufacturing Process 16

13: Diagram of Sheet Molding Manufacturing Process 17

14: Diagram of Bulk Molding Method Manufacturing Process 17

15: Diagram of RTM Manufacturing Process 18

16: Diagram of VARTM Manufacturing Process 21

17: Diagram of Pre-Impregnated Manufacturing Process 22

18: Example of Unidirectional Fabric with Transverse Fibers 23

LIST OF FIGURES - CONTINUED

Figure Page

19: Example of a Multiaxial Fabric 25

20: Simultaneous Stitch Process for Multiaxial Fabrics 26

21: Weave and Stitch Method for Multiaxial Fabrics 26

22: Example of Resin Rich Area in a Composite Structure 28

23: Example of CSM 29

24: Diagram of a Plain Weave Fabric 30

25: Diagram of Twill Weave Fabric 31

26: Various Diagrams of Examples of Satin Weave Fabrics 32

27: Diagram of Basket Weave Fabric 33

28: Diagram of Leno Weave Fabric 34

29: Diagram of Mock Leno Weave Fabric 34

30: A Carbon/Aramid Hybrid Fabric 36

31: Braiding Process of Glass Fibers for a Tubular Structure 39

32: SEM of Matrix Cracking 42

33: SEM of Fiber Pullout 43

34: SEM of Fiber Debond 44

35: SEM of Fiber Failure 45

36: Typical Stress-Strain Curve for a Load-Unload-Reload Test and the Dissipated Energy 46

37: Basic Schematic of an AE Sensor 51

LIST OF FIGURES - CONTINUED

Figure Page

38: Parts of an Ideal Lamb Wave for Acoustic Emissions 54

39: An Example of a Typical AE Waveform in the Time Domain 59

40: FFT of the AE Waveform in the Frequency Domain 60

41: Front Side of Vectorply Fabric Showing the Difference between Stitching Removed Versus Intact 70

42: Back Side of Vectorply Fabric Showing the Difference between Stitching Removed versus Intact 70

43: What Various Coupons Looked Like Before Being Tested 71

44: The Test Setup for a Coupon in an Instron 8562 72

45: Calibration Sheet for WD AE Sensors 74

46: Sensor with In-Line Pre-Amp Setup Used for all of the Testing 75

47: Attachment Setup for AE Sensors Used in Every Test 77

48: Glass-A1 Coupon 2440-4 after Catastrophic Failure 81

49: Glass-A1* Coupon 2439-4 after Catastrophic Failure 82

50: Glass-C1 Coupon 2449-25 after Catastrophic Failure 82

51: Stress vs. Strain for Glass-A1 Coupon 2440-4 83

52: Event PFRQ vs. Strain for Glass-A1 Coupon 2440-4 85

53: Event PFRQ vs. Stress for Glass-A1 Coupon 2440-4 85

54: Event PFRQ vs. Time for Glass-A1 Coupon 2440-4 86

55: Absolute Energy vs. Strain for Glass-A1 Coupon 2440-4 87

LIST OF FIGURES - CONTINUED

Figure Page

56: Absolute Energy vs. Strain for Glass-A1 Coupon 2440-4 Truncated at $9*10^5$aJ 87

57: Recorded PFRQ Events by Damage Corresponding Type of Damage for Glass-A1 Coupon 2440-4 88

58: Stress vs. Strain for Glass-A1* Coupon 2439-4 89

59: Event PFRQ vs. Strain for Glass-A1* Coupon 2439-4 90

60: Event PFRQ vs. Stress for Glass-A1* Coupon 2439-4 90

61: Event PFRQ vs. Time for Glass-A1* Coupon 2439-4 91

62: Absolute Energy vs. Strain for Glass-A1* Coupon 2439-4 92

63: Absolute Energy vs. Strain for Glass-A1* Coupon 2439-4 Truncated at $8*10^5$aJ 92

64: Recorded PFRQ Events by Damage Corresponding Type of Damage for Glass-A1* Coupon 2439-4 93

65: Stress vs. Strain for Glass-C1 Coupon 2449-25 94

66: Event PFRQ vs. Strain for Glass-C1 Coupon 2449-25 95

67: Event PFRQ vs. Stress for Glass-C1 Coupon 2449-25 96

68: Event PFRQ vs. Time for Glass-C1 Coupon 2449-25 96

69: Absolute Energy vs. Strain for Glass-C1 Coupon 2449-25 97

70: Absolute Energy vs. Strain for Glass-C1 Coupon 2449-25 Truncated at $9*10^6$aJ 98

71: Recorded PFRQ Events by Damage Corresponding Type of Damage for Glass-C1 Coupon 2449-25 99

72: Glass-A2 Coupon 2451-23 after Catastrophic Failure 101

LIST OF FIGURES - CONTINUED

Figure Page

73: Glass-A2* Coupon 2452-22 after Catastrophic Failure 101

74: Glass-C2 Coupon 2450-23 after Catastrophic Failure 102

75: Stress vs. Strain for Glass-A2 Coupon 2451-23 103

76: Event PFRQ vs. Strain for Glass-A2 Coupon 2451-23..... 104

77: Event PFRQ vs. Stress for Glass-A2 Coupon 2451-23..... 104

78: Event PFRQ vs. Time for Glass-A2 Coupon 2451-23..... 105

79: Absolute Energy vs. Strain for Glass-A2 Coupon 2451-23..... 106

80: Absolute Energy vs. Strain for Glass-A2 Coupon 2451-23 Truncated at $1*10^4$aJ 106

81: Recorded PFRQ Events by Damage Corresponding Type of Damage for Glass-A2 Coupon 2451-23..... 107

82: Stress vs. Strain for Glass-A2* Coupon 2452-22 108

83: Event PFRQ vs. Strain for Glass-A2* Coupon 2452-22..... 109

84: Event PFRQ vs. Stress for Glass-A2* Coupon 2452-22..... 110

85: Event PFRQ vs. Time for Glass-A2* Coupon 2452-22..... 110

86: Absolute Energy vs. Strain for Glass-A2* Coupon 2452-22..... 111

87: Absolute Energy vs. Strain for Glass-A2* Coupon 2452-22 Truncated at $8*10^6$aJ 112

88: Recorded PFRQ Events by Damage Corresponding Type of Damage for Glass-A2* Coupon 2452-22..... 113

89: Stress vs. Strain for Glass-C2 Coupon 2450-23..... 114

90: Event PFRQ vs. Strain for Glass-C2 Coupon 2450-23 115

LIST OF FIGURES - CONTINUED

Figure Page

91: Event PFRQ vs. Stress for Glass-C2 Coupon 2450-23 115

92: Event PFRQ vs. Time for Glass-C2 Coupon 2450-23 116

93: Absolute Energy vs. Strain for Glass-C2 Coupon 2450-23 117

94: Absolute Energy vs. Strain for Glass-C2 Coupon 2450-23 Truncated at $6*10^5$aJ 117

95: Recorded PFRQ Events by Damage Corresponding Type of Damage for Glass-C2 Coupon 2450-23 118

96: Glass-A3 Coupon 2441-6 after Catastrophic Failure 121

97: Glass-A3* Coupon 2443-2 after Catastrophic Failure 121

98: Glass-B1 Coupon 2434-4 after Catastrophic Failure 122

99: Glass-B2 Coupon 2435-3 after Catastrophic Failure 122

100: Glass-C3 Coupon 2446-11 after Catastrophic Failure 123

101: Stress vs. Strain for Glass-A3 Coupon 2441-6 124

102: Event PFRQ vs. Strain for Glass-A3 Coupon 2441-6 125

103: Event PFRQ vs. Stress for Glass-A3 Coupon 2441-6 125

104: Event PFRQ vs. Time for Glass-A3 Coupon 2441-6 126

105: Absolute Energy vs. Strain for Glass-A3 Coupon 2441-6 127

106: Absolute Energy vs. Strain for Glass-A3 Coupon 2441-6 Truncated at $1*10^6$aJ 127

107: Recorded PFRQ Events by Damage Corresponding Type of Damage for Glass-A3 Coupon 2441-6 128

108: Stress vs. Strain for Glass-A3* Coupon 2443-6 129

LIST OF FIGURES - CONTINUED

Figure Page

109: Event PFRQ vs. Strain for Glass-A3* Coupon 2443-4 130

110: Event PFRQ vs. Stress for Glass-A3* Coupon 2443-4 130

111: Event PFRQ vs. Time for Glass-A3* Coupon 2443-4 131

112: Absolute Energy vs. Strain for Glass-A3* Coupon 2443-4 132

113: Absolute Energy vs. Strain for Glass-A3* Coupon 2443-4 Truncated at $8*10^5$aJ 132

114: Recorded PFRQ Events by Damage Corresponding Type of Damage for Glass-A3* Coupon 2443-4 133

115: Stress vs. Strain for Glass-B1 Coupon 2434-4 134

116: Event PFRQ vs. Strain for Glass-B1 Coupon 2434-4 135

117: Event PFRQ vs. Stress for Glass-B1 Coupon 2434-4 135

118: Event PFRQ vs. Time for Glass-B1 Coupon 2434-4 136

119: Absolute Energy vs. Strain for Glass-B1 Coupon 2434-4 137

120: Recorded PFRQ Events by Damage Corresponding Type of Damage for Glass-B1 Coupon 2434-4 138

121: Stress vs. Strain for Glass-B2 Coupon 2435-4 139

122: Event PFRQ vs. Strain for Glass-B2 Coupon 2435-4 140

123: Event PFRQ vs. Stress for Glass-B2 Coupon 2435-4 140

124: Event PFRQ vs. Time for Glass-B1 Coupon 2435-4 141

125: Absolute Energy vs. Strain for Glass-B2 Coupon 2435-4 142

126: Recorded PFRQ Events by Damage Corresponding Type of Damage for Glass-B2 Coupon 2435-4 143

LIST OF FIGURES - CONTINUED

Figure Page

127: Stress vs. Strain for Glass-C3 Coupon 2446-24 144

128: Event PFRQ vs. Strain for Glass-C3 Coupon 2446-24 145

129: Event PFRQ vs. Stress for Glass-C3 Coupon 2446-24 146

130: Event PFRQ vs. Time for Glass-C3 Coupon 2446-24 146

131: Absolute Energy vs. Strain for Glass-C3 Coupon 2446-24 147

132: Absolute Energy vs. Strain for Glass-C3 Coupon 2446-24 Truncated at $1*10^6$aJ 148

133: Recorded PFRQ Events by Damage Corresponding Type of Damage for Glass-C3 Coupon 2443-24 149

ABSTRACT

Fabric reinforced polymer matrix composites are integral structural materials used in wind turbine blades. Wind turbines are expected to increase in size and utilization as global focus turns toward power generation utilizing renewable sources. How these materials change properties due to damage accumulated are important to the future of wind energy. They feature damage mechanisms that are unique from any other engineering material. These factors are now driving innovation for design and manufacturing of the blades. This has led to investigation in characterizing the mechanical behavior of the composites.

These composites were manufactured using unidirectional and biaxial fiber layups from three fabrics composed of an epoxy matrix and glass fibers. The effect of the architecture of the fibers on damage progression was determined with acoustic emission sensors that were attached linearly to capture elastic waves emitted by damage mechanisms inside the samples during testing. The critical data extracted from the elastic waveforms include the peak frequency and absolute energy released by the samples and how they are associated with the strength of the samples. A static loading scenario was determined to be the optimal testing method.

The use of AE measurements proved to be an invaluable tool to determine how the damage progression of composite materials lead to failure for some, while not being accurate for others. Results found that simple architecture differences for the same fibers have drastic effects on damage progression. However, the energy measurements proved to be imperfect with current technology and application; improvement will be necessary for AE instruments to be a viable tool for energy measurement in the future.

AE provides a unique analysis that can identify and characterize damage related to fabric composition. The frequency content provides a consistent method of identifying damage mechanisms between varying materials. Optimal architecture and layup can be determined with the help of AE. Correlating acoustic energy to actual energy dissipated still has potential as a valuable tool if improvement in sensor technology can be achieved. Ultimately, a foundation for correlating mechanical properties of the materials and damage progression to fabric architecture and layup using AE tools was created.

1. INTRODUCTION TO STUDY

The demand for renewable energy has increased dramatically in recent years, but the want for more green energy has been a concern in the US since the Clean Air Act (CAA) passed in 1970. More companies and people are trying to do away with old forms of energy production due to environmental and health concerns. Currently, more than half of the states in the US have standards or targets to increase the overall percentage of renewable energy used. Legislation was introduced into the US senate in May of 2015, sponsored by Union of Concerned Scientists USA (UCSUSA), which would establish a national Renewable Electricity Standard (RES) that require a blanket standard for every state to have at least 30% renewable energy by 2030. Figure 1 below is what the UCSUSA project the energy market in the US would look like by 2030 if the RES is passed.

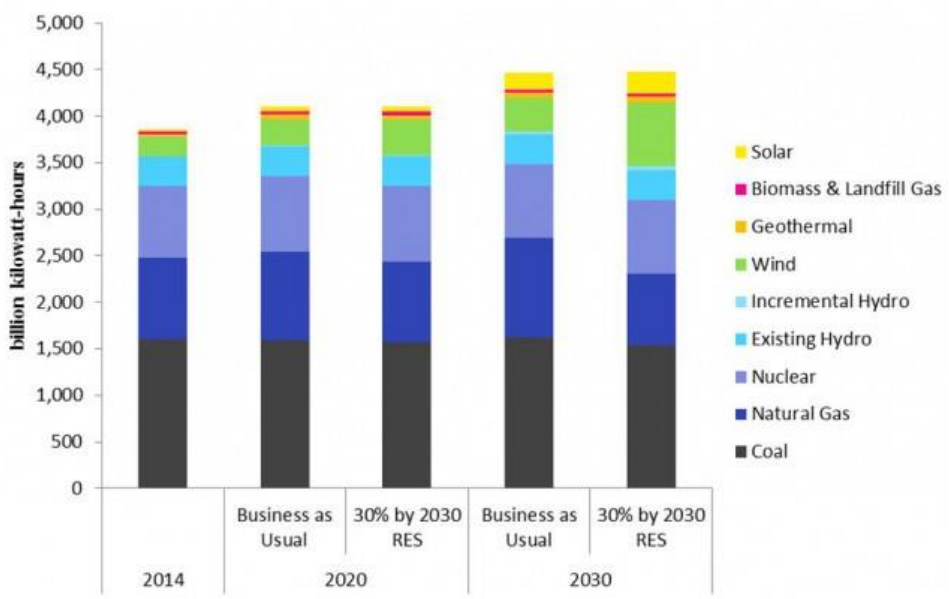


Figure 1: Electricity Generation Mix by 2030 Implementing a National 30% RES Compared to Our Current Progression (Bailie, 2015)

Figure 1 shows that with the implementation of a national 30% RES would significantly increase the diversity of energy sources in the US. The majority of the renewable energy would come from the overall increase in consumption, rather than taking away from existing non-renewable energy sources. According to UCSUSA, the most significant cuts to non-renewable energy sources are a 27 % cut in natural gas generation and a 6% in coal generation. With these cuts, combined with the increase in energy demand for the country, the renewable energy generation will increase by an estimated 57%.

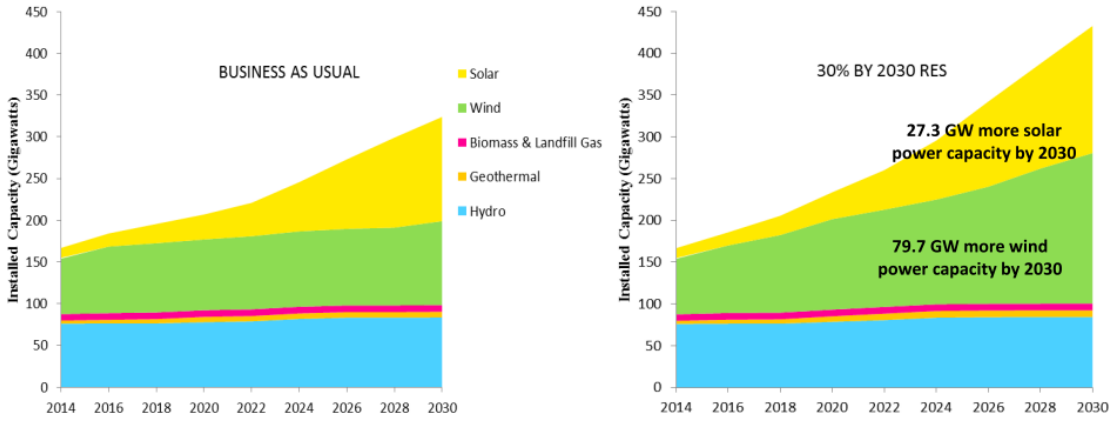


Figure 2: Renewable Energy Development by 2030 Implementing a National 30% RES Compared to Our Current Progression (Bailie, 2015)

The increase in renewable energy will be most heavily concentrated in wind and solar energy. Figure 2 shows that wind energy will increase the greatest of the two, with a 79.7 GW increase compared to a 27.3 GW increase for solar energy generation. This is combined with the fact that new wind energy, in terms of new power generation capacity, is growing the fastest in the United States (AWEA, 2013). The increase in demand of wind energy production and capacity has, and will continue, to require an increase in the

efficiency and size of wind turbines and their blades, as shown in Figure 3 below. The increase in tower height and blade-span will create more efficient turbines by allowing the blades to be in at a higher altitude where airflow is more consistent. The increase in height will also reduce ground effects that can interfere with airflow around the blades, thus reducing the power output. The increase in the size of the blades will create more swept area that they pass through. When the swept area increase, the energy gains increase exponentially. Another factor to consider is that the cost of wind energy is one the cheapest forms of energy that exists, as shown in Figure 3.These factors, along with an increase in public consciousness regarding environmental health and sustainability, is likely going to see a substantial increase in the production of wind turbines and other wind energy harvesting structures.

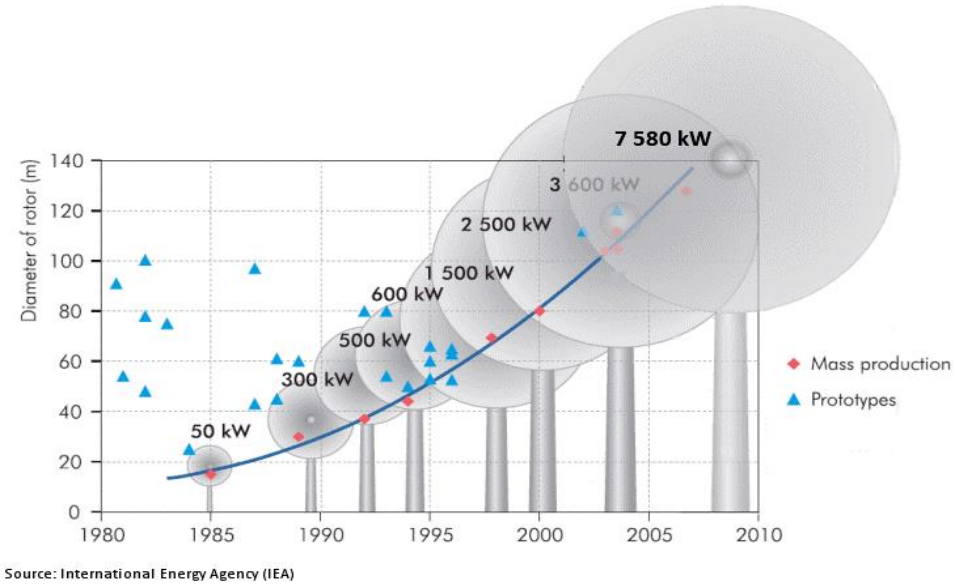


Figure 3: Various Commercial Wind Turbine Sizes Through Time (ChemViews, 2012)

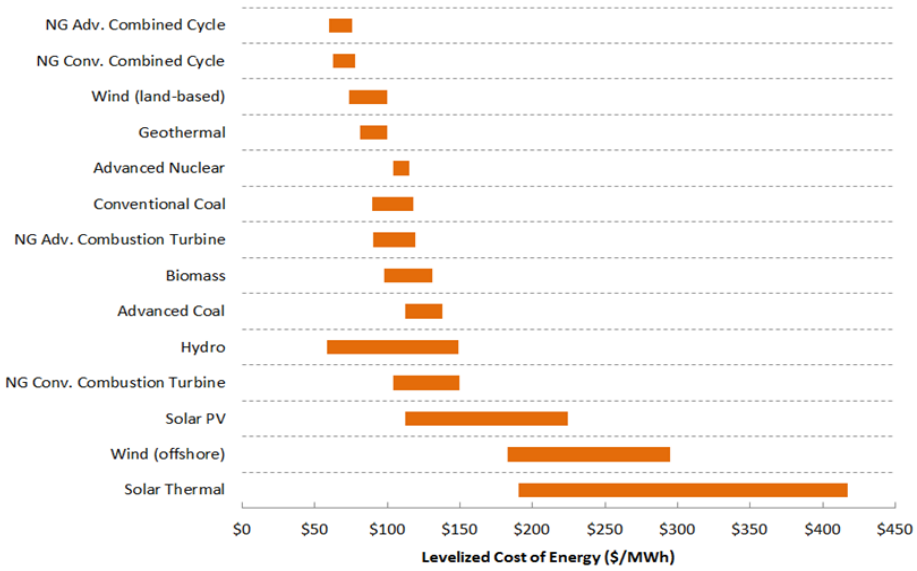


Figure 4: Levelized Cost of Various Forms of Energy (USEIA, 2013)

The main component of wind turbines are the blades, which are made entirely of composite materials. These composite materials can be, and typically are made with very complex construction creating many material interactions during mechanical testing. These various interactions can all lead to different types of damage that can all progress differently to blade damage or catastrophic failure. This complexity is one of the main differences between composites and other typical engineering materials. Composites are irregular (anisotropic) in their assembly, whereas more typical engineering materials like metals are uniform (isotropic) throughout the structure. The uniformity of metals and other materials allow for more simplistic modeling and analysis for failure. Composite materials have more complex modes of failure due to the construction, making mechanical behavior and failure modes much harder to predict. This makes one of the main obstacles of wind energy determining the how and when the failure of the windblades are going to occur. Another aspect that is important to the wind energy

market is the progression of the damage that eventually leads to failure. When damage occurs in one or more of the blades the entire turbine needs to be shut down until they are repaired. 11% of downtime of wind turbines in the United States is caused specifically by blade damage, according to Sandia National Labs. This percent is expected to increase proportionally to the increase in blade and tower size, as mentioned earlier (Sandia, 2014). The cause of damage of the blades can be any and all of the following reasons: environmental (lightning, hail, etc.), construction error (fiber waviness, poor bonding of adhesives, etc.), and general operational fatigue.

Another aspect that needs to be taken into consideration is that when damage in the blades occur, they begin to lose efficiency (Sandia, 2012). Every company wants all of their wind turbines operating as efficiently as possible, but damage can go undetected beyond when the decrease in energy output occurs because it goes unnoticed by the employees overseeing it. If these internal and complex damage modes go undetected long enough, they will eventually lead to catastrophic blade failure. These events can not only be very costly to the proprietor, but also very dangerous for the employees working on it. Siemens now makes blades that are 75 meters long and over 25 tons (Siemens, 2012). Structures that size are very dangerous and also cause a great deal of damage to its own tower and possibly other surrounding wind turbines when catastrophic failure occurs. Maintenance on blades causing downtime is something that most companies try to avoid, but it much preferred over total blade failure.

The only method to determine the damage type and progression of composite materials use to be to destroy the sample during internal inspection. As mentioned

earlier, when composite materials are mechanically tested they have many material interactions between the various interfaces of the different materials. It has been found that when these mechanical interactions happen, they emit certain frequencies. These frequencies are then identified as to pertaining certain events within the composite material structure (Bohse, 1986). The most important gain from using this method of damage detections is that the acoustic emissions (AE) can be recorded using ultrasonic sensors while the blade is still in operation and without having to destroy the blade, as was done in the past. Also, locational data can be obtained from this method. Recording of these emissions can be used to determine where a composite material windblade is along its life cycle depending on the type of internal damage. This type of test can also be used on small test coupons in a lab or it can be used for entire structures like windblades. That means the type of damage that is occurring can be detected in real-time and can also be located within a few millimeters inside of the blade. AE testing is quickly becoming the preferred method of damage detection for composites for these reasons.

Another obstacle to overcome, not only for wind energy companies but all composite material consumers, is that hindering growth is the great amount of variability in manufacturing. Due to the complexity in construction mentioned earlier, it leaves a lot of room for error. Composite material companies adhere to standards for manufacturing, such as in the Composites Material Handbook, to help eliminate this inconsistency. Due to the different assembly and manufacturing methods that can be used, the composite materials are not as consistent as isotropic materials despite the introduction of such

standards. The end product material properties typically vary greater than the design calculations and models (Nelson, 2013). Composite material companies have combatted this problem by increasing the factors of safety. This increase in safety factors causes the parts to be overdesigned, which greatly increases the weight and but also limits the size, thus limiting the efficiency and power generation (Riddle, 2013).

This research will investigate the damage progression behavior of composite materials through AE analysis during destructive testing and how various composite material assemblies can effect it. This will be accomplished by using coupons in tensile destructive testing, while AE is being recorded. Each sample group will have slight changes in fiber construction and ply assembly. Different assemblies will allow for different types of damage to occur but will also change how the damage progresses through the samples. The various layups and material construction will also change the mechanical properties of the samples during testing, which is also of interest. AE signals recorded will allow for accurate analysis of the cause and progression of damage comparable to destructive inspection. The assertion of this research is that this data recorded can be extrapolated to full scale windblades.

2. BACKGROUND

Composite Materials

A composite material is defined as any material containing multiple constituent materials wherein the final material has properties representative of the whole and not of the individual constituents (Barbero, 2011). Typically, they are put together in a way so that the most desirable qualities of both of the original materials are present in the final, assembled material. The most common forms of composite materials used in wind energy are fiber or particle reinforced. The fibers are usually made of very stiff material that is bonded together and supported by a material that is called the matrix material. Some composite materials have been used for hundreds of years, such as ancient Mesopotamians using straw to reinforce mud bricks used in buildings or the Mongol army in the 1200's using composite bows made of wood, bone, and silk. The development of polymerization in the late 1800's led to the creation of synthetic resins that could go from liquid to solid states. Finally, the invention of plastics and the use of fiber reinforcement in the early 1900's led to the types of composites most commonly used today (Mar-Bal, 2013). Probably the most common composite material that has been instrumental to modern society is the invention of concrete which is made up of cement and aggregate (rock, sand, or gravel). Fibers can be either organic (grass, bamboo, etc.) or inorganic (e-glass, carbon, etc.) (Barbero, 2011). Matrix materials for any application are most commonly elastic materials such as polymers or thermoplastics that reduce stiffness and weight. Other types of composites that have been developed

more recently are nanotube, metal matrix, and ceramic composites. Each type has a very specific set of material properties with specific applications and functions.

The most common types of composites used to build windblades are glass or carbon fibers with an elastic matrix material that is a polymer, known as glass fiber reinforced polymer (GFRP) and carbon fiber reinforced polymer (CFRP). The use of polymer significantly reduces the weight and stiffness of the structure, as mentioned earlier. Another consideration to take into account for windblades manufacturing is that polymers are much cheaper than the fibers used, whereas a blade made entirely out of metal would be substantially more expensive. The focus of this work is specifically on GFRPs.

Fiber Reinforced Polymer Composite Materials

The most common type of composite materials that are used for the manufacturing of windblades are fiber reinforced polymer composites (FRPC). These fibers are usually made of glass or carbon that are processed into a roll of fabric. These fabric rolls are unrolled and cut to specific dimensions that are then stacked on one another into certain orientations, called a layup. Each individual layer of fiber is called a ply. The layups are determined by how the composite structure is going to be used. Some layups are best when used in uniform loading direction in tension, but have poor strength when loaded in a transverse direction tensile force. Other layups can cause the FRPC to behave like an isotropic material, like metals.

Most fabrics consist of tightly bound fibers called tows, that are stitched together to make a tightly or loosely bound fabric mat. The tows are laid evenly side by side with

consistent thickness. The way these tows are oriented is what determines the layup. When the tows are all oriented in the same direction in a straight line are called unidirectional (UD) layup. A biaxial (biax) layup is when each of the plies are only oriented in one of two directions. For example, a composite material with only two plies, one that is oriented at 0° and the other is oriented 90°, is a biaxial layup. A tri-axial (triax) layup is the same premise as a biax, but with three fiber directions (Rusmee, 2005).

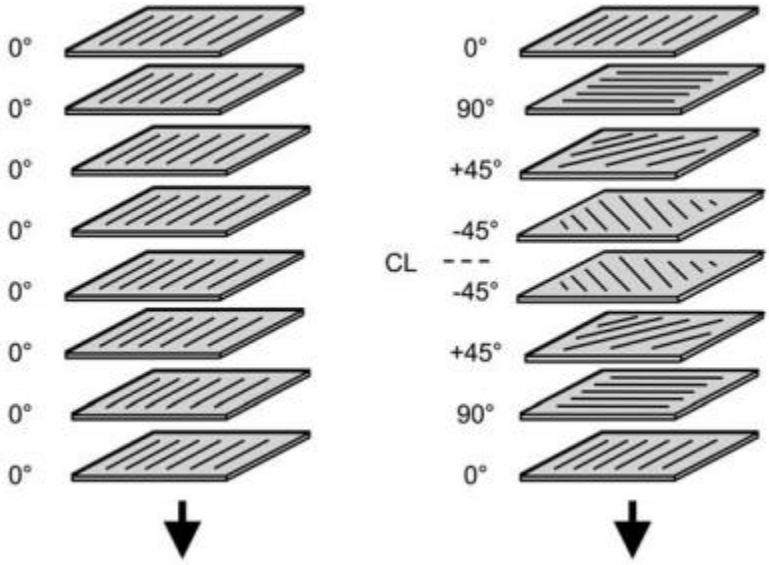


Figure 5: Examples of Unidirectional ($[0]_8$) and Quadriaxial ($[0/90/\pm45]_S$)Fiber Layups (Campbell, 2010)

To help support and stabilize the UD fibers manufacturers will stitch mats of randomly oriented fiber mats or chopped fiber strands to a side of the UD fibers. This is the most common form of stitching to stabilize UD tows in the wind energy market. The random fibers orientation impede crack growth and other forms of damage from progressing, which is vitally important in extending the lifetime of windblades (Swolfs,

2013). Another method of stabilization is to stitch transverse individual fiber tows to one side of the UD fiber tows. Any of these construction types used for support are referred to as backing. There are many other types of fiber construction that are used, such as weaves, which have advantages and disadvantages. These are discussed in greater detail later on.

The mats that are used in the finished composite material are stacked in layers can be at different orientations, materials, sizes and thicknesses; each one those layers is called a ply. The final composite material with multiple plies infused with the resin material, or matrix, to form a single adjoining material is called a laminate. As mentioned earlier, the stitching material is made of a secondary material that is typically low strength, relative to the fibers. This stitching is not normally accounted for in the designation of the composite. For example, a glass fiber composite with an epoxy matrix and polyester stitching is referred to as a glass/epoxy composite, completely foregoing the mention of the polyester.

For specifying the layup of a composite laminate, the most widely accepted notation is where angles are in brackets for each ply that indicate the direction of the primary fibers. The secondary fibers used for stitching are not indicated in the layup, but any time chopped strand fibers and other discontinuous fiber mats are included. For example, $[0]_n$ specifies that the primary fibers run in the 0° direction with respect to the loading direction while the n indicates that there are n numbers of repeated plies in this direction. Likewise, $[90]_n$ signifies that n numbers of plies are oriented perpendicular to the loading direction at 90° and $[90/0]_s$ indicates that plies are oriented at 90° and 0° and

this is then mirrored about a centerline to produce a symmetric four ply laminate, as indicated by the subscript "s." This standard notation allows for engineers and technicians to quickly determine the layup of the laminate.

The matrix material for FRP composites can be one of many different polymers. The most common polymers used in composite materials are thermoset or thermoplastic polymers. Thermosets are typically the most common matrix material used for composite materials because they require lower cure temperatures, which allow for simpler and less expensive production. The greatest disadvantage is that they result in having brittle behavior once cured. The most common thermosets include polyester, epoxy, phenolic, vinylester, polyurethane, silicone, and polyamide and epoxy. Epoxy is the most broadly used matrix resin system in the wind energy industry and other aerospace applications because of its improved flexibility and damage progression retardant over the other thermosets. For these reasons it is typically the most expensive of the thermosets. Another disadvantage is that it has the greatest difficulty bonding to glass fibers, causing the cure times to take much longer than the other thermosets. This handicaps the amount that can be produced in a limited amount of time, thus limiting the manufacturability. Thermoplastic matrices behave more flexibly, similar to common plastics, once cured but are more difficult to work with and manufacture (Cervanka, 1999).

The scanning electron microscope (SEM) image below, Figure 6, is an example of a multiaxial multiple ply laminate composed of 0° and 90°. The fibers that are seen running parallel are the 90° fibers. The fibers that are perpendicular to those, that look

like small circles coming out of the page, are the 0° fibers. This specific image also features areas without visible fibers, which are referred to as resin rich areas; this will be discussed in greater detail later on. Another feature in this image are regions of porosity and some large voids, which appear as white circular shapes that vary in size. This is the most common, but most undesirable defect produced in the manufacturing process of FRPs.

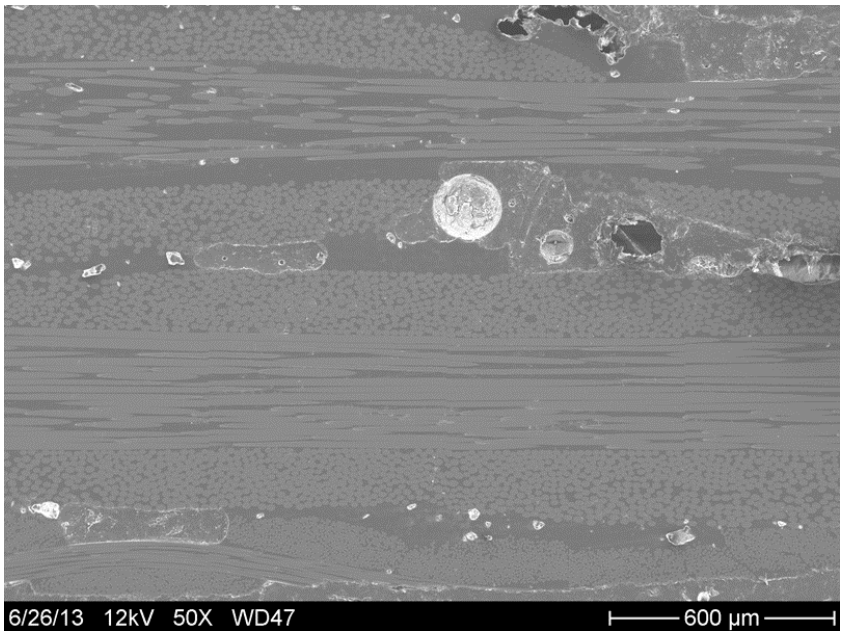


Figure 6: SEM Cross Section of an FRPC (Bauer, 2014)

Fiber Reinforced Polymer Composite Manufacturing

There are several different methods of manufacturing that can be used FRPCs. These methods vary greatly in overhead equipment costs, materials used and intensity of required manual labor. The most common forms of composite material manufacturing are hand lay-up, pre-preg forming, pressure molding, vacuum bagging, filament winding, pultrusion, spray method, sheet molding, bulk molding, resin transfer molding (RTM),

and vacuum assisted resin transfer molding (VARTM) (Qui, 2008); Figure 7 through Figure 17 illustrate these various processes.

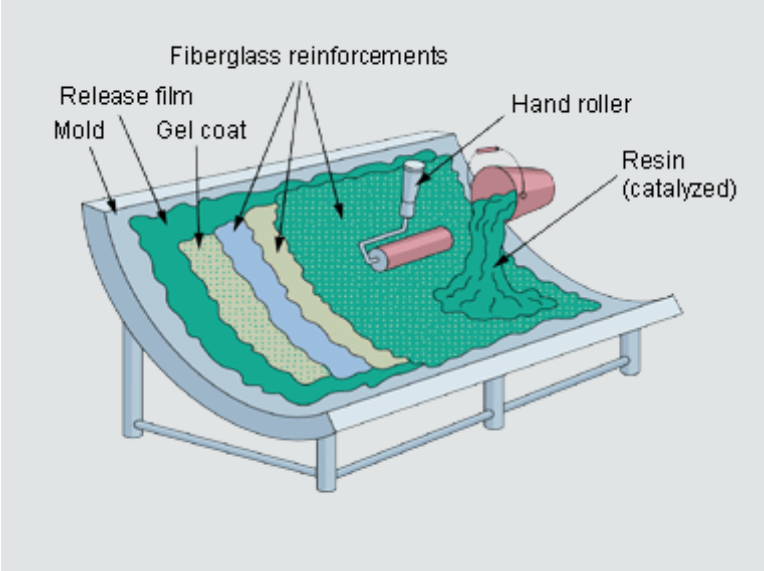


Figure 7: Diagram of a Hand Layup Process (Qui, 2008)

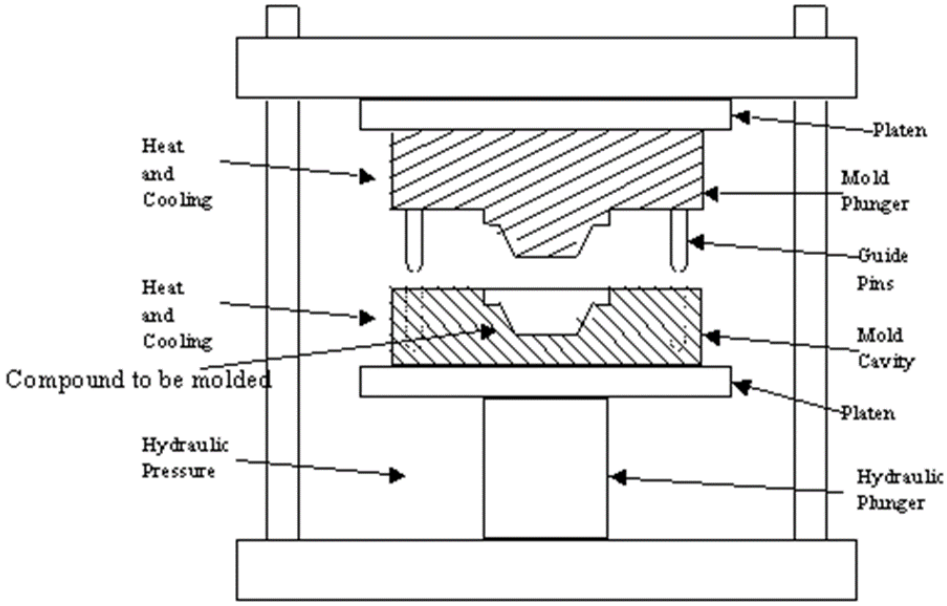


Figure 8: Diagram of Pressure Molding Manufacturing Process (Qui, 2008)

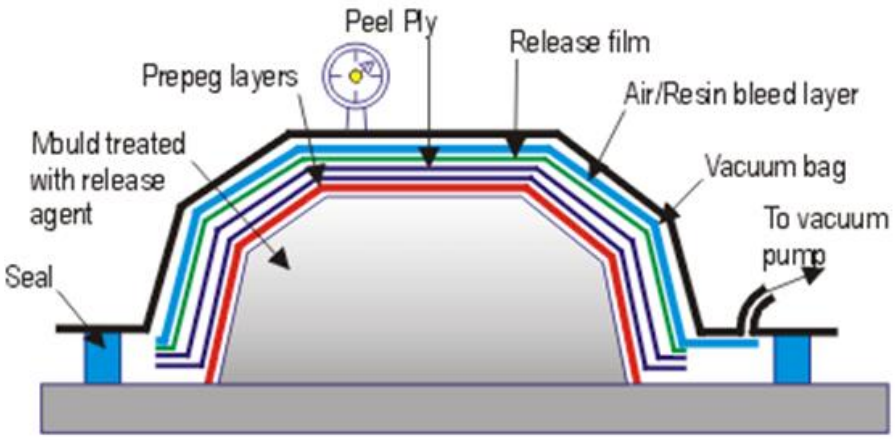


Figure 9: Diagram of Vacuum Bagging Manufacturing Process (Qui, 2008)

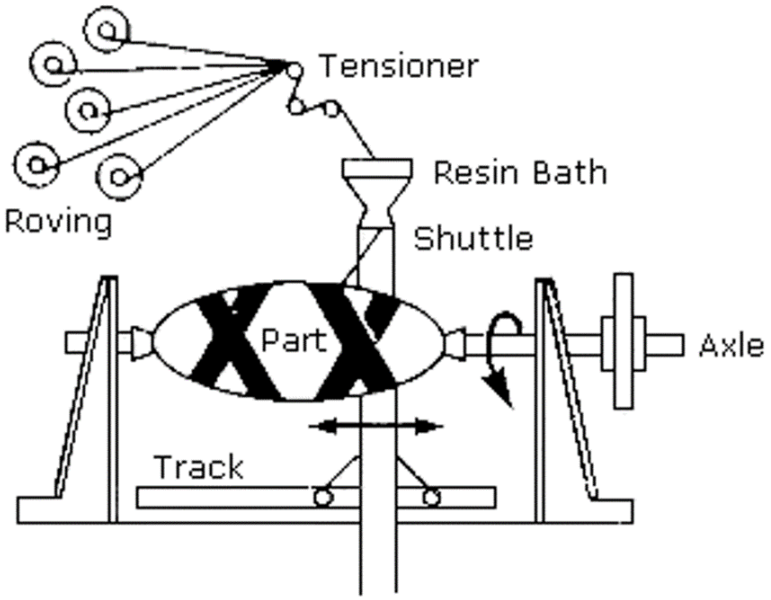


Figure 10: Diagram of Filament Winding Manufacturing Process (Qui, 2008)

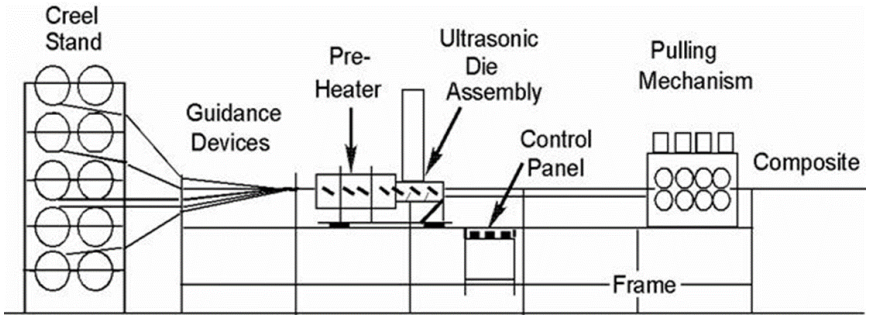


Figure 11: Diagram of Poltrusion Manufacturing Process (Qui, 2008)

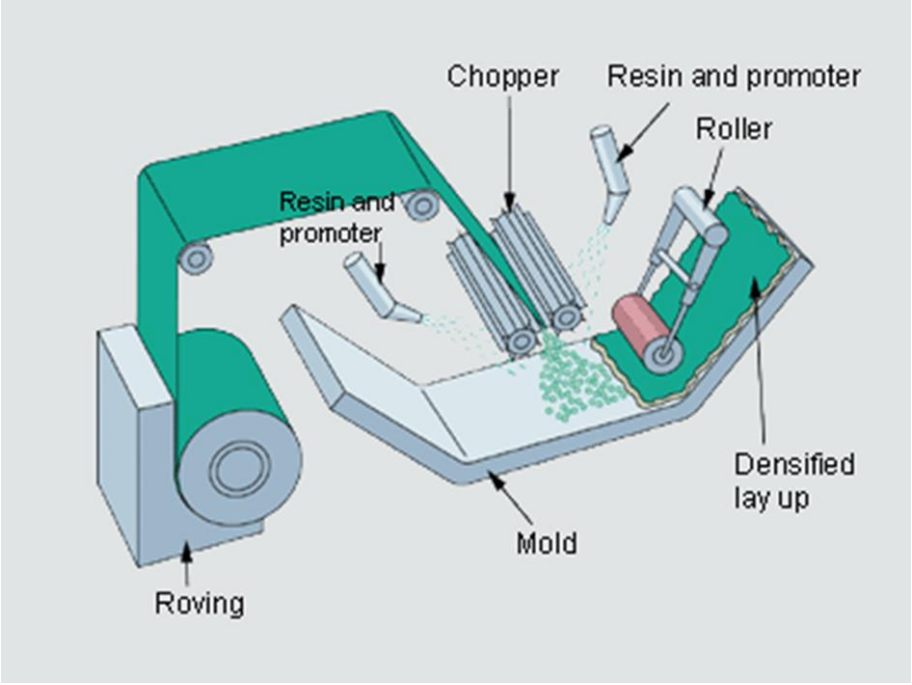


Figure 12: Diagram of Spray Method Manufacturing Process (Qui, 2008)

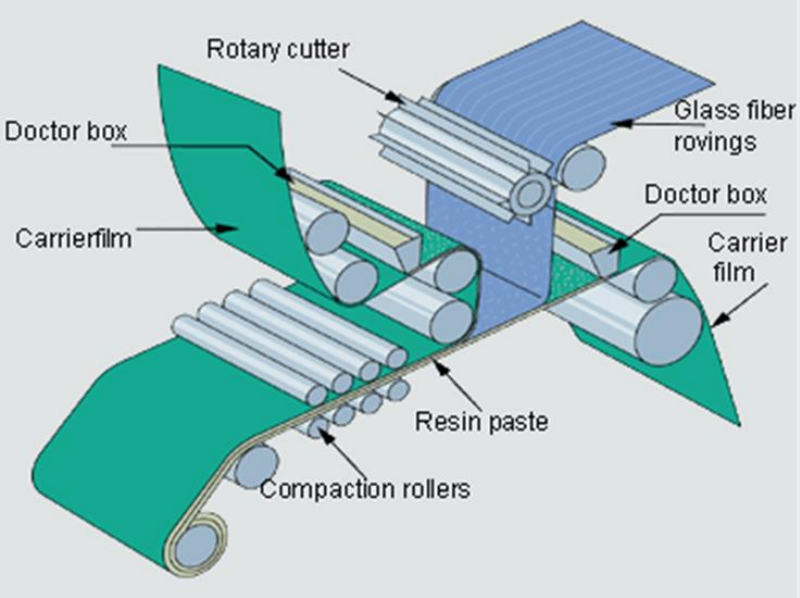


Figure 13: Diagram of Sheet Molding Manufacturing Process (Qui, 2008)

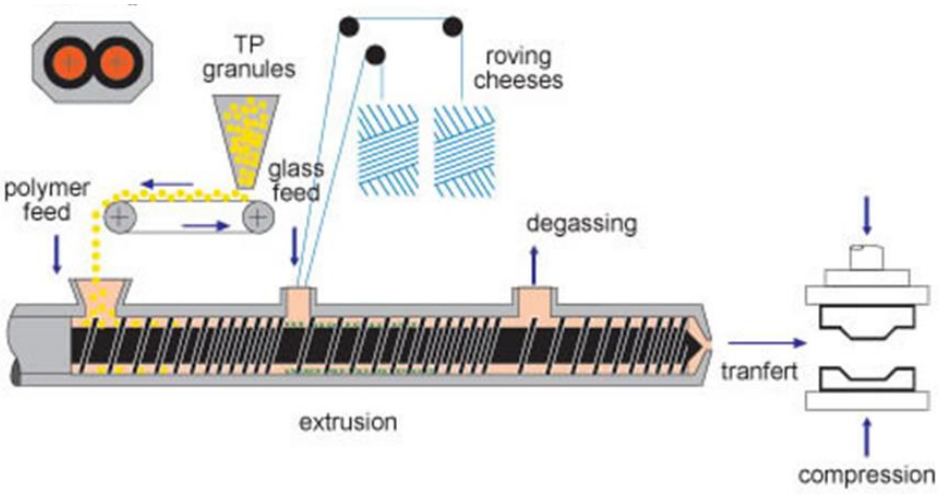


Figure 14: Diagram of Bulk Molding Method Manufacturing Process (Qui, 2008)

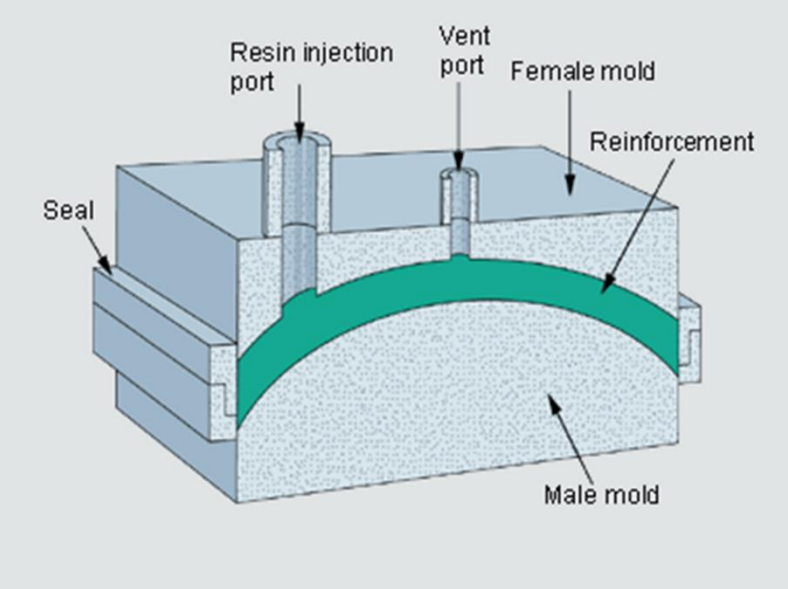


Figure 15: Diagram of RTM Manufacturing Process (Laminating System, 2011)

Table 1 below highlights the advantages and disadvantages of all the manufacturing processes. VARTM and pre-preg forming will not be included in this table, but will be discussed in detail later.

Process	Advantages	Disadvantages
Hand Layup	• Low cost tools • Versatile geometry	• Slow speed • Air bubbles and fiber skewing • Inconsistent
Pressure Molding	• Versatile geometry • Integrate parts • Consistent • Structural stability • Relatively simple	• High machine costs • Time consuming • Expensive molds • Simple geometry • Large production volume
Vacuum Bagging	• Simple geometry • Any fiber/matrix combination • Cheap mold material • High quality for the cost	• Low heat • Breeder cloth short lifespan • Low pressure • Slowest speed and inconsistent
Filament Winding	• Uses existing textile processes • Easy to handle package • Parts can have huge size	• Spinning speed is limited • Curing heat is hard to apply • Only cylinders possible
Pultrusion	• High speed automation • Versatile geometry • Continuous reinforcement	• Die can be easily ruined • Expensive die • Mainly thermoset matrix
Spray Method	• Continuous process • Any materials for mold • Error can be corrected by re-spraying	• Slow and inconsistent • No control of fiber orientation • Only one side finished • Environmentally unfriendly
Sheet Molding	• Inexpensive • Consistent	• Low fiber volume • Only flat plates can be made
Bulk Molding	• Highest fiber volume • Good mechanical properties • Finish can be applied • Inserts and attachments possible	• High temperature and pressure • No control of fiber orientation • Simple geometry • Staple fibers only
RTM	• Good surface finish • High uniformity • Can be automated • Complex structural and hollow shapes	• Waste material (spill) • Long curing time • Simple geometry

Table 1: Advantages and Disadvantages of Different Manufacturing Processes

VARTM. Windblade production predominantly utilizes the VARTM process but also uses aspects of hand layup. Blades are usually produced in an open mold to create a closed press style assembly featuring the two cured halves that are adhered together with

an inner spar running down most of the blade. VARTM processes are almost exclusively used by the MSUCG to create flat plates with varying thickness, sandwich beams, spar caps and other complex geometries commonly used in the wind industry. At MSUCG they preferred method of the VARTM process starts by placing peel ply on an aluminum mold, then fabrics placed at the angles and layups that are desired, then another peel ply layer, then flow media on top of that, then finally a plastic vacuum bag over the entire stack that is sealed with tacky tape around the sides of the mold. Injection ports and vacuum ports for the resin matrix material infusion are machined into the mold, which is the preferred process for the MSUCG. Suction is applied to the laminate through the port to create a vacuum inside the stack which is sealed by the tape. When this happens it compresses the fibers and helping to remove any voids found in the fabric stack. After the vacuum is the best it can be, since it is never going to be a perfect vacuum, resin is suctioned into the fiber stack and to saturate the fibers. The matrix material used for this research is epoxy resin, since that is the most common matrix material used to manufacture windblades. The epoxy is cured for at room temperature, typically 25°C, for 48 hours on the mold while it is still sealed under a vacuum. Then a post cure is applied by taking the stack, which is now called a laminate, off the aluminum mold and stripping off the peel ply and bagging material and placing it in an oven at 60°C for 12 hours.

Figure 17 displays a detailed diagram of the stacking sequence and resin transfer process for VARTM manufacturing.

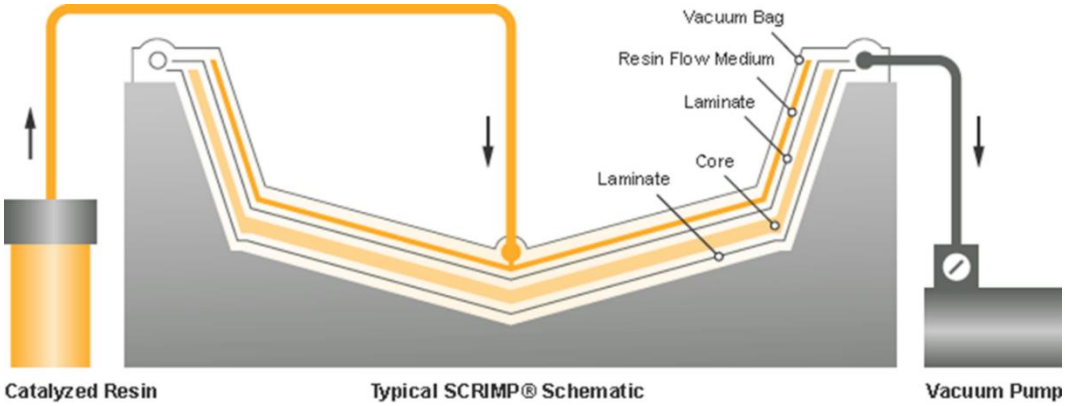


Figure 16: Diagram of VARTM Manufacturing Process (VARTM Infusion, 2006)

Pre-Preg. Another common composite manufacturing process is using pre-impregnated fabrics, commonly called pre-preg, which is predominantly used for smaller and more geometrically complex parts. There are two processes to make prep-preg composites. The first is called the hold melt process, which can be used for woven and UD fibers. It is a two-step process, the first stage involves coating a thin film of resin material that is heated onto a paper substrate. The fabric mat is saturated in the resin while it sits in an autoclave. Once it is properly saturated, the autoclave is activated to apply heat and pressure. The pressure fully impregnates into the fabric, resulting in a finished pre-preg, which is then wound onto a core. The second is the solvent dip process, which can only be used for UD fabrics. It is typically automated where the fabric is placed on a conveyor and first pulled through a solvent resin bath to impregnate. Then it is pulled through a drying oven to evaporate of the resin. The final step is the pre-preg fabric is pulled through a separator roll to scrape off excess resin and to give it a

better surface finish. This process ends with the composite being wound on a roll. When the manufacturer sells it to a customer it needs to be refrigerated until it is ready to be used. The laminate that is created is really only half cured so the customer then takes it and unrolls as much as needed then places it in an oven for the final curing process to create the finished laminate .

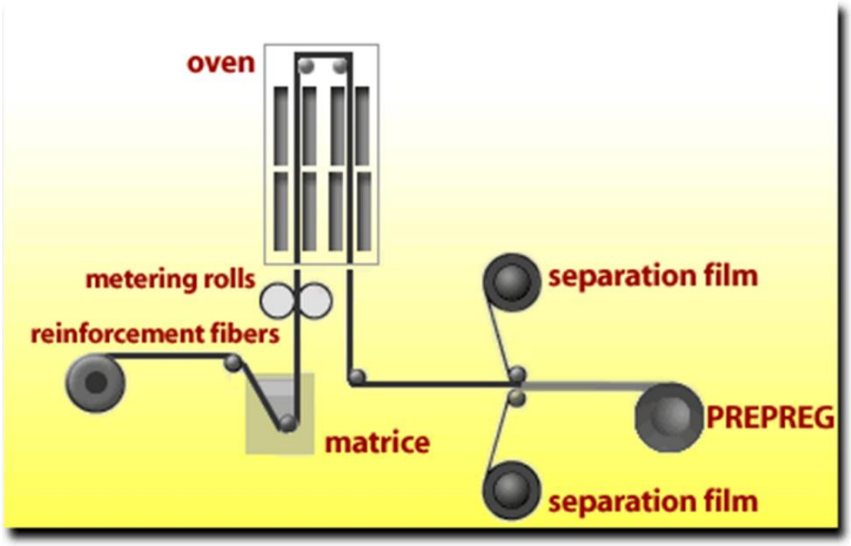


Figure 17: Diagram of Pre-Impregnated Manufacturing Process (Qui, 2008)

Assembly and Geometry of Different Fabric Types

Most often when fabrics used for composites materials are produced in a flat sheet with long fibers that can be made of carbon, aramid, glass, or a combination of them. The flat sheet construction makes for easier layering that can be held together by mechanical interlocking of the fibers or a secondary structure that binds the fibers together so that the assembly has the proper integrity to be used without falling apart. Common fabric construction includes, but is not limited to UD, woven, hybrid,

multiaxial, chopped strand, tissue, and braided fabrics (Fabric Types, 2015). UD, multiaxial and chopped strand fabrics will be the focus of this research.

Unidirectional Fabrics

Unidirectional fabrics are ones that have between 75% and 90% of its fiber tow weight pointed in the same direction, depending on the manufacturer. The primary reason for having tows pointed in the transverse direction is to ensure stability for the primary fibers, as seen in Figure 6. Only pre-preg composite materials have no other fibers in any other direction, which will be discussed later. The tows are straightened to the best of the manufacturer's ability to deter crimped tows that would have an adverse effect on the mechanical properties of the finished composite (Unidirectional Fabric, 2015).



Figure 18: Example of Unidirectional Fabric with Transverse Fibers (Selcom, 2016)

The purpose of stitched UD fabrics is to gain the optimal mechanical properties of the fibers. This is due to the fact that there is less secondary material than a woven fabric, for example and it also has more uniform mechanical properties when all the tows

are pointed in the same direction. These mechanical properties can only be improved upon when they are made for pre-preg, due to the complete lack of secondary material or fibers in transverse directions to hold the primary fibers in place. Most often, when a UD fabric is made that is not used in pre-preg or has no fibers in the transverse direction, it is required to have a tissue or matting material to hold them in place.

The secondary material can have several adverse effects on the properties of the fabric. The first is that the tissue or mat combined with the stitching holding it to the UD fibers tends to have a parasitic effect on the strength of the finished composite. The secondary material tends to be a polyester or some other type of material that usually has lower strength than the fiber material. This is volume of the composite material dedicated to inferior materials, strength-wise. The next negative of having to use stitching and tissue or mats is that it can also cause the weight of the fabric to increase a great amount. This can be problematic in applications that have strict weight requirements that must be adhered to. This also includes a financial cost, due to the fact that the heavier fabric costs more to ship for the same amount of fabric that would have no stitching. The final detraction is that the UD tows can be very difficult to set up initially, thus costing more for the manufacturer because of labor costs. This is combined with the cost of added stitching materials.

Multiaxial Fabrics

Multiaxial fabrics consist of one or more layers of fiber tows that are held in place by a secondary material stitching, unless it is being used for pre-preg. Once again, the secondary material is usually polyester because of its low cost and weight. The stitching

allows the fibers tows to be oriented in essentially any direction the consumer wants it to be (Multiaxial Fabrics, 2015). As the name suggests, multiaxial fabrics will have a variety of fiber orientations, rather than the single direction of UD fabrics, as shown in Figure 19.



Figure 19: Example of a Multiaxial Fabric (Selcom, 2016)

These types of fabrics are typically made using one of two methods: weave and stitch or simultaneous stitch. The simultaneous stitch method requires specialized machines that use knitting processes. These machines have a frame that pulls each ply simultaneously so that they are stacked and assembled into the desired geometry. After that the plies are stitched together all at once until they are pulled from the frame with the finished fabric, as shown in Figure 20. The weave and stitch method is usually done by taking UD tows in the 0° and 90° directions and weaving them together into a single ply. If the ply is made to be at any orientation other than 0° and 90°, the single 0/90° ply is skewed until they are at the desired angle. If there are multiple skewed plies to combine,

they are laid on top of each other in the desired orientation then stitched together using a simple stitch frame, as shown in Figure 21.

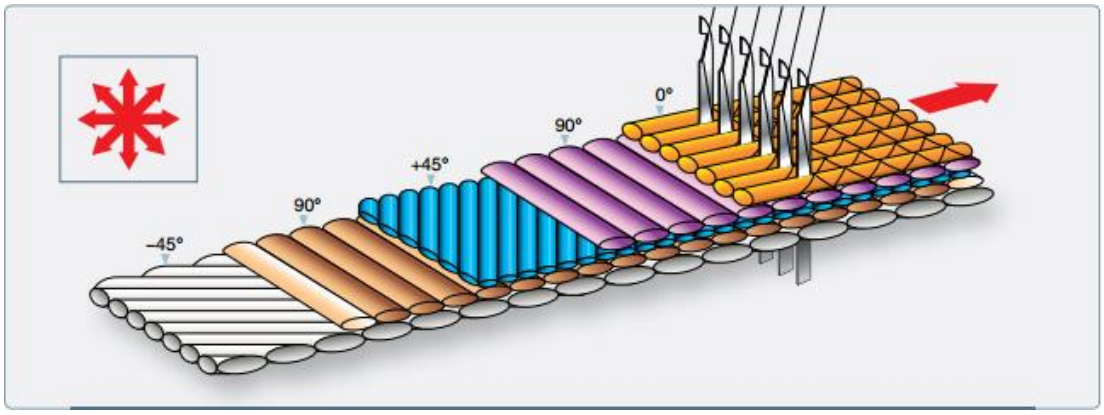


Figure 20: Simultaneous Stitch Process for Multiaxial Fabrics (USDoT, 2012)

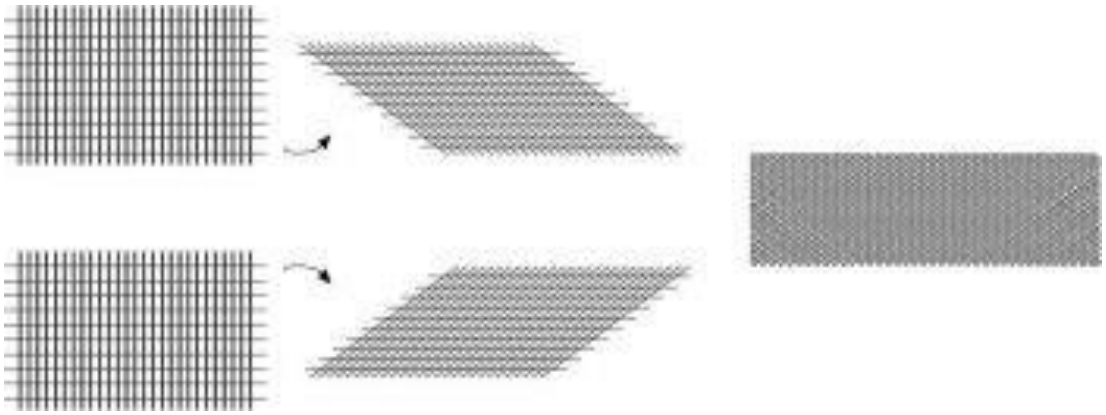


Figure 21: Weave and Stitch Method for Multiaxial Fabrics (Multiaxial Fabrics, 2015)

Multiaxial fabrics have begun to be the preferred type of fabric in recent years due to several advantages. First, the fiber tows are pulled straight so as not to crimple, similarly to UD fabrics, which provides optimal strength. Next, they require less layers than a UD fabric because the multiple orientations in a multiaxial fabric require fewer layers to achieve essentially the same effect. For example, if a consumer wants to create a layup that is [0/±45/90] using only UD fabrics it will require four layers to do so.

Whereas a multiaxial fabric could recreate the same layup using only one or two layers. Finally, it is more advantageous to use because the assembly time can be significantly faster than that of UD fabrics. They can be made thicker with more fiber orientations contained in a single layer, allowing for faster construction for the consumer that could be working on a project with size requirements. The multiple orientations can all be contained in a single layer, as mentioned earlier, which lends itself to faster assembly time for a finished product.

There are some disadvantages using multiaxial fabrics that can deter consumers from using them, depending on the application. The stitching can have a more difficult time holding the tows together compared to UD fabrics, due to the increased complexity of the construction. This means that wicking or damage initiation is more likely to occur at the stitching locations. It still holds that assembly time for the consumer can be reduced, but it usually increases from the manufacturers end. The complexity of each layer typically requires more time to assemble. The complexity of each layer also requires more advanced machinery to assembly them. This is combined with the fact that more expensive and lower density fibers are normally needed to achieve quality surface coverage for low weight fabrics, which means the relative cost of high quality fabrics that are stitched can have a significant increase in price compared to that of other fabric types. Another downside to these types of fabrics is that the increase in thickness for each layer, especially for heavy fabrics, can be very difficult to impregnate with the resin material. This can create composite structures that can have incomplete infusions, which is generally not desired. The final disadvantage is that the stitching process can have many

problems with current methods and machinery. Typically this is manifests by a bunching together of the fibers, especially for the fibers in the 0° fiber direction. This bunching up can create what are called resin-rich areas. These are areas in the finished composite that are large pools of matrix material with no fibers, as shown in Figure 22. This can negatively affect the mechanical properties by making them weaker in those areas.

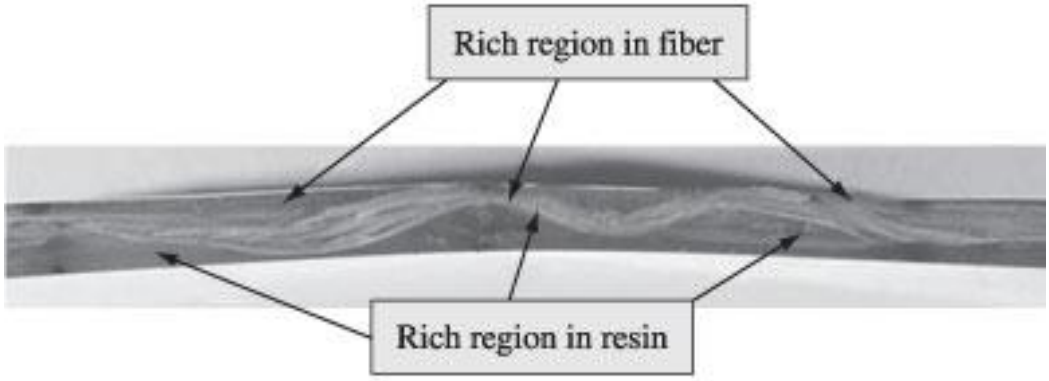


Figure 22: Example of Resin Rich Area in a Composite Structure (Leão, 2011)

Chopped Strand Mat

Chopped strand mats (CSM) are made of randomly oriented strands of fibers, usually between three or four inches, that are unwoven or stitched, as seen in Figure 23. Instead of using weaving methods or stitching material, they are typically held together with a binding adhesive material or a polyvinyl acetate (PVA) emulsion. The reason that PVA is commonly used is because it is water resistant, and CSMs are most often used for marine applications. This is due to the fact that the randomly oriented fibers provide for a more even distribution of stress due to uniformity of the physical properties (isotropic) which is important when submerged under water because of the hydrostatic pressure on the structures. This is unique in that most composite materials are not isotropic

(anisotropic), as mentioned with for UD fiber composites. Another advantage of using CSMs is that they tend to be the least expensive of the fabric types. The simplicity of throwing random fibers into the shape of a mat then treating it with an adhesive makes it very quick to manufacture. Also, the use of binders or PVAs tends to be cheaper than secondary materials like tissue or stitching (Other Fabrics, 2015).



Figure 23: Example of CSM (Chopped Strand Mat, 2015)

CSMs are not typically used for structures that are used in high loading scenarios. The fibers in many directions and being layered on top of each other causes there to be more voids than an average fabric made of fiber tows, thus making it impossible to have a high fiber density. This means CSMs cannot have high strength-to-weight ratios. Another limiting factor is that it tends to be only compatible with polyester matrix materials. The surface tension and gel time of other matrix materials can cause the composite to not be completely saturated when cured.

Woven Fabrics.

Woven fabrics are created by interlacing 0° and 90° fiber tows. The strength of the fabric comes from the mechanical interlocking of the tows, causing them to support one another. The primary benefits of this fabric type are the conformity to complex surfaces, surface smoothness, and the advanced stability, i.e. not crimping of the tows commonly found in UD fabrics. The most common setback for this style of fabric architecture is that it requires advanced machinery to accomplish this effect. The most commonly weave styles are plain, twill, satin, basket, leno, and mock leno.

Plain Weave. A plain weave is a simple weave in which the 0° and 90° tows interlace with each other and tends to be very symmetrical and good stability, as seen in Figure 24. The drawbacks of this structure are that it tends to have high porosity and is much harder to conform to complex surfaces. Due to the lack of conformity, it tends to crimple the easiest of the weave styles, which is made worse by larger fiber tows. The increase in crimping causes this weave style to also have the lowest strength relative to the others.

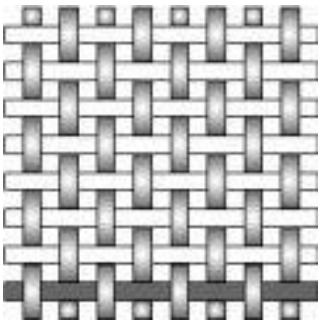


Figure 24: Diagram of a Plain Weave Fabric (Woven Fabrics, 2015)

Twill Weave. Twill weave construction 0° fiber tows that weave under and over two of the 90° fiber tows in a consistent, repeated pattern through the entirety of the fabric, as shown in Figure 25. This structure causes a superior infusion of the resin during manufacturing. It also has a much improved conformity to surfaces, which is why it is the most common weave style for complex structures. It has less crimping than the plain weave, thus slightly higher strength and smoother surface finish. The main drawback of the twill weave is that it creates diagonal 'rib' in the fabric, which is where it tends to fail under mechanical load.

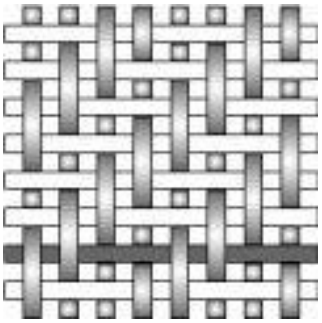


Figure 25: Diagram of Twill Weave Fabric (Woven Fabrics, 2015)

Satin Weave. The satin weave are fundamentally the same as twill weaves but assembled in a way so that the intersections between the 0° and 90° tows are reduced. These weaves are categorized by the harness number, which is the number of tows passed over and under before the pattern is repeated. The most common harness numbers are 4, 5, and 8. Various types of satin weave fabric construction are shown in Figure 26.

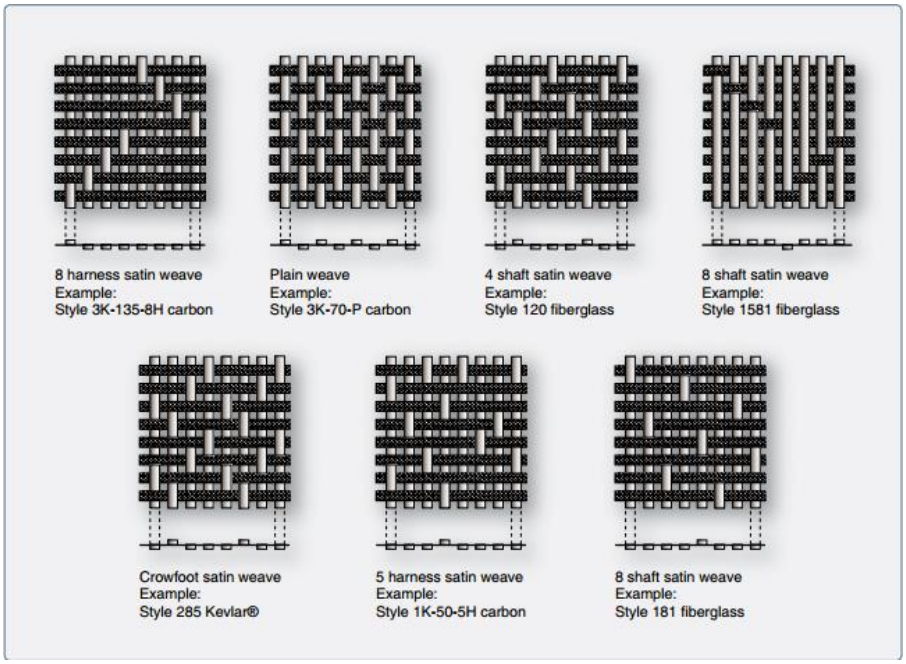


Figure 26: Various Diagrams of Examples of Satin Weave Fabrics (USDoT, 2012)

The biggest benefit of using this style of weave is that they come out to be extremely flat, thus have superior surface smoothness, and very good infusion when injected with resin. The superior flatness greatly reduces crimping, thus creating superior strength and conformity to advanced complex surfaces. This weave style also creates the closest fiber tows, giving a very high fiber density in a finished composite material. The greatest drawbacks of the satin weave are the reduced stability and asymmetry. Since these fabrics have 0° fibers that are dominant on one side while having 90° fibers on the other. This can cause asymmetry and to pre-stress the composite structure. Great consideration must be taken when layup of the plies is being constructed.

Basket Weave. Basket weave is essentially the same as a plain weave except that two or more 0° fiber tows interlace under and over with two or more 90° fiber tows, but not necessarily symmetrically. This weave is flatter causing it to have reduced crimping

than a plain weave, thus a higher strength under mechanical load. The main problem with the basket weave is that it has greater instability than the plain weave. This forces the manufacturer to use almost exclusively larger and heavier fibers to avoid crimping. The common designation for the weave is the number of 0° fibers by the number of 90° fibers. For example, three 0° fibers tows interlacing with five 90° tows would be designated a 3x5 basket weave. Figure 27 below shows an example of a 2x2 basket weave fabric.

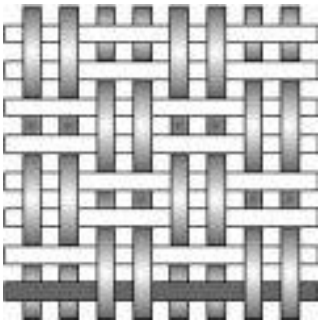


Figure 27: Diagram of Basket Weave Fabric (Woven Fabrics, 2015)

Leno Weave. The leno weave is a variation of a plain weave in which nearby 0° fiber tows are twisted around consecutive 90° fibers to form a corkscrew pairing, as seen in Figure 28. This forces each 90° tow to be locked into place. This type of weave is used exclusively to provide extra stability for open fabrics, which means that it can only be used in conjunction with other fabric types due to the lack of low fiber density and strength.

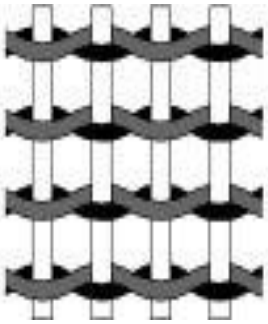


Figure 28: Diagram of Leno Weave Fabric (Woven Fabrics, 2015)

Mock Leno Weave. Mock leno weave pattern is essentially the same as a plain weave in which occasional 0° fibers at regular intervals and usually several fibers apart and deviate from the alternate under and over interlacing, and instead interlace every two or more fibers. It occurs with equal frequency in the 90° direction, and the overall effect is a fabric with increased thickness, rougher surface, and increased porosity.

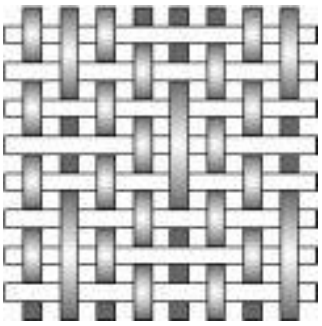


Figure 29: Diagram of Mock Leno Weave Fabric (Woven Fabrics, 2015)

Each type of weave pattern has their benefits and hindrances, with each being optimal in different applications. Table 2 below has a detailed breakdown of the various types of woven fabrics and there advantages and disadvantages regarding mechanical properties. Drape is the ability of the fibers to naturally conform to a shape. Low crimp is the fibers ability to resist waviness and kinks in the tows during manufacturing.

Overall, woven fabrics are generally the most expensive to fabricate and are not used unless high strength-to-weight ratio is the most desired property. The use of woven fabrics is steadily increasing as manufacturing equipment advances in efficiency and will probably be the standard for composite materials in the near future.

Property	Plain	Twill	Satin	Basket	Leno	Mock Leno
Stability	Good	Acceptable	Poor	Poor	Excellent	Acceptable
Drape	Poor	Good	Excellent	Excellent	Acceptable	Very Poor
Low Porosity	Acceptable	Good	Excellent	Poor	Very Poor	Poor
Smoothness	Poor	Acceptable	Excellent	Poor	Very Poor	Poor
Balance	Good	Good	Poor	Good	Poor	Good
Symmetrical	Excellent	Acceptable	Very Poor	Acceptable	Very Poor	Good
Low Crimp	Poor	Acceptable	Good	Poor	Poor/ Excellent	Poor

Table 2: Comparison of Properties of Various Weave Patterns (Woven Fabrics, 2015)

Hybrid Fabrics

Hybrids are fabrics that use more than one type of fiber in its construction. Traditionally, when multiple mechanical properties are desired the consumer will use multiple plies with each ply using a different material for fibers. This method is limited in application in cases where low weight and thin laminates are the most important features. Hybrid fabrics allow for two different materials of fibers with completely different mechanical properties to be combined in a single ply. The most common construction of hybrid fabrics features each fiber tow alternating material. Less commonly, hybrids can be constructed so that the two materials are woven where one material is in the 0° direction and the other in the 90° direction, but this can be very expensive and time consuming. They are usually made as woven fabrics that are 0/90°, but can also be applied to multiaxial and UD fabrics. The most common material combinations for hybrid fabrics are carbon/glass, aramid/glass, and carbon/aramid.



Figure 30: A Carbon/Aramid Hybrid Fabric (Yellow is Aramid, Black is Carbon) (KEVLAR®/ Carbon Hybrid, 2010)

Carbon/Glass Hybrids. This is the least expensive form of hybrid fabric because the glass is mostly used as filler material. The glass has substantially lower tensile and compressive strength but it is much cheaper than the carbon. For example, some research has found that these hybrid fabrics have a 37.4% lower tensile strength and a 16.5% reduction in compressive strength, but a 6.4% increase in weight compared to all carbon composite materials. All-glass composites have a 52.4% reduction in tensile strength and a 55.0% reduction in compressive strength, with a 21.9% increase in weight (Zhang, 2012). The combination results in a fabric that is stronger than glass but also lighter.

Aramid/Glass Hybrids. Aramid is a manmade fiber that is made from the organic polymer that is called an aromatic polyamide which is made from spinning solid fiber tows from a fluid chemical compound. It is most commonly known by the proprietary Dupont name 'Kevlar' in which it was invented. It has extremely high impact resistance and low density so it is commonly used in applications like personal protection and the military. Aramid fabrics also have very low compressive strength, analogous to that of glass fibers. It also has high resistance to physical and chemical wear, but can degrade when exposed to ultraviolet light (Aramid Fiber, 2015). Similarly to carbon/glass hybrids, the glass is mostly used as filler material to lower cost. The only difference between an aramid/glass hybrid and an all-glass fabric is that it has much higher impact strength, attributed to the aramid material, otherwise the tensile and compressive strengths are comparable.

Carbon/Aramid. This is the strongest of the three common hybrid fabrics. It has very high tensile and compressive strength due to the carbon fibers and very high impact resistance from the aramid fibers. Also, since both carbon and aramid have lower density, it is a very lightweight material. This is also the most expensive of the three hybrid fabrics presented here (Hybrid Fabrics, 2015).

Other Fabric Types

Many other types of fabric construction are used for composite material, each with their own advantages and disadvantages and unique properties. The focus of this research will not explicitly use these types of fabrics other than as other than as a component of other fabrics, but a brief explanation of each will be needed when discussing certain aspects of various tests and manufacturing methods.

Braided Fabrics. Braided fabrics are produced by interlacing fiber tows in a spiral shape to produce tubular structures. The diameter of the tubular fabrics are determined by the number, angle, number of intersections, and size of the tows. Fiber tows can be oriented at an angle of ±45°, 0/90°, or between the angles of 25° and 75°. That is all determined by the number and size of the tows. The angles, thus the diameter of the tube, can be manufactured so that they vary along the same tubular structure. Typically, the narrower angle will produce smaller diameters while the wider angles will provide a larger diameter. Braided fabrics are most typically used for antenna structures, boat masts, and drive shafts for lightweight race cars.

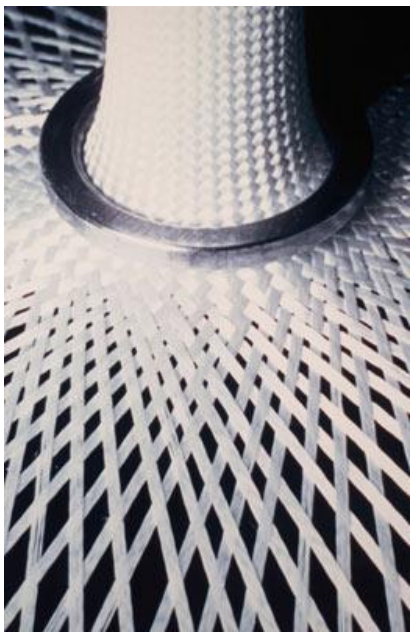


Figure 31: Braiding Process of Glass Fibers for a Tubular Structure (Braid Basics, 2016)

Tissues. Tissue fabric is made with continuous filaments of fiber spread uniformly but randomly over a flat surface. They are typically bound together using organic bonding agents such as PVA or polyester. They or not normally used as primary reinforcement fibers, mostly due to their relatively low strength. They are most commonly used as a surface layer on one side of a fabric to provide a smoother surface for the finished composite. If a composite is cured without a tissue layer on the outside it can create a rough surface finish that would be the same surface of the fiber tows, referred to as print-through, which can be undesirable, depending on the application. Tissue is most commonly made out of glass fiber due to its very high resistance to corrosion, helping to provide longevity to a composite material structure.

Damage Progression for Composite Materials

Composite materials have specific classifications for types of damage that are all unique in how they are initiated and progress. The is caused by the fact that the fibers and matrix materials tend to have substantially different mechanical properties in different directions within a laminate, which as mentioned earlier, is known as anisotropy. Polymer matrices, in this case it is epoxy, have low strength and low stiffness. The matrix has isotropic properties that transfer loads and stresses throughout the material and to the surrounding materials effectively. Whereas, the fibers have high strength and high stiffness, but are not nearly effective as a standalone structural material. Individually, unsupported fibers behave comparably to rope; meaning they cannot hold load that is compressive. Also, they tend not to perform well when a transverse load is applied. These two features mean that the fibers are typically only effective with tensile, axial loads. The dissimilarity of strength and stiffness at the fiber/matrix interface lead to a certain type of damage, while the individual constituents have their own individual damage mechanisms. A composite can experience a single type of damage leading to failure, but most often there are multiple types of damage leading up to that point. There are many motives for why a type or types of damage manifest within the laminate. Mostly they are dependent on the materials present for both the fibers and matrix materials, the orientations of the fibers and how the laminate is loaded. A single instance of damage does not entail total failure of the composite material. The reality, according to this research, is that much of this damage can occur unnoticed by humans but will alter the physical state of the composite. Eventually, if enough damage is accumulated for one

or all of damage types, the part will fail. It is these complex interactions and damage mechanisms that occur in a non-homogenous, fully orthotropic material system that complicates failure and requires greater understanding.

Matrix cracking is typically the earliest type of damage to manifest during loading and can lead to failure in a weakly supported material, depending on the layup. The cracks usually initiate from one or more of a few different reasons. The first is a defect in the matrix material. The second is at the material interface of the fibers and the matrix. The last is the presence of some other occurrence of a sharp radius at the edge or center of the laminate. These cracks will propagate through the matrix transverse to the stress acting on the initial crack. This type of damage occurs as a result of low strength and/or brittle behavior of a thermosetting polymer, like epoxy. If there are no fibers in a contiguous ply that is perpendicular to the crack matrix it can fail the part once the crack reaches a critical length. Otherwise, the load that is present in the matrix is distributed to the surrounding materials. A diagram of matrix cracking and how it propagates can be seen in Figure 32.

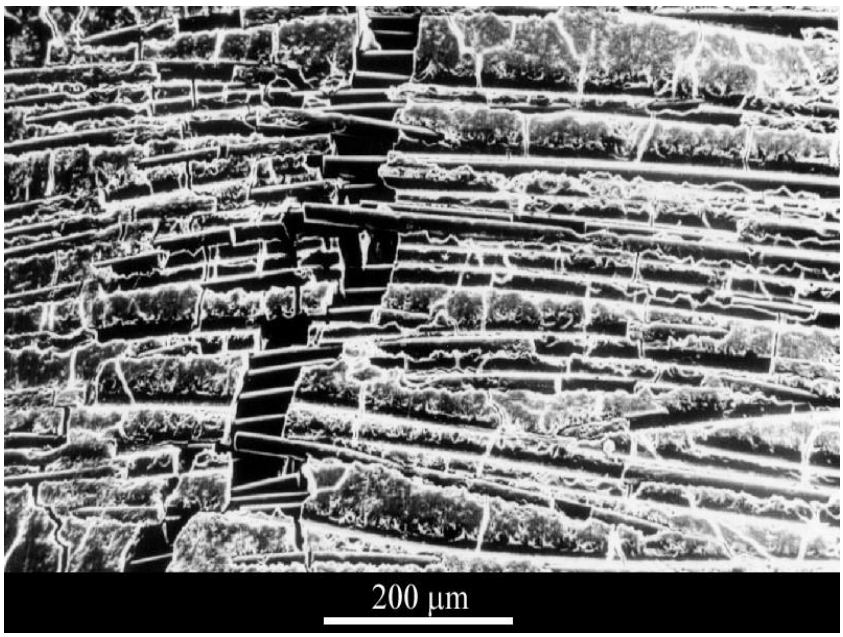


Figure 32: SEM of Matrix Cracking (Knowles, 2002)

Fiber pullout and debond are two similar damage mechanisms in which the interface between fiber and impregnated resin loses cohesiveness. The interface between the matrix and fiber materials separate and the overall composite material loses stiffness. Some scientists that have extensive research in the field of acoustic emissions in the use of composites combine the overall characterization as interphase failure, but there are differences. Fiber pullout is the result of excessive shear stress at the interface of the fibers and matrix. The fibers pull out and slip through the matrix in the direction of load. Fiber debond occurs before pullout when the load stress is greater than the strength of the interface and the two materials separate, but can sometimes occur independently. These types of damage usually require microscopic inspection methods post failure. The most common cause of this type of failure is normally due to lack of cohesiveness between the matrix and fibers. The cohesiveness can be dependent on fiber material, matrix material,

fiber construction, and manufacturing process. Interphase and matrix failures are known as having lower fracture energy, thus they often occur at lower loads and strains for a statically loaded material (Cantwell, 1992). Sample failure due to these modes is uncommon but may occur because surrounding material is can no longer carry a load. Figure 33 and Figure 34 show fiber pullout and fiber debond, respectively.

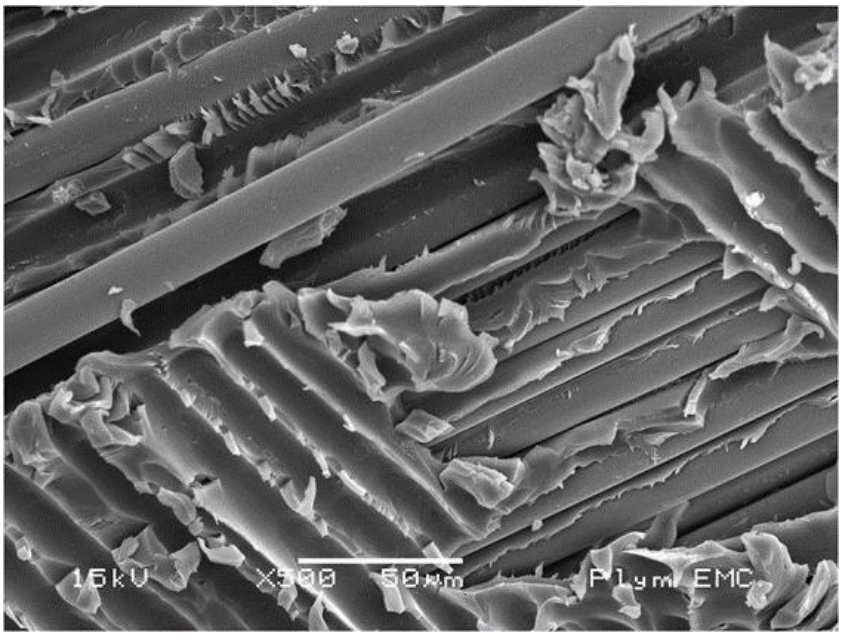


Figure 33: SEM of Fiber Pullout (Summerscales, 2015)

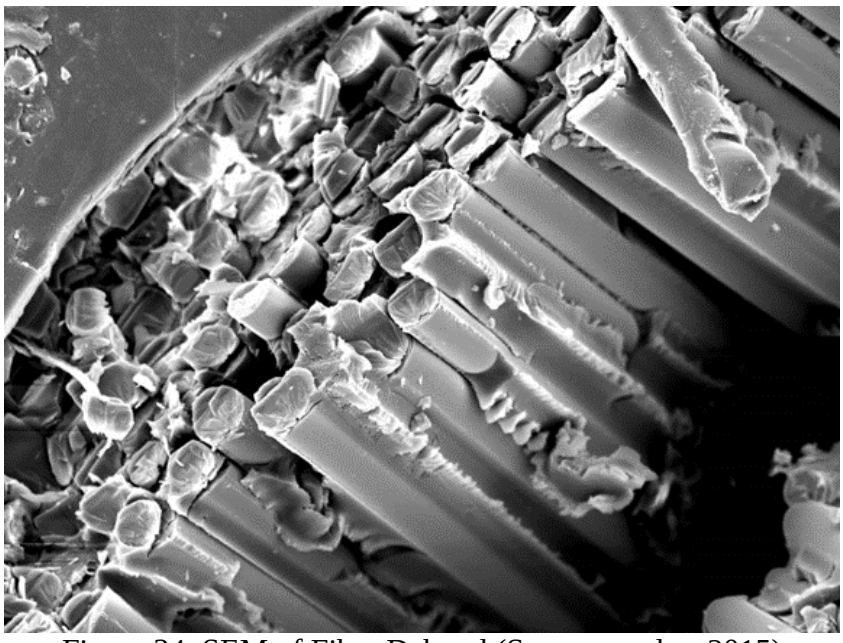


Figure 34: SEM of Fiber Debond (Summerscales, 2015)

Another type of damage that occurs in composite materials is called delamination. This happens when plies separate due to shear stress between them. The gap between propagates the plies becomes severe enough that the composite fails. For the purposes of this research, this is not discussed in detail.

The final type of damage that is a common cause of composite failure is fiber breakage. This most often constitutes the final and catastrophic failure of a composite sample under load. Fibers are the stiffest parts in a polymer matrix composite, so they carry the majority of the load. Fibers are loaded until the strains increase so much so that they reach the strain limit of the fibers, causing fracture occurs. Fiber failure is often preceded by interphase failures (Kim, 2002). As individual fibers become damaged and fail this load is distributed to other fibers and plies. This will cause the remaining fibers to fail due to the significant increase in load with the reduction in total number of fibers

carrying the same load. This pattern of load shedding and resulting failure is called cascading failure and will eventually result in final failure of a simply supported laminate. Fiber failure, as shown in Figure 35, is much easier to notice since the significant amount of energy that is released combined with catastrophic failure.

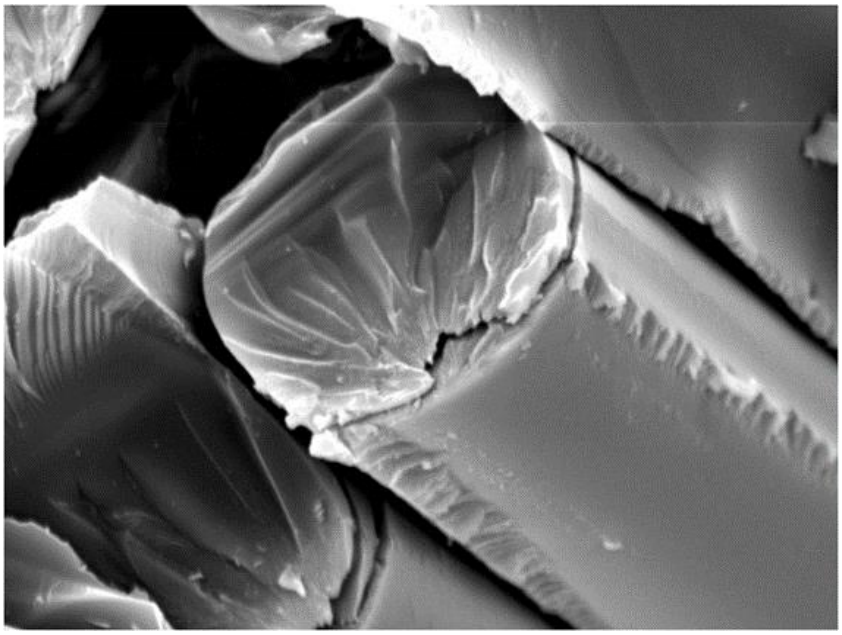


Figure 35: SEM of Fiber Failure (Summerscales, 2015)

Energy Released and Strain

Energy is generally defined as the ability to do work. Energy falls into either a kinetic or potential form. Kinetic energy is motion that is doing work while expending energy. Potential energy stored by some medium that can be released to do work. Energy is always in a system, which is chosen based on the system in question. Energy within this arbitrary system can be added, removed or converted to another medium, however, it must always be accounted for. If the system is taken to be a composite coupon in a test machine the force that is applied to the coupon causes it to deform,

energy is added to the system and is stored as elastic spring force. The spring force, is termed strain energy and is a measure of the potential energy put into a material as it is being strained. For an idealized mechanical test this energy storage process is well represented visually below in Figure 36. It is an ideal stress-strain curve for a uni-axial tensile test and is applicable to many materials.

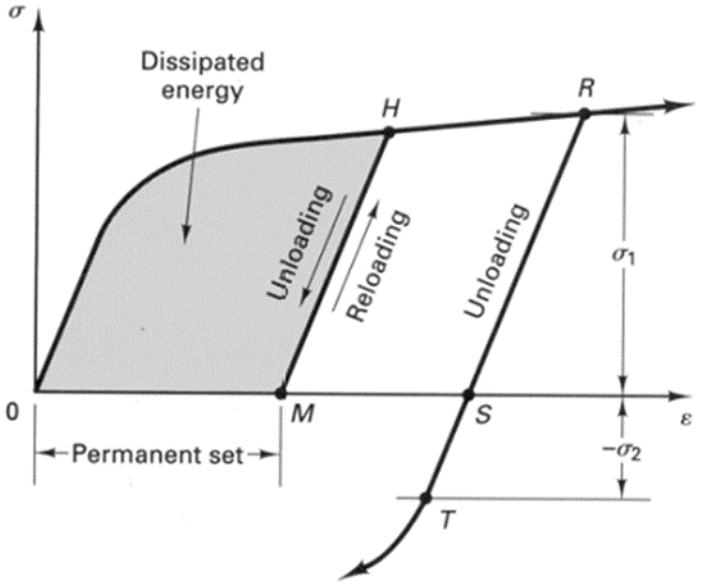


Figure 36: Typical Stress-Strain Curve for a Load-Unload-Reload Test and the Dissipated Energy (Gandelsman, 1999)

When a small axial load is placed on a sample, the stress and strain increase with a proportional relationship to each other in a linear fashion, determined by the laminate's elastic modulus. This creates a straight line on the stress-strain diagram. The integral of that line is the amount of strain energy put in to the material is calculated by a simple integral, shown in Equation (1). σ is the stress measured in force/area and ε is the strain which is unitless since it is length/length, which often multiplied by 100 to be used as a percent.

$$u = \int_0^{\varepsilon_{ij}} \sigma_{ij}\, d\varepsilon_{ij} \quad (1)$$

The units are Joules per volume and this is called the strain energy density. Multiplying by the measuring volume results in the strain energy contained within that volume in Joules. If it is then unloaded, both the stress and strain returns to zero in the lowest energy manner, represented by a straight line in the diagram Ideally, the entire potential energy accumulated would be conserved and recovered similar to a spring being released, assuming no damage. If during this same test, a load is reached that produces stresses large enough to initiate one of the damage mechanisms discussed earlier, the linear stress-strain relationship no longer holds and becomes non-linear as energy is released from the coupon via different types of damage. According to the law of conservation of energy, the damage mechanisms convert the strain energy accumulated in the sample and dissipates into other means such as the creation of new surfaces, frictional heating, or many other many other forms of damage. The curve flattens as higher strain is required to reach higher stresses, due to the energy dissipation. As the sample goes beyond the linear part of the stress-strain diagram, when it is unloaded, the stress-strain curves returns to zero in a straight line, but the strain does not reach zero and there is a space between the two curves. This is referred to as plastic deformation. This type of deformation is what is known as damage, because the sample has been stressed to the point that it cannot return to its original form. When a sample is unloaded while it is still on the linear part of the stress-strain curve, it is known as elastic deformation. This means that the sample has been stressed, but not enough to caus permanent deformation. This means it will return to its pre-tested geometry and should not have any permanent

damage. If Equation (1) is performed on the load and unload curves for both the linear and nonlinear parts, the two results subtracted from each other the section of area between the two curves is what is left; this is the strain energy. In FRPCs, each instance of damage releases energy that summed together with all other damage events and their equivalent energies released, should equate the total energy dissipated. This concept has not been equivocally proven for composite materials yet, although advances are being made relating singular dissipative energy forms for single well-defined damage types. Currently, these damage mechanisms are being explored with acoustic emission (AE) testing. Thousands, or sometimes tens of thousands, of instances of damage can occur in a uni-axial test and AE analysis has proven to be one of the only reliable methods to provide a measure the number of damages instances and the associated energy released for composite materials.

Acoustic Emission

It is well known that flaws and damage in composite materials greatly alter the strength of coupons and large scale components. When test subjects become larger and more complex, such as industrial scale structures or windblades, these deviations become more difficult to detect. Damage detection can be of varying difficulty depending on the types of damage, locations, materials, and at what stage of the composite's lifetime is analyzed. Detection methods are either destructive or non-destructive. When a sample is tested destructively that means the material will be permanently damaged in same way and will no longer be able retain its original mechanical properties. Examples of this are

when specific parts may be sampled and tested to failure or cut out and visually inspected to see the damage that occurred below the surface of the composite. Non-destructive test (NDT) methods leave the sample or structure intact. This is ideal for parts that are still going to be used or sold to determine the quality before it is commissioned into operation. This is popular in many industries including the wind turbine industry. NDT can be useful after a composite structure is in operation and damage has occurred. Examples of NDT are digital image correlation (DIC), computerized tomography (CT) scanning, ultrasonic (UT) inspection, and of course AE testing. The focus of this research will exclusively utilize AE testing.

Another use of AE testing is it that can be applied during a test to monitor individual damage events in real-time, whereas most NDT and all destructive testing must be to done post mortem. The potency of AE is in its utility in the types of application and its ability to directly assimilate the energy release from each of those damage events. The National Renewable Energy Laboratory (NREL) and the National Wind Technology Center (NWTC) has already performed extensive testing of AE and the other NDT techniques on full scale and partial scale windblades to identify the strengths and weaknesses of the different sensing techniques (Rumsey, 2008).

As mentioned before, AE testing is an NDT evaluation method that can be used during a destructive mechanical test to provide real-time data on the accumulating damage. As composites materials strain, damage occurs and releases transient elastic stress waves that acoustically travel through the material. An AE system utilizes sensors that can detect these waves and turn them into a representative electrical signal and

processes this data into various metrics. AE systems have been increasing in use for composite material testing because they have the capability to detect when, where and what type of damage is occurring within a laminate. This something that has always been difficult in materials that anisotropic and quasi-isotropic, like composites.

AE sensors consist of a piezo-electric crystal mounted behind a wear plate that transmits the acoustic wave transmitted from the test subject to the crystal, as seen in Figure 37. Piezo-electrics work by outputting a voltage signal proportional to the deflection it experiences. One type of AE sensors, called wideband sensors, produce a relatively constant voltage output regardless of the input frequency. To create a wideband response the most common method is to use multiple crystals and a damping system, but this leads to decreased sensitivity of the frequencies emitted. Sensitivity of an acoustic sensor can be increased by using a tuned piezo that is tuned to a specific resonant frequency, these are called narrowband sensor. The main disadvantage of these sensors are that they have a very limited response outside of that specific frequency range. The choice between wide- and narrowband sensors is dependent on the desired application. With each type of sensors, the analog voltage is typically miniscule and has to be amplified by a pre-amplifier so that it can drive the signal through longer lengths of cables that are attached to the sensors. The data acquisition system then records the acoustic waves via a high bitrate A/D converter and which the software then interprets into significant data. Recent advances in computing power of packaged commercial systems allows for more real-time calculations, whereas before AE testing more heavily

dependent on post processing methods. This data is dependent on the structure of the acoustic waveform emitted from the damage mechanisms in question.

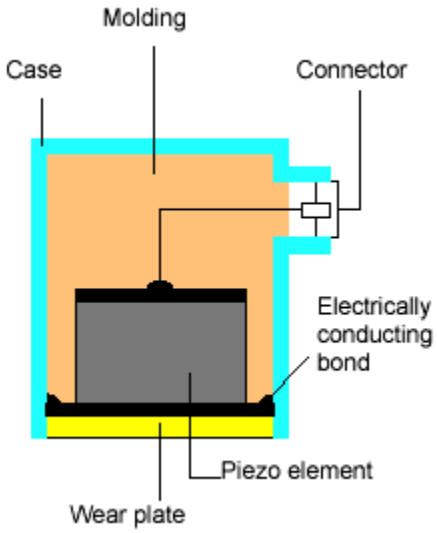


Figure 37: Basic Schematic of an AE Sensor (Vallen, 2002)

Elastic Wave Theory

The AE analysis technique is based on elastic wave theory (EWT) which is required to fully understand the technology. EWT specifies that stress imparted in a material behaves as a wave and can be modeled by a traditional wave equation. There are also subsets of theories in the EWT to describe wave motion. Examples of these subsets are longitudinal and shear waves in a free volume theory and Rayleigh waves on surfaces theory. The wave equation was broken down into various components of different orders that could be applicable to plate geometry by Horace Lamb in 1917. The zero order components are the most useful for applications regarding surface waves of thin plates of composites. The zero-order Lamb wave components are defined as the symmetric (s_0) and anti-symmetric (a_0), which more commonly known as the extensional

and flexural wave modes. The boundary conditions determine simultaneous solutions of these two modes, allowing for both modes to be excited independently and at different magnitudes. Extensional waves contract and extend material symmetrically about the mid-plane of the plate in the direction of propagation. Flexural waves transfer asymmetrically out of plane of the plate, transverse to the direction of propagation (Lamb, 1917).

The analytic solution of the wave equation by Lamb is not ideal for composite materials unfortunately. He created the EWT with the intention to only be used for isotropic and homogenous material, which are not composite materials. Composite plies are composed of various fabrics and orientations in a multi-layer laminate that result in varying properties through the thickness of the laminate. The multiple constituent materials also result in a non-homogeneous microstructure as well as anisotropy. Another setback is that the original solution assumes the use of elastic media and the boundary conditions are of an infinite plate. Obviously an infinite plate is not physically possible, causing further deviation from the theory. The reason composite materials that have finite dimensions cannot work with the ideal EWT is that waves reflect off surfaces of material mismatch, i.e. the matrix and fiber interfaces; as well as reflections off the also the edges of the plate. This induces directionality in the emissions that cause overlapping of the extensional and flexural wave modes due to the reflection off of the sides and interfaces (Scholey, 2010). Progress has been made to combat these shortfalls by using several plate assumptions and 3D elasticity models that account for anisotropic

layered media, both of which have helped to narrow the gap between theory and application (Wang, 2007).

Exact solutions that are needed to fully model elastic wave propagation are not needed to determine wave velocity estimations. A composite laminate analysis can be performed that generates overall laminate properties using certain assumptions. An assumption that simplifies this is that composites are macroscopically homogenous materials and is especially applicable to Lamb waves when the wavelength of the elastic wave is large with respect to the plate thickness. This simplifies the governing equations while accurately describing the wave propagation. The primary tensile (A_{11}) and bending (D_{11}) stiffness coefficients can be used for the modulus in the extensional and flexural equations wave speed equations for the elastic wave analysis, as shown in Equations (2) and (3).

$$c_e = \sqrt{\frac{A_{11}}{\rho h}} \tag{2}$$

$$c_f = \sqrt[4]{\frac{D_{11}}{\rho h}} * \sqrt{\omega} \tag{3}$$

ρ is the material density, h is the thickness and ω is the frequency of the wave (Gorman, 1991). It is important to note that for the extensional wave speed (c_e) it is assumed that the speed is not dependent on the frequency, this is quality is referred to as non-dispersive, but flexural waves are dispersive. This is an acceptable assumption at the low frequencies commonly found in AE applications. Extensional wave speed (c_f) is also

much higher than that of flexural waves. The various parts of a basic AE waveform are illustrated below in Figure 38.

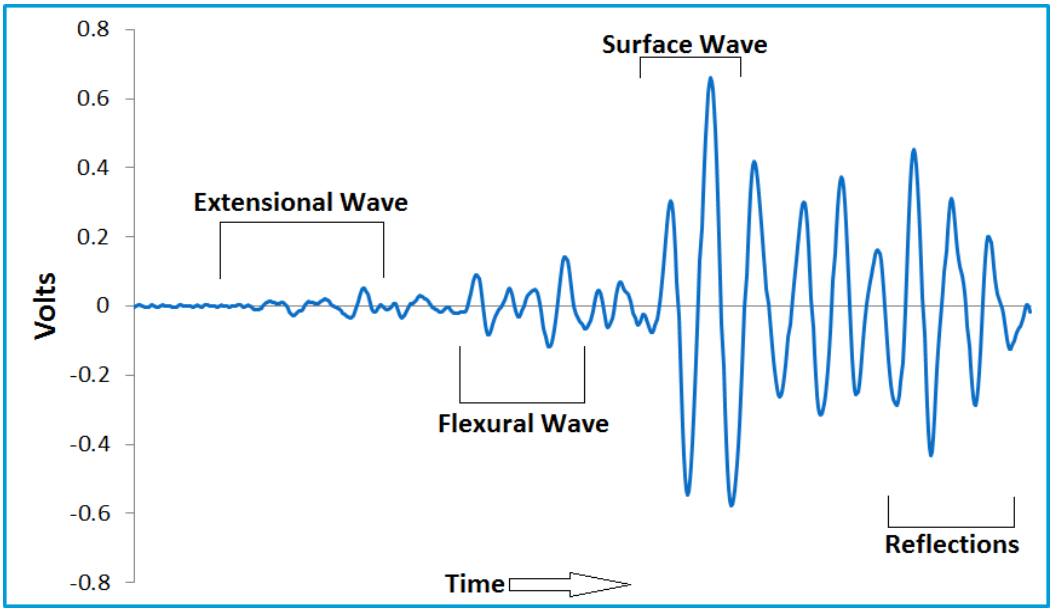


Figure 38: Parts of an Ideal Lamb Wave for Acoustic Emissions

Previous research has been conducted to compare the behaviors of the flexural and extensional waves and which of one of them should be used for AE analysis. It has been concluded extensional waves should be used for AE since they are higher velocity and non-dispersive, although the signal is often significantly smaller as detected by the sensor because of its lower energy behavior (Prosser, 1999). Typically in real world application, an extensional wave is superimposed onto the flexural wave. To combat this there are several methods that have been developed to separate them but they can add significant post-processing time (Surgeon, 1999). AE software parameters that shape the captured waveform will be used for the waveform acquisition for this research. They are not perfect however, so some superposition and overlapping may still occur, affecting the

accuracy of the results. Fortunately, these errors are typically minimal to nonexistent when using these programs.

Location Data

The primary used of AE analysis for composite materials is the ability to locate the exact position of damage as it is occurring. It is the most useful piece of information in practical applications and is the area of AE that is receiving the most amount of attention for innovation. An event is when independent hits have been detected on separate AE sensors and the software has determined that the hits have come from a single source. The most common method for determining location is calculating time of flight difference between the sensors combined with the known speed of sound in the composite. The program will record the difference in time between when each sensor records a hit and will determine for an accurate position. An increase in sensors used increases the accuracy of the event locating. This research uses flat coupons linearly loaded, so only two sensors are necessary that give one dimensional locating, i.e. the event will only be detected lengthwise on the coupon and not where it is in the width direction. Three sensors allows for two dimensional locating and four sensors allow for three dimensional locating; those amounts of sensors are typically used for structures that are much larger than coupons. Research from 1995 has found that a two sensor setup is accurate within 3.2 mm (Prosser, 1995). Improved processing technology and sensor materials have shrunk this error. However, if an AE sensor happens to miss the initial extensional wave or triggers on the slower flexural wave traditional time of flight locating schemes can have error in excess of 50% (Gorman, 1991).

Correct wave velocity inside a composite test sample is necessary to determine accurate location data, which can be complicated with the complex structure and material interfaces. When damage occurs, new surfaces are created from matrix cracking and fiber breakage for the waves to reflect off of and therefore a reduction in wave velocity. Catastrophically damaged material, especially when gaps in the material appear, can block waves from reaching the sensors at all. Acoustic emission accurately locates initial damage locations but significant damage can skew time-of-flight location data, especially on larger structures that can damage mechanisms happening in many locations.

There have been other methods developed that have improved upon the time-of-flight approach for locating. A two-step picker method was successfully formulated for thin composite plates, but once the geometry becomes more complex it becomes less effective (Sedlak, 2013). Research on larger structures have been performed using an advanced method called ΔT locating, specifically for geometrically complex aerospace parts (Baxter, 2007). More advanced locating methods require post-processing which is not necessary for software used in a linear setup, like the research presented here. No advanced locating methods were utilized in this research. Basic time-of-flight methods of locating can still be used on complex structures if attention is given to sensor positioning and if the geometry are accounted for, according to research performed on windblades (Zarouchas, 2013).

Absolute Energy Data

Energy released is one of the most important characteristics when characterizing and understanding material deformation. Having a value of energy from an acoustic

emission event provides a piece of data to formulate an understanding of the damage progression of the material being tested. There are two main methods for determining an energy value that are used in AE analysis. The first is referred to simply as energy or PAC-energy; this value is derived from the integral of the voltage signal over the duration of the AE. This method is limited in application because it does not give a very good physical representation of the hit. It is not a true value of energy due to having units of counts; rather it is a representation of the magnitudes relative to each other. The method that is seeing greater utilization is the absolute energy (E_{abs}) measured in attojoules (10^{-18} J). The equation to calculate these values is seen below in Equation (4). V_s is the voltage signal, R_s is the reference resistance over the duration of the AE waveform where t_f and t_i denote the waveform duration time limits.

$$E_{abs} = \sum_{t_i}^{t_f} \frac{{V_s}^2}{R_s} \; x \; 10^{-6} \tag{4}$$

It is a value that represents the area under the waveform voltage signal and is equivalent to theoretical strain energy described earlier. The value is dependent upon the voltage signal from the sensor and it has been proven that thickness affects the amplitude and therefore the voltage. This makes the E_{abs} method a thickness dependent value. This method also assumes that all energy released from the event reaches the sensors. It is known this not possible, because when damage occurs the AE propagates in multiple directions, not just towards the sensor. Energy is also released from the damage, as mentioned earlier, in the form of heat and friction. The combination of all these detractions indicates that the absolute energy is not the true value of energy released

during a damage event. The MISTRAS software used in this research has the ability to make up for the effects of attenuation but that only corrects for one type of energy lost. The attenuation correction is primarily for larger structures where the effects of attenuation are greater. With the size of coupons anticipated for this research, attenuation was confirmed to be minimal.

Although these effects detract from the energy transmitted to the AE sensors, the E_{abs} measure has shown strong correlation to other established energy measurements. Energy loss from directionality is minimal for a linear setup the E_{abs} reported from the AE system has been shown to be proportional to the actual release of energy due to damage. This research will focus on tensile coupon tests which remains the most basic mechanical test performed on a material to produce the material properties. Work on static loaded tensile coupons has found that the E_{abs} method for AE analysis provide good measure of the accumulation of damage (Bourchak, 2007). A goal of many researchers is to develop a direct correlation to dissipated energy in a composite material with AE. If that happens the E_{abs} method becomes more effective and universal for damage detection, failure modeling and life estimates for a composite materials.

Frequency Data

Probably the most important data collected using AE analysis is frequency data which has shown to be a promising method of real-time NDT for damage characterization of composite materials. The waveform of the frequency of an AE hit is a complex amalgamation of frequencies that have been altered from their initial form by reflections, attenuation, wave speed variations and outside noise. A Fourier transform

can be performed to convert the AE waveform from the time domain to the frequency. The MISTRAS program does this during testing as a fast Fourier transform (FFT).

One of those components is relevant to this research is the peak frequency (PFRQ). This is, as the name suggests, the maxima of the magnitudes that are reached for each wave. So, if a frequency spikes very slowly, only the very top value of the spike will be recorded as the PFRQ. Figure 39 below contains an AE waveform in the time domain, captured by a voltage signal that represents an elastic wave captured by the sensor. Figure 40 is then the same waveform after the FFT has been performed and the relative decomposition of frequencies present in the original waveform can be seen. Frequencies that contribute more to the final waveform have a larger magnitude in the frequency domain.

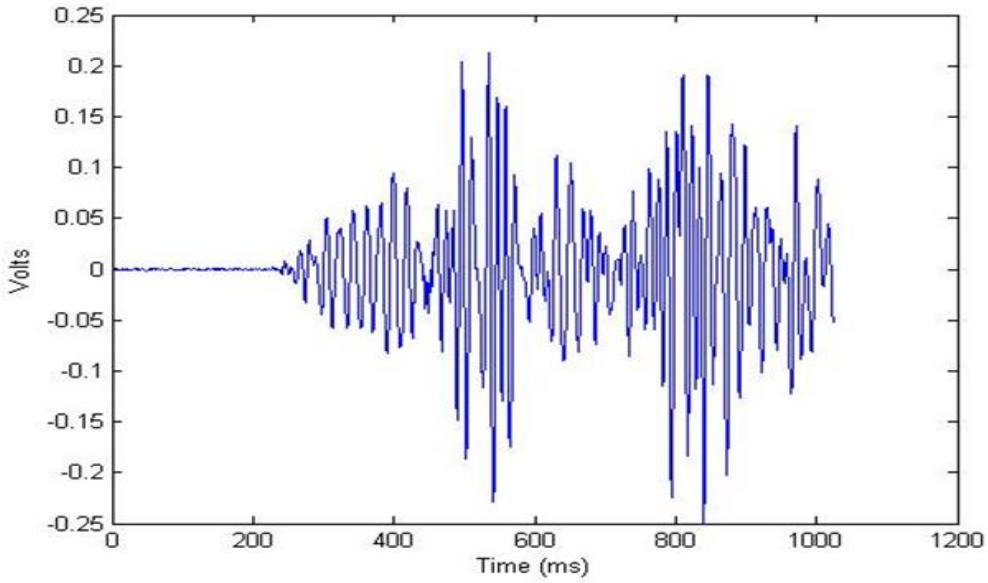


Figure 39: An Example of a Typical AE Waveform in the Time Domain

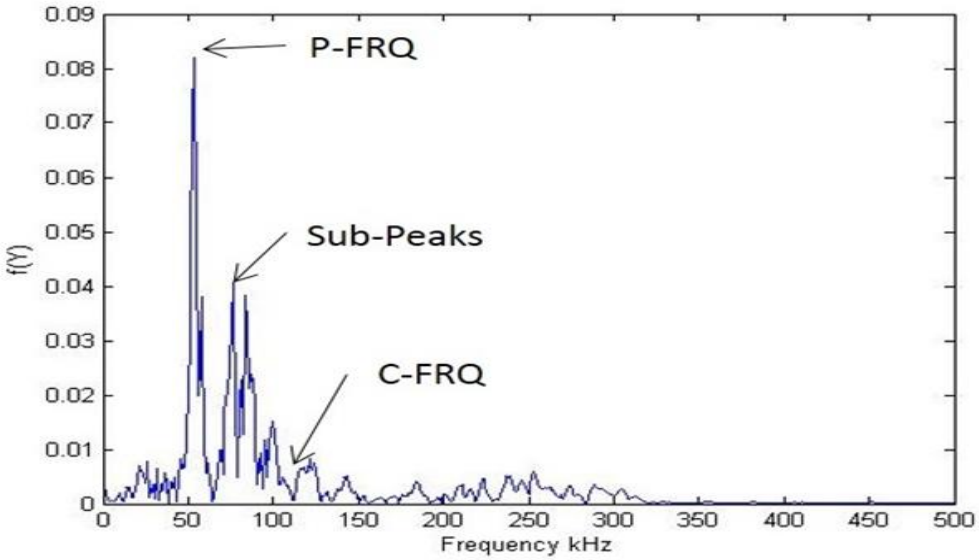


Figure 40: FFT of the AE Waveform in the Frequency Domain

Frequency data became seen as more viable for damage analysis once the advancement of processing technology became capable. Previous research from the 1980's and 1990's found that the PFRQ data for mechanical testing found that they fell into distinct bands. This prompted researchers to correlate these frequency bonds with specific physical circumstances occurring within the test samples. They found that these bands were the result of microscopic damage mechanisms, each of which were releasing their own unique range of frequencies. These tests were initially performed with homogenous materials like metals to generate baseline characteristics of the frequencies. Research advanced from there by testing matrix material only samples, known as neat resin samples, to characterize the frequency range of matrix material. After that, research was performed on single fiber samples, which are coupons that only have a single fiber inside a sample of matrix material. The next logical step was to test samples that only contained one fiber tow that was contained in a coupon of matrix material. All of these

tests helped to establish general characteristics of the simplest geometries found in composite materials; the results of which will be discussed in great detail.

In 1988, a researcher observed that the bands of damage mechanisms for PFRQ correlated to matrix cracking was from 30 to 150 kHz, interphase failures were 180 to 290 kHz and fiber breaks from 300 to 400 kHz for GFRPs (Suzuki, 1988). Another researcher extensively compiled data in 1995 that proclaimed to have identified frequency bands using UD fiber tow coupons oriented at 0°, 10° and 90° orientations for lap shear, double cantilever beams (DCB), neat resin, and single fiber coupons for carbon/epoxy composites (deGroot, 1995). This research concluded that matrix cracking emits a PFRQ band from 100 to 180 kHz, fiber pullout from 180 to 240 kHz, matrix debonding from 240 to 300 kHz and fiber breaks were above 300 kHz. This research by deGroot specifically is probably the most influential for AE analysis for composite materials and is the bases for most new research today. Later research by Jürgen Bohse utilized both thermoplastic and thermoset, both carbon and glass FRPs for a broader baseline of tests. He concluded that matrix cracks and fiber breakage range from 100 to 200 kHz and 350 to 700 kHz, respectively; with fiber pullout frequencies being somewhere in between those two (Bohse, 2000). Research by Qing-Qing Ni reached the conclusion that matrix cracking, interphase failure, and fiber breakage occurred at PFRQs of 20 to 180, 180 to 450, and 450 kHz and greater, respectively. For his research he used longitudinal and transverse direction single carbon fibers and neat resin epoxy coupons narrow ranges of AE activity (Ni, 2001). Finally, research built upon this work with CFRPs using SEM images to physically confirm damage mechanisms for more complex

layups (Ramirez-Jimenez, 2004); it was concluded that 100 to 130 kHz are due to matrix cracking, 200 to 300 kHz are caused by interphase failure, and fiber breakage is above 400 kHz. Table 3 below is a summary of the five independently researched results correlating damage mechanisms to PFRQ that were discussed above.

Researcher	Damage Type Frequency Range (kHz)				
	Matrix Cracking	Fiber Pullout	Interphase	Fiber Debond	Fiber Breakage
Suzuki	30-150	N/A	N/A	180-290	300-400
deGroot[16]	100-180	180-240	N/A	240-300	300+
Bohse[8]	100-200	N/A	200-350	N/A	350+
Ni[34, 35]	20-180	N/A	180-450	N/A	450+
Ramirez-Jimenez[38]	100-130	N/A	200-300	N/A	400+

Table 3: Compilation of Various Independent Research on PFRQs Related to Various Mechanisms

This table should be used for general reference only since the details of the research results were not provided due to proprietary information. Looking at the publishing dates of the data shows that researchers have taken a step back from trying to categorize each type of damage mechanism in the middle frequency ranges. This is because it is extremely difficult to physically confirm fiber pullout and debonding. It is broader term, but more accurate to say interphase damage rather than what is specifically happening. It can be seen that for the later investigations that the frequency ranges align for similar damage mechanisms. Referring to the middle frequency data as interphase damage is the term this research use, since specific instances of fiber pullout and debonding were not able to be found separately; that is to say this research could not find

one without the other present at the same time. More specifically, the term "fiber pullout/debond" damage will be used in place of interphase damage.

Research performed by Gutkin, Arumugam, Loutas, Sause, Yousefi, and additional research by Ni and Kurashiki have performed further analysis for many types of fibers, matrices, geometries, loading setups, and layups. All of which have contributed to the correlation between PFRQ emissions and damage mechanisms and progression and how that effects composite materials.

Due to the exorbitant available sources on baseline characterizations, the present research will not attempt to reproduce these same efforts but instead expand to characterization of material systems and the progression frequency content leading up to final failure. Low frequency hits in the range of 50 to 120 kHz will be considered matrix cracking, 120 to 300 kHz as fiber pullout/debond, and 300 kHz and above as fiber breakage. Similar ranges were used by in more recent research that utilized these ranges as partial powers ranges to identify AE events in DCB tests (Sause, 2012 and Waller, 2010). Instead of categorizing the frequency spectrum of singular waveforms using partial powers as they did, the peak frequencies throughout the course of an entire test will be categorized and analyzed. These bins are denoted F1, F2, and F3 and are tabulated below in Table 4. The analysis will take into account various material architectures and layups while utilizing the previously discussed baseline frequency spectra. Performing this analysis will further the understanding of how these fabric materials fail, investigate the effects of fabric architecture and provide a dataset with which future tests can be analyzed for damage mechanisms. Eventually, this information

will aid in development of analysis techniques for more complex structure testing when material architecture and damage location can be much more difficult to identify.

Bin	PFRQ Range	Identified Mechanism
F1	50-120 kHz	Matrix Cracking
F2	120-300 kHz	Fiber pullout/debond
F3	300+ kHz	Fiber Break

Table 4: Peak Frequency Bin Ranges

Thesis Goals

The previous work done on frequency analysis is indicative of the ability of AE to represent the damage occurring in a composite material as it is loaded. The numerous failure modes in composites are well understood and predictable but AE gives researchers the ability to show exactly when, where and what type of damage is occurring from real-time data. The background above lays the groundwork and motivations for the study presented herein. Frequency and energy data from AE analysis will be used to characterize the damage progression and failure modes for several GFRP layups and fiber architecture. The E_{abs} calculated from AEs will be analyzed to identify a damage parameter that could be used to better understand and experimentally determine the damage state and how the fiber geometry effect its progression.

3. EXPERIMENTAL PROCEDURES

Test Coupon Manufacture

MSUCG has a database that is composed of previous students' research in for glass/epoxy and other composite materials utilized in the wind industry, which this work is contributing to. The materials chosen for this research are a small subset of the types found commonly in the wind industry, but have vastly different fiber architecture and layups. This will provide a baseline for the type of damage found in glass/epoxy composites and allow for vastly different damage mechanisms how they progress. Three different fiber materials were chosen for testing, all of which were E-glass, that were manufactured using different methods and fiber architecture. PPG-Devold L1200/G50-E07 is a Hybon 2026 E-glass fibers that is mainly used for windblades and spar caps for the wind industry and has an area weight of 1250 g/m^2. It is composed of 92.2% UD 0° E-Glass tows, 4.16% 90° backing strands used for stabilization, 4.0% CSM and 0.56% of Tricot polyester strands used for stitching for the total fabric weight. This material was chosen for its wide use in the wind industry and complex construction from the CSM that may yield more complex AE signals during a test. Vectorply E-LT-3900 is a high density, structural fabric, with an area weight of 1346 g/m^2 that has been utilized in a wide array of analyses performed at MSU (Schuster, 2014). It is composed of 90% 0° UD tows made of Hybon E-Glass fibers, 8% 90° backing tows for stabilization and the final 2% is Tricot polyester stitching. This material was chosen because it is has a simpler architecture than the E-LT-1200, which is the more commonly used variation, yet

is a denser fabric. The tows on this material are physically have lower drape than the E-LT-1200 fabric, causing the fabric to have a smaller chance of forming wrinkles and other flaws in the manufacturing process. Density should not alter the AE characterization, but the way in which the fabric utilizes different architecture and within those different layups will greatly change the damage mechanisms observed. Finally, Newport NCT307-D1-E300 UD E-glass with an area weight of 300 g/m^2 will be used. This fabric is theoretically exclusively 0° fiber, as most pre-impregnated fibers have that characteristic. The exact percentages of the constituents are unknown since the material is proprietary and no data sheet is available. A summary of these selected fabric features can be seen below in Table 5 and will be designated Glass-A, B, and C for the remainder of this paper. The Glass-B coupons in which the stitching was removed will be denoted with an asterisk (*). Full material data sheets are in Appendix B.

Company	Product	Designation	Fiber Volume Fraction (%)	Weight (g/m^2)	Fabric Fiber Composition (%)				
					0°	*90°*	*±45°*	*CSM*	*Stitch*
Vectorply	E-LT-3900	Glass-A	47.5	1346	90	8	0	0	2
Newport	NCT307-D1-E300	Glass-B	68.0	1765	100	0	0	0	0
PPG-Devold	L1200/G50	Glass-C	56.2	1261	91	4	0	4	1

Table 5: Fabric Types with Corresponding Architecture and Weights

Several simple layups were selected to give the best representation of AE behavior, so as to establish a baseline to understand the characteristics of each material. Each of the particular layups will induce a primary mode of failure that is expected and well understood. By applying AE to these basic layups it will be possible to look into the various fabrics' micromechanical damage leading up to final failure and how it changes throughout the course of a test. This damage progression can then be compared and quantified between the fabrics. Coupons with the fibers oriented transverse to the loading direction, denoted [90], produce transverse failures as matrix cracks and fiber pullout/debonding. This layup type should reveal some characteristics of the fiber/matrix interface as well as the influence of backing strands and CSMs on the damage mechanisms and fabric characterization in a weakly supported material. Coupons with fibers oriented in the direction of loading, denoted [0], fail by fiber breakage and fiber pullout/debonding. Recall that it is very difficult to determine the difference between fiber pullout and fiber debonding using PFRQ, so they were combined into a single damage category. In theory, the pullout should only be present in the 0° fibers and debonding should only be present for the 90° fibers, but since this cannot be proven visually, the separation of the two must be disregarded. The slightly more complex laminates composed of both 0° and 90° plies in a symmetric layup provide a chance to observe and characterize the damage progression without failing the coupon at the onset of matrix cracking.

A total of six single ply plates were manufactured as the [90] and [0] coupons. Plates with the CSM, denoted as [B], are considered to be a single ply since the CSM is

combined with a single UD ply. Three two ply biaxial plates, denoted [0/90], were manufactured. Finally, for the pre-impregnated composites, Glass-B, only 0° and 90° UD tows were used but with more plies because of manufacturer recommendation that two and single ply coupons not be manufactured due to complications during the curing process. The test matrix can be seen below in Table 6. An Instron 8562 was utilized for testing because it features an electrical screw actuated load frame, which is much quieter than a hydraulic machine, to allow for lower AE thresholds and less noise in the data. This machine has a 100 kN max load limit, which is another reason that single and two ply composites were used. Typically, anything that has more than two plies does not fail in that machine, using the dimensions that were desired for the coupons.

	Material	Designation	Totals Tested
Layup	Glass-A		170
	[0]	Glass-A1	30
	[0] (stitching removed)	Glass-A1*	30
	[90]	Glass-A2	30
	[90] (stitching removed)	Glass-A2*	30
	[0/90]	Glass-A3	25
	[0/90] (stitching removed)	Glass-A3*	25
	Glass-B		30
	$[0/90]_S$	Glass-B1	15
	$[0/(90)_2]_S$	Glass-B2	15
	Glass-C		80
	[0/B]	Glass-C1	25
	[90/B]	Glass-C2	25
	$[0/(B)_2/90]$	Glass-C3	30

Table 6: Test Matrix for Each Coupon Type

Infusion

Manufacturing of the test coupons was performed at MSU using the VARTM method described above. The matrix for these laminates was a two-part epoxy developed for the wind industry. The resin used was Epikote™ RIMR 135 and the hardener was Epicure™ RIMH 1366. The resin system was mixed at ratios following manufacturer's recommendations of 100:30±2 parts resin to hardener by weight for 10 minutes. Vacuum was applied to the laminates at 80 kPa for 30 minutes and then the ports were sealed off to check for leaks in the vacuum bag. The vacuum was then reapplied and the resin allowed to flow into the laminate through tubing connected to the inlet port. After the infusion was complete, laminates were cured at room temperature for 48 hours and post-cured in an oven at 70 °C for 12 hours. Manufacturing sheets can be found in Appendix B.

Stitching Removal

For the Glass-C* coupons, an extra step had to be added before the infusion. The stitching was removed, to determine how it affected the AE signals and strength of the coupons. The process was performed by cutting them at either end of the fiber roll and slowly pulling them out while ensuring that the act was not damaging or effecting the structure of the tows at all, as seen in Figure 41 and Figure 42 below. To ensure that the samples were not pre-damaged, the ends of the coupons where the stitching was cut were cut off of the samples after they were infused. The reason that only the Glass-A samples had the stitching removed was that it was the only fabric in which that it was possible to remove them.

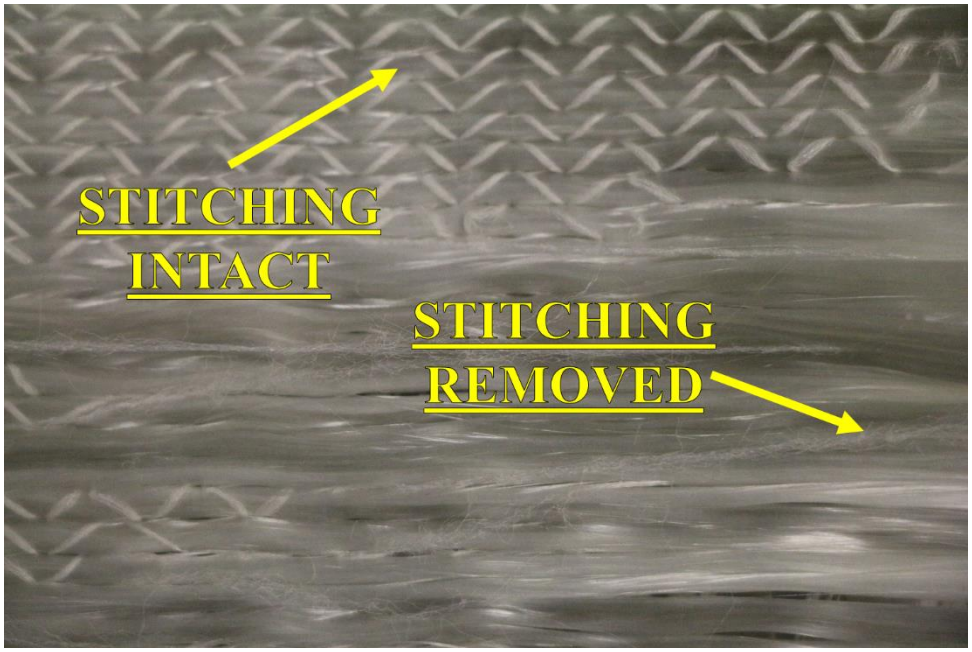


Figure 41: Front Side of Vectorply Fabric Showing the Difference between Stitching Removed Versus Intact

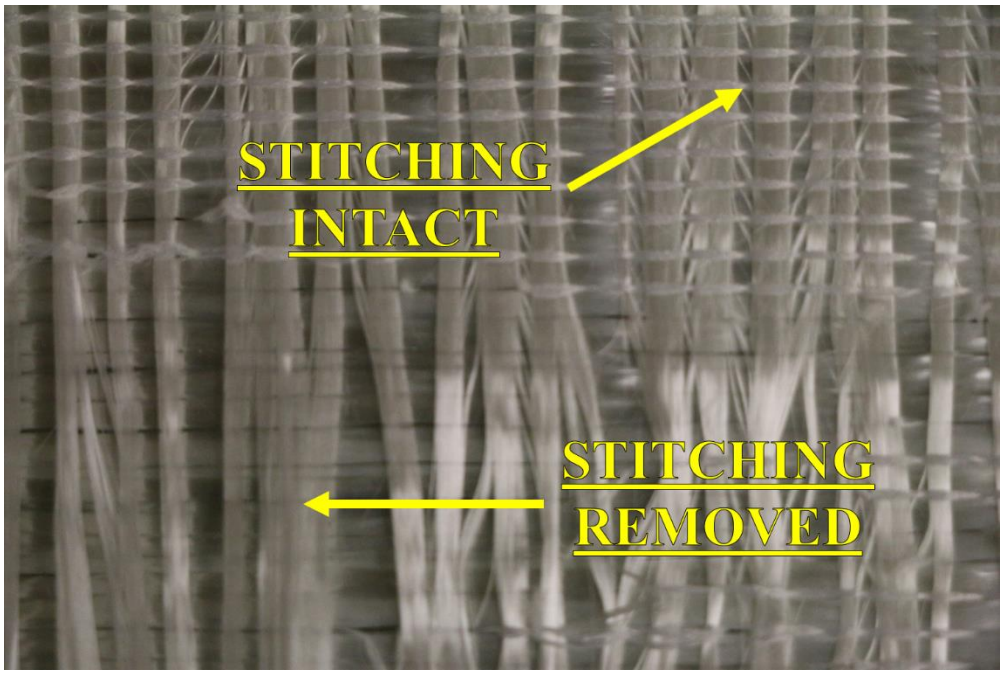


Figure 42: Back Side of Vectorply Fabric Showing the Difference between Stitching Removed versus Intact

Cutting and Preparation

Following successful plate manufacturing, coupons were cut to an average of 275 mm long by 27 mm wide with a tile saw. Thickness was dependent on the particular fabric used. Loading grip tabs of G10 fiberglass material were applied with 3M DP460 two-part epoxy adhesive and clamped for 24 hours. The 90° coupons were not tabbed. The AE sensors were placed on the mold side of the coupons during testing to provide optimal contact between the sensors and coupons. Sensor positioning marks were drawn on each of the coupons to aid in alignment during the test process. An example of what the finished coupons can be seen below in Figure 43.

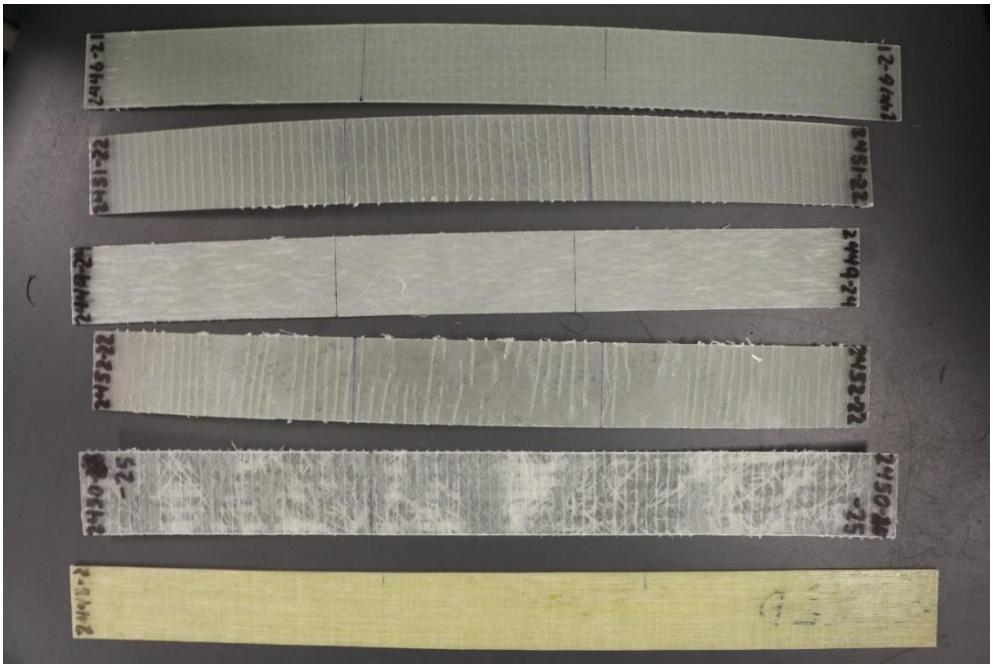


Figure 43: What Various Coupons Looked Like Before Being Tested

Mechanical Test Setup

Coupon layups and dimensions were chosen specifically so that all coupons could be tested to final failure in an Instron 8562 with a 100 kN maximum load, as stated earlier. All mechanical tests were completed in room temperature conditions, 23°C, and at 20% - 40% humidity. A full round of quasi-static, monotonic testing was first completed with three coupons per each layup and fabric type to develop the AE material characterization. The statics tests were executed with a single ramp waveform in at a rate of .06”/min for all of the samples tests. An Instron 2620-824 extensometer with a gage section of 12.7mm and a range of +/-40% strain was used to collect strain data. The strain data and load data from the 100 kN load cell were input to the AE system via parametric inputs to correlate directly to AE events.

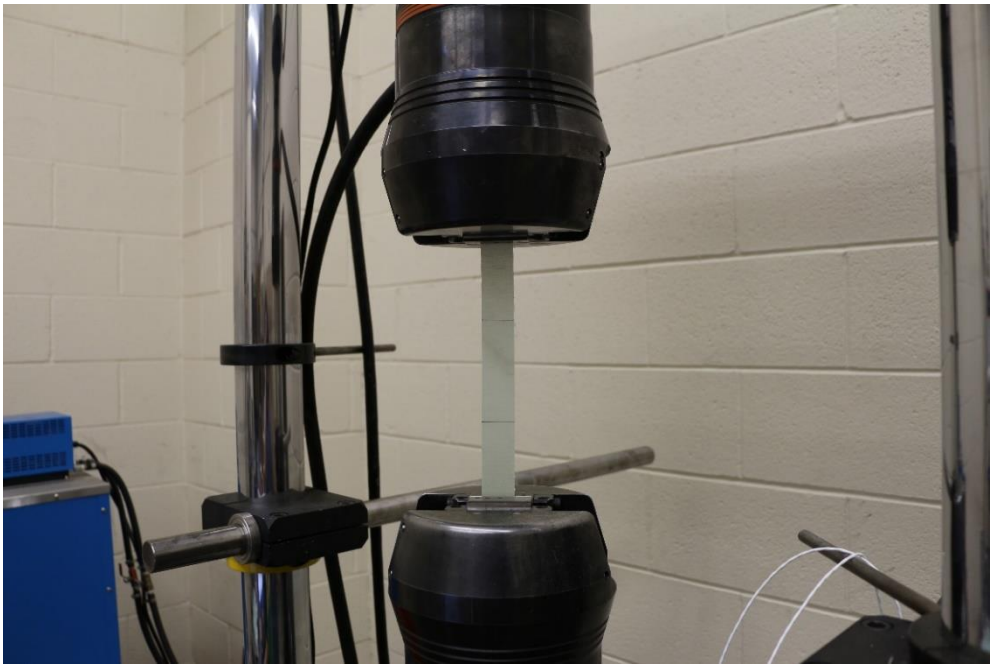


Figure 44: The Test Setup for a Coupon in an Instron 8562

Acoustic Emission Setup

Acoustic emission analysis was accomplished through the use of a MISTRAS PCI-8 Micro-II SAMOS system. Two WD - AST sensors with in-line 40 dB pre-amps were used for coupon tests and had an operating range of 50 kHz to 1000 kHz. The triggering and acquisition system collected waveforms at 3 MS/s with 128k of pre-trigger data and a total waveform length of 1024 kHz. The on-board frequency filter was set to allow frequencies between 50 kHz and 900 kHz. The upper frequency limit was dependent upon the PCI board, which in this case was limited to 600 kHz while the lower limit was chosen based on the fact that the WD-AST sensors provide minimal returns below 50 kHz. The calibration sheet showing the sensitivity response for a WD sensor is shown in Figure 45. The PDT, HDT, HLT and max duration were set to 50, 100, 300 microseconds and 99 milliseconds respectively. A software filter was applied to energy to filter out hits with AE PAC-energy lower than 1 count. This was done to help eliminate reflections, noise and erroneous hits that were observed below this level during preliminary tests.

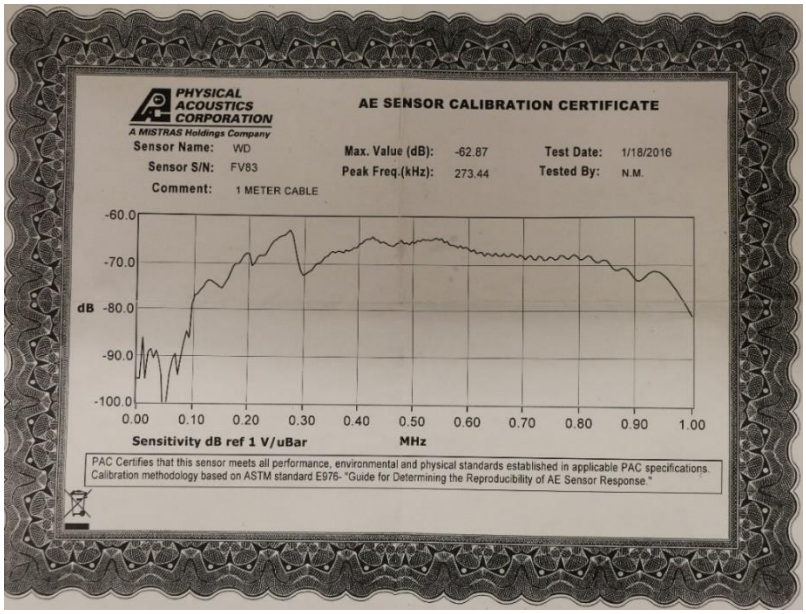


Figure 45: Calibration Sheet for WD AE Sensors

The two WD sensors were applied to the coupons in a linear arrangement at an average of 80 mm apart. Figure 46 below shows how the sensors and pre-amp were assembled and connected to the computer processor. The linear setup as opposed to a single sensor configuration allowed for a ΔT filter to be applied that could filter events based on the time of flight difference of the individual hits. By setting limits on the allowable time of flight (D_t), events were limited to within a linear span of distance that corresponds to the specified D_t limits multiplied by the input velocity given. The D_t limits were set to 85% of the total wave transmission time between sensors. This effectively limited acceptable AE events to between the closest physical edges of the two WD sensors.

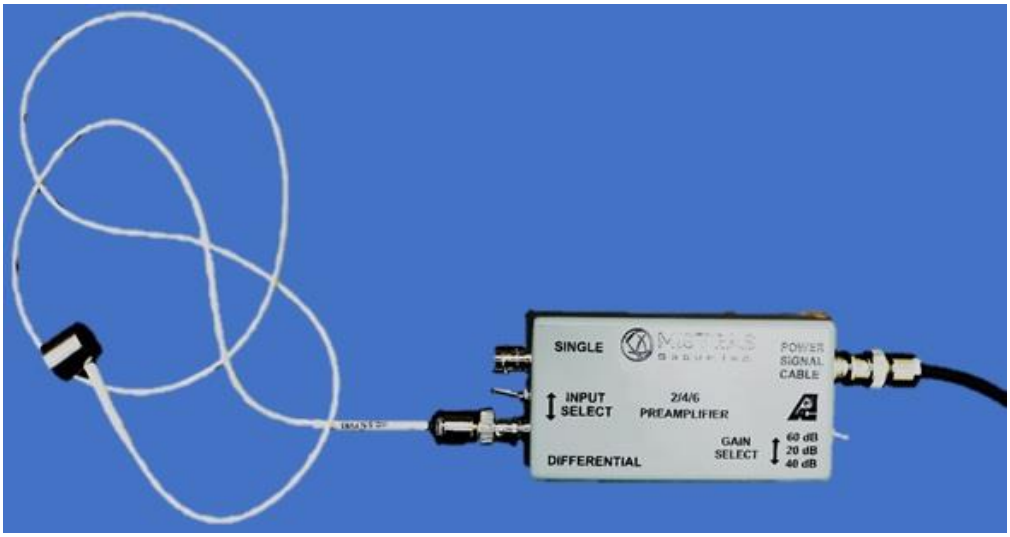


Figure 46: Sensor with In-Line Pre-Amp Setup Used for all of the Testing

The settings for AEWin software were set up in the exact same way as Michael Shcuster had previously done, to allow continuity between research. Those settings are summarized here. The AE system was set to acquire parametric data at 50 millisecond intervals in the AEWin software and plots set to update either at 5 second intervals and/or 500 event data points. If the plot update speed was set to update on every point, parametric data would be dropped from memory and fail to plot when high rates of AE activity occurred. Plots that were closely monitored during static tests included E_{abs} and PFRQ versus strain or position scatter plots as well as accumulated E_{abs} and parametric data line plots. Auto-generated reports and statistics files were saved as well as an ASCII file of parametric data via the utilities menu. Then a text file of individual AE events was generated with the data replay function. These text files were then processed with a combination of Microsoft Excel and custom MATLAB scripts. Screenshots of all software options can be seen in Appendix C.

Test Process

The following test process remained standard and repeatable throughout all static tests. The coupon was mounted carefully in the hydraulic grips evenly so that one side of the sample was not favored. The grips were then closed while the coupon held in place. The grip pressure was approximately between 4 and 5.3 MPa, confirmed with a force gauge found on the loading frame. Test results could vary if higher, lower, or unbalanced grip forces were applied. This is the main reason for avoidance of a screw or other forms of mechanical grips to be used. The AE sensors were then applied to the coupon with a small amount of vacuum grease to be used as a coupler and aligning the sensor on the positioning marks and centered on the coupons. The sensors were firmly pressed onto the coupon surface to ensure that there were no air pockets trapped in the grease. Small clamps were applied to the centers of the sensor housing to provide enough resistance to keep the sensors from moving to maintain contact between the wear plate and coupon, as seen in Figure 47 below. The clamps were tightened as much as they would allow thus giving a consistent clamp force for all tests. The clamps were measured as having a 90 N clamp force. The load was zeroed on the load frame to remove any built up forces created during coupon mounting. The AE automatic sensor test (AST) was then run to check for proper sensor attachment, wave velocities, and D_t times. If the D_t values varied by more than 10% between the two reported values, the offending sensor was re-mounted and the AST was repeated. The reported wave velocity was checked against theoretical velocities calculated for major discrepancies using Equation (2). A rounded value for velocity was entered into the location settings.

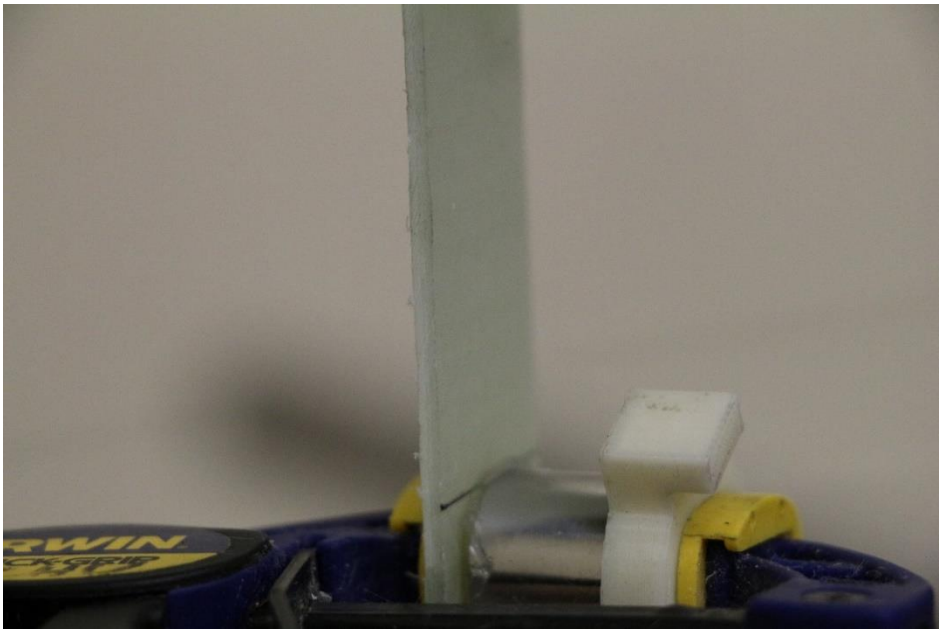


Figure 47: Attachment Setup for AE Sensors Used in Every Test

Following the software adjustments, a standard pencil lead break (PLB) test, or Hsu Test was performed at several locations along the length of the coupon (Hsu, 1981). This involves breaking a portion of pencil lead on the coupon while acquiring data and observing the result to determine if the AE returns are satisfactory in position and relative frequency and energy. Specifically for these tests, accurate positioning of the PLB and D_t values within the limits set according to the AST results were of chief concern and provided sufficient metrics to judge the quality of sensor attachment. More accurate and consistent calibration waveforms could be produced by breaking the lead on the edge of the coupon thus producing an extensional wave in contrast to a true Hsu-Nielsen source which produces a larger flexural wave (Gorman, 1991).

After setup and calibration of the AE system was completed, the extensometer was attached to the coupon with rubber bands. The proper load levels, load control rates or position control rates were set on the Instron controller and the strain balanced. The

AE system was then set to acquire data and the test started. Although the primary final failure mechanism of these coupons occurred in-plane, there was often some out of plane component in the subsequent release of energy. Once the sample reached catastrophic failure, that is to say that it could no longer carry a significant load, the test was stopped and the sensors removed.

Actuator strain was used in this research even though an extensometer was used, which is not usually considered ideal. This due to that fact that the extensometer that was used to record strain in the coupons would slip off of the sample typically when the first crack appeared. When it slipped it would greatly skew the recorded strain so that it was impossible to gather any useful data. For example, if the extensometer was reading 0.9% strain, then a crack suddenly propagated, it would suddenly cause the extensometer to output a strain of -13%. This is obviously incorrect, and would only get worse as more cracks and other types of damage occurred during testing. Most of the time the slippage of the strain gage would occur around 1% strain, which is well below the ε_f for most of the samples. This is fine if this research only focused on the AE characteristics until first damage, but it is the desire of this work to characterize these samples until catastrophic failure. The most detrimental argument against the use of actuator strain is that samples can slip in the grips during tensile loading, causing inaccurate results to be recorded. The reasoning for allowing actuator strain to be used instead is that these are mostly single and two ply samples, so the load that is needed to reach catastrophic failure is relatively low, thus slippage of the samples in the grips of the testing machine is reasoned to be none at all or unnoticeable for the purposes of this research. Another reason for this

decision is that the load profile of all the samples was based off a positional feed rate, rather than a load or strain based feed rate. Whether a sample had a sudden load drop due to damage or not, the positional feed rate steadily increased no matter what the conditions were. The testing machine would steadily increase the distance of the actuator, in this case .06”/min, causing the sample to have the linear increase in strain despite load drop caused by accumulating damage.

4. RESULTS

The impetus for this research is to determine how different architecture and layups of glass/epoxy composite materials effect the overall mechanical properties, such as strain to failure (ε_f), ultimate tensile strength (UTS), and time to failure (T_f). The equation for ε_f below in Equation (5) uses initial length (l_i) and final length (l_f). The equation for UTS below in Equation (*6)* uses maximum load (P_{max}) and initial cross-sectional area (A_i). The second objective is to determine how these various geometry changes affect the AE signals that are recorded during tensile testing and how they relate to various types of damage observed during testing and post-processing. The final objective is to analyze to compare the various geometries and layups to determine which are the best for specific scenarios, i.e. which is the best if high ε_f is desired or if matrix cracking is the preferred method of failure. The results and comparisons of the data are analyzed below.

$$\varepsilon_f = \frac{l_i}{l_f} \tag{5}$$

$$UTS = \frac{P_{max}}{A_i} \tag{6}$$

0° Coupons Results

In Figure 48, Figure 49, and Figure 50 below, show the various 0° coupons and what they looked like after failure is seen below. It can be seen that they all appear to have failed by the 0° tows failed by first separating, then splitting across the coupon,

transverse to the tows. For the Glass-A1 samples, after the separation of the tows, they are still held together somewhat by the stitching. The Glass-A1* sample shows splitting between the tows that are completely separated because there is not stitching keeping them together. The Glass-C1 sample shows the same splitting, but not much separation due to the CSM. These types of coupons most often fail in the grips of the testing machine, called grip failure, which is typically not desired. The only way to combat this was to do a high volume of testing so as to collect enough samples that did not generate grip failure to form a quality data set. Only the coupons that did not exhibit grip failure, for all sample groups, were accounted for in this research.



Figure 48: Glass-A1 Coupon 2440-4 after Catastrophic Failure

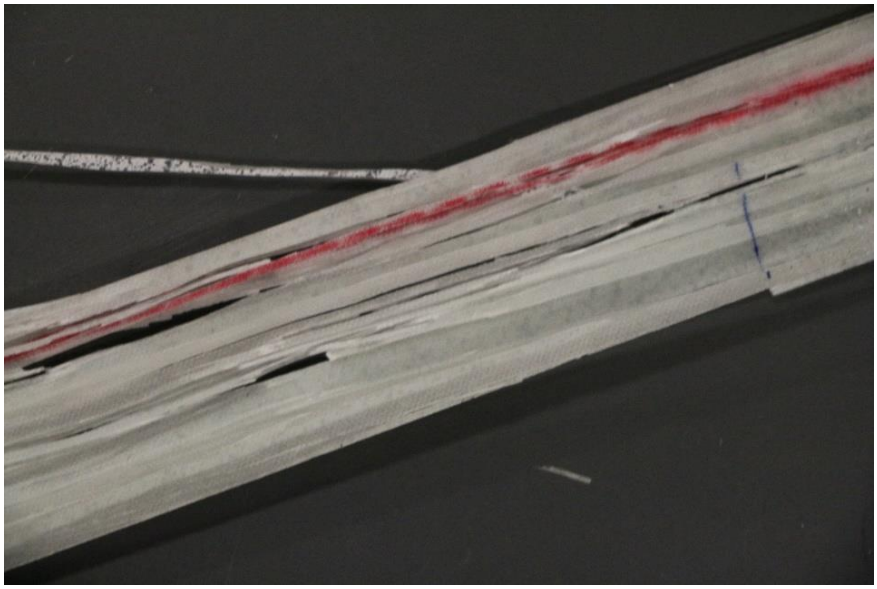


Figure 49: Glass-A1* Coupon 2439-4 after Catastrophic Failure

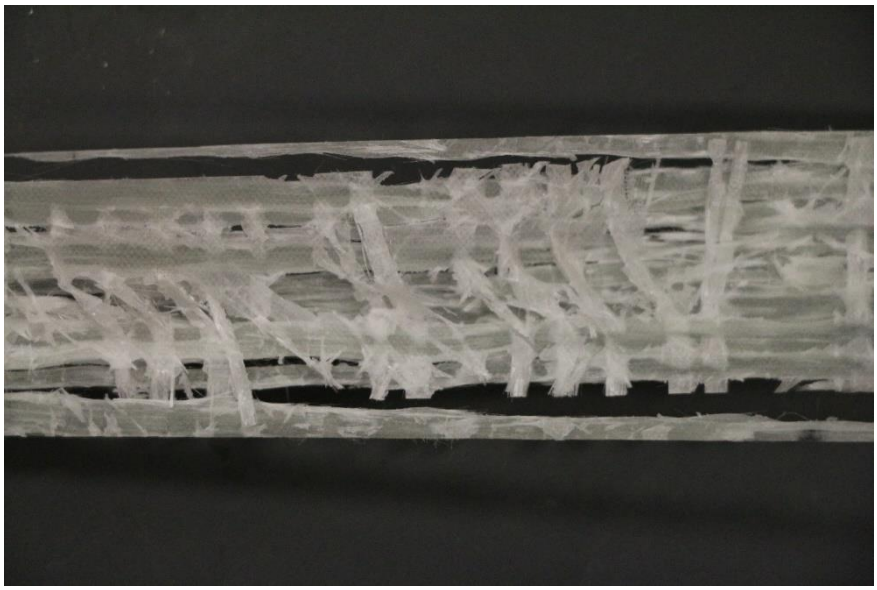


Figure 50: Glass-C1 Coupon 2449-25 after Catastrophic Failure

Glass- A1 Results

The first set were the Vectorply E-LT-3900 UD 0° single ply coupons with the stitching intact. In Figure 51 below, is a stress-strain curve of the Glass-A1. The jumps in the graph that occur around a strain of 1.4% to 1.8% are when cracks and other types

of failure occur. When a crack or other type of damage propagates, the sample loses load for a few seconds because the damage is an example of E_{abs} being released that is stored in the sample. Physically this means that some tow or tows of the sample were under high amount of stress causing reach UTS and eventually breaking. After the first tow failed, the load transferred to a new tow that then became the primary load bearer. The second tow was at a lower load, thus lowering the stress of the coupon, since stress is a function of load. The machine then increased the tensile load until the second tow failed, repeating the same process until the coupon reached catastrophic failure.

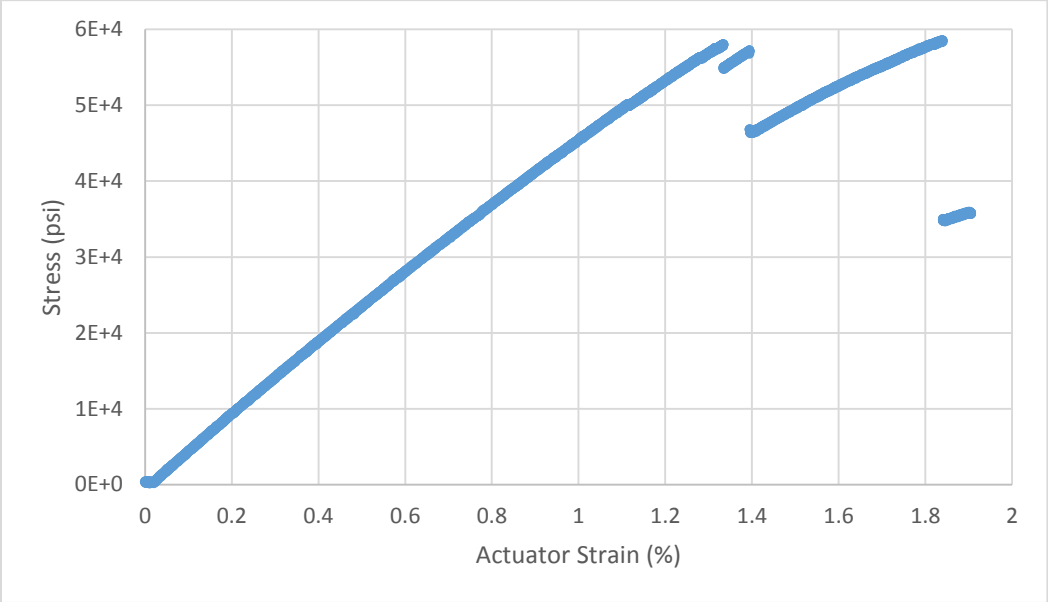


Figure 51: Stress vs. Strain for Glass-A1 Coupon 2440-4

The stress-strain curve above for Glass-A1 shows the sample had a UTS of 57986 psi, or 58.0 ksi. The stress then dropped to 46.3 ksi, but still had a steadily increasing strain due to the positional actuator speed. After the initial damage occurred the load ramped up again to approximately the same value as the UTS; additional significant

damage occurred again and the coupon reached catastrophic failure. The ε_f recorded was 1.84% before catastrophic failure was reached. This result is typical as found in the MSUCG database assembled by previous students.

The next three graphs in Figure 52, Figure 53, and Figure 54 show that the majority of PFRQ events associated with matrix cracking damage (MCD) were the first events to be detected in the test. The first AE signals picked up were the MCD around 0.36% strain, 16.9 ksi, and 54 seconds. The next set of AE signals recorded were the fiber breakage damage (FBD) mechanisms. The first instance of this was at 0.89% strain, 41.0 ksi, and 134 seconds. The final damage type to be recorded was the fiber pullout/debond damage (FPDD), and was in fact the only instance of such type of damage to be recorded for the entire test. It occurred at 1.30% strain, 56.7 ksi, and 194 seconds. The first observation is that the first group of FBDs occur between 0.93% and 0.97% can most likely be attributed to edge effects because of discontinuous fibers on the edge of the coupon. This is supported by the fact that no change in stress occur, meaning that the damage was not significant enough to cause a sudden load drop due to loss of strength in the sample. The next group of FBDs occur between 1.40% and 1.80%, which correlate to the major damage propagation and the eventual catastrophic failure as seen in Figure 51 above. Next observation, is that the FPDD is lacking until immediately preceding the second group of FBDs.

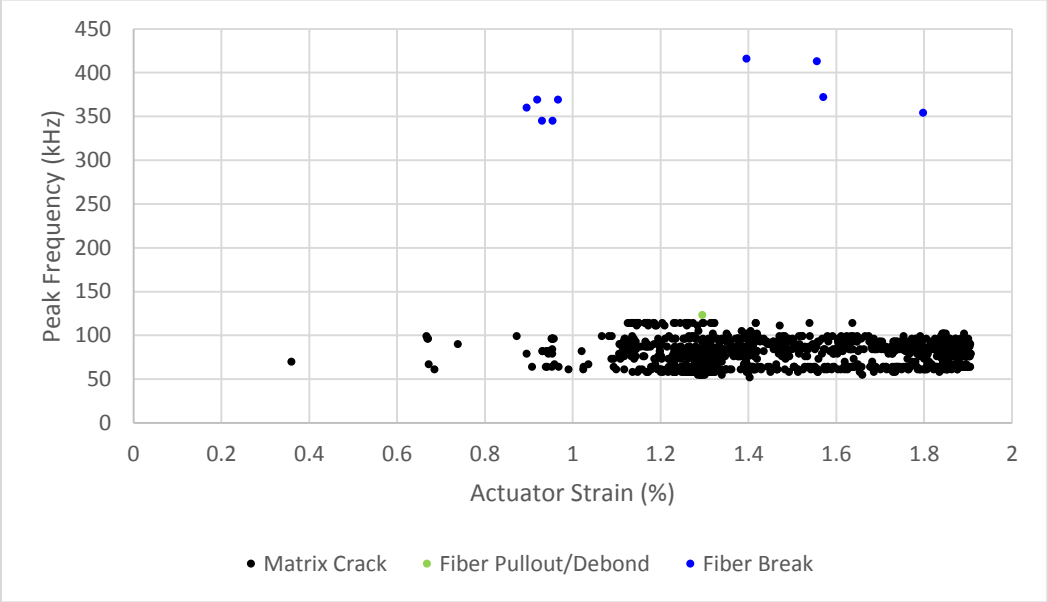


Figure 52: Event PFRQ vs. Strain for Glass-A1 Coupon 2440-4

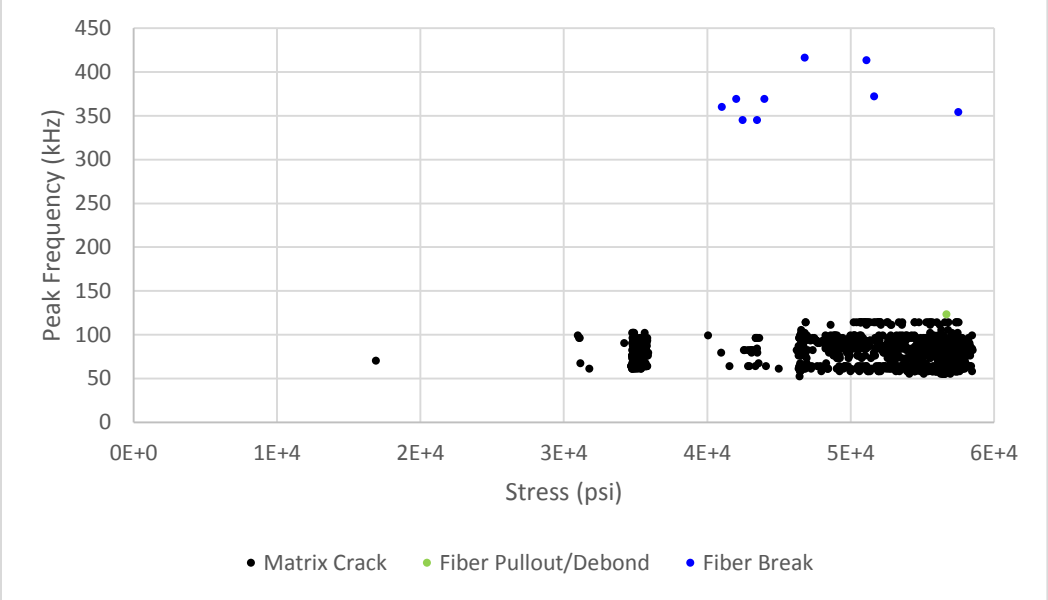


Figure 53: Event PFRQ vs. Stress for Glass-A1 Coupon 2440-4

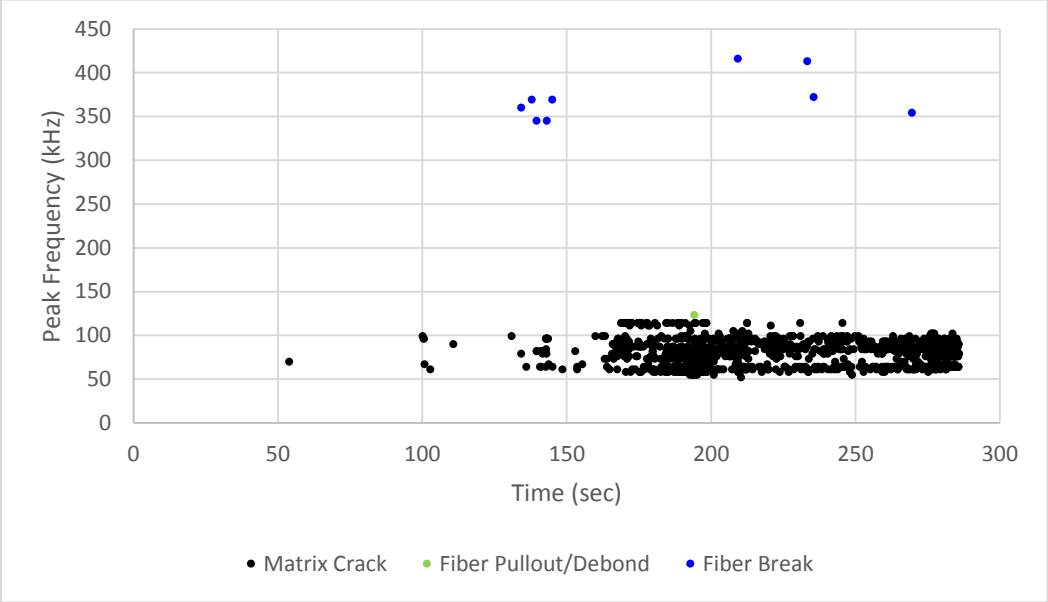


Figure 54: Event PFRQ vs. Time for Glass-A1 Coupon 2440-4

The next two graphs in Figure 55 and Figure 56 show the E_{abs} released by each during the test versus the strain, and a truncated version for higher resolution. The first shows that a single damage type of damage instance of damage was recorded that released $1.09*10^9$ aJ at 1.33% strain. This event aligns with happening between the FPDD and the FBDs as seen in Figure 51 that happens at the same strain. The second figure shows the same graph truncated at $9*10^5$ aJ. It shows two spikes of energy released at the FPDD event and the FBDs before catastrophic failure. The peak of E_{abs} released for the FPDD event is $5.98*10^5$ aJ and the second E_{abs} peak released for the FBDs is $6.78*10^5$ aJ.

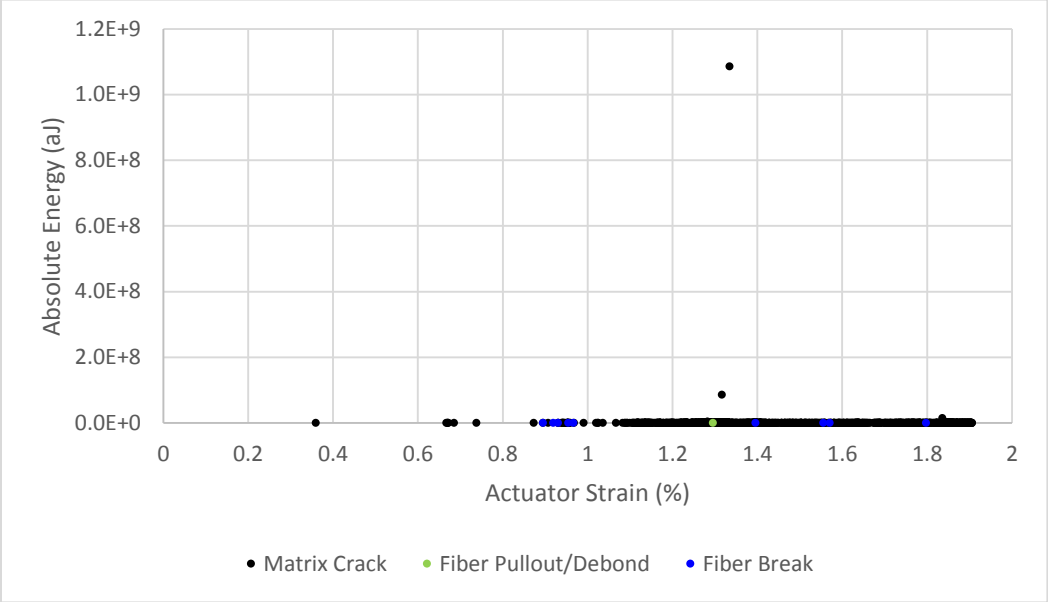


Figure 55: Absolute Energy vs. Strain for Glass-A1 Coupon 2440-4

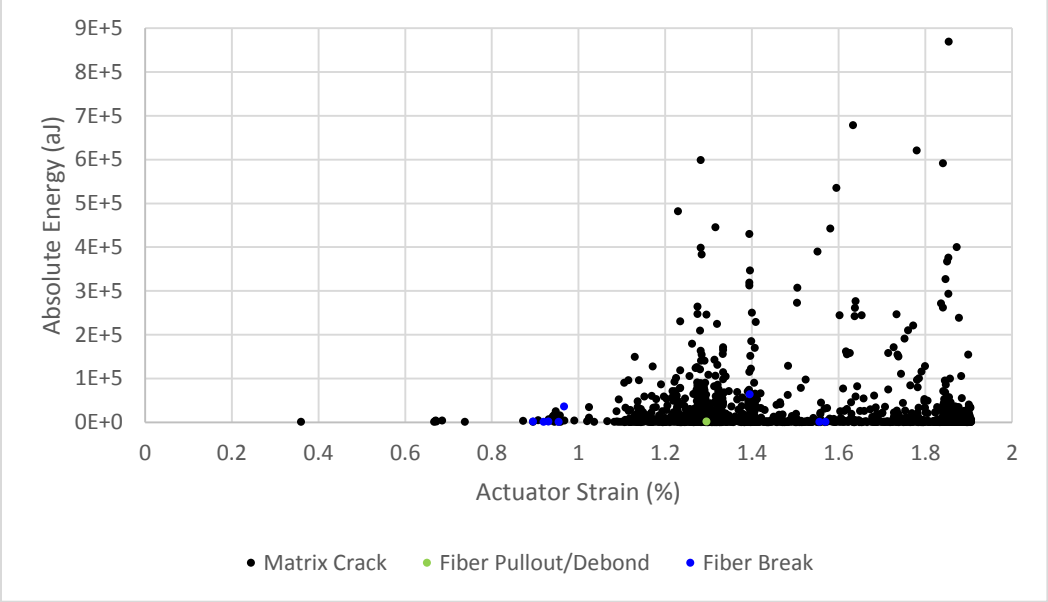


Figure 56: Absolute Energy vs. Strain for Glass-A1 Coupon 2440-4 Truncated at $9*10^5$aJ

Figure 57 below shows the breakdown of the total number of PFRQ events (N_{PFRQ}) recorded during testing and how they compare by percentage. MCDs make up

99.38%, the single FPDD makes up 0.06%, and FBDs make up 0.56% of events recorded.

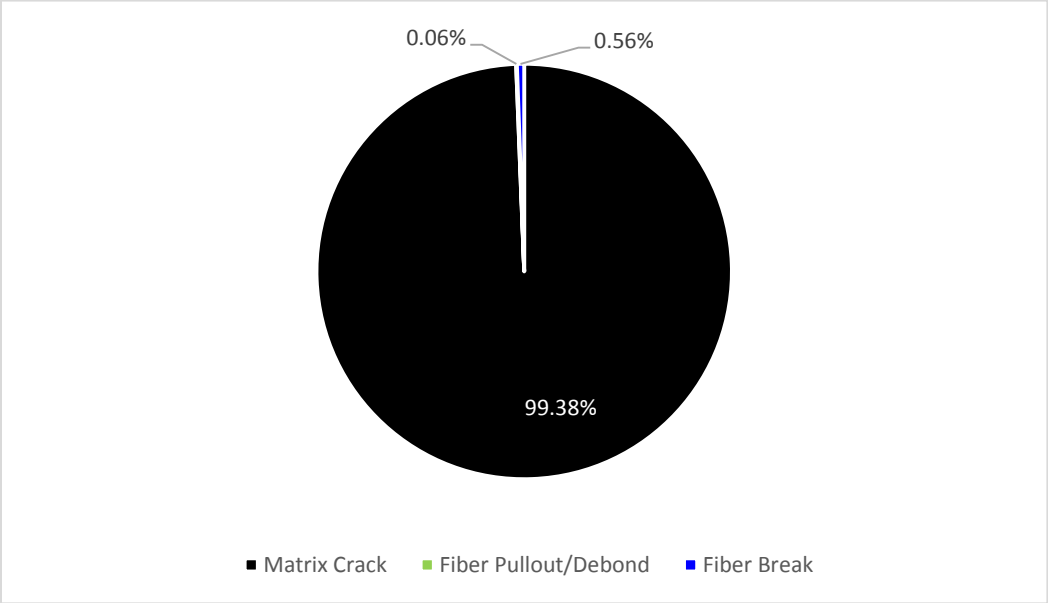


Figure 57: Recorded PFRQ Events by Damage Corresponding Type of Damage for Glass-A1 Coupon 2440-4

Glass- A1*

The next sample set features Vectorply E-LT-3900 UD 0° single ply coupons with the stitching removed. Figure 58 below shows the stress strain curve with a UTS of 74.7 ksi and a ε_f of 1.96%. An observation of this stress-strain curve is that compared to the Glass-A1, it achieved catastrophic failure immediately rather than a load drop caused by internal damage with another ramp up in load. This is due to the fact that each of the Glass-A1* samples had a clean break when they failed. Once internal damage formed and propagated, the samples could no longer support load, whereas Glass-A1 samples sustained several types of damage before failing.

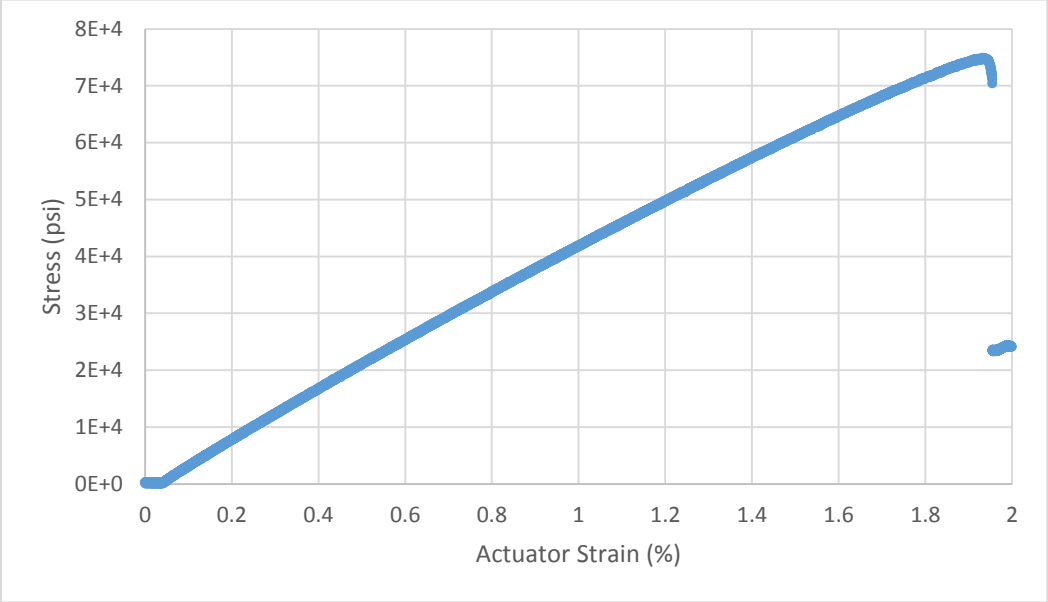


Figure 58: Stress vs. Strain for Glass-A1* Coupon 2439-4

The three graphs below in Figure 59, Figure 60, and Figure 61 show that Glass-A1* samples showed MCD PFRQ events dominated all recorded events for the majority of testing until several FPDDs and one FBD event recorded immediately prior to catastrophic failure. The first instance of damage to be recorded was MCD 0.54% strain, 22.7 ksi, and 80 seconds. The next damage type to be recorded was a single FBD at 1.86% strain, 73.3 ksi, and 279 seconds. The final events to be recorded were FPPDs at 1.89%, 73.9 ksi, and 283 seconds. An observation regarding these figures is that the FBD was detected before FPPDs, which is not typical.

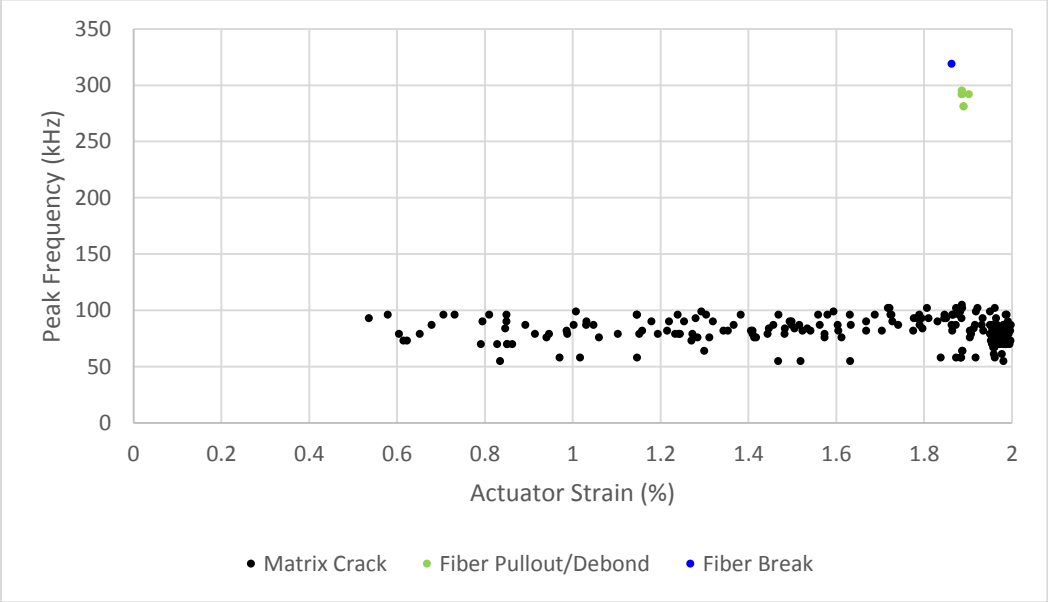


Figure 59: Event PFRQ vs. Strain for Glass-A1* Coupon 2439-4

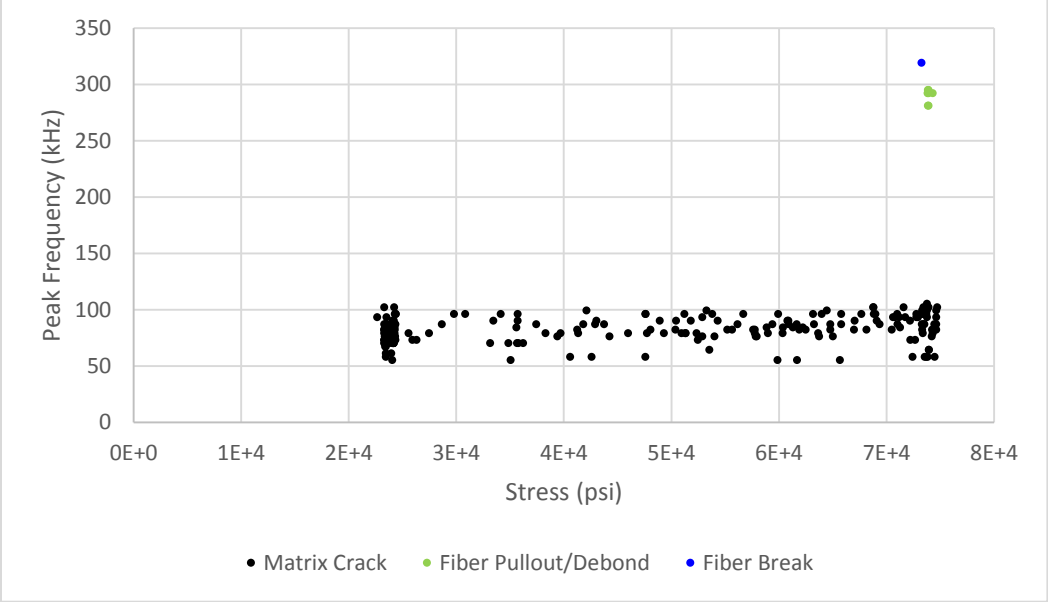


Figure 60: Event PFRQ vs. Stress for Glass-A1* Coupon 2439-4

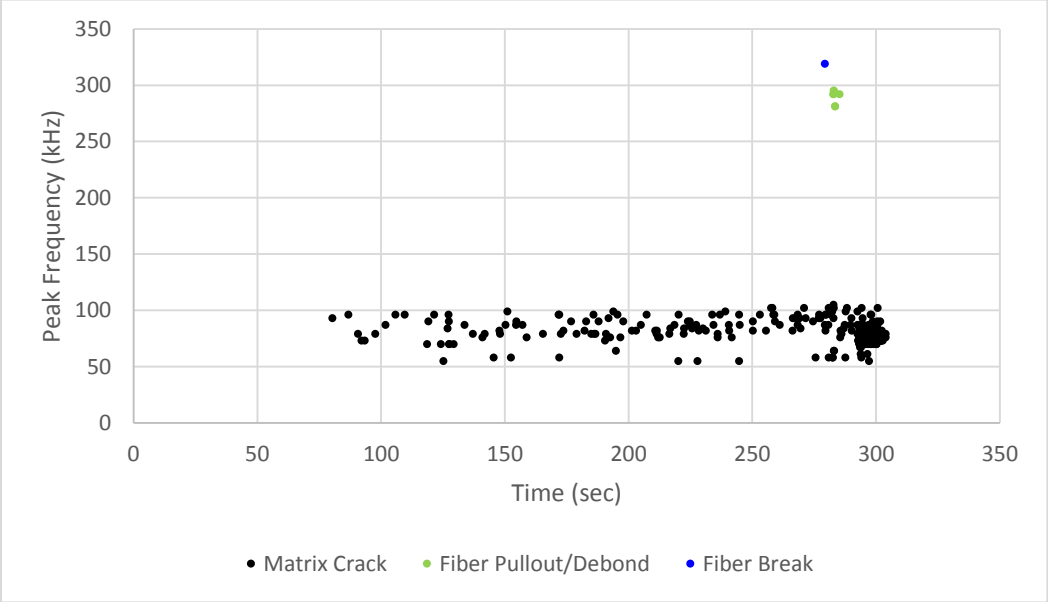


Figure 61: Event PFRQ vs. Time for Glass-A1* Coupon 2439-4

The next graph shown below in Figure 62 show the E_{abs} released with an increase in strain. The largest energy release was $6.63*10^6$ aJ at the end of the test, which is about 1000 times lower than Glass-A1. This energy release aligns with the catastrophic failure for the coupon seen in Figure 58 above. Figure 63 below shows the same graph truncated at $8*10^5$ aJ. The energy released spikes at the same time as the FBD and FPPDs shown as previously stated.

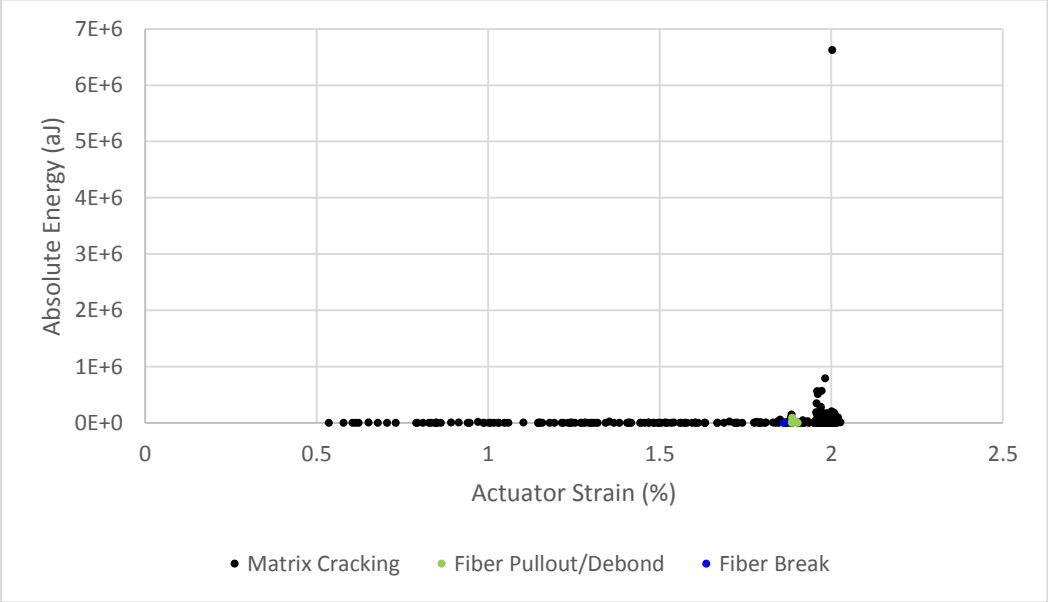


Figure 62: Absolute Energy vs. Strain for Glass-A1* Coupon 2439-4

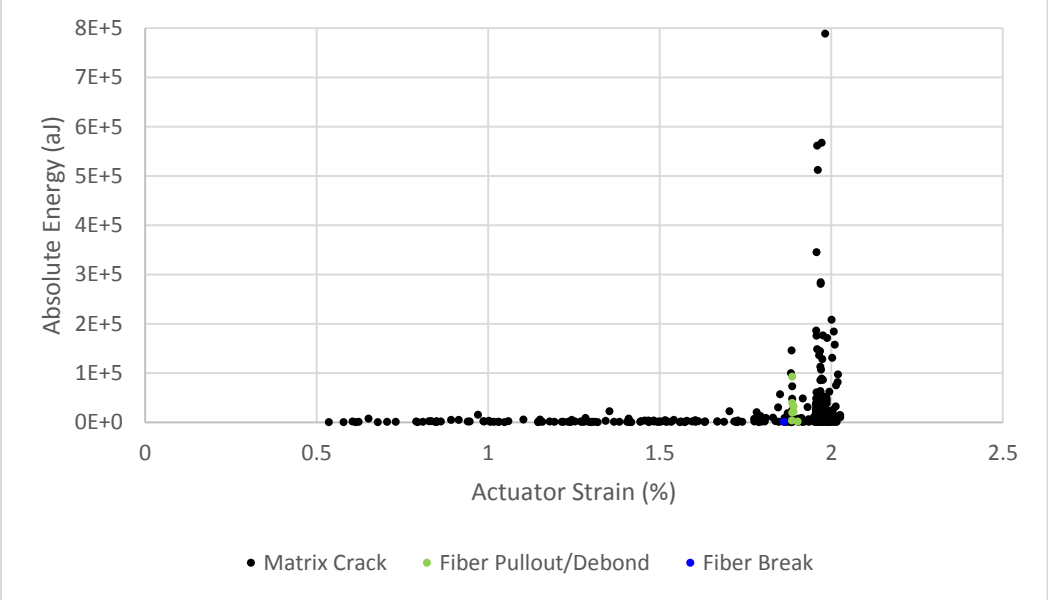


Figure 63: Absolute Energy vs. Strain for Glass-A1* Coupon 2439-4 Truncated at $8*10^5$aJ

Figure 64 below shows the breakdown of each PFRQ event with the associated damage type by percentage. MCDs make up 97.7%, 1.98% is FPPDs and 0.28% is the FBD event. Compared to the Glass-A1, FPPD and FBD make up a higher percentage of

the PFRQ events. Also, the FPPDs and the FBD numbers are reversed in that there are several FPPDs and a single FBD. Overall, there is a substantially lower N_{PFRQ} recorded for these samples than Glass-A1, which will be discussed in further detail in the summary sections.

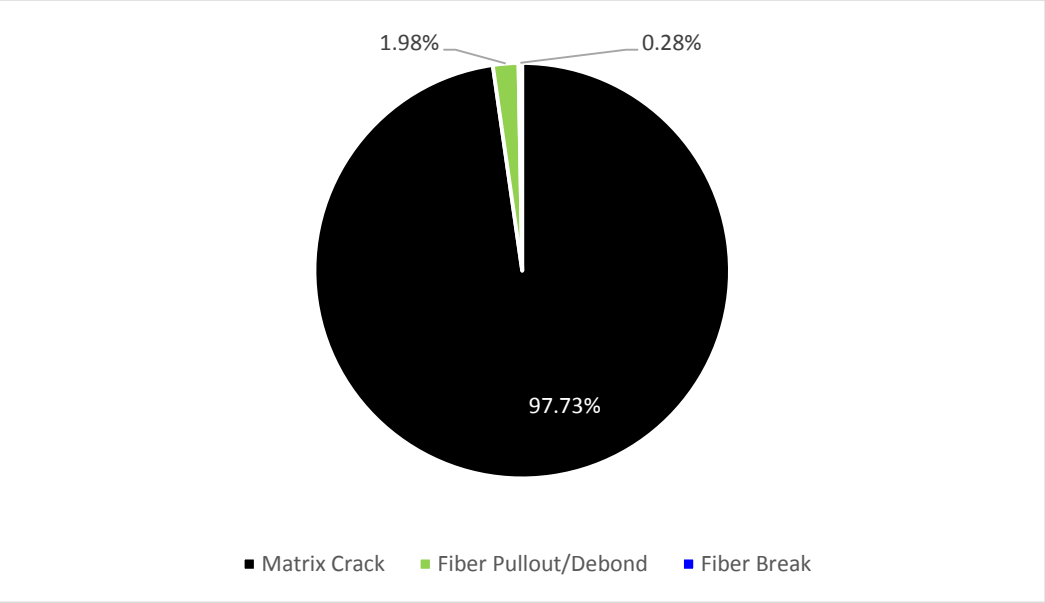


Figure 64: Recorded PFRQ Events by Damage Corresponding Type of Damage for Glass-A1* Coupon 2439-4

Glass-C1

The next sample set features PPG L1200/G50 UD 0° with CSM backing single ply coupons. Figure 65 below shows a stress-strain curve for Glass-C1 material with an UTS of 98.9 ksi and a ε_f of 1.83%. This graph shows a similar feature to Glass-A1 in which there is internal damage that occurs that causes a load drop and an increase until damage propagates and caused another sudden load drop. The first load drop occurs at 85.0 ksi and 1.28% strain. The stress then drops to 77.5 ksi and ramps up until another

load drop at 91.1 ksi and 1.54% strain. That load drop decreases to 85.7 ksi and increases again until UTS and ε_f are reached.

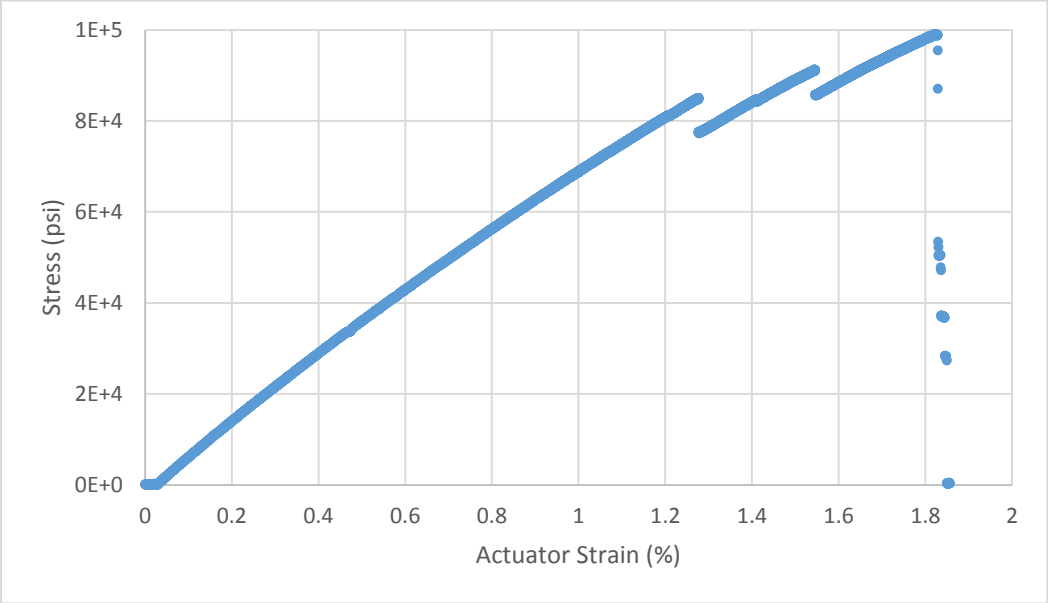


Figure 65: Stress vs. Strain for Glass-C1 Coupon 2449-25

The three graphs below in for Figure 66, Figure 67, and Figure 68 show that all three types of damage events were present in abundant numbers throughout the test. The first damage type to be recorded were MCD events at 0.31% strain, 21.9 ksi, and 33.5 seconds. The second damage type to occur were the FPPD events at 0.33% strain, 23.7 ksi, and 35.9 seconds. The final damage type to be recorded were the FBD events at 0.74% strain, 52.6 ksi, and 81.0 seconds. The first observation from these figures is that MCDs are present throughout the entire test and steadily increase in number as it progresses. The next observation is that there are distinct bands that form in the FPPD range, which as stated earlier can be the fiber pullout and matrix debond are propagating separately. This is due to the substantial increase in the number of recorded events, so a

separation within the damage type is noticeable, whereas with the previous tests the low N_{PFRQ} recorded cannot generate any definable trend. This work will continue to group these two damage types together because physical confirmation of them through microscope or other is unable to be verified. Finally, the last observation from these graphs is that the PFRQs recorded for the FBD events are substantially higher than in the previous 0° samples. For Glass-A1 and Glass-A1* materials, the PFRQs were in the mid-300s to mid-400s kHz range, and the Glass-C1 samples consistently had PFRQ events over 500 kHz. There are of course events in the mid-300s kHz occurring, but the overall PFRQ is much higher than the previous samples on average.

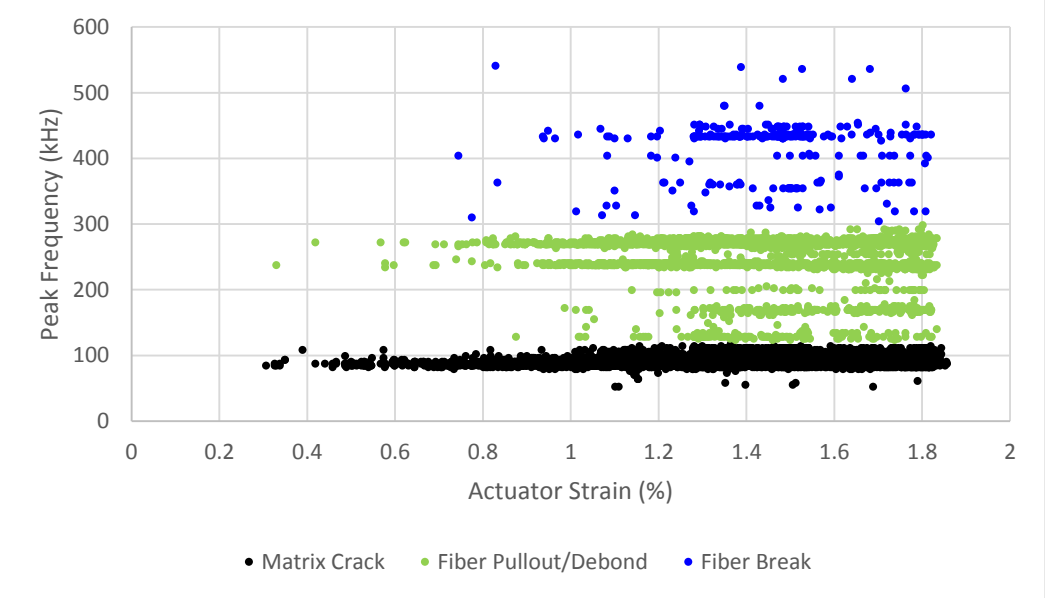


Figure 66: Event PFRQ vs. Strain for Glass-C1 Coupon 2449-25

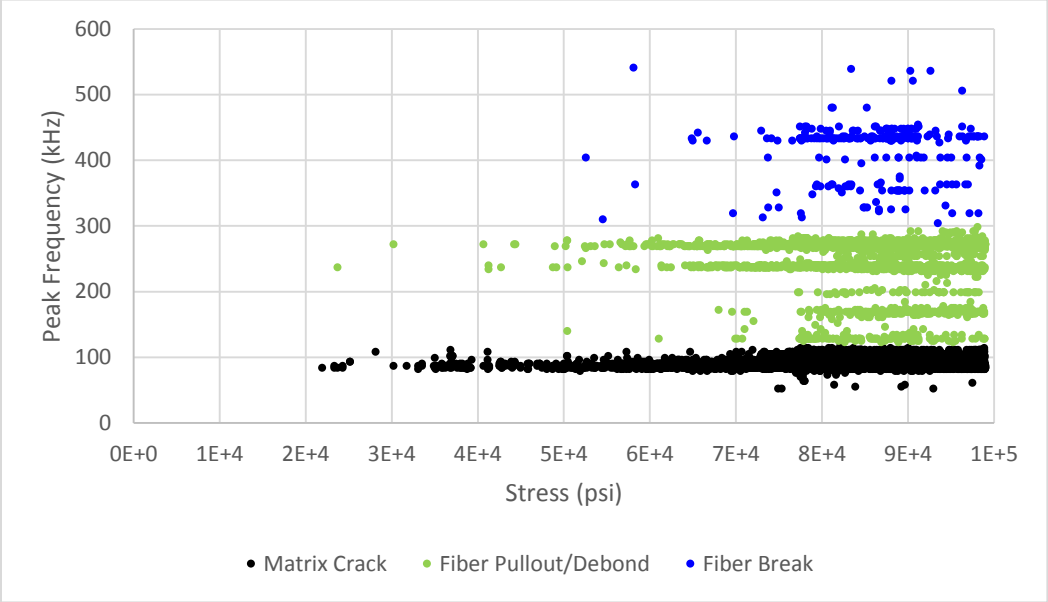


Figure 67: Event PFRQ vs. Stress for Glass-C1 Coupon 2449-25

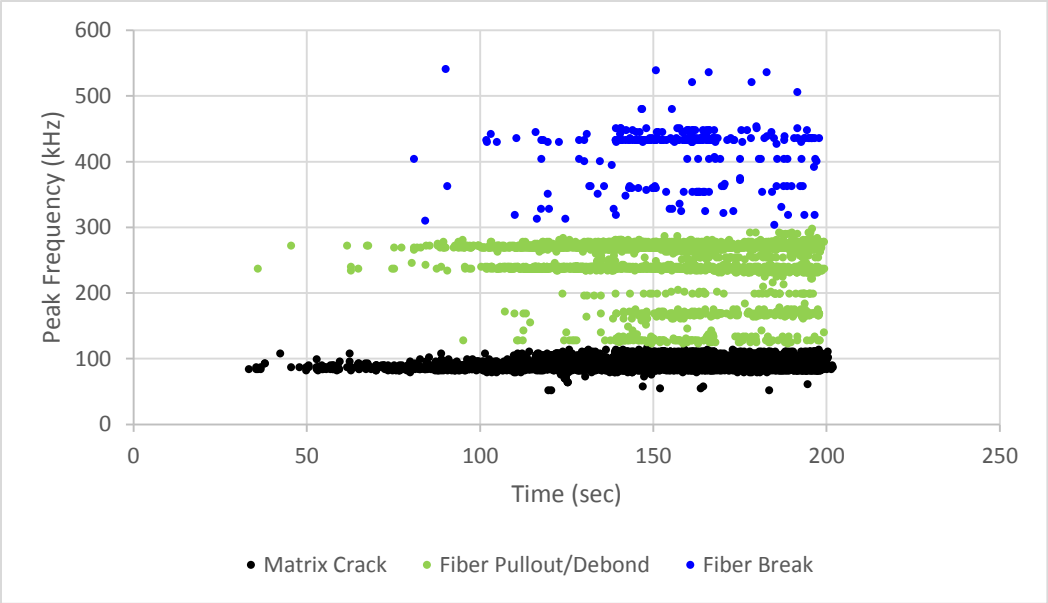


Figure 68: Event PFRQ vs. Time for Glass-C1 Coupon 2449-25

The two graphs below for Figure 69 and Figure 70 feature the E_{abs} released for each recorded event versus the strain. The largest energy release recorded for the test was $1.19*10^{8}$ aJ at 1.84% strain, immediately prior to the samples catastrophic failure.

Figure 70 features the same plot as the previous with a truncation at $9*10^6$ aJ for higher resolution for the events. The first energy spike occurs at 1.07% strain and the second occurs at 1.39% strain. Both of these energy spikes, along with the final spike at catastrophic failure, align with the sudden load drops found in the stress-strain curve.

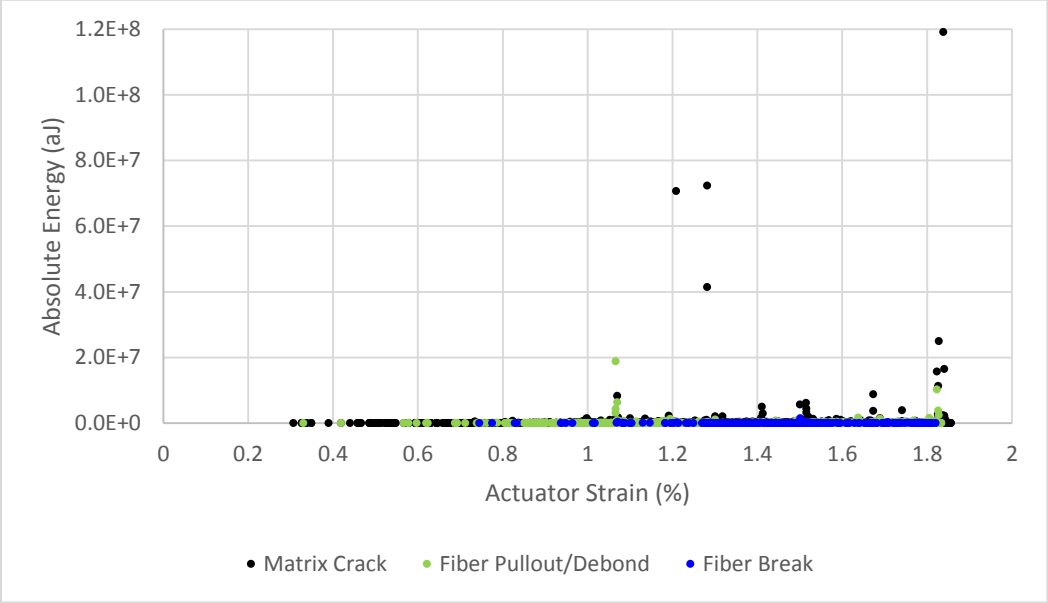


Figure 69: Absolute Energy vs. Strain for Glass-C1 Coupon 2449-25

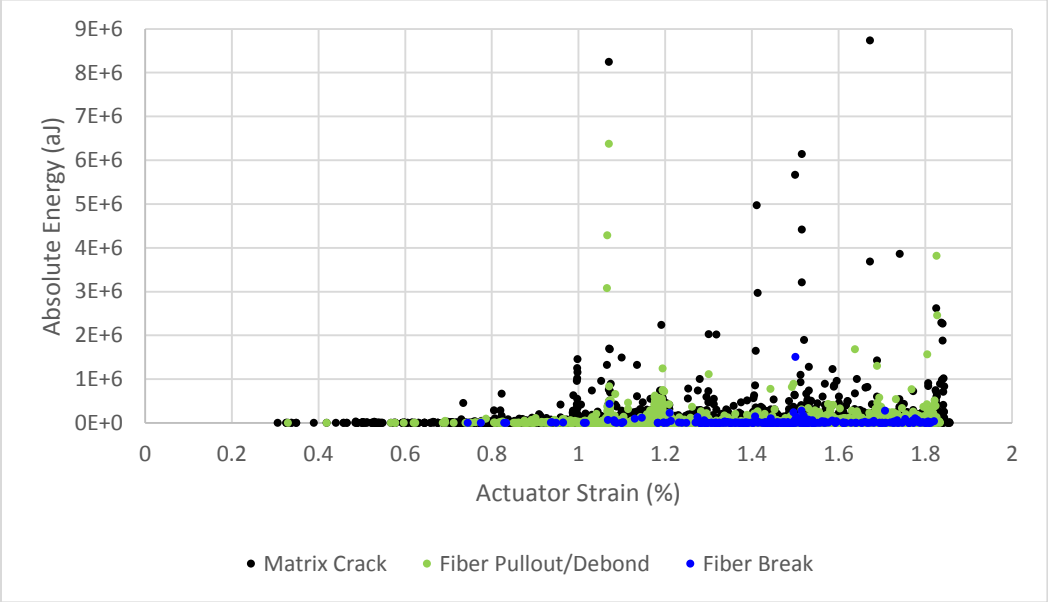


Figure 70: Absolute Energy vs. Strain for Glass-C1 Coupon 2449-25 Truncated at $9*10^6$aJ

Figure 71 below features a breakdown of the N_{PFRQ} that occur within the coupon by percentage. MCDs make up 69.92%, FPPDs account for 28.35%, and FBDs are 1.73%. This sample, unlike Glass-A1 and Glass-A1*, has a much higher proportion of FPPDs and FBDs occurring during testing. This is especially true for FPPDs, as it makes up more than a quarter of N_{PFRQ}, whereas the previous 0° samples had less the 2% on average.

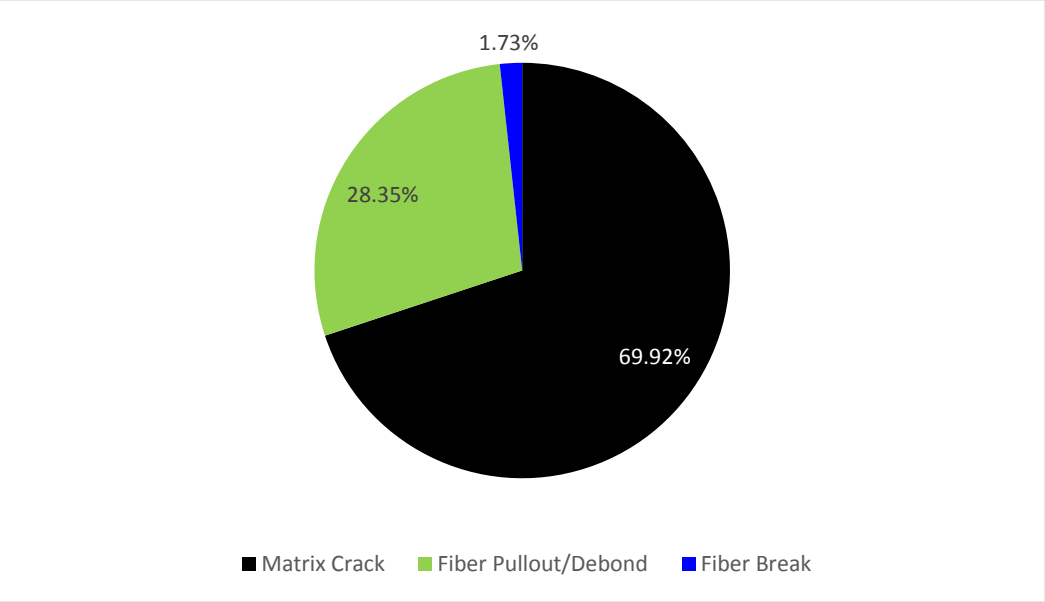


Figure 71: Recorded PFRQ Events by Damage Corresponding Type of Damage for Glass-C1 Coupon 2449-25

Summary of 0° Coupons

The summary of UTS, ε_f, N_{PFRQ}, and total E_{abs} released for each of the 0° samples are in Table 7 below. As can be seen in the table, the removal of the stitching from the Glass-A1 material caused and increase in UTS, but a decrease in the ε_f. Also, the Glass-A1* material had a substantial decrease in the N_{PFRQ} , thus a substantial decrease of energy released; in this case it was 29.9% of N_{PFRQ} and 25.4% of the E_{abs} released compared to Glass-A1. Glass-C1, with the addition of CSM backing, performed similarly to Glass-A1* for ε_f. The UTS for Glass-C1 had the highest N_{PFRQ} of the 0°, but even with 10 times as many events as Glass-A1, it had approximately the three times that of E_{abs} released. This is mainly due to the single event the released $1.09*10^9$ aJ for Glass-A1. Without that event, the total E_{abs} release would be $1.55*10^8$ aJ.

The differences between the stitched fabric (Glass-A1) the unstitched fabric (Glass-A1*) features an increase in UTS by 30.7%, a decrease in ε_f by 3.09%, a decrease in the N_{PFRQ} recorded by 70.1%, and decrease in total E_{abs} released by the coupon by 74.6%.

	Glass-A1	Glass-A1*	Glass-C1
V_f (%)	43	42	44
UTS (ksi), [σ]	65.5, [6.5]	85.6, [10.6]	95.2, [8.39]
ε_f (%), [σ]	1.94, [0.11]	2.00, [0.04]	1.65, [0.17]
N_{PFRQ}, [σ]	1771, [194]	529, [189]	18134, [4539]
Total E_{abs} (nJ), [σ]	71.0, [38.9]	18.0, [25.0]	221, [108]

Table 7: $\bar{x}$ and σ of V_f, UTS, εf, N_{PFRQ}, and E_{abs} for Every 0° Coupon

90° Coupons

In Figure 72, Figure 73, and Figure 74 below, all of the tested 90° samples can be seen with the various ways that they reached catastrophic failure. Typically the failure occurred at an interface of two 90° tows by separation. Grip failure was not typically a problem with this coupon set, as they did not reach high enough stresses. The Glass-A2 sample shows there is small stitching threads that attempted to hold the fiber tows together during failure. The Glass-A2* sample shows a clean break between the tows with the absence of stitching. The Glass-C2 samples shows a well-defined break between tows with lots of CSM fibers that are actually still attached from one side of the coupon to the other. Also, it is important to notice that the CSM whitened under stress, which implies FPDD.

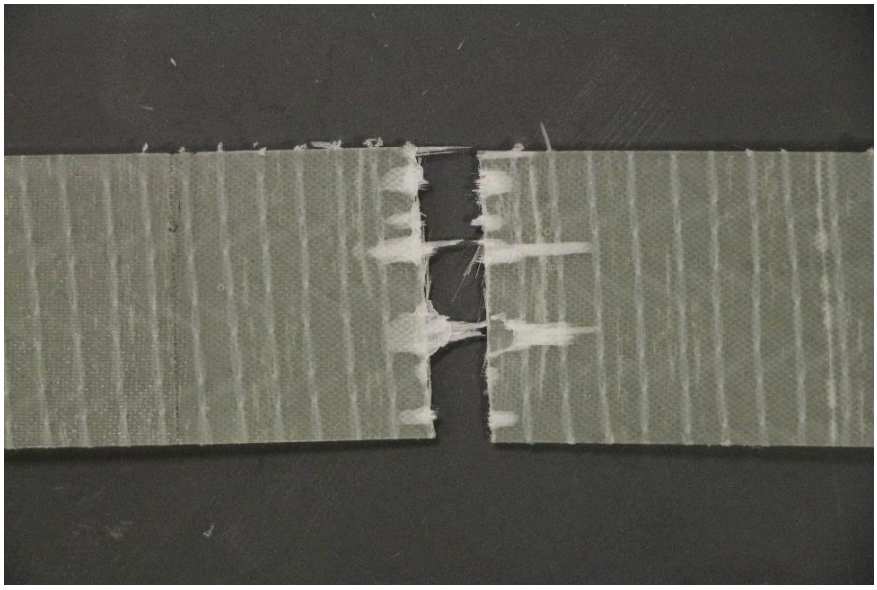


Figure 72: Glass-A2 Coupon 2451-23 after Catastrophic Failure

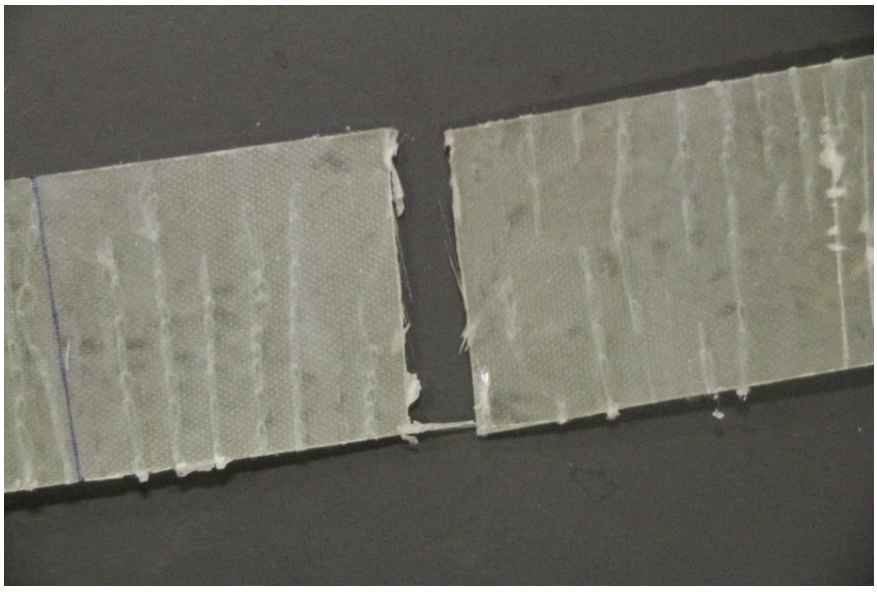


Figure 73: Glass-A2* Coupon 2452-22 after Catastrophic Failure

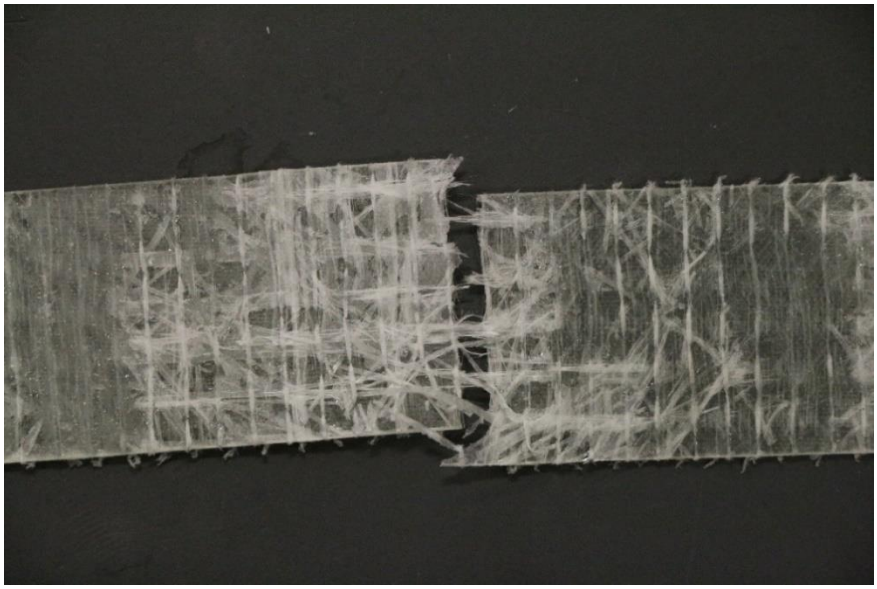


Figure 74: Glass-C2 Coupon 2450-23 after Catastrophic Failure

Glass-A2

In the graph below, Figure 75 features the stress-strain curve for the Vectorply E-LT-3900 UD 90° single ply coupons with the stitching intact. The UTS 6.48 ksi and a ε_f of 0.36%. This sample features three separate instances of internal damage causing sudden load drop before catastrophic failure. The first sudden load drop occurs at 5.06 ksi and 0.24% strain, which causes the stress to decrease to 4.74 ksi. The load then increased to the next load drop at 6.48 ksi and 0.32% strain, which then causes the stress to decrease to 5.92 ksi. The load increases from there to the final load drop before catastrophic failure at 6.33 ksi and 0.34 % strain, which then decreased to 5.92 ksi. After that the stress increases to the UTS and catastrophic failure is achieved.

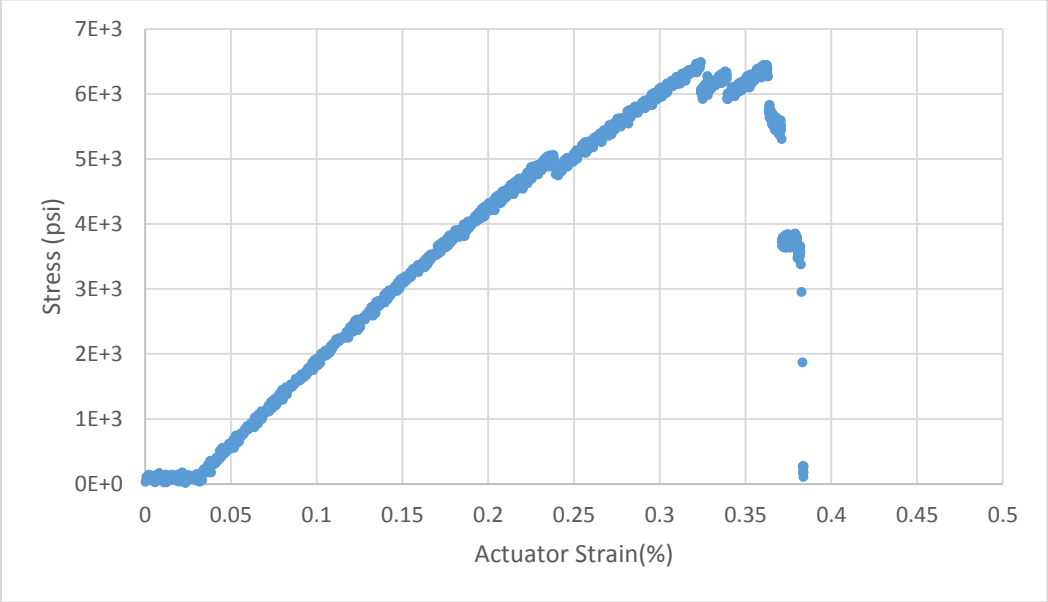


Figure 75: Stress vs. Strain for Glass-A2 Coupon 2451-23

The next three graphs in Figure 76, Figure 77, and Figure 78 below feature the N_{PFRQ} related to the damage types. In Figure 77 four events are recorded at a very low stress of about 550 psi, which can be attributed to load drop during catastrophic failure, as the vast majority of PFRQ events occur at much higher stresses. Disregarding that initial group, the first type of damage recorded is FPPD at 0.16% strain, 3.42 ksi, and 17.6 seconds. The second damage type to be recorded is MCD at 0.19% strain, 3.47 ksi, and 20.0 seconds. The final damage type to be recorded is the FBD at 0.19% strain, 4.04 ksi, and 20.4 seconds. The first observation is that FPPD is recorded before any other damage type, which is not typical. The next interesting feature is that all of the FBDs have relatively low PFRQs, as all of them are not greater than 315 kHz, which is barely within the acceptable range for FBDs.

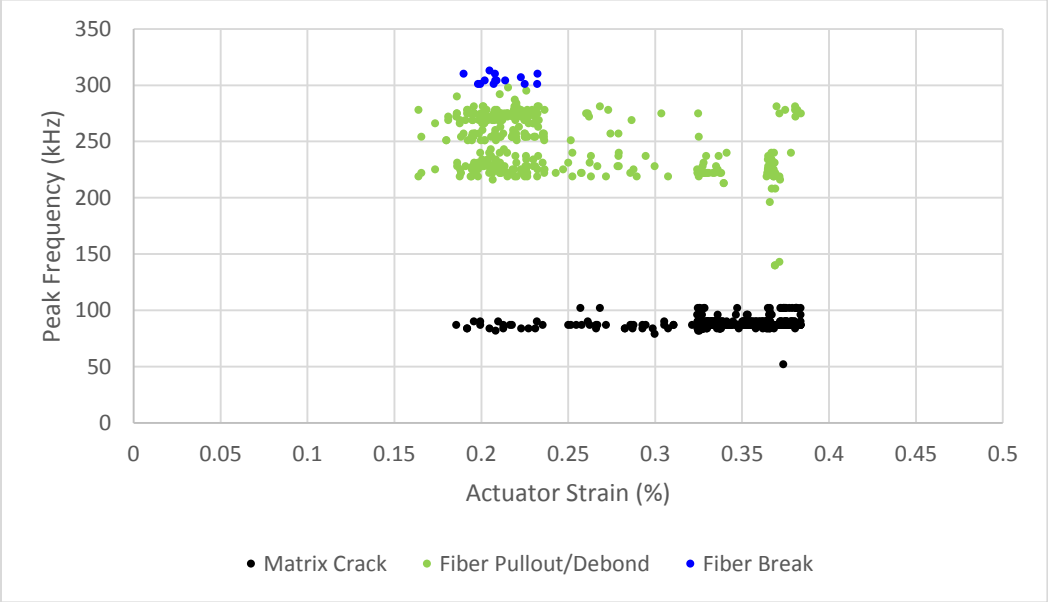


Figure 76: Event PFRQ vs. Strain for Glass-A2 Coupon 2451-23

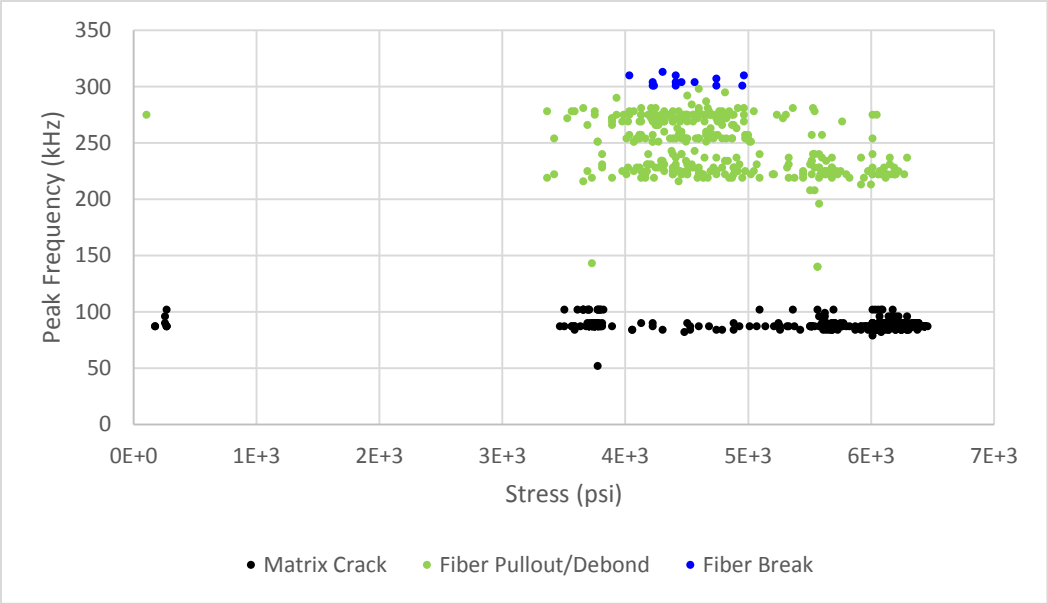


Figure 77: Event PFRQ vs. Stress for Glass-A2 Coupon 2451-23

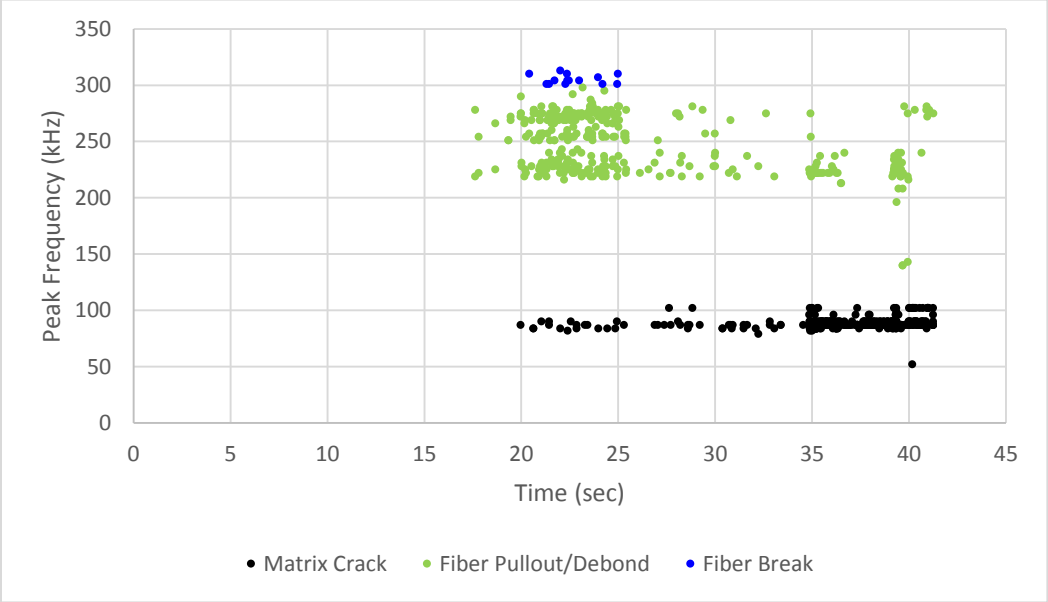


Figure 78: Event PFRQ vs. Time for Glass-A2 Coupon 2451-23

The two graphs below for Figure 79 and Figure 80 feature the E_{abs} released versus the strain of the sample. The first graph shows a maximum energy released for an event at $2.77*10^8$ aJ at 0.32% strain. The graph below that is the same as the previous, but with a truncation at $1*10^4$ aJ for higher resolution. There are three energy spikes at 0.24% strain, 0.32% strain, and 0.34% strain, with a final spike at 0.36% strain prior to catastrophic failure. All three of these energy spikes correlate with the sudden load drops as previously stated.

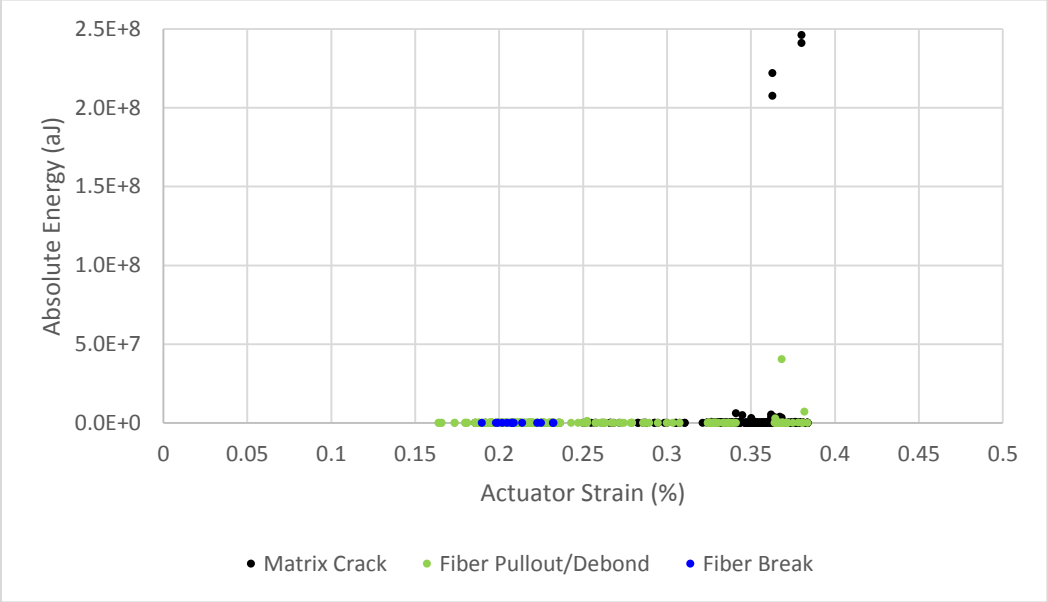


Figure 79: Absolute Energy vs. Strain for Glass-A2 Coupon 2451-23

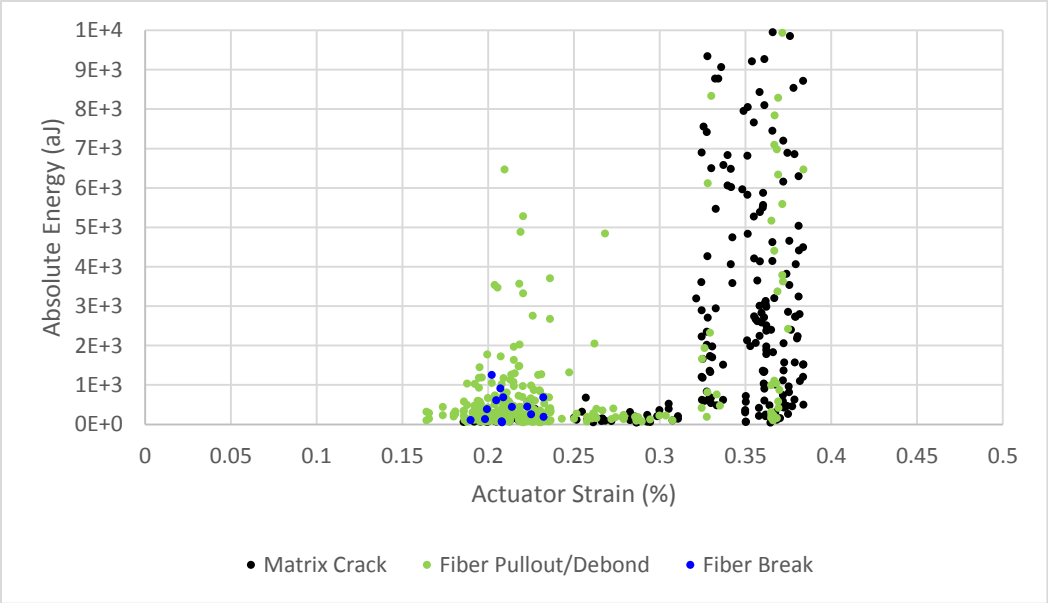


Figure 80: Absolute Energy vs. Strain for Glass-A2 Coupon 2451-23 Truncated at $1*10^4$aJ

Figure 81 below features a breakdown of the N_{PFRQ} corresponding to the three damage types occurring with the sample by percentage. MCDs make up 57.47 of N_{PFRQ}. The FPPDs account for 40.86% and FBDs are 1.67% of damage types. The FPPDs and

MCDs account for a relatively high percentage of the damage due to the low N_{PFRQ}. It has similar overall numbers to Glass-A1*, which will be discussed in the summary section.

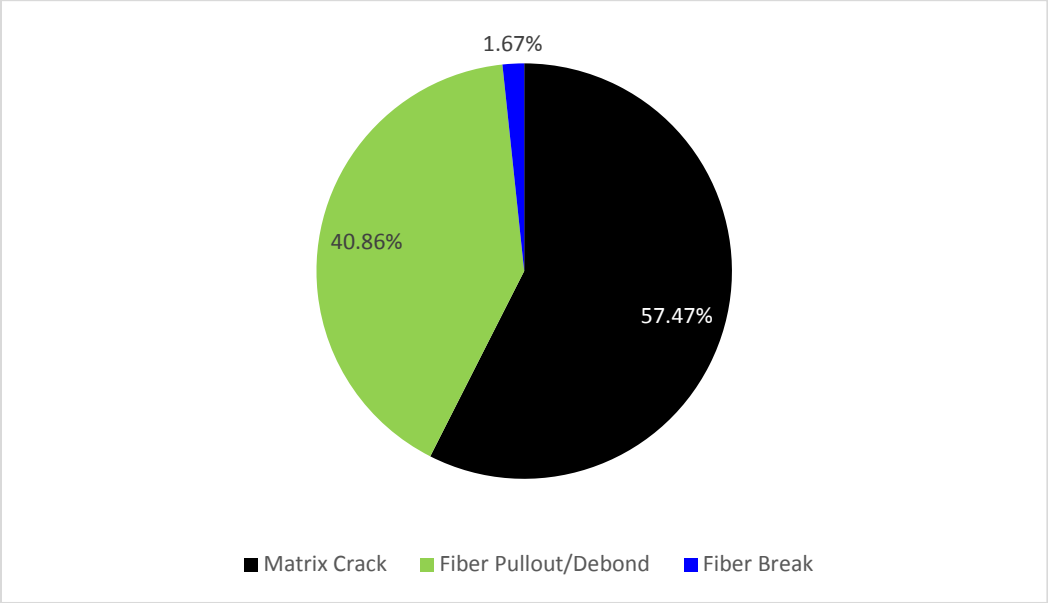


Figure 81: Recorded PFRQ Events by Damage Corresponding Type of Damage for Glass-A2 Coupon 2451-23

Glass-A2*

The next sample set features the Vectorply E-LT-3900 UD 90° single ply coupons with the stitching removed. Figure 82 below features the stress-strain curve for the Glass-A2* material and shows a UTS of 5.13 ksi and a ε_f of 0.41%. It is interesting to note that the test continues on past the UTS by a substantial amount due to the fact that the damage that occurred was not enough to completely cause the sample to lose all load-bearing ability and events were still being recorded. In most other samples, once UTS is achieved the samples load drops to essentially zero in less than a second, but that was not the case for this sample set. Also, the ability to still record damage events after UTS is

the main reason that this test was not stopped. The first sudden load drop occurs at the time of UTS, but two more are observed before catastrophic failure. After the initial load drop, the stress in the sample then becomes 926.4 psi at 0.27% strain which is held steady until 0.30% strain. Another load drop occurs, and the stress decreases to 596.46 psi and 0.31% strain. The load increased again to 901.04 psi and 0.38% strain, which then leads to a gradual decrease in load over several seconds to 672.60 psi and 0.41% strain. This load is held steady for approximately 4 seconds. At this point the final sudden load drop occurs and catastrophic failure is achieved.

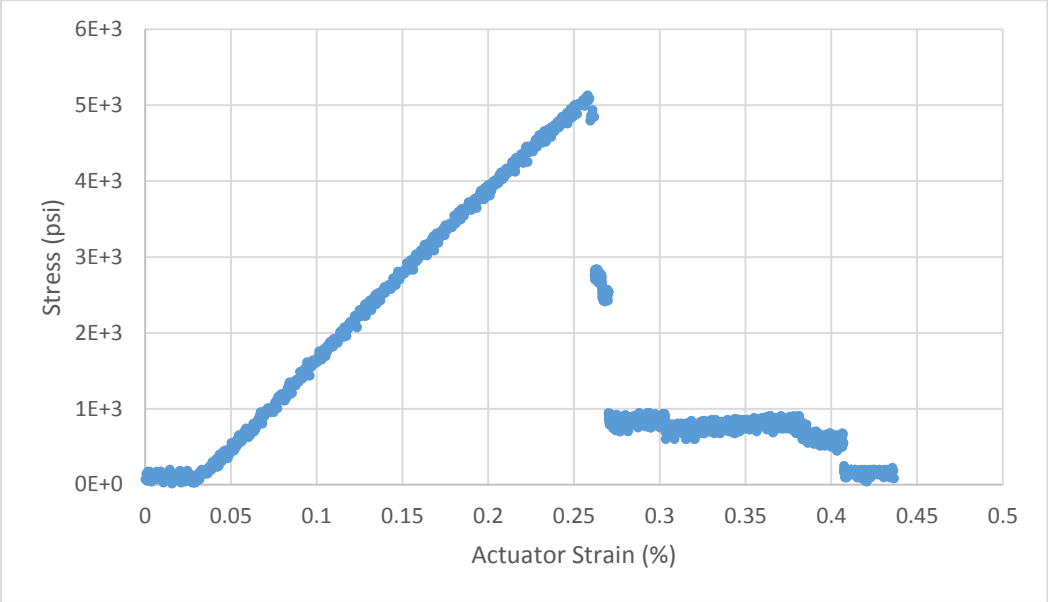


Figure 82: Stress vs. Strain for Glass-A2* Coupon 2452-22

The next three graphs in Figure 83, Figure 84, and Figure 85 feature the PFRQ events and their associated damage type. The first type of damage to be recorded is MCD at 0.22% strain, 4.12 ksi, and 23.1 seconds. The second damage type to be detected was FPPD events at 0.23% strain, 4.61 ksi, and 24.7 seconds. There were no

instances of FBD events recorded during testing. This samples is unique in that there are three separate groupings of events for the stress graph in Figure 84, where the grouping at the highest value are the actual first events recorded. The second grouping recorded is the one in the middle, and the final is the one at the lowest stress values. This is due to the test being allowed to continue past UTS, due to the fact that the sample was still load bearing, as previously stated. All of the events recorded after 27 seconds are after UTS is achieved. The most damage propagating are in the third group, in which the stresses are the lowest. In particular, when the load was held steady between 0.27% and 0.30% strain as seen in the stress-strain diagram; this is also between 28 and 33 seconds in Figure 85.

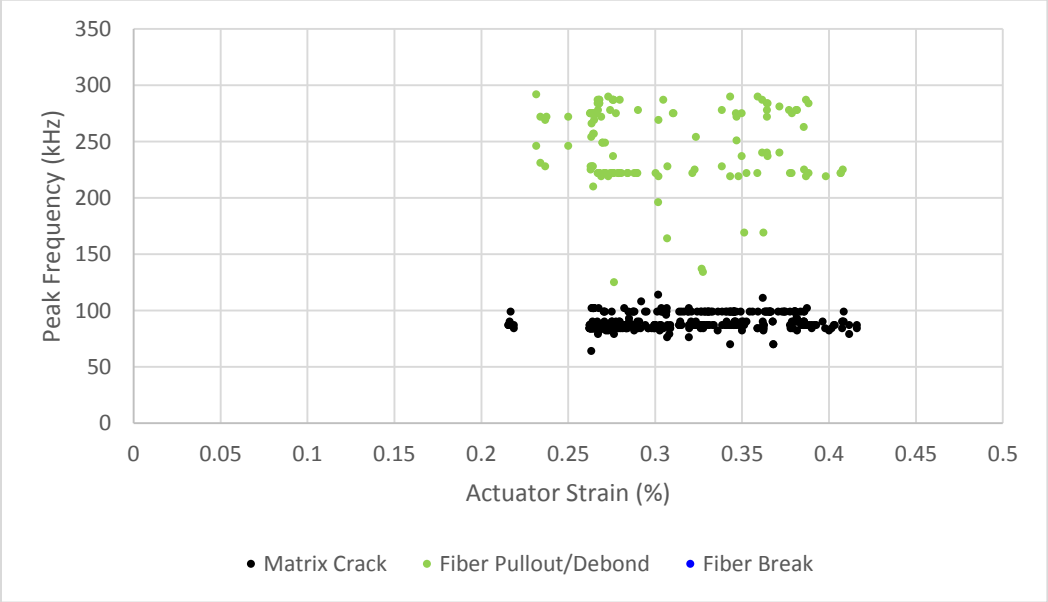


Figure 83: Event PFRQ vs. Strain for Glass-A2* Coupon 2452-22

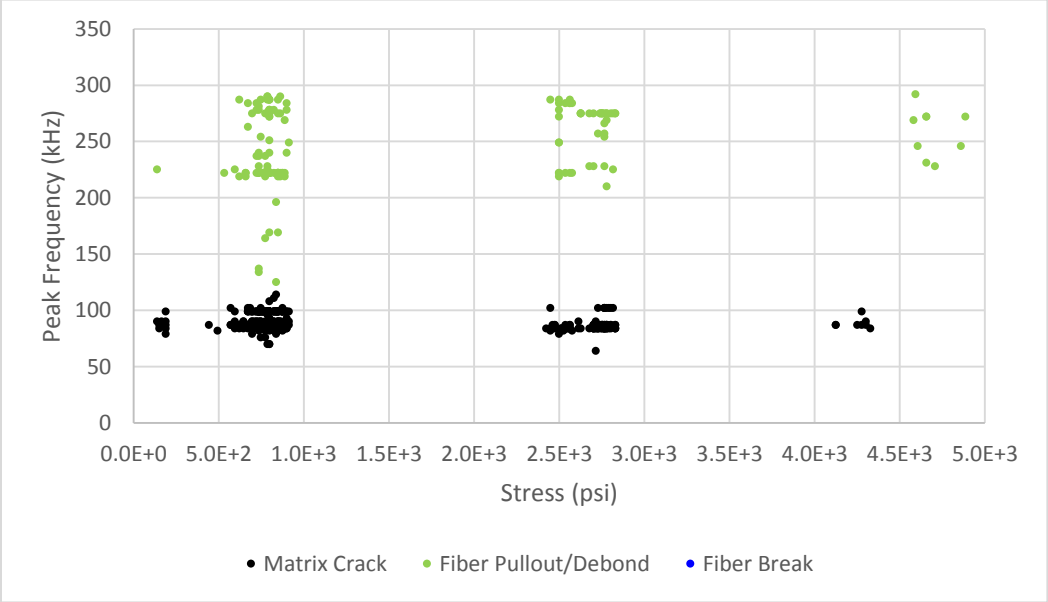


Figure 84: Event PFRQ vs. Stress for Glass-A2* Coupon 2452-22

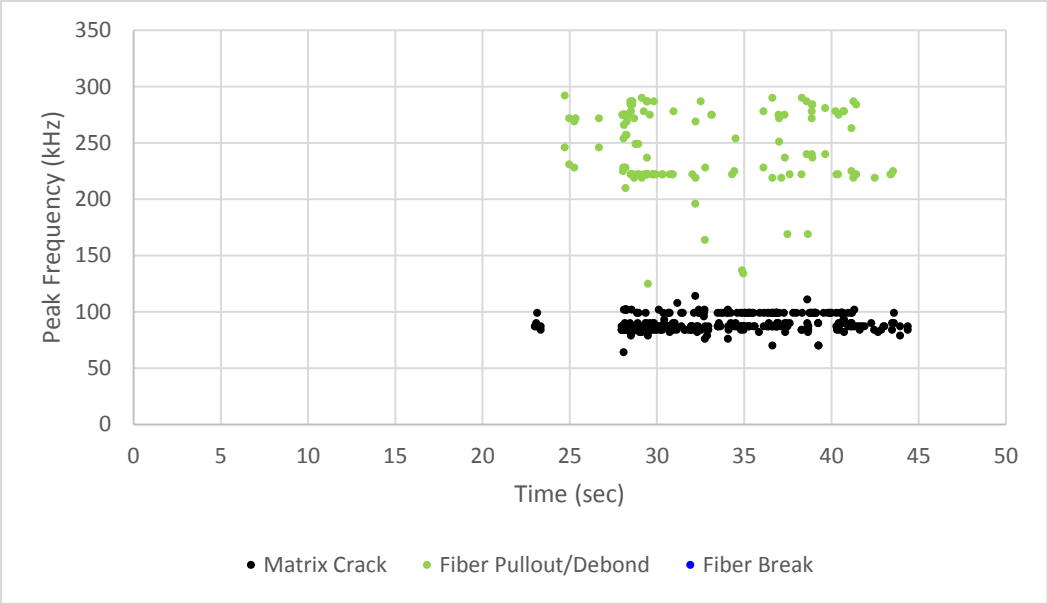


Figure 85: Event PFRQ vs. Time for Glass-A2* Coupon 2452-22

Figure 86 and Figure 87 below feature the E_{abs} released by the sample versus the strain and the truncation of the energy at $8*10^6$ aJ for higher resolution for Figure 87. The maximum energy released is $3.49*10^8$ aJ at 0.30% strain. The first spike in E_{abs} is at

0.27% strain, the second is at 0.31% strain, the third is at 0.38%, and the final spike is at 0.41% strain. All four spikes correlate with the sudden load drops and catastrophic failure seen in the stress-strain curve. It is interesting to note that the highest magnitude of the energy released is when the sample was holding the load steady between 0.27% and 0.30% strain, as previously stated, instead of during a load drop. This shows that the highest energy damage was occurring during that time of testing.

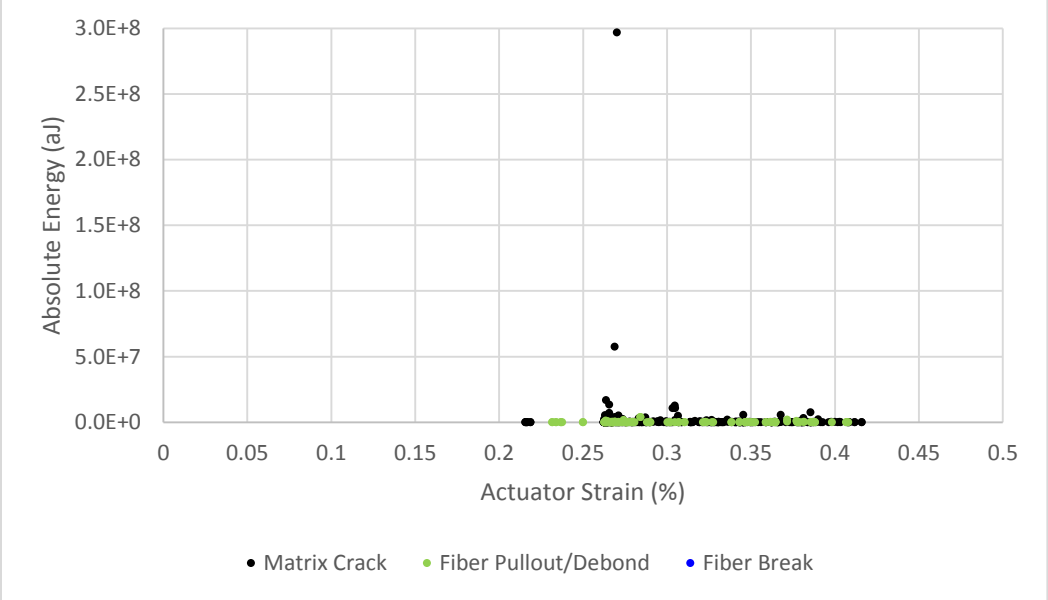


Figure 86: Absolute Energy vs. Strain for Glass-A2* Coupon 2452-22

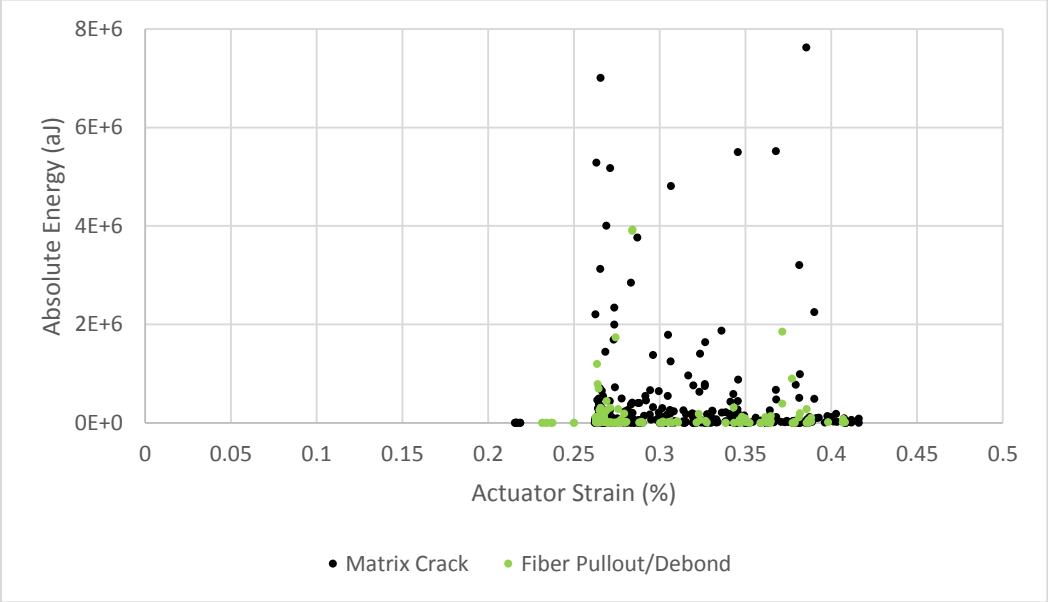


Figure 87: Absolute Energy vs. Strain for Glass-A2* Coupon 2452-22 Truncated at $8*10^6$aJ

Figure 88 features the breakdown of N_{PFRQ} and there corresponding damage types by percentage. MCDs account for 72.76% of N_{PFRQ}, while FPDDs make up the remainder. This sample is unique in that it no instances of FBDs were recorded, primarily due to the relatively low stresses during testing. The stresses between the 90° tows were large enough to cause failure, but not large enough to cause fibers to break. This is common for coupons only made of 90° plies.

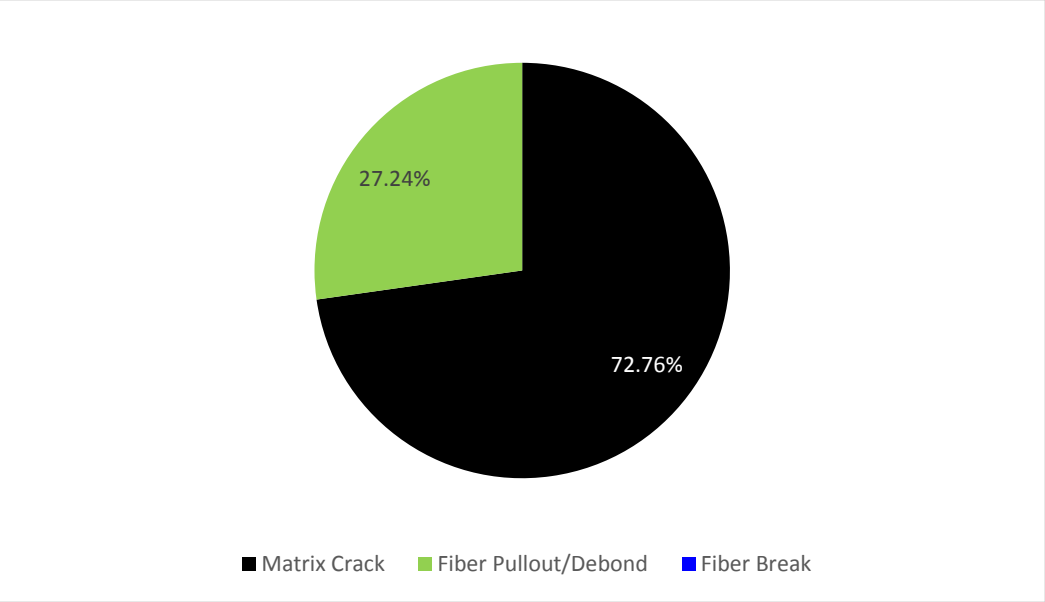


Figure 88: Recorded PFRQ Events by Damage Corresponding Type of Damage for Glass-A2* Coupon 2452-22

Glass-C2

The next sample set features PPG L1200/G50 UD 90° with CSM backing single ply coupons. In Figure 89 below, the UTS is 5.51 ksi and a ε_f of 0.81% strain. This sample features eight sudden load drops that occur between 0.14% and 0.25% strain, and another eight occur between 0.25% and 0.54% strain. The biggest load drop occurs at 3.69 ksi and 0.25% strain, in which it drops to 3.20 ksi. An important observation is that all of the load drops occur after the sample reaches plastic deformation at 3.32 ksi and 0.14% strain. Once this happens, the first grouping of load drops occur but the sample still increases load bearing. It is not until catastrophic failure occurs the trend of increasing stress stop. It is also the only sample for the 90° coupon set that achieves greater than 0.5% strain.

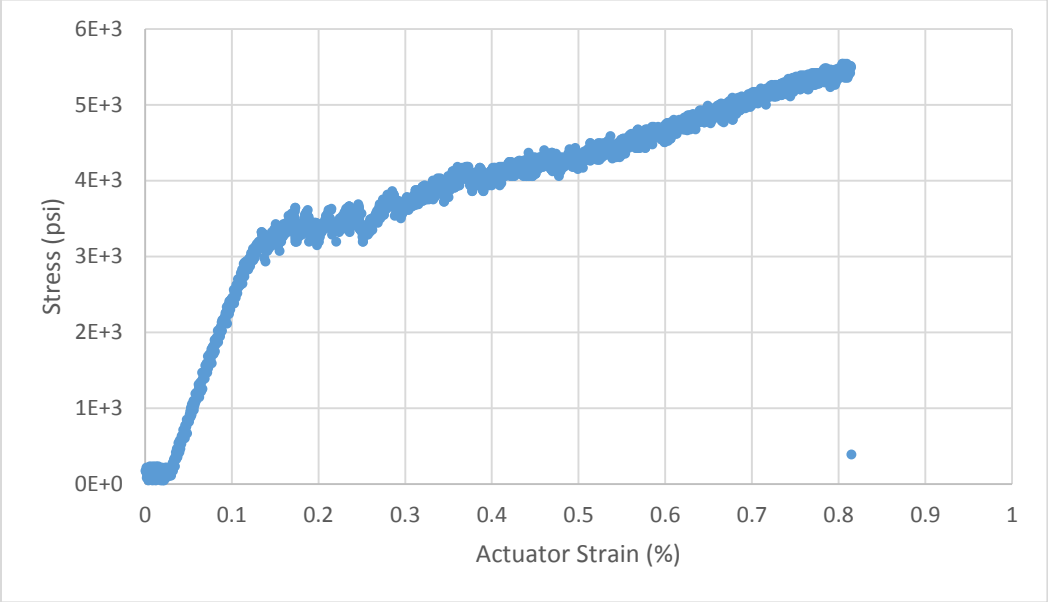


Figure 89: Stress vs. Strain for Glass-C2 Coupon 2450-23

The next three graphs in Figure 90, Figure 91, and Figure 92 features the PFRQ events with their corresponding damage type. The first damage type events to be recorded are FPPDs at 0.12% strain 2.95 ksi, and 13.7. The second damage type to be recorded is MCDs at 0.12% strain, 3.00 ksi, and 13.8 seconds. The final damage type to be recorded are was the sole FBD at 0.20% strain, 3.4 ksi, and 22.7 seconds. It is of interest to note that the first instances of MCDs and FPPDs occur almost simultaneously. Similarly to the Glass-A2* material, there is a lack of FBDs. It occurs so early in the test that it is most likely caused by edge effects. There is no physical confirmation of this, so it must be taken into account for the data set.

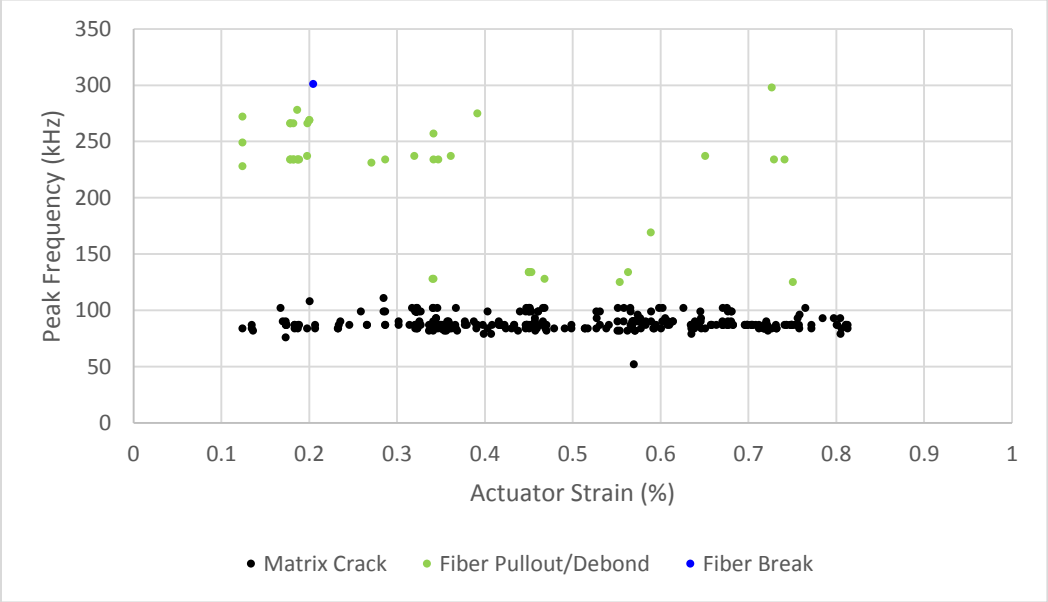


Figure 90: Event PFRQ vs. Strain for Glass-C2 Coupon 2450-23

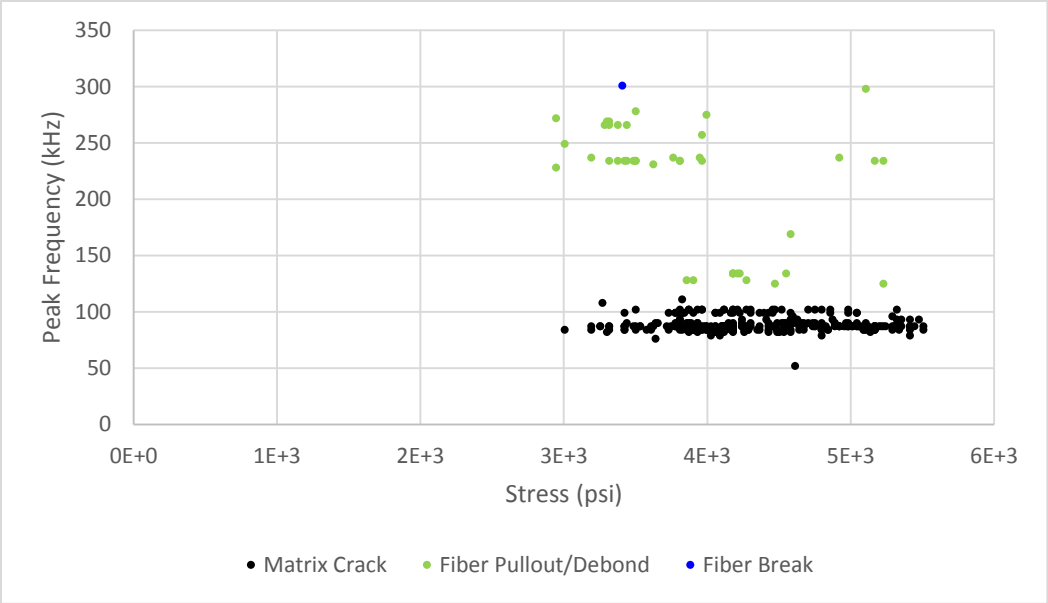


Figure 91: Event PFRQ vs. Stress for Glass-C2 Coupon 2450-23

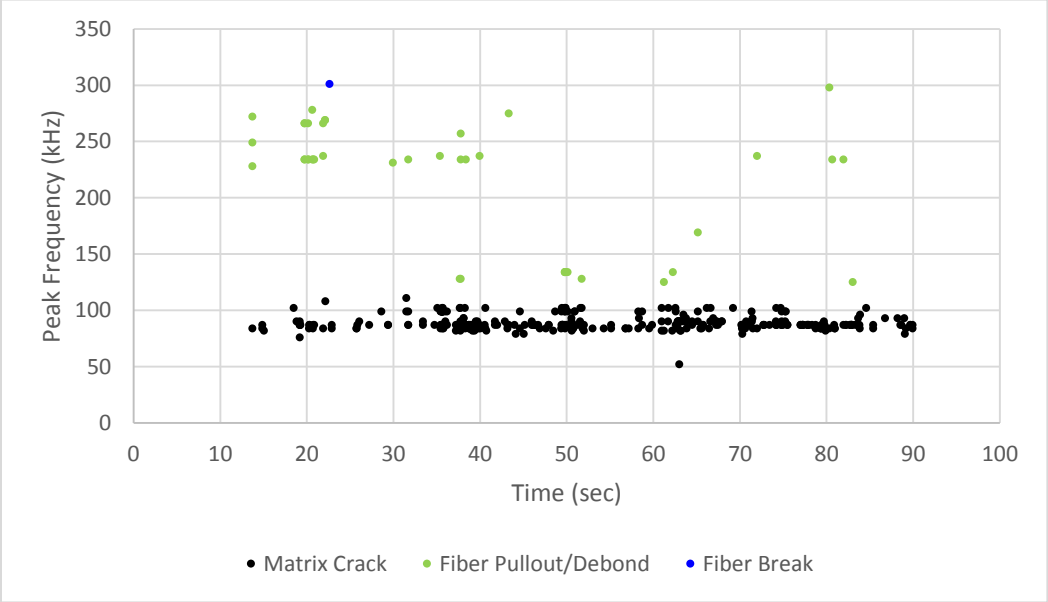


Figure 92: Event PFRQ vs. Time for Glass-C2 Coupon 2450-23

The next two graphs feature the E_{abs} released versus the strain of the sample in Figure 93, and the same graph with a truncation at $6*10^5$ aJ for Figure 94. The maximum amplitude of E_{abs} released is $3.78*10^8$ aJ at 0.45% strain. This point correlates with the load drop as seen in the stress-strain diagram and a large increase in MBDs as seen in Figure 93. The truncated graph shows the two largest spikes are at 0.20%, which correlates with the largest load drop in the test and another at 0.78%, prior to catastrophic failure.

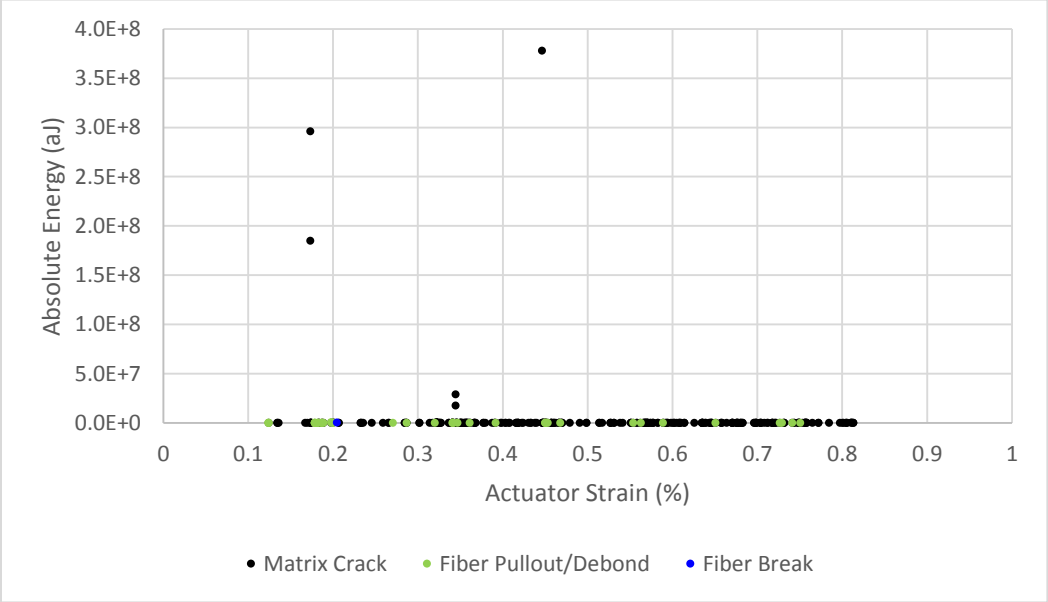


Figure 93: Absolute Energy vs. Strain for Glass-C2 Coupon 2450-23

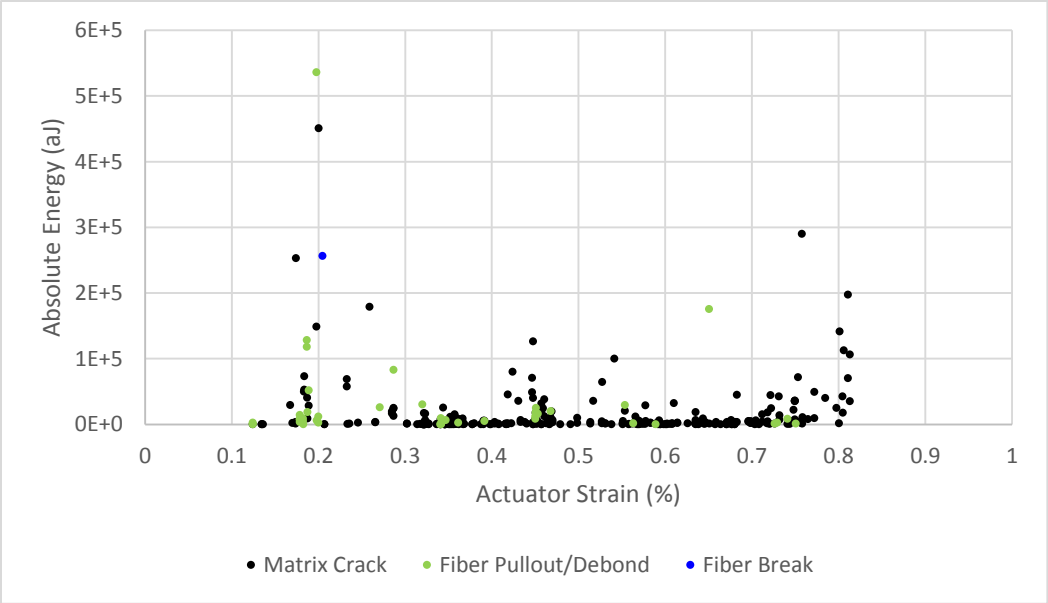


Figure 94: Absolute Energy vs. Strain for Glass-C2 Coupon 2450-23 Truncated at $6*10^5$aJ

Figure 95 feature a breakdown of N_{PFRQ} with their corresponding damage type by percentage. MCDs account for 88.28%, FPPDs 11.4%, and the FBD is 0.27% recorded during testing. The MCDs dominate the damage type for these samples, with the sole

FBD possibly being caused by edge effects. Glass-C2 looks more similar to Glass-A* material than it does to either of the other 90° samples.

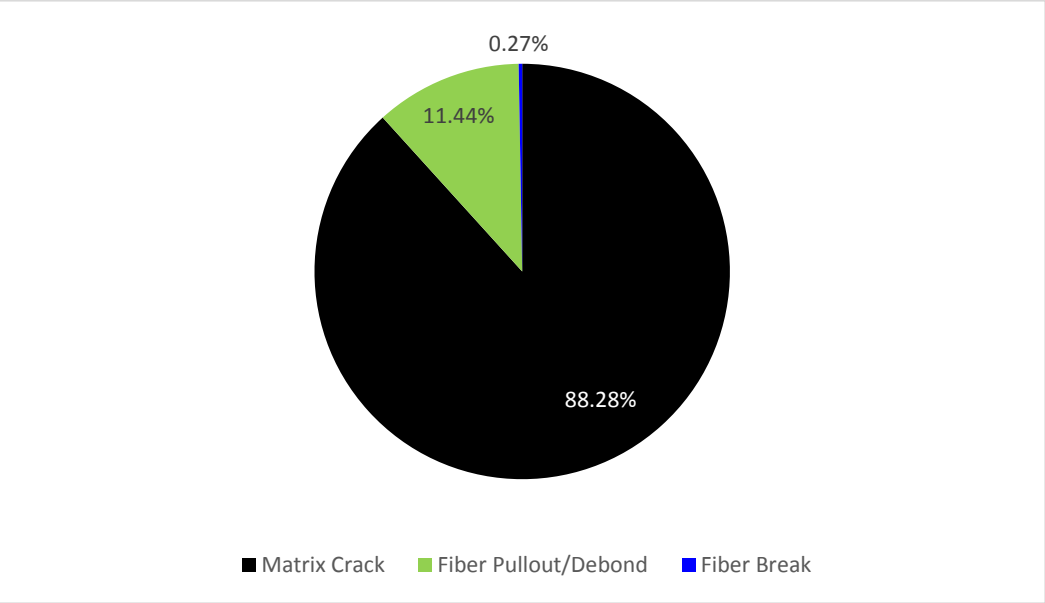


Figure 95: Recorded PFRQ Events by Damage Corresponding Type of Damage for Glass-C2 Coupon 2450-23

Summary of 90° Coupons

The summary of UTS, ε_f, N_{PFRQ}, and total E_{abs} released for each of the 90° samples are in Table 8 below. The most obvious observation of the table is that the removal of the stitching for the Glass-A material seems to have the opposite effect on the mechanical properties as the 0° samples. Glass-A2 has a higher UTS and total E_{abs} released and lower ε_f than Glass-A2*; the opposite effect as on Glass-A1 to Glass-A1*. The only similar trend between the four is that the material with the stitching intact has a greater N_{PFRQ} than the samples with the stitching removed. It released approximately 99.7% more energy. Glass-C2 has a lower UTS than Glass-A2, which it had the highest UTS for the 0° samples. Conversely as well, it had the highest ε_f for all of the samples,

whereas it had the lowest for the 0° samples. It also has the lowest N_{PFRQ}, which is drastically different than its 0° counterpart. It had approximately the same energy release to Glass-A2, which is similar to the 0° samples. Going from Glass-A2 to Glass-A2* the UTS decreased by 44.0%, ε_f decreased by 55.2%, N_{PFRQ} decreased by 97.8%, and a decrease in total E_{abs} released by the sample by 97.7%.

	Glass-A2	Glass-A2*	Glass-C2
V_f (%)	43	42	44
UTS (ksi), [σ]	7.79, [0.79]	4.36, [0.63]	5.70, [0.33]
ε_f (%), [σ]	0.58, [0.15]	0.26, [0.01]	0.79, [0.05]
N_{PFRQ}, [σ]	764, [348]	17, [3.0]	423, [163]
Total E_{abs} (aJ), [σ]	56.6, [37.0]	0.16, [0.19]	68.0, [73.8]

Table 8: $\bar{x}$ and σ of V_f, UTS, εf, N_{PFRQ}, and E_{abs} for Every 90° Coupon

Glass-A2 had an 88.1% decrease in UTS, 70.1% decrease in ε_f, 56.9% decrease in N_{PFRQ}, and a 14.4% decreased in total E_{abs} released compared to Glass-A1. Glass-A2* had a 93.3% decrease in UTS, 86.6% decrease in ε_f, 99.0% increase in N_{PFRQ}, and a 99.8% decrease in total E_{abs} released compared to Glass-A1*. Glass-C2 had a 94.0% decrease in UTS, a 52.1% decrease in ε_f, a 97.7% decrease in total N_{PFRQ}, and an 69.2% decrease in total E_{abs} released compared to Glass-C1.

Biaxial Coupons

In Figure 96, Figure 97, Figure 98, Figure 99, and Figure 100 below, all of the tested biaxial samples can be seen with the various ways that they reached catastrophic failure. The most common type of failure for this set of samples was a combination of separation at the 0° plies and 0° plies breaking. These types of coupons often exhibited

grip failure, which is typically not desired. The only way to combat this was to do a high volume of testing so as to collect enough samples that did not generate grip failure to form a quality data set. Only the coupons that did not exhibit grip failure, for all sample groups, were accounted for in this research. Glass-A3 shows that the failure occurred between two 90° tows, which extended until cracks formed between the 0° tows that were partially held together with stitching. Glass-A3* shows failure at a 90° tow interface but the lack of stitching did not hold the 0° fiber tows in place. They had a shear break at the same spot at the splitting of the transverse tows. They did show some FPDD at the break point, but substantially less than the its stitched counterpart. Glass-B1 shows another initial break at a transverse tow interface with some FPDD of the outer 0° tows. Glass-B2 shows a break at the inner transverse plies, which caused a break of the 0° tows at the same location on one side. This different from the other pre-preg sample because the other side's 0° ply did not fail at all, causing debonding between the outermost and next ply. Glass-C3 a break that is not at any well-defined point. The transverse ply had a failure in several places while the normal tows had an abundance of FPDD. The CSM failed in many locations around the areas of failure holding the two plies in place where possible.

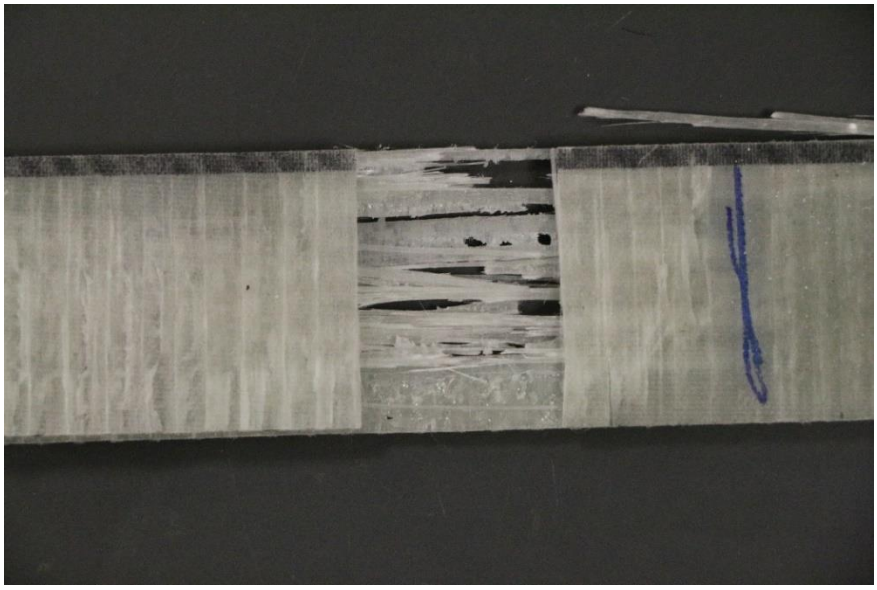


Figure 96: Glass-A3 Coupon 2441-6 after Catastrophic Failure

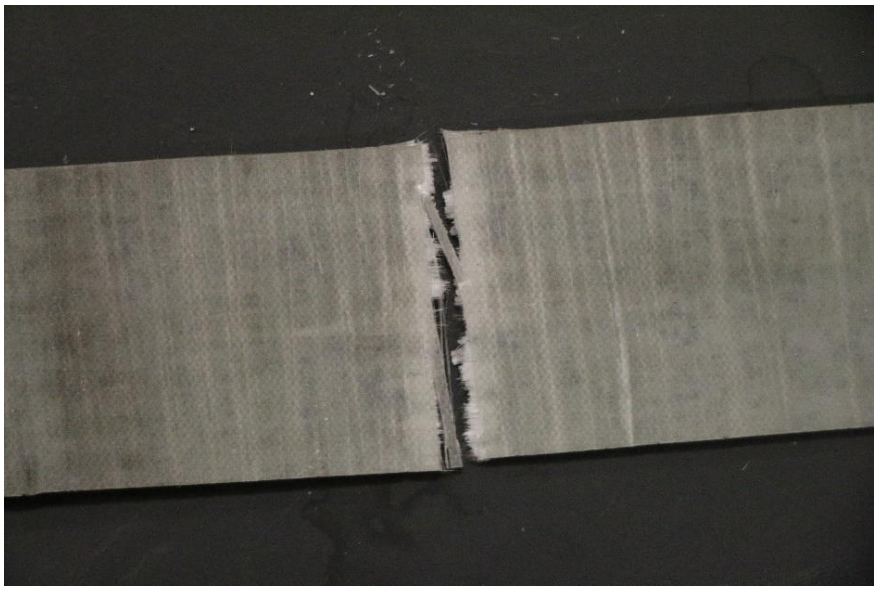


Figure 97: Glass-A3* Coupon 2443-2 after Catastrophic Failure

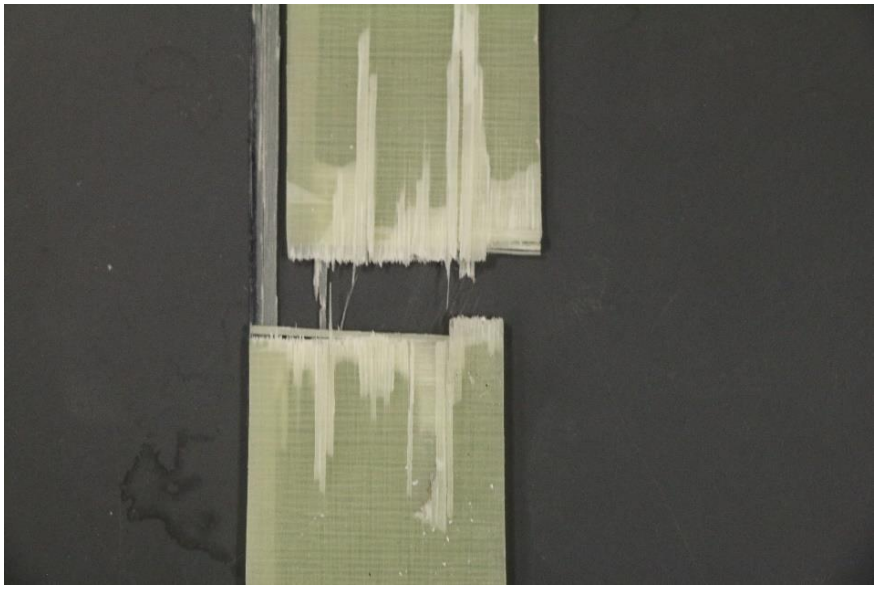


Figure 98: Glass-B1 Coupon 2434-4 after Catastrophic Failure

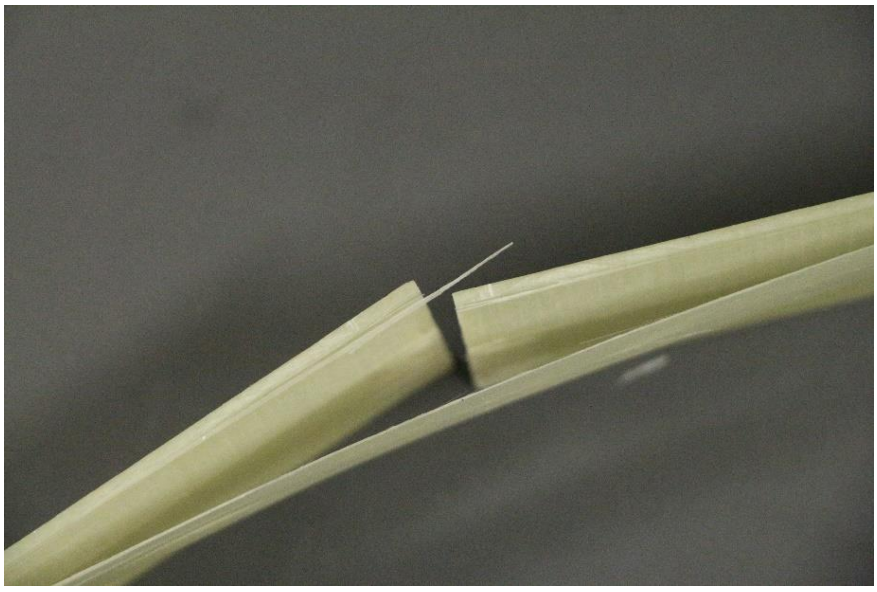


Figure 99: Glass-B2 Coupon 2435-3 after Catastrophic Failure

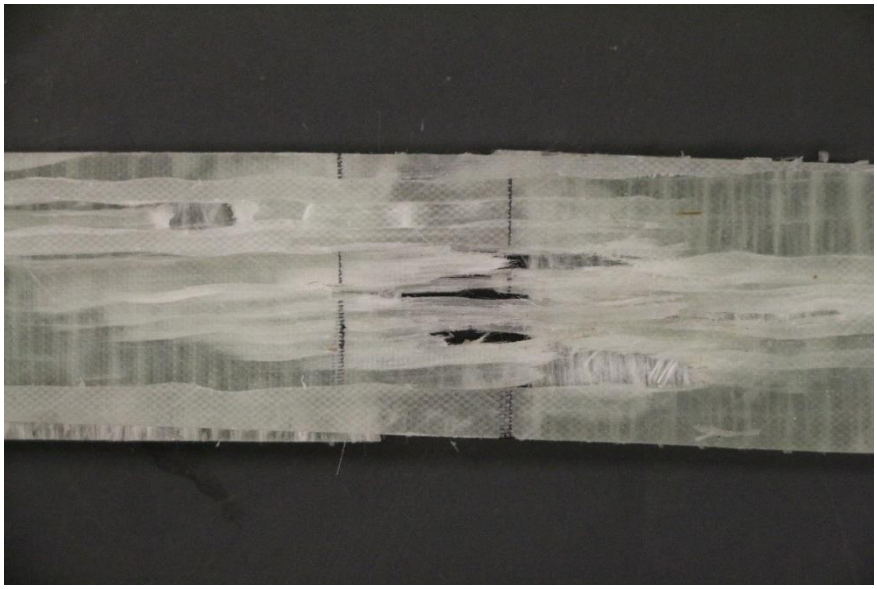


Figure 100: Glass-C3 Coupon 2446-11 after Catastrophic Failure

Glass-A3

This sample set features Vectorply E-LT-3900 UD biaxial two ply coupons with the stitching intact. Figure 101 below shows the stress-strain curve of a sample that had a UTS of 44.8 ksi and a ε_f of 2.15%. There are no noticeable sudden load drops as commonly found with the 90° coupons. There is also no apparent plastic deformation except immediately prior to catastrophic failure. There is also a slight load drop at 9.35 ksi and 0.36% strain. It has lower and higher UTS than Glass-A1 and Glass-A2, respectively. It also has a greater ε_f than either of them.

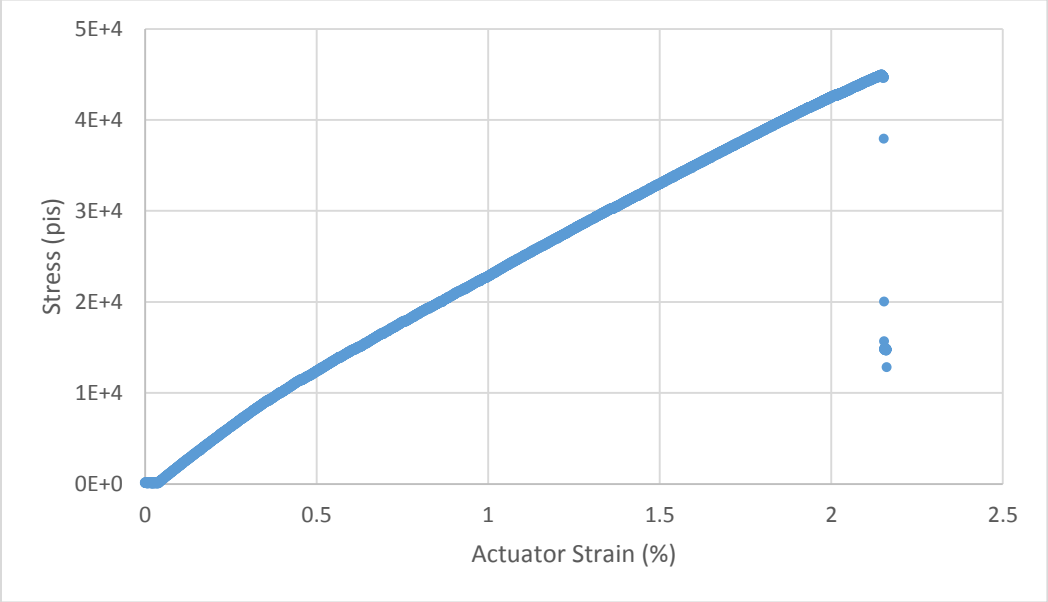


Figure 101: Stress vs. Strain for Glass-A3 Coupon 2441-6

The next three graphs in Figure 102, Figure 103, and Figure 104 feature the PFRQ events with the associated damage types. The first recorded damage event is are MCDs at 0.17% strain, 4.13 ksi, and 25.8 seconds. The next damage event to be recorded is a FPPD at 2.01% strain, 42.7 ksi, and 300.3 seconds. No instances of FBD events were recorded during this test. An observation of these graphs is that the samples almost entirely composed of MCDs. The single FPPD event occurs shortly before catastrophic failure.

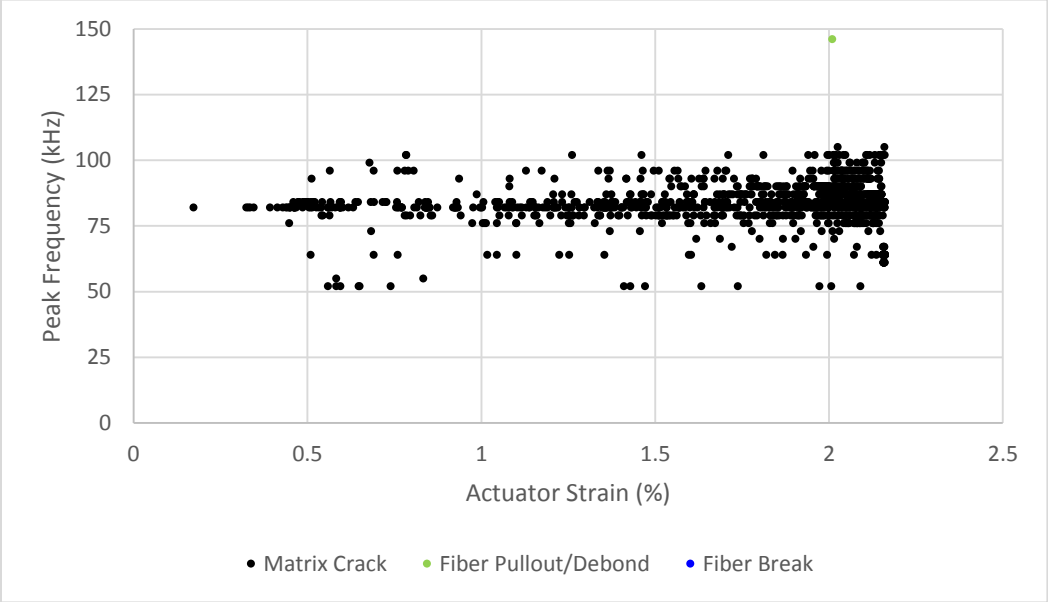


Figure 102: Event PFRQ vs. Strain for Glass-A3 Coupon 2441-6

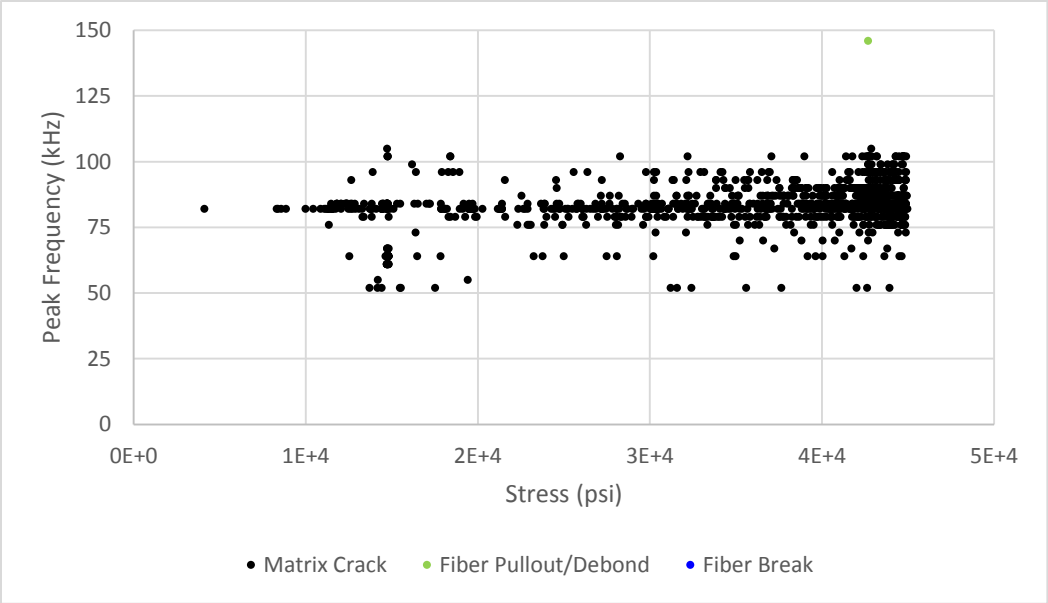


Figure 103: Event PFRQ vs. Stress for Glass-A3 Coupon 2441-6

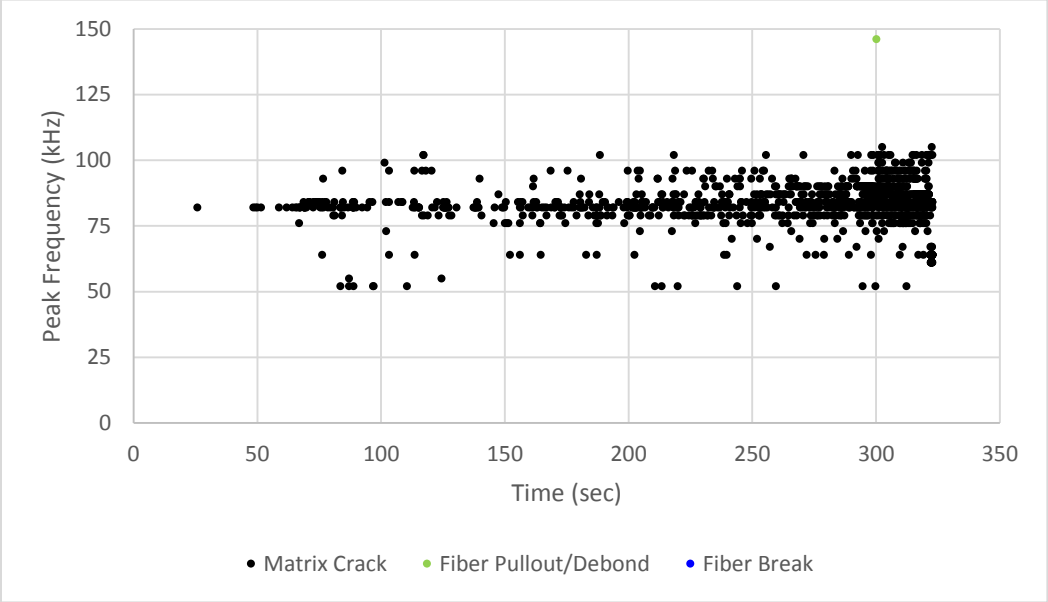


Figure 104: Event PFRQ vs. Time for Glass-A3 Coupon 2441-6

The next two graphs in Figure 105 and Figure 106 feature the E_{abs} released by the coupon during testing versus the strain, with the same graph with a truncation at $1*10^6$ aJ for the one below for higher resolution. The highest E_{abs} value is $3.29*10^8$ aJ at 0.65% strain. There are several spikes that can be observed, the first is at 0.36% strain, which correlates to the small load drop described previously. This is followed by another energy spike at approximately 0.65% strain, then another at 1.52% strain. These energy spikes show an influx in MCDs that at the corresponding strains. The final spike in energy occurs at 1.94% strain, which correlates with the FPPD. It is also the second highest energy release at $2.93*10^8$ aJ.

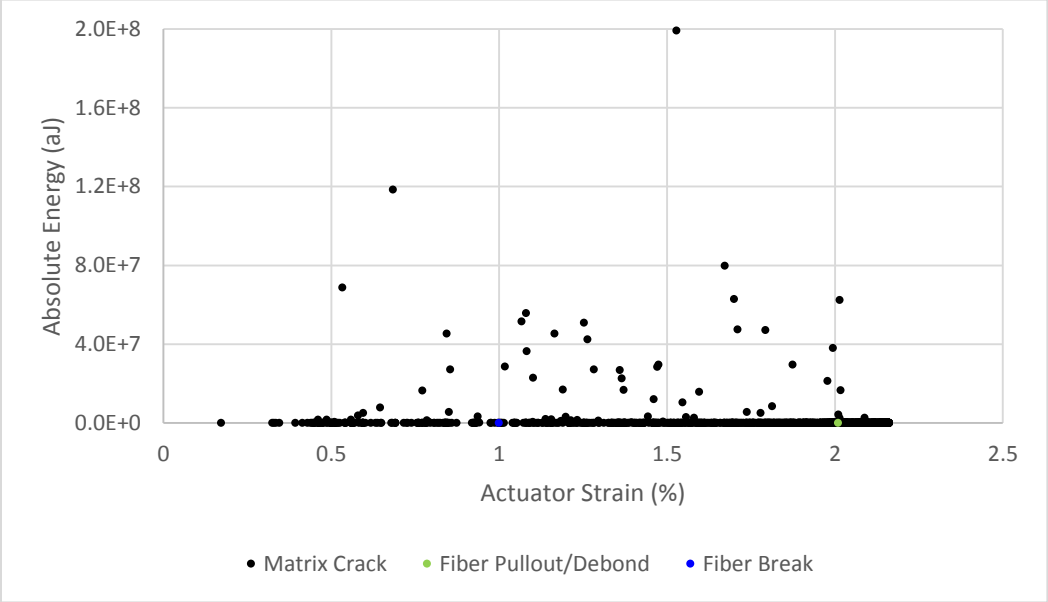


Figure 105: Absolute Energy vs. Strain for Glass-A3 Coupon 2441-6

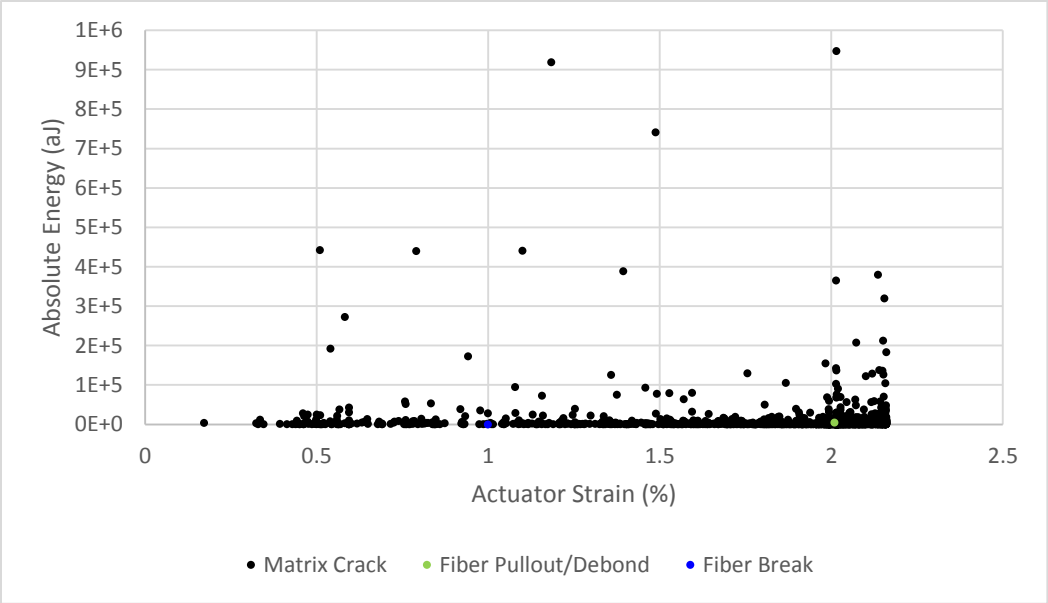


Figure 106: Absolute Energy vs. Strain for Glass-A3 Coupon 2441-6 Truncated at $1*10^6$aJ

Figure 107 below features the breakdown of N_{PFRQ} with their associated damage types by percentage. MCDs make up the vast majority of damage with 99.93% and the remainder 0.07% is the dingle FPPD. It is worth noting that the absence of FBDs is

similar to Glass-A2* material. This particular material is unique in that the MCDs are almost the entire damage profile that occurred during the test. The FPPD is the separation of the two 90° tows previously shown in Figure 96.

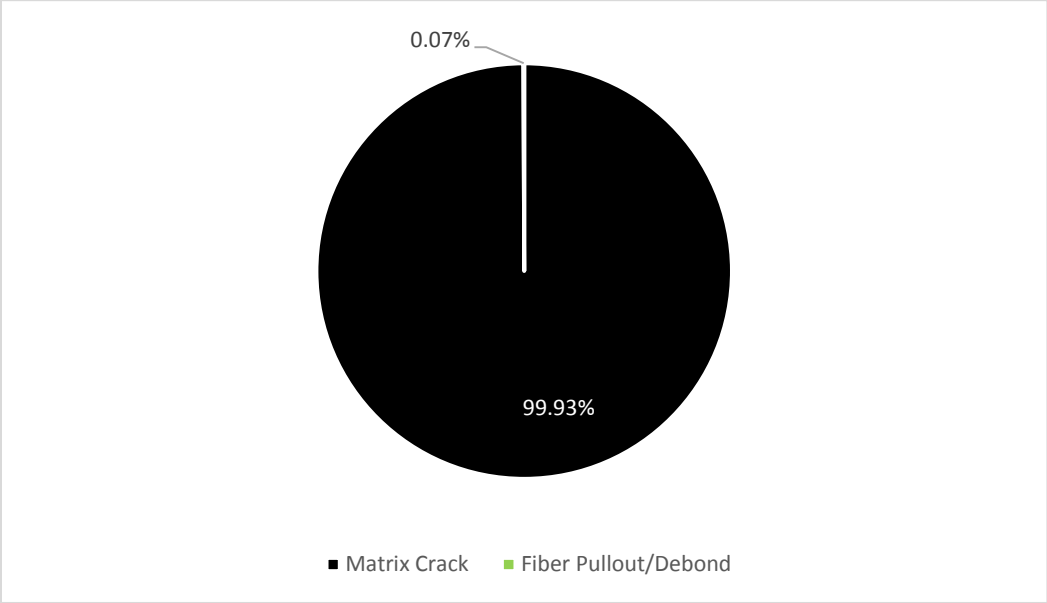


Figure 107: Recorded PFRQ Events by Damage Corresponding Type of Damage for Glass-A3 Coupon 2441-6

Glass- A3*

This sample set features Vectorply E-LT-3900 UD biaxial two ply coupons with the stitching removed. The stress-strain curve in Figure 108 below shows that the sample had a UTS of 37.5 ksi and a ε_f of 1.52%. There is a small load drop that occurred at 0.22% strain and 5.75 ksi. There is another, even smaller load drop at 0.95% strain and 24.6 ksi. Neither of the load drops found in this sample are remotely near the same magnitude featured in the single ply samples. The sample does not plastically deform until immediately prior to catastrophic failure

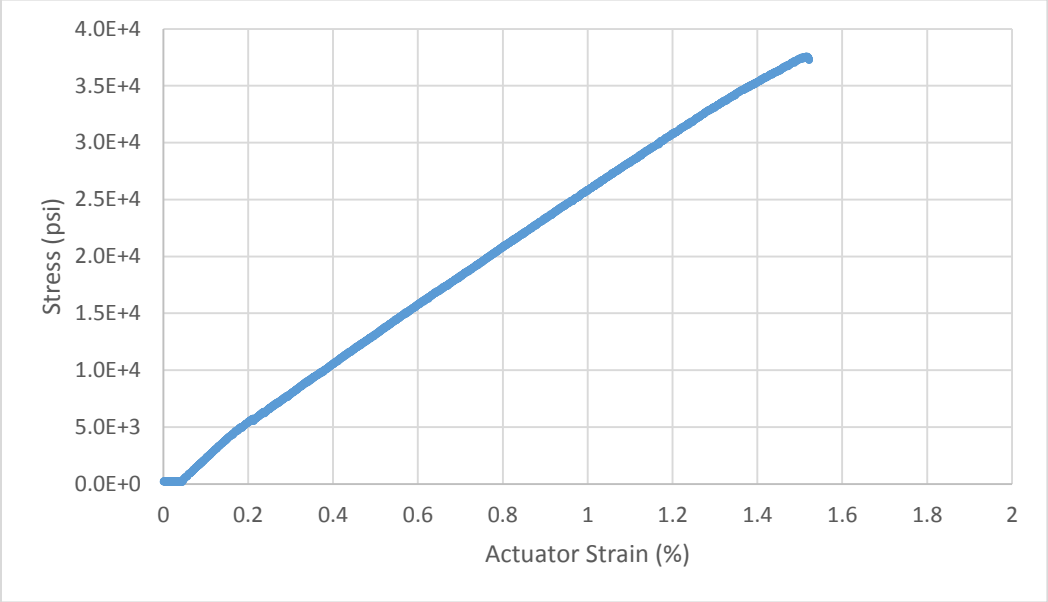


Figure 108: Stress vs. Strain for Glass-A3* Coupon 2443-6

The next three graphs for Figure 109, Figure 110, and Figure 111 feature the recorded PFRQ events with their associated damage types. The first damage type to be recorded were MCDs at 0.17% strain, 3.41 ksi, and 22.2 seconds. The second damage event to be recorded were the FPPDs at 0.21% strain, 5.57 ksi, and 36.0 seconds. The last damage event to be recorded were the FBDs at 0.96% strain, 24.8 ksi, and 162.1 seconds. The first instances are FPPD events correlate with the small load drop that occurred at 0.22%, as previously stated. This pertains to the first instance of the FBD and the second grouping of FPPDs at 0.95% strain as well. The second grouping of FBDs and third grouping of FPPDs occurred at the end of the test, correlating with catastrophic failure of the sample.

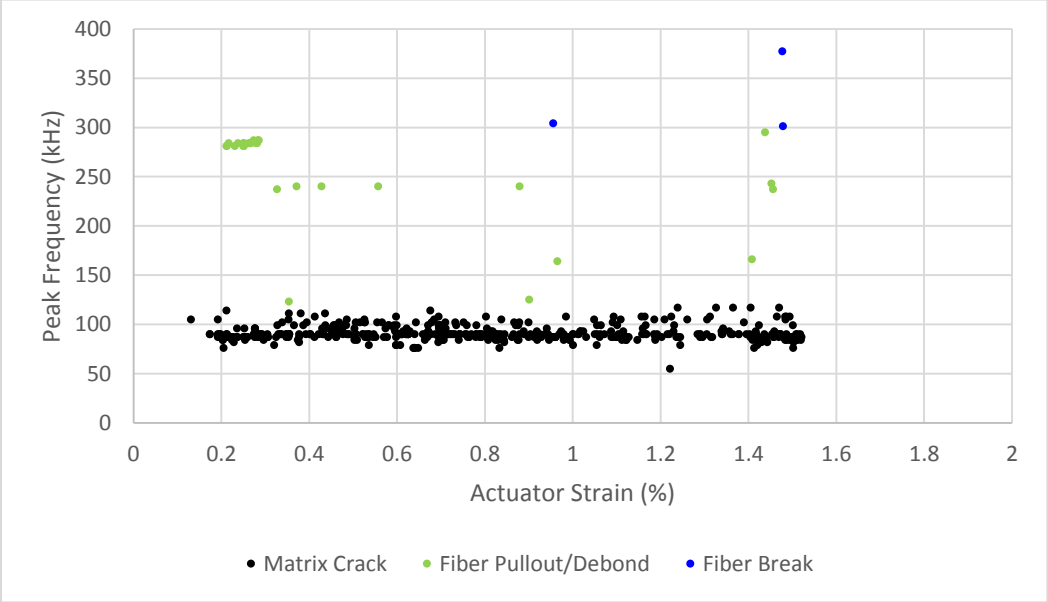


Figure 109: Event PFRQ vs. Strain for Glass-A3* Coupon 2443-4

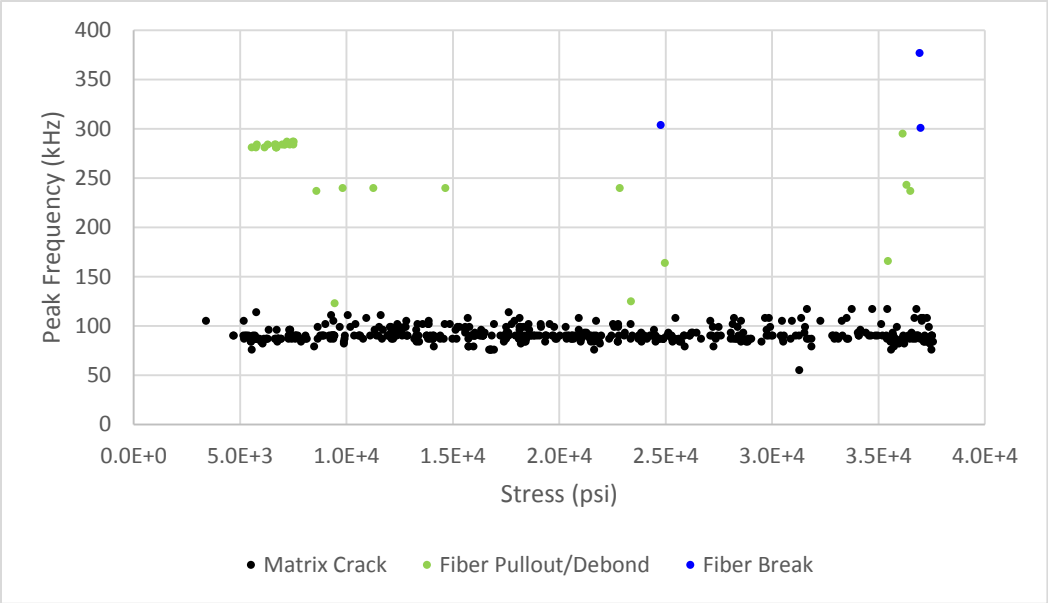


Figure 110: Event PFRQ vs. Stress for Glass-A3* Coupon 2443-4

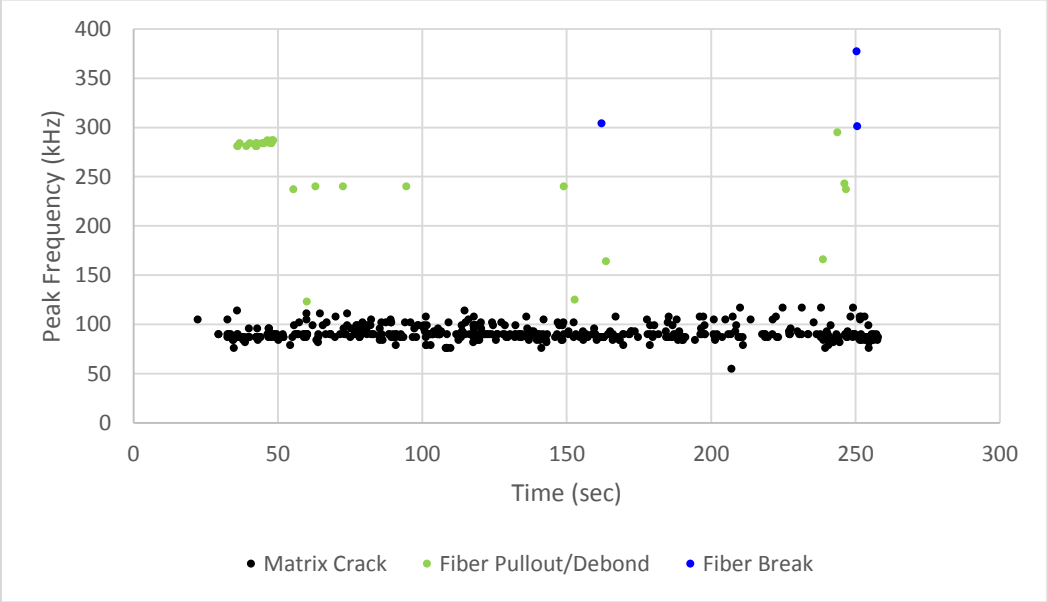


Figure 111: Event PFRQ vs. Time for Glass-A3* Coupon 2443-4

The next two graphs in Figure 112 and Figure 113 feature the E_{abs} released by the sample versus the strain and below that is the same graph, but truncated at $8*10^5$ aJ for higher resolution. The maximum energy release for the sample was $3.00*10^8$ aJ at 0.19%, which correlates with the first grouping of FPPDs discussed previously. The next spike correlates with the first FBD recorded at 0.96% strain and the final energy spike occurred at the second grouping of FBDs prior to catastrophic failure.

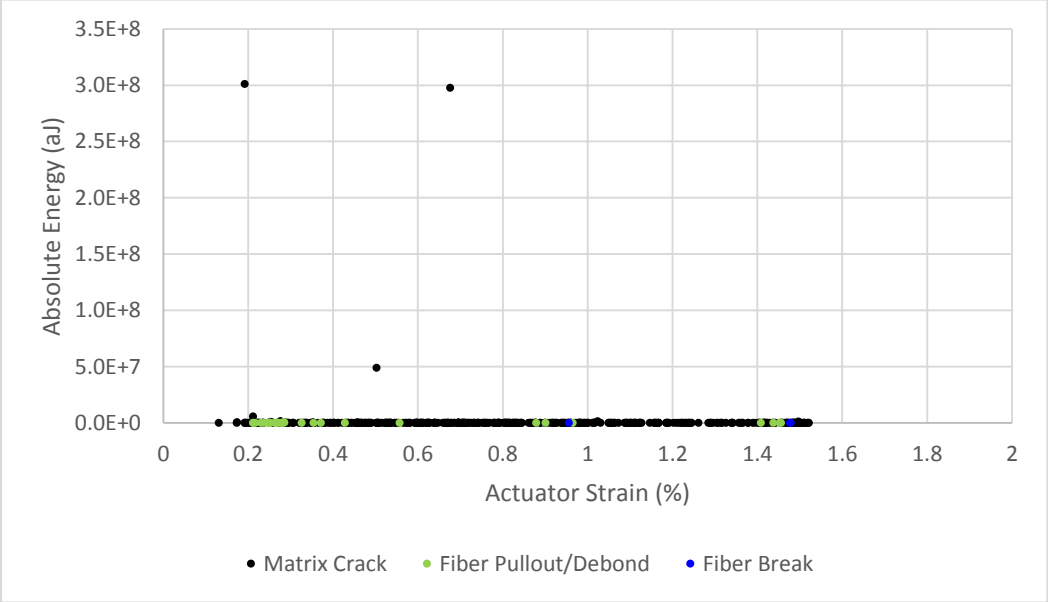


Figure 112: Absolute Energy vs. Strain for Glass-A3* Coupon 2443-4

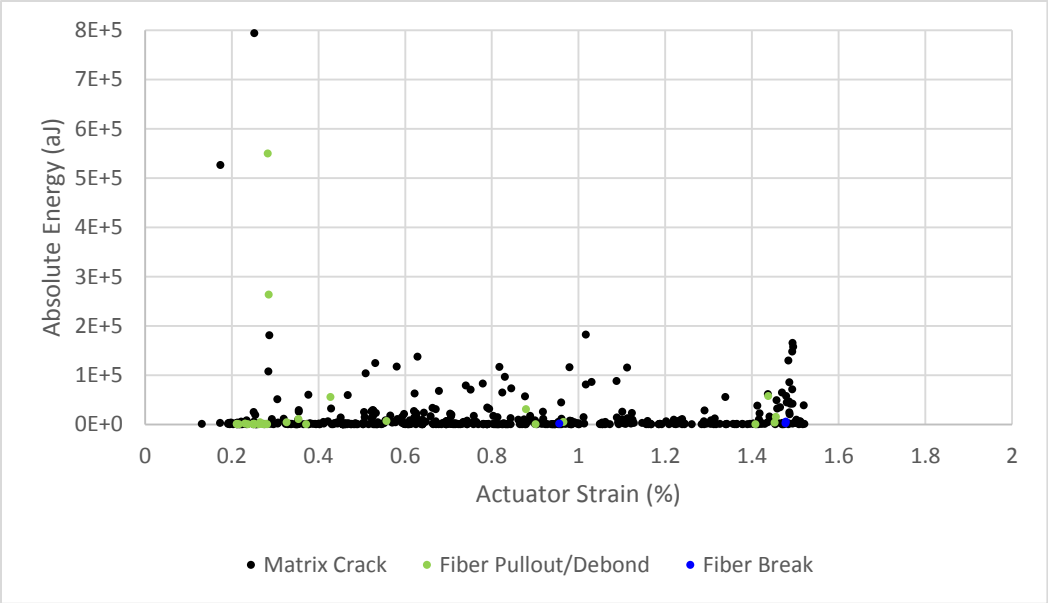


Figure 113: Absolute Energy vs. Strain for Glass-A3* Coupon 2443-4 Truncated at $8*10^5$aJ

Figure 114 below feature the breakdown of recorded PFRQ events with associated damage types by percentage for Glass-A3*. MCDs account for 93.55% of all recorded damage, while FPPDs and FBDs are at 5.86% and 0.59%, respectively. These

results are similar to Glass-A3 in that MCDs dominate the recorded damage events. This sample features a slight increase in FPPDs and actual instances of FBDs, unlike Glass-A3.

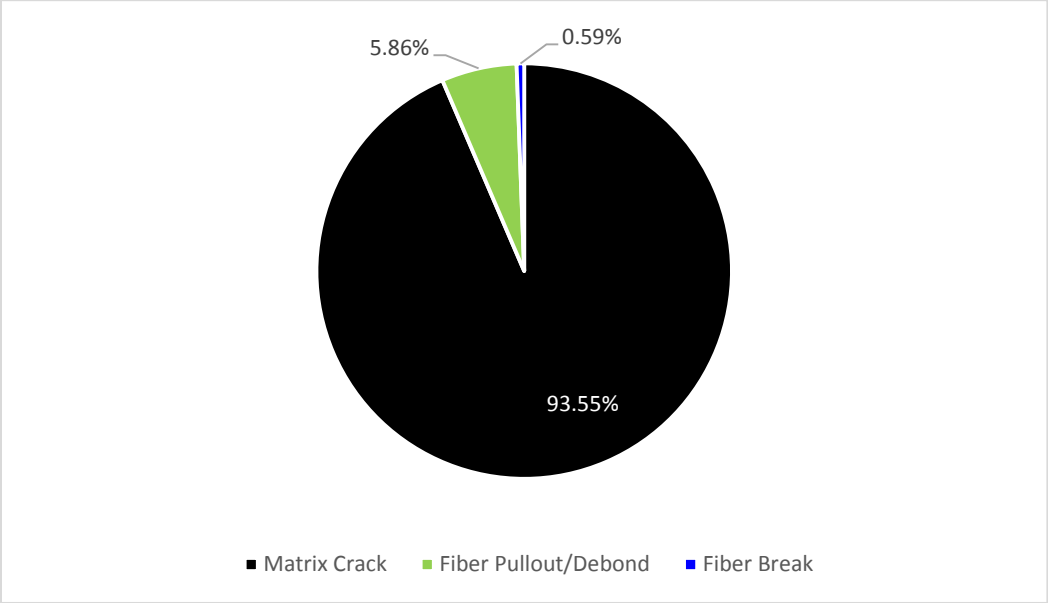


Figure 114: Recorded PFRQ Events by Damage Corresponding Type of Damage for Glass-A3* Coupon 2443-4

Glass- B1

This sample set features Newport NCT30-D1-E300, which is pre-preg UD biaxial four ply coupons. Figure 115 below features the stress-strain curve with a UTS of 29.4 ksi and a ε_f of 1.77%. There is only one noticeable load drop, which is miniscule compared to the previous samples, which occurred at 0.99% strain and 18.4 ksi. There is no plastic deformation for the coupon present at all. It appears to have remained stiff until catastrophic failure.

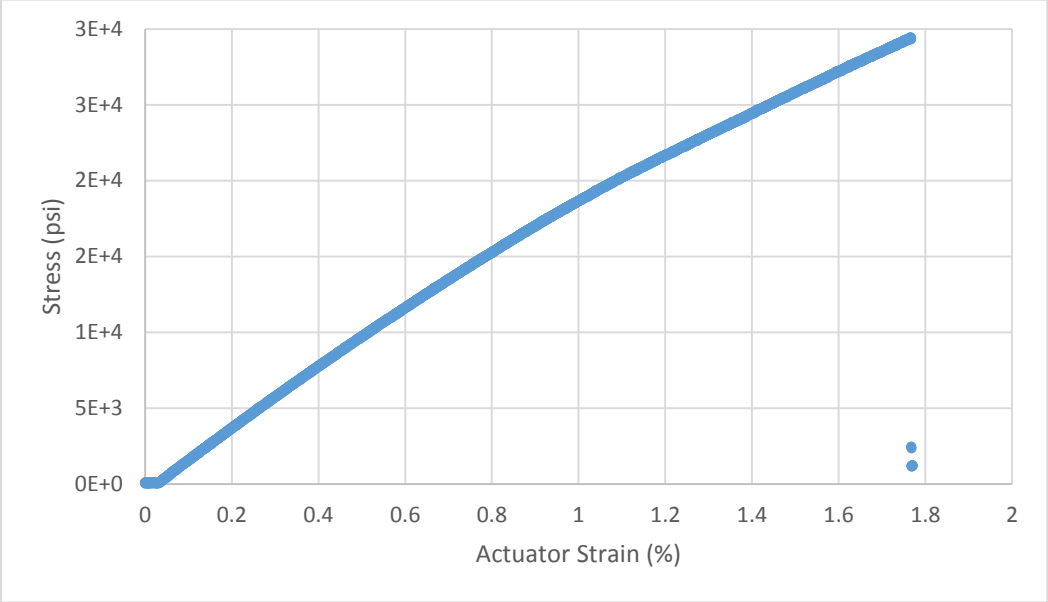


Figure 115: Stress vs. Strain for Glass-B1 Coupon 2434-4

The next three graphs in Figure 116, Figure 117, and Figure 118 feature the recorded PFRQ events with corresponding damage types. The first and only damage events to be recorded were the MCDs starting at 0.76% strain, 14.6 ksi, and 135.7 seconds. The most obvious observation is that the damage recorded are only MCDs, which is unlike any other sample set. The first influx of MCDs at 0.99% strain correlate with the slight load drop previously stated. Then the influx of MCDs at the end of the test correlate with the catastrophic failure. The PFRQs of the events begin to rise prior to catastrophic failure, but the sample broke before any higher frequencies could be recorded. Another observation pertaining to this sample is that the first events recorded did were not present at all until the test was already 43% over, timewise. The onset of damage is sudden and, in this case, can lead to quick failure.

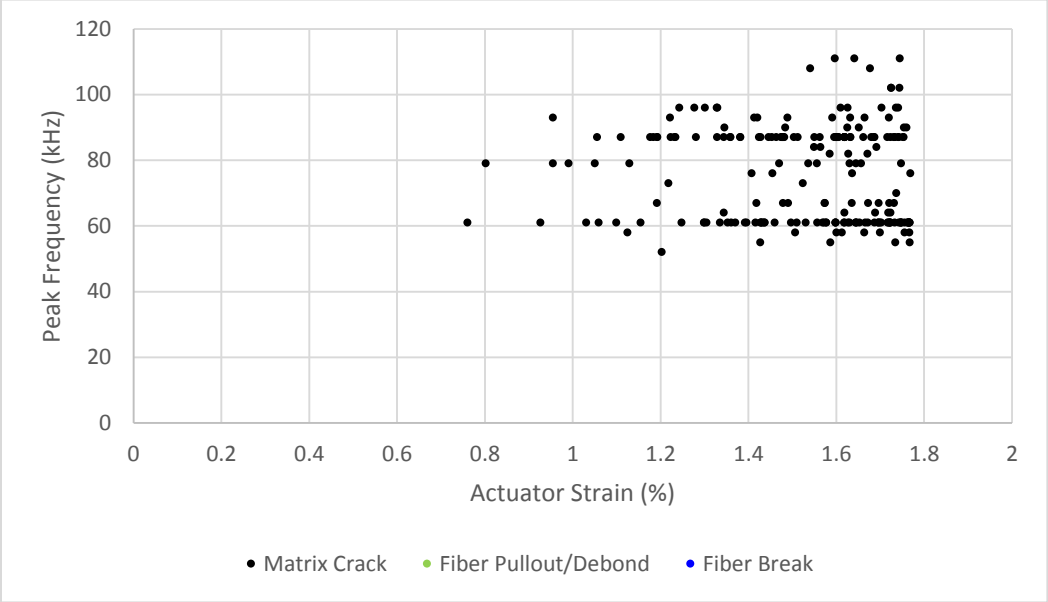


Figure 116: Event PFRQ vs. Strain for Glass-B1 Coupon 2434-4

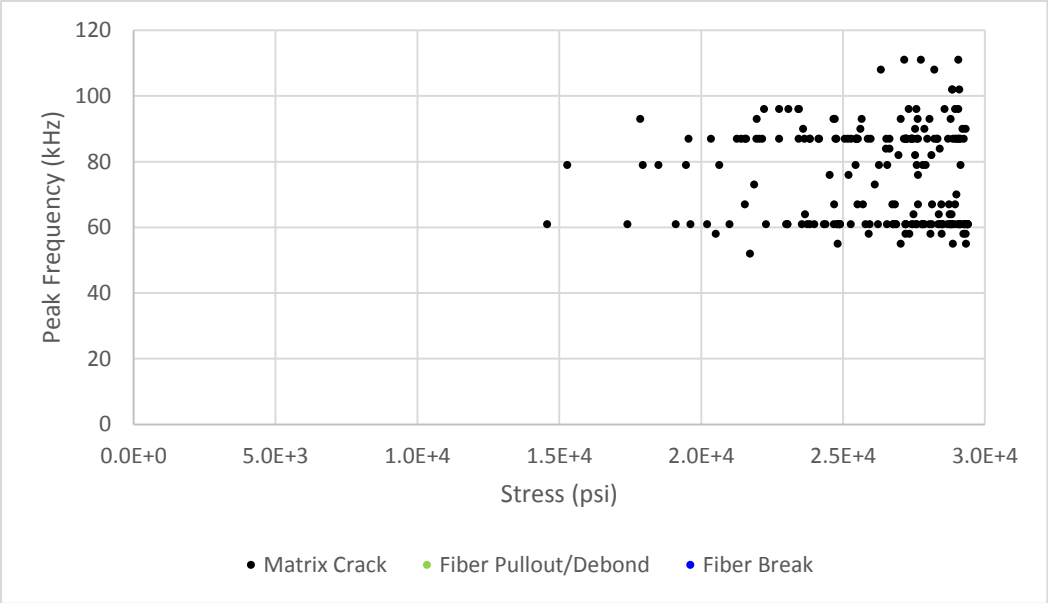


Figure 117: Event PFRQ vs. Stress for Glass-B1 Coupon 2434-4

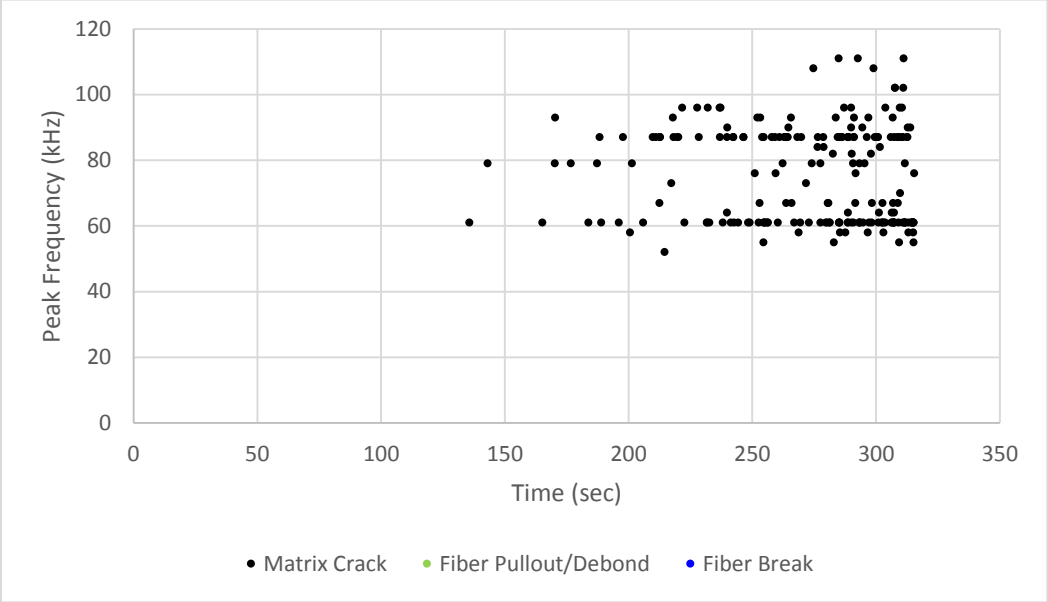


Figure 118: Event PFRQ vs. Time for Glass-B1 Coupon 2434-4

The next graph in Figure 119 features the E_{abs} released by the sample versus the strain. The largest magnitude of energy released is $4.52*10^6$ aJ at 1.74% strain. The first spike of energy occurred at 0.99% strain, which explains the load drop previously stated. The second and final energy spike, featuring the largest energy release, corresponds prior to the catastrophic failure at the end of the test.

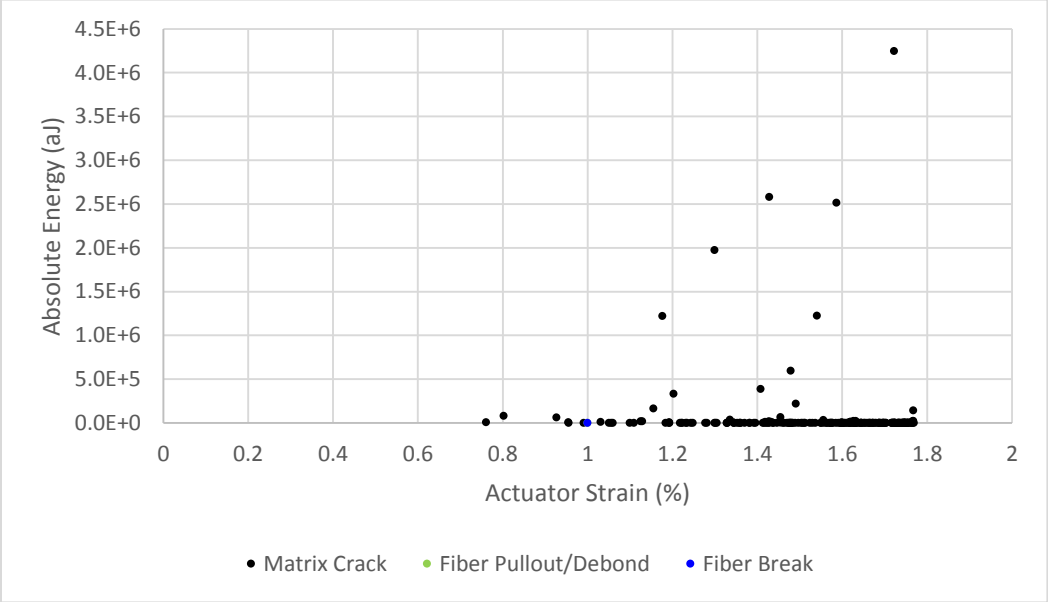


Figure 119: Absolute Energy vs. Strain for Glass-B1 Coupon 2434-4

Figure 120 below features the breakdown of N_{PFRQ} with corresponding damage types by percentage. Unique to only this data set, no other damage occurred other than MCDs. This is obviously not true since the sample broke, as seen in Figure 98. What happened is that the sample had such a brittle failure that the sample broke before the AE waves could travel through the coupon to the sensors. This means the only FBDs and FPPDs occurred at catastrophic failure.

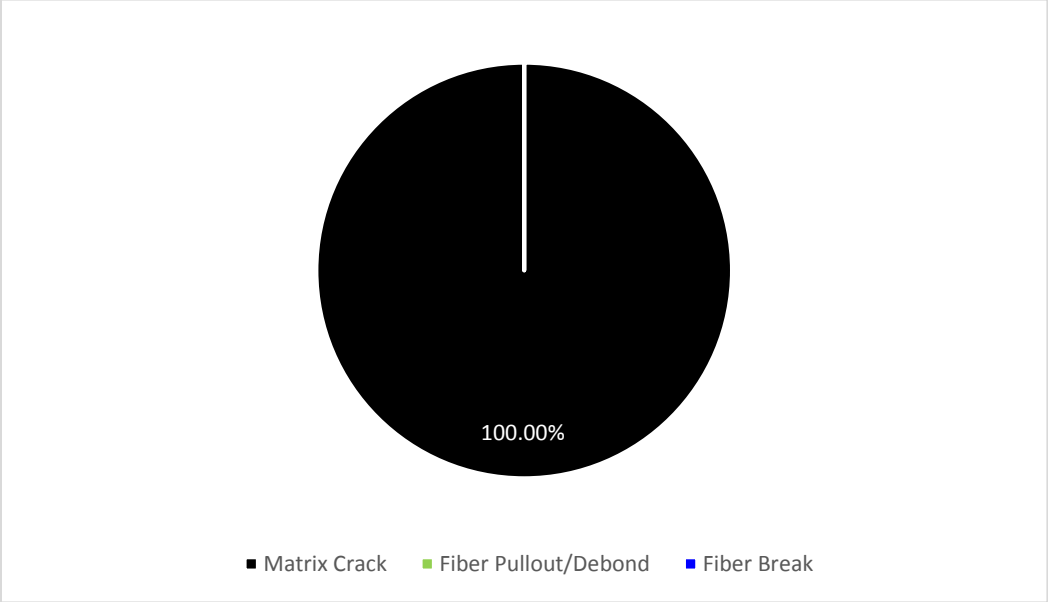


Figure 120: Recorded PFRQ Events by Damage Corresponding Type of Damage for Glass-B1 Coupon 2434-4

Glass-B2

This sample set features Newport NCT30-D1-E300, which is pre-preg UD biaxial six ply coupons. Figure 121 below features the stress-strain curve for Glass-B2 which has a UTS of 28.6 ksi and a ε_f of 1.66%. There is a slight load drop that begins at 0.68% strain and 15.1 ksi. After that occurred, there is no noticeable plastic deformation, which implies a brittle failure of the coupon. It is of interest to this work that Glass-B1 and Glass-B2 both have approximately the same UTS, which will be discussed further in the summary section. Other than the slight load drop, there are no discernable features, similar to metals.

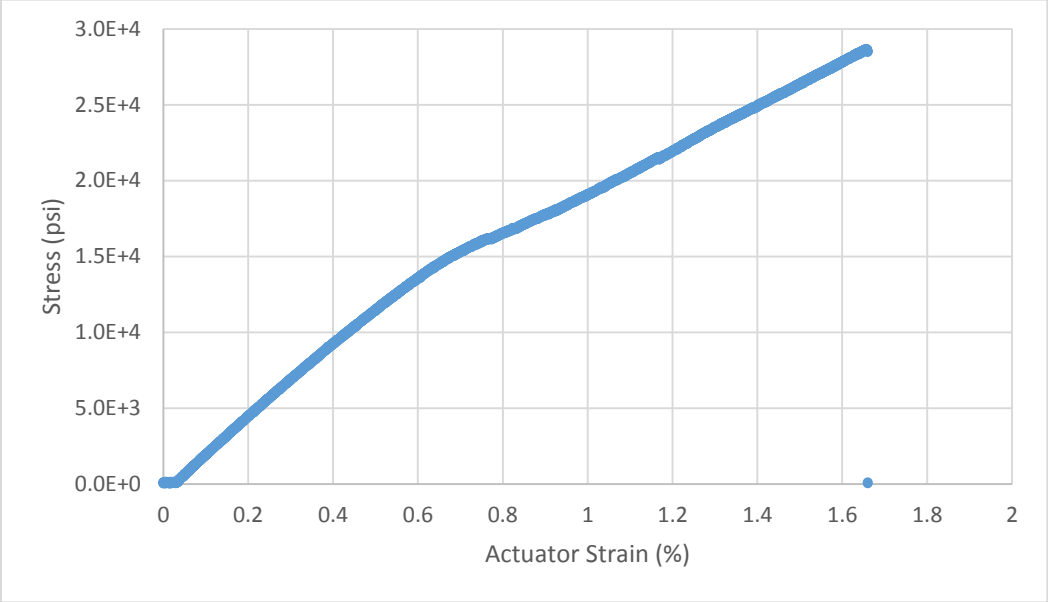


Figure 121: Stress vs. Strain for Glass-B2 Coupon 2435-4

The next three graphs in Figure 122, Figure 123, and Figure 124 feature the recorded PFRQ events with the associated damage type. The first events to be recorded were the MCDs at 0.31% strain, 7.02 ksi, and 54.9 seconds. The second damage type to be recorded were the FPPDs at 0.68% strain, 14.8 ksi, and 123.0 seconds. The final damage type to be recorded were FBDs at 1.38% strain, 24.6 ksi, and 248.1 seconds. The initial grouping of FPPDs correlates to the small load drop previously discussed. The first FBD does not seem to correspond any load drop in the stress-strain curve, but the second and final FBD and influx of FPPDs correlate to the catastrophic failure at the end of the test.

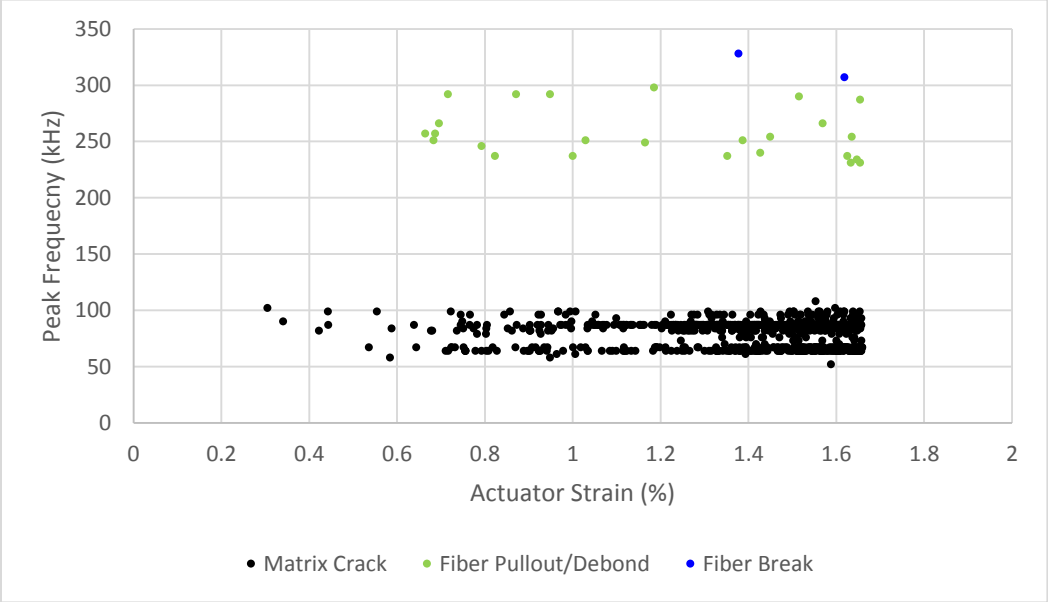


Figure 122: Event PFRQ vs. Strain for Glass-B2 Coupon 2435-4

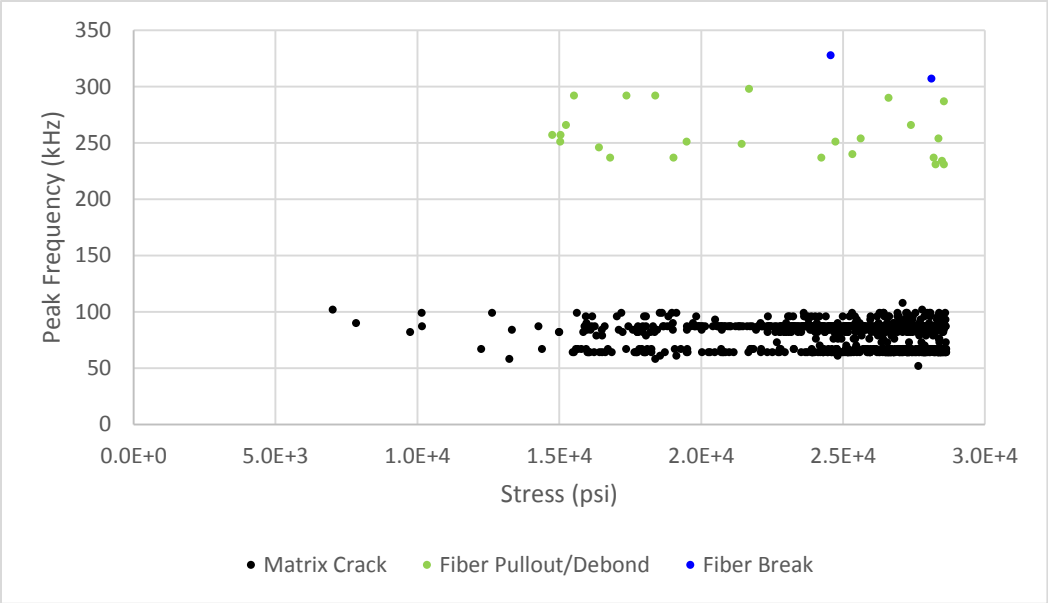


Figure 123: Event PFRQ vs. Stress for Glass-B2 Coupon 2435-4

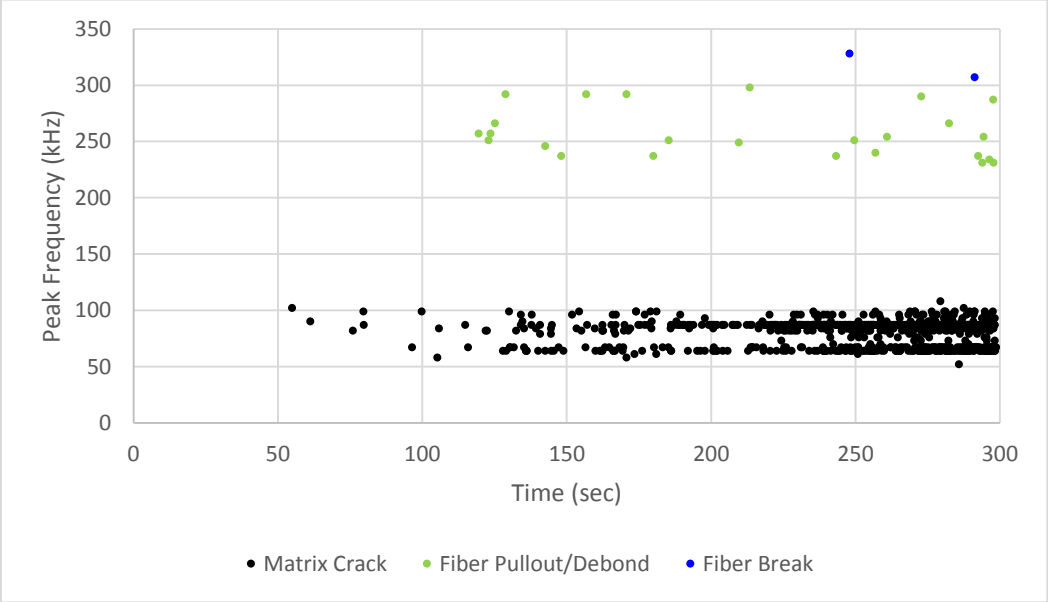


Figure 124: Event PFRQ vs. Time for Glass-B1 Coupon 2435-4

The next graph for Figure 125 features the E_{abs} released by the sample versus the strain. The highest energy released is $1.1*10^8$ aJ at 0.83%. This energy spike correlates with the small load drop previously discussed. The next spike in energy occurred at 1.38% strain, which correlates to the first FBD. The final energy spike is at 1.58% strain, which corresponds with the FBD prior to catastrophic failure.

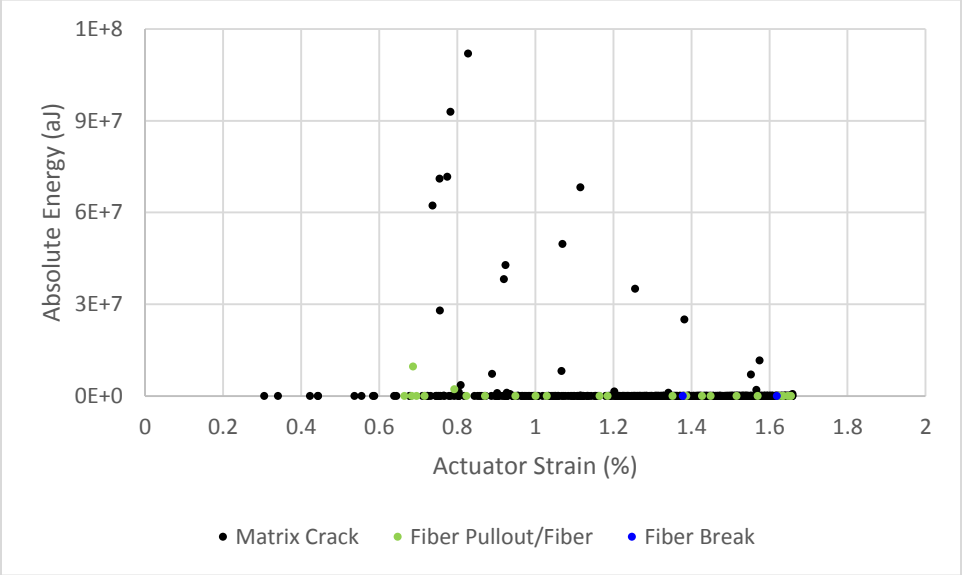


Figure 125: Absolute Energy vs. Strain for Glass-B2 Coupon 2435-4

Figure 126 below features the breakdown of N_{PFRQ} with the corresponding types of damage by percentage. MCDs dominate with 97.95% of N_{PFRQ}. FPPDs and FBDs fill out the remainder with 1.90% and 0.15%, respectively. This is different than the Glass-B1 sample in that other forms of damage occurred other than MCDs. The addition of two more plies created a small amount of FPPDs and two FBDs, but MCDs are certainly the primary mode of damage propagation in the sample.

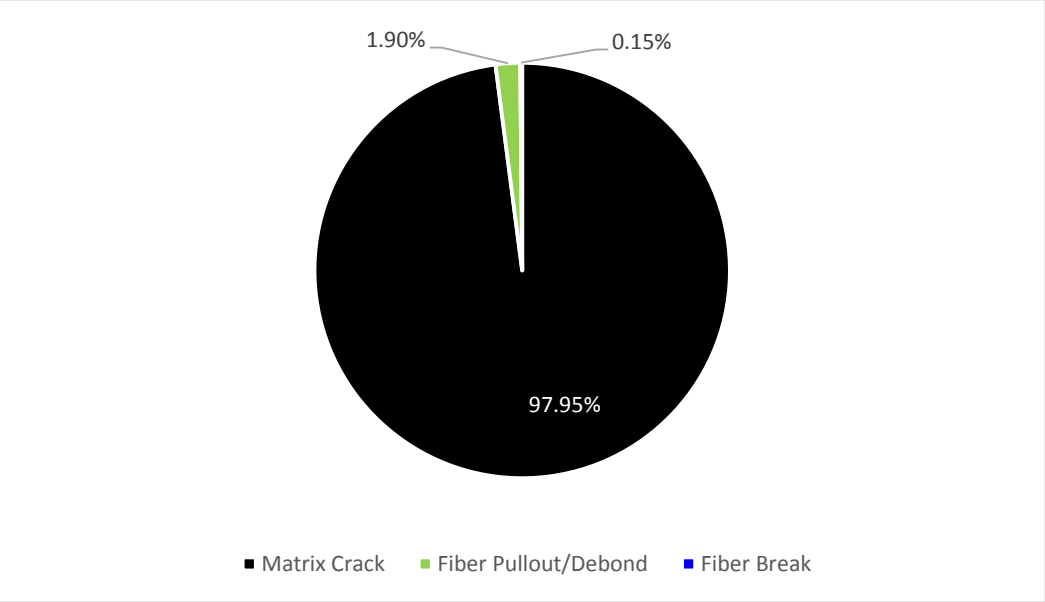


Figure 126: Recorded PFRQ Events by Damage Corresponding Type of Damage for Glass-B2 Coupon 2435-4

Glass- C3

The final biaxial set of coupons is the PPG L1200/G50 with CSM backing two ply coupons. Figure 127 below features the stress-strain curve for Glass-C3, which has a UTS of 62.1 ksi and a ε_f of 1.78%. There are three sudden load drops before catastrophic failure is achieved. The first is small drop at 1.25% strain and 53.2 ksi, which falls to 52.6 ksi. The load increase to the second drop at 1.45% strain and 59.8 ksi, which falls to 56.3 ksi. After that the load increase to the final sudden load drop at 1.59% strain and 60.5 ksi, which then falls to 56.3 ksi. The sample the proceeds to increased load until catastrophic failure. This sample is unique in that, compared to the other biaxial samples, there are sudden load drops present. Samples for Glass-A3 and Glass-A3* feature slight load decreased over a short span, but do not have sudden load drops seen here for Glass-C3. The pre-preg sample, Glass-B1 and Glass-B2 behave similarly to metals in that they

show almost no plastic deformation and have brittle failure. It is also different from the other Glass-C samples in that after a sudden load drop, it is able to achieve a higher stress than before the drop. Typically with the other samples, once a drop occurred, the sample could not reach the same magnitude of stress.

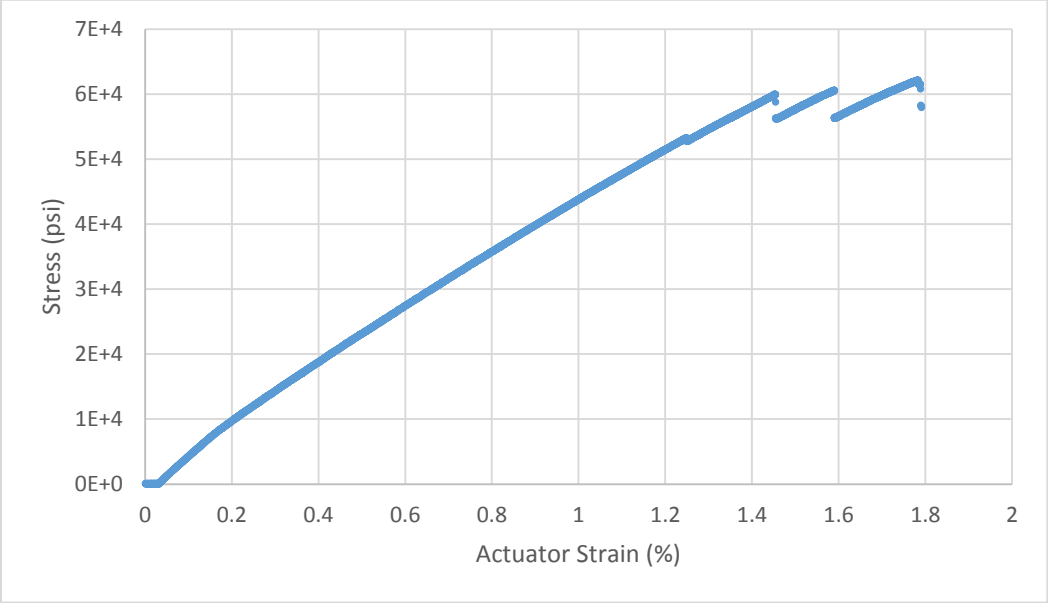


Figure 127: Stress vs. Strain for Glass-C3 Coupon 2446-24

The next three graphs in Figure 128, Figure 129, and Figure 130 feature the recorded PFRQ events with the corresponding damage type. The first damage recorded was the MCD events at 0.17% strain, 7.25 ksi, and 16.7 seconds. The next damage event recorded was FPPD at 0.18% strain, 8.77 ksi, and 20.1 seconds. The final damage recorded was the FBD events at 1.19% strain, 51.3 ksi, and 133.0 seconds. This event correlates with the first FBD, previously discussed. Also, the second FBD correlates with the second load drop, previously stated. The third sudden load drop correlates to the substantial influx of MCDs at the same strain of 1.59%. An observation of this sample is

that the FBDs all occurred during one of the corresponding load drops, rather than at or prior to catastrophic failure. There is an influx of FPPDs at these stresses as well, implying that the load drops were when the majority of the damage to the sample was occurring. The test continued on for another 40 seconds before catastrophic failure was achieved.

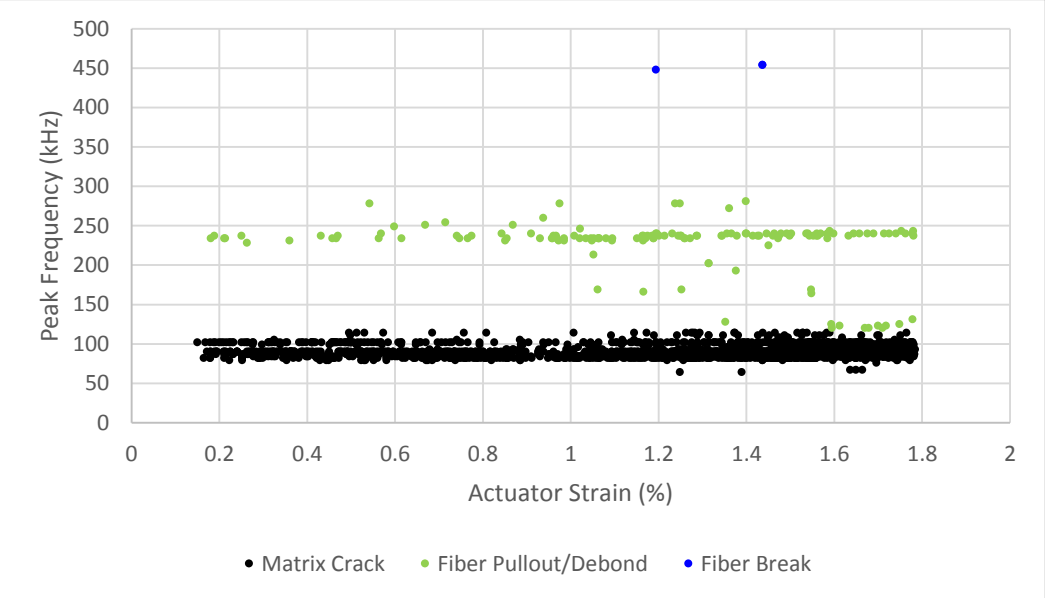


Figure 128: Event PFRQ vs. Strain for Glass-C3 Coupon 2446-24

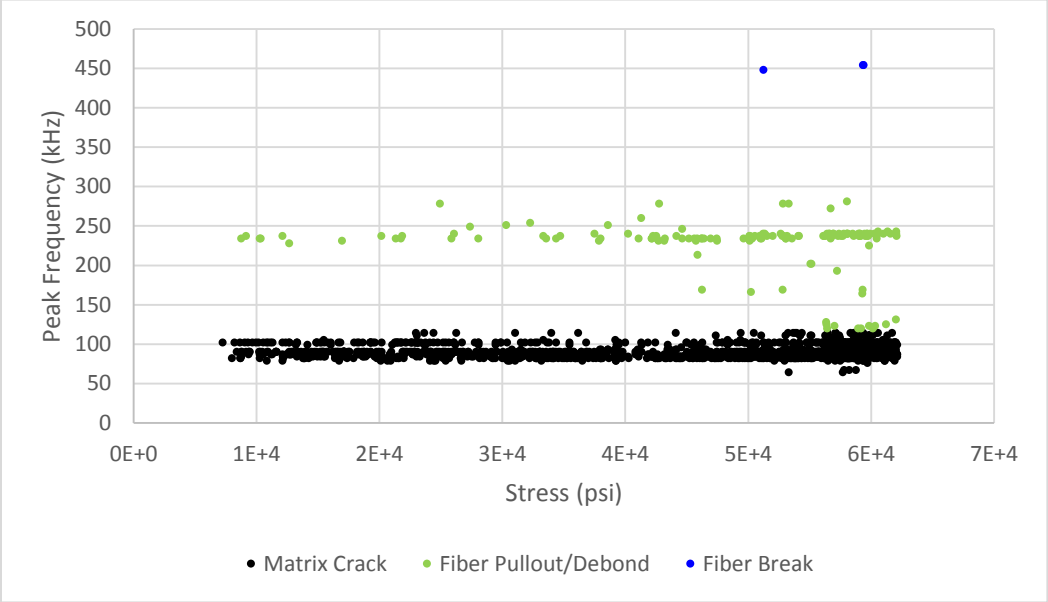


Figure 129: Event PFRQ vs. Stress for Glass-C3 Coupon 2446-24

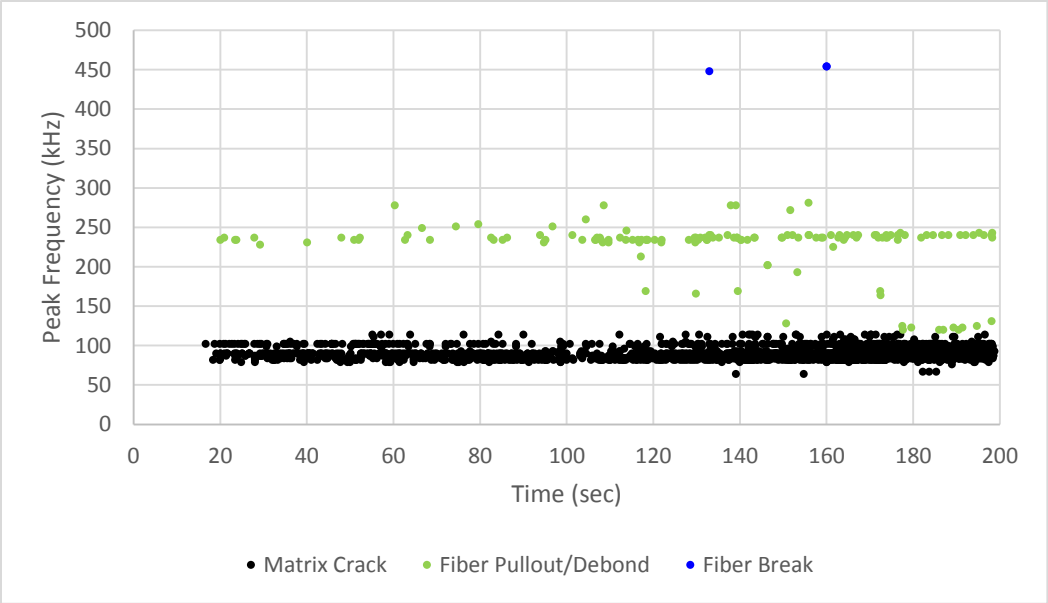


Figure 130: Event PFRQ vs. Time for Glass-C3 Coupon 2446-24

The next two graphs for Figure 131 and Figure 132 feature the E_{abs} released by the sample during testing versus the strain. The second graph is the same as the first but with a truncation at $1*10^6$ aJ for higher resolution. The largest magnitude of energy

released is $9.22*10^9$ aJ at 1.59% strain. This event corresponds with the sudden influx of MCDs and FPPDs and the final sudden load drop prior to catastrophic failure. There are three noticeable energy spikes in the truncated graph. They occurred at 0.36% strain, where the initial damage began to occur in the sample; 1.25% strain for the first load drop; 1.45% strain for the second drop; 1.59% for the third drop; then the final energy spike was at 1.78%, signaling catastrophic failure has been achieved.

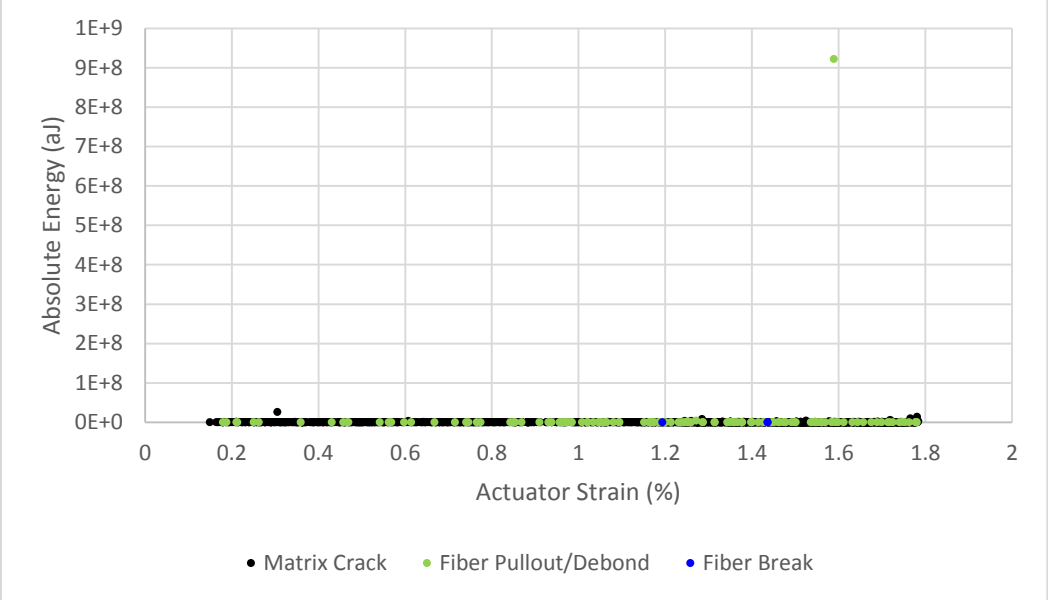


Figure 131: Absolute Energy vs. Strain for Glass-C3 Coupon 2446-24

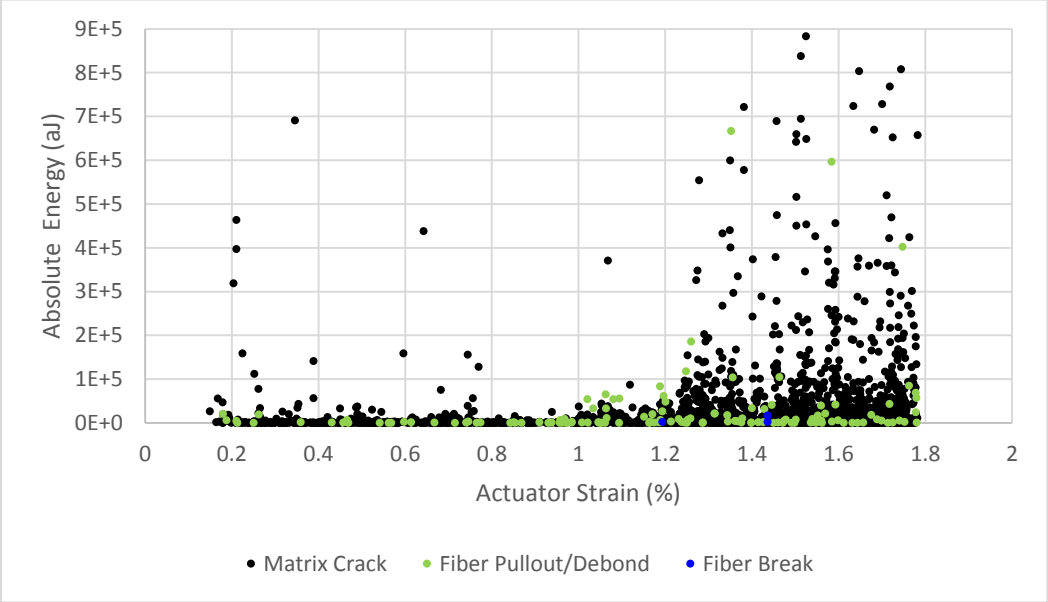


Figure 132: Absolute Energy vs. Strain for Glass-C3 Coupon 2446-24 Truncated at $1*10^6$aJ

Figure 133 below feature the breakdown of N_{PFRQ} with associated damage types by percentage. MCDs account for 95.33% of N_{PFRQ}. FPDDs and FBDs fill out the remainder with 4.58% and 0.10%, respectively. Glass-C3 is very similar to sample Glass-B2 sample with respect to relative amount of each type of damage present. Like most of the biaxial samples, MCDs dominate the damage present in the coupon. It is the primary mode of damage that contributed to catastrophic failure. The main difference between this and the previous biaxial samples is that N_{PFRQ} are substantially larger, which will be discussed in the summary section.

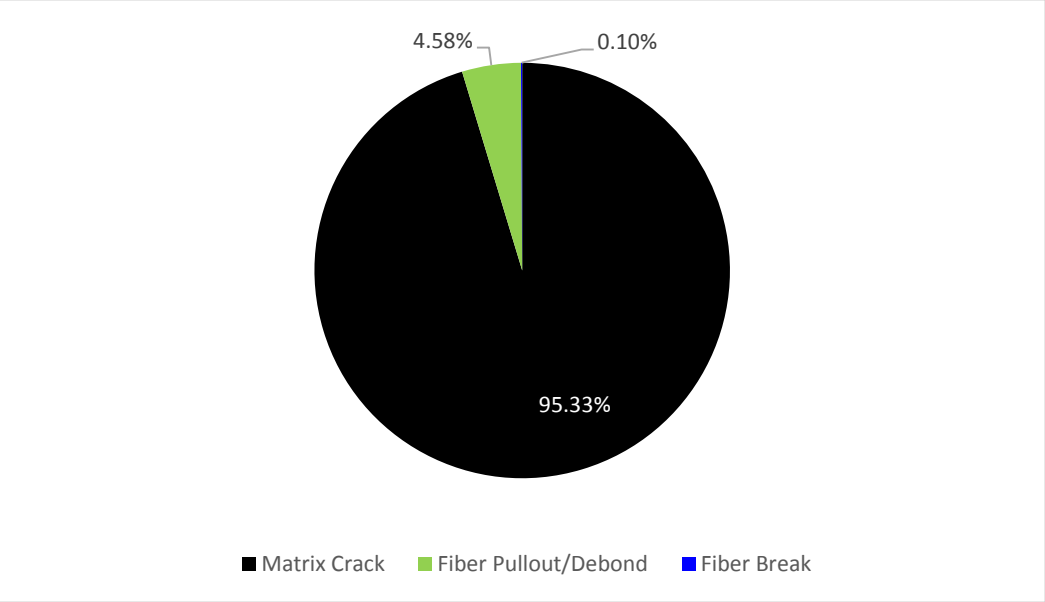


Figure 133: Recorded PFRQ Events by Damage Corresponding Type of Damage for Glass-C3 Coupon 2443-24

Summary of Biaxial Coupons

The summary of UTS, ε_f, N_{PFRQ}, and total E_{abs} released for each of the biaxial samples are in Table 9 below. The trend between the five samples show that the removal stitching for the Glass-A material has substantial impact on the mechanical properties of the samples as well as the AE signals emitted. Glass-A3* features a decrease in all of the categories: UTS by 26.4%, ε_f by 38.8%, N_{PFRQ} by 55.8%, and total release of E_{abs} by 84.9% compared to Glass-A3. The Glass-B also features some drastic changes, but only in the AE data and not in the mechanical properties. It is also not a consistent decrease, like from Glass-A3 to Glass-A3*, because the AE signal data increase in both N_{PFRQ} and E_{abs} released by the sample. Going from a four ply in Glass-B1 to a six ply for Glass-B2 features a decrease in UTS by 38.9%, an increase in ε_f by 8.18%, an increase in N_{PFRQ} by 210.9%, and an increase in total E_{abs} released by the coupons by 436.8%.

	Glass-A3	Glass-A3*	Glass-B1	Glass-B2	Glass-C3
V_f (%)	43	42	49	49	44
UTS (ksi), [σ]	47.8, [3.32]	35.2, [2.56]	54.3, [14.4]	33.2, [2.91]	64.0, [3.72]
ε_f (%), [σ]	2.19, [0.10]	1.34, [0.17]	1.59, [0.20]	1.72, [0.04]	1.63, [0.12]
N_{PFRQ}, [σ]	1539, [371]	680, [297]	1178, [1025]	3662, [2006]	3444, [487]
Total E_{abs} (aJ), [σ]	219, [44.2]	33.0, [24.1]	38.0, [49.4]	204, [62.4]	58.4, [43.6]

Table 9: $\bar{x}$ and σ of V_f, UTS, εf, N_{PFRQ}, and E_{abs} for Every Biaxial Coupon

Comparison Summary of All Samples

Table 10 below features a composite of the previous tables containing UTS, ε_f, N_{PFRQ}, and total E_{abs} released by the sample grouped together by material type. This is to assist in visualizing the values relative to the similar materials, rather than the previous, which feature the same values grouped together by layup. The Glass-A samples with the stitching intact showed that they have highest N_{PFRQ} and E_{abs}, no matter the layup. The effect of stitching on the reduction N_{PFRQ} and E_{abs} is more substantial on the 90° samples than the 0° samples. This material also shows that the removal of the stitching increases the ε_f and UTS for the normal samples and both decrease for the transverse samples, the effects of which are less impactful in the biaxial samples. The increase in strength and strain do not correlate to an increase in energy or other AE data. Overall, the biaxial samples have the highest release of E_{abs}, while the biaxial and normal samples have similar numbers for N_{PFRQ}. The transverse samples have the lowest of these two values for Glass-A. The other consistent trend for all of the Glass-A samples is that the N_{PFRQ} decreases with the removal of stitching. The Glass-A1 and Glass-A1* samples are

unique in that they have an increase in UTS with the removal in stitching, since the Glass-A2, -A2*, -A3, and –A3* samples all decrease.

	A1	A1*	A2	A2*	A3	A3*	B1	B2	C1	C2	C3
V_f (%	43	42	43	42	45	44	49	49	44	44	46
UTS (ksi)	65.5	85.6	7.79	4.36	47.8	35.2	54.3	33.2	95.2	5.7	64.0
ε_f (%)	1.94	2.00	0.56	0.26	2.19	1.34	1.59	1.72	1.65	0.79	1.65
N_{PFRQ}	1771	529	764	17	1539	680	1178	3662	18134	423	3444
E_{abs} (nJ)	71.0	18.0	56.6	0.16	219	33.0	38.0	204	221	68.0	58.4

Table 10: $\bar{x}$ of V_f, UTS, εf, N_{PFRQ}, and E_{abs} for Every Coupon

The next material group, Glass-B, the addition of two 90° plies in the center of the layup causes a reduction of UTS, but an increase in ε_f, N_{PFRQ}, and E_{abs}. The addition of transverse plies inserted between the 0° plies lead to an increase in damage mechanisms that led to catastrophic failure. The increase in E_{abs} indicates the additional damage propagation offset any additional strength the coupon may have had due to extra plies. Recall, the reason the pre-preg samples were not single and two ply asymmetric like the others is that the manufacturer strongly recommended against it, stating that the finished product could have flawed or undesirable traits not true to the actual properties of the material. The effect on UTS is the same as the Glass-A3 and Glass-A3* samples, which are also biaxial layups, but they have a reverse effect on the strain to failure, N_{PFRQ}, and E_{abs} values.

The UD with CSM backing, Glass-C, samples behaved most similarly to the Glass- A samples without the stitching removed. The common trend is that the 0° samples have the highest UTS and ε_f, confirming classic composites mechanics. The largest N_{PFRQ} and E_{abs} values are associated with the biaxial samples. This is due to the increase in the fiber materials that contain the majority of the strain energy compared to the matrix material. The 90° samples have the lowest of all four values for both Glass- A and Glass- B samples.

	A1	A1*	A2	A2*	A3	A3*	B1	B2	C1	C2	C3
E_{abs}/N_{PFRQ} (nJ/event)	0.040	0.034	0.074	0.009	0.142	0.049	0.032	0.056	0.012	0.161	0.017

Table 11: Energy Released per Event Recorded for Each Sample

Table 11 above shows the energy that the released per event recorded show that the values in ascending order are Glass- A2*, -C1, -C3, -B1, -A1*, -A1, -A3*, -B2, -A2, -A3, -C2. Overall, the samples with the stitching removed has the lowest energy per event released compared to their counterparts. That means the stitch-less material had less events recorded, as previously mentioned, that also had less energy released when damage was occurring. The Glass- A materials with the stitching intact have the most energy released per event, despite being in the middle range of number of events recorded. The Glass-A materials make up both ends of the spectrum show that the stitching drastically effects the energy released per damage event. Other than Glass-A2*, the two other 90° samples and the six ply pre-preg sample have the highest values, despite having by far the least of amount of damage events recorded. The presence and

increase of 0° lends to more instances of damage occurring. The 0° tows have less instances of damage until catastrophic damage is approached, but the 90° tows easily allow damage propagation. The primary mode of damage for the transverse tows is MCCD, suggesting the majority of energy released is in the matrix materials.

An analysis of variables (ANOVA) method using MS Excel Data Analysis Toolpak was used to determine if there is a significant relation or similarity of the E_{abs} values between each sample group. The arrangement of the sample data in Excel can be seen in Appendix D. The result of the analysis output the Table 12 below.

Source of Variation	SS	df	MS	F	P-value	F_{crit}
Between Groups	313468.2	10	31346.9	7.54	$2.98603*10^{-6}$	2.11
Within Groups	145589.2	35	4159.7			
Total	459057.4	45				

Table 12: ANOVA for E_{abs} for each Sample Group

As seen above, the two most important values in this table for this research is the F and F_{crit} values between the sample groups. If $F > F_{crit}$ is, then the null hypothesis is rejected. If that happens then there is not a commonality or equality of values between the sample groups. In the case of this research, $7.54 > 2.11$, so the null hypothesis is rejected. That means the E_{abs} values for the 11 separate sample groups are not considered to be similar. In other words, the values are too different to consider them to be statistically similar when observing them overall. The only samples groups to not have the null hypothesis rejected are Glass- A1 and –C2, Glass- A2 and –C3, Glass- A3 and –

B2, and Glass- A3* and –B1. These four pairings are considered to be the only statistically similar values for E_{abs} using ANOVA method.

5. CONCLUSIONS

The use of AE data to determine damage of composite materials is, and increasingly will be, the optimal tool to use in the application of real world consumers. The ability of the equipment to extract real-time data during testing to determine the damage that is occurring in FRPCs. There are strong correlations between PFRQs and the three types of micro damage and the absolute energy released, that many other researchers are in agreement with. The different types of fabric and layups illustrated how the damage initiated and propagated and how that can affect the choices that consumers choose to use FRPCs for the wind industry and others. The shift in PFRQs from material and layup can provide valuable insight to how different industries can use them to create structures that have similar properties to each other, which may be easier and/or cheaper to manufacture. This work shows that the same materials can have drastically different properties when using different layups, and vice versa. This was most apparent for the 0° samples and the samples that had the stitching removed. On the other hand, the change in layup can very little effect on the properties of the samples, as seen with the CSM samples.

The AE data also provided insight as to how damage progression can affect the overall strength and stiffness of a sample. Slight changes to the ply count can have little effect on the UTS and ε_f, but drastic effect on the N_{PFRQ}, as seen with the Glass-B material. This shows that more occurrences of damage do not necessarily indicate lower loads to failure. Conversely, there is strong trend between 0° and 90° samples and the N_{PFRQ}. This is due in part to the substantially lower load that the transverse coupons fail

at. These samples fail so quickly that there is very little times for AE data to be recorded before the sample reaches catastrophic failure. The only 90° samples to feature significant amounts of FBD were the CSM samples. The other samples failed almost entirely due to FPDDs and MCDs. The CSM provides a more even distribution of load among the random fibers, therefore a more even distribution of types of damage. That being said, the overwhelming majority of the damage caused for all of the samples was MCDs. It is important to note that, even with the addition of plies for the biaxial samples, the 0° samples typically had a much higher N_{PFRQ}. The second most important thing to note is that the removal of stitching contributed to a sharp decrease in N_{PFRQ} compared with those that had it still intact, although this did not necessarily mean lower UTS or ε_f. The CSM samples showed that the addition of a single ply reduced the amount of N_{PFRQ} by 80.5%. The addition of the 90° caused catastrophic failure to occur before the 0° ply failed. Glass-C1 was able to continue with the test until fibers tows separated and eventually broke, whereas Glass-C3 failed when the 90° exhibited tow complete separation. The failure between tows would cause the sample to exhibit debonding between the two plies that lead to failure. That means with the normal tows still intact, complete separation from the transverse ply caused it to slide off in the direction of load at a lower load. This claim is supported by observing the same damage propagation for the Glass-A and Glass-B samples. This effect was reduced with the addition of a CSM and leaving the stitching intact. The stitching allowed for the transverse tows to stay bonded together slightly better, but not to the same extent of CSM, as seen by the reduction in both UTS and N_{PFRQ} for the Glass-A and Glass-C

materials. Glass-B showed that having 50% more transverse tows increased N_{PFRQ} as well as types of damage. When the layups were even, only MCDs were present in the AE data. The reduction in strength caused by the addition of 90° fiber tows created a scenario in which damage propagation occurred in the center of the coupon where it was weakest. The increase in instances of damage taking place lead to a quicker weakening of the coupon. The reduction of transverse plies for Glass-B1 required more high frequency events for damage to propagate; which as stated earlier, there was certainly FBDs that occurred that were not recorded due to them happening at the exact same time of catastrophic failure. The 90° tows had more low frequency damages that occurred, which happen at lower loads. This suggests that the amount of damage taken place at the center overcame the strength of the 0° tows. Taking into consideration that the addition of plies did not enhance the strength, but only the increase in N_{PFRQ} supports this claim. The lack of stitching material for pre-preg also reduced the amount of damage occurrences, but did not correlate to higher UTS or ε_f.

The types of damage that occurred for each sample set is also important to note here. The removal of the stitching increased to MCDs for Glass-A. The stitching helped to the tows in place until there was fiber failure. The tows were more freely able to move than when the stitching was left intact. This also contributed to the reduction in FBDs since the tows could move and separate, contributing to the catastrophic failure. This is the opposite for the stitched samples, since the tows were held in place, they failed when the fibers broke. The addition of plies also created more instances of lower frequency damage, which was exhibited by all three sample groups. This is due in large part to the

separation of plies as discussed earlier. The transverse plies that are in direct contact with the normal plies experience tow separation first and in turn that extension cause the two plies to become separated. This is why FPDDs are more prevalent in the biaxial samples.

The UTS of the 0° samples on average is much higher than that of the biaxial samples and especially compared to that of the 90° samples. The one instance where this does not hold true is in the case of the 0° Glass-A samples. The removal of stitching actually enhanced the UTS of the samples. This would suggest that with the lack of stitching holding the tows in place allowed for more flexing and movement of the tows, as stated earlier. The tows were able to move in a way that created a more even distribution of the stress inside the sample. The tows moving helped to release energy as well, without causing the sample to have a sudden load drop and maintain a steady load. In the stitched samples, this energy was built up in the fibers until they reached the UTS and forced catastrophic failure. The samples may have had parts where the fibers were approaching UTS and others that still had a more to go. This would cause an overload in some of the fibers and since they were locked into place by the stitching, they could not move to redistribute the stress in the sample. The removal of the stitching for the transverse samples caused the opposite effect on UTS. This is because of the same reason as the normal samples. The Glass-A2* does not have the stitching to hold the tows together, which is more important when load in the transverse direction. The tows are allowed to separate more freely, causing catastrophic failure by FPDD. Another atypical result regarding the UTS was Glass-C3 having a greater value than Glass-A1. This suggest that the CSM caused a more even distribution of the load not only for each

ply, but for inter-ply mechanics as well. The events for a normal sample with the CSM were the highest and the transverse the lowest. The reduction in events and increase in UTS suggests that the biaxial sample evenly distributed the stress from the transverse ply to the other. The sample still failed primarily due to the 90° ply, but the 0° ply was able to take on more of the load. It was a load that was substantially lower than what the 0° ply could handle alone, so the propagation of large amounts of damage did not occur as seen with Glass-C1. Glass-C2 featured a reduction in UTS and N_{PFRQ}, so to relate to Glass-C3, this means that the transverse ply had just as many events plus the events from the normal ply that was nowhere near failing. The UTS and N_{PFRQ} was between that of Glass-C1 and Glass-C2. This trend is found for both Glass-B and Glass-A with the stitching intact samples, but to a lesser degree. Glass-B samples, as discussed earlier, had a reduction in UTS and an increase in N_{PFRQ} with the addition of transverse plies. The UTS is not as significant a drop off as the others, but this could be contributed to the extra plies it had.

The effect of architecture and layups on ε_f have a harder trend to determine. Glass-A1 and Glass-A3 both have greater ε_r compared to their stitch-less counterparts, but the opposite occurs for the Glass-A2 and Glass-A2 samples. This makes sense with the previous finding that the stitching causes the fiber tows to lock into place. Glass-A2* allows the tows to separate slightly while under load before failure. This not increase the UTS, but allows more flex to occur in the sample. The normal and biaxial sample have the tows move too much when the stitching is removed, thus causing catastrophic failure. This is the same reason for the effect on UTS and Glass-A1 is the same for ε_f. The

locked in tows create an uneven stress distribution, so the UTS is entirely dependent on the strength of the fibers. The fibers may be overloaded but they can achieve very high strain, conversely the samples without stitching distribute the stress more evenly helping to achieve higher values, but the movement of the tows cause FPPDs and form cracks that propagate along the sample, which means the ε_f of the sample becomes dependent on the matrix material, which is typically much lower than the fibers. The Glass-C samples show that the 0° samples have the highest ε_f and the 0° samples the lowest. The low strain of the transverse and high strain of the normal samples combined, cause the overall ε_f to have a value between the two, similar to the UTS. This similarity to the effect on UTS for the Glass-B samples holds true as well. The damage propagation in the center, more abundant transverse plies overcomes the strength of the outside 0° plies, causing it to fail at a lower value.

The E_{abs} for all of the sample groups can be difficult to use to determine any meaningful trends at face value. There is no strong correlation between the architecture and layup and how much energy is released. There are also samples that are magnitudes different and have higher or lower values than what was expected. The only fact that can be stated is that the increase in N_{PFRQ} typically leads to a decrease in E_{abs}, but even that does not always hold true. That means, in general, that the samples that had less damage propagation also had more high energy events. The lack of damage events would cause a massive buildup of energy within sample, which would then be released by sudden damage. This is different from the samples with lots of AE events to be recorded, because they had many low energy events that occurred and propagated throughout the

test. But as stated previously, that is not always the case, as with Glass-A1* and Glass-B1. For these two samples specifically, this is most likely due to the combination of the lack of damage propagation and sudden catastrophic failure caused the energy that was released to not be able to be recorded by the AE equipment. If it could have been recorded with the sudden failure, there is a very good chance that the E_{abs} values would have been very high for these two samples. This assumption is important to remember this moving forward.

AE signal recording technology is an excellent tool for characterizing the damage propagation of composite materials during testing. In this work it allowed for real-time measurements to determine the damage accumulated and what type eventually lead to the catastrophic failure of each sample. In the case of the Vectorply, the first indication that the sample was approaching failure was the gradual increase of MCD, followed by the appearance of FPDDs. Once the FPDDs had a sudden increase, FBDs initiated and with short propagation to sudden failure. The usefulness in AE for this test is that it known that when there is a sharp spike in FPDDs, the structure will fail shortly and should be put out of commission before any FBDs are detected, speaking in a consumer-sense. For the PPG fabric, which is more difficult to characterize using AE signals, MCDs and FPDDs are both present early in the testing of each sample. The arrival of FBDs also occur relatively early in the lifetime of the PPG fabric, so that is not an indicator of failure. The FBDs gradually increase as the test continues, then level off with propagation and no sharp increase, as was the case for the Vectorply fabric. Instead, the impetus for catastrophic failure was the sharp spike in FPPD. This is due in large part to the CSM

debonding from the UD tows, eventually leading to failure. In the case of the pre-preg fabric, there is almost no damage propagation recorded with AE equipment. The only time PFRQs manifested during testing was with an increase in the low strength 90° plies. Pre-preg, for the most part, only output MCD emissions. The only indicator of impending failure was the first appearances of FPDDs, with little to no propagation. Pre-preg material will have a limited effectiveness in the case of AE testing. The manufacturing process for this material is such that each fiber tow are placed under immense pressure and heat causing the internal structure of each sample to be extremely rigid. The shear amount of internal stress to cause any amount debonding or any movement by the fibers or matrix material indicates immediate failure. Although, as previously stated, the addition of 90° plies allows for more damage propagation. This method may lower the strength of the structure, but will create circumstances in which AE testing will be a more effective indicator of damage propagation and impending failure.

The greatest detractor to the use of AE testing will be in the use for monitoring structures that have sudden failure, like with the Newport, because the energy released at the moment of catastrophic failure cannot be captured. The vast majority of the damage that occurs is the failure itself. Composite materials that do not have a large quantity of internal damage before failure will not output the appropriate AE signals to accurately determine the energy released. The best use of AE analysis for energy released measurements still needs to be developed, as it is not a viable option for the real values right now. As stated earlier, energy measurements were only used to compare them to

one another in this research, but that is also imperfect. There are currently methods that incorporate the use of sensors that capture airborne AE signals, which would be ideal for the problems presented here.

AE monitoring in conjunction with different fiber architecture would be best used in the wind industry as a tool to be used as for new composite materials before deployment. The wind industry and the use of composite materials will continue to grow and diversify, and so will the types of fiber architecture will continue to change. AE monitoring should be utilized on these new materials during research and development. It would be ideally used to characterize types of internal damage and how they propagate. A better understanding of how these new materials behave will lead to several changes in the use. First, it can help balance performance and cost for the reachability and ease to which a unit can be monitored. A material that will not need constant monitoring, determined through AE testing will best be used in more remote or hard to reach locations. This can be a composite that does not feature significant damage occurrences throughout the life of the structure, but has a sudden catastrophic failure. Materials that have substantial internal damage during service, but has other qualities that are desired, would best be utilized in smaller and easier to reach units. That way when certain types of damage begin to occur that indicate catastrophic failure is imminent confirmed with onsite AE monitoring, repair to the unit can take place more frequently as needed. Second, a better understanding of the effect of fiber architecture will be more important as turbines continue to be deployed in more diverse areas. Turbines are no longer being deployed in empty fields in remote locations, other areas include underwater and off of

coasts. Different architecture can cause a unit to perform vastly different in these places. The fiber architecture that is efficient and has long service life in a field can be substantially less effective underwater. Third, AE monitoring can assist in safety and minimizing destruction of work cell when deploying a unit. Different fibers and layups damage and fail in many ways, and a better understanding of how that is going to occur can lead to less destruction or danger in the area of a unit in service. The unit can fail due to fatigue or lightning strikes or any other reason, if the damage propagation is better understood, it can be positioned in a way that minimal damage occurs to other units in the area or other buildings or to itself. If the windblades are using a fiber and layup that is optimized for its position, use, and environment it could still be repaired rather than completely replaced, which would be more cost effective. Optimizing the fibers and layups will be vital moving forward for the renewable energy industry, and AE testing has proven that it will be the most effective tool in providing that.

Overall, it appears that the best option for fabric architecture are dependent on the desired operation. If the structure is predicted to undergo high loads with low flexure, the best option is to use the PPG with CSM. The CSM is very good at blunting damage propagation and cracks. The Vectorply is much better suited to withstand high strain situations, but may not be good for high stress situations because of its inability to stop or slow the propagation of damage. The removal of the stitching can help this, but it will cause a slight reduction in the ability to handle high strains. The Vectorply is best used in a multi-directional layup due to its high ε_f, but can cause a loss in strength if the majority of plies are used in a transverse loading direction. That is where the removal of the

stitching can come in handy. If the direction of loading is known, the best application of the Vectorply may be to keep stitching of the plies in the loading direction intact and then remove it for the plies transverse to it. The PPG would best be used in situation that the structure is not going to be able to be inspected at a high frequency. This is preferable for the wind industry, since low frequency inspection is common. The pre-impregnated materials are probably best suited for situations in which low deformation with relatively low strength is preferred. It is ideal for things like bikes and fishing poles, since rigidity is important. It also fails the most suddenly of the materials tested in this work, so that would be preferred for non-professional consumers that do not have the resources to regularly inspect and repair the composite material structure.

Future Work

The most interesting work for the future regarding fabric architecture and the use of AE detection methods is expansion of more material types and how the combination of them can change the mechanical properties. The inclusion of more types of fabric will expand the database that has been laid here. The first suggestion would be to use AE on CSM only fabric. It would be very interesting to see how the damage initiates and propagates and how well the events recorded can help with characterizing it. The system could have difficulty, because in theory all three types of damage would be occurring the entirety of the test. If that were the case, then it could be difficult to have any value in using the AE system. Another material architecture that was not used here would be the use of woven fabrics. It is well know that woven fabrics are used similarly in the way

that UD fabrics with CSM backing are used, in that they are best used to help distribute stress evenly throughout the structure. The important findings there would be to help determine how the AE signals can be used to differentiate how damage propagates differently than that of CSM. It is generally that that UD with CSM CFRPs are better to use because of lower cost, but it may be that the reduction of damage may make it worth the extra cost. Also, there are many types of architecture for woven fabrics, as explained earlier, that could yield many different results regarding AE monitoring of damage progression. Finally, an important material to test would be hybrid fabrics. These are used generally to reduce cost while combining the desired properties of two fabric materials. Previous work was attempted to characterize carbon fibers composite, but the strength of the fibers made it difficult. There are other fiber types that could be tested that could be useful to the consumer base. This includes Aramid fibers and natural fibers like grass and bamboo. The first step to determining how these fibers effect damage propagation would be to characterize the PFRQ events of them. Recall, that this work only had the PFRQs with corresponding types of damage for carbon and glass. The frequencies could be entirely different which could require different equipment. These are only some of the architectures that could be expanded upon.

Another series of tests that could be performed is that of combining different materials and fabric architectures. As stated previously, a suggestion would be to combine Vectorply with and without the stitching intact within the same structure. It is the conjecture of this work that the finished composite could have higher strength and strain to failure than that of its constituents. But that is not the only combination that

could occur, another would be to combine UD fabrics with UD fabrics with CSMs. The CSMs could be oriented in a way that has them in the center of the sample pointed inward or outward, then encased in simple UD fabrics on the outside of the sample. The test could then be repeated with the CSMs on the outer plies pointed in either direction. AE equipment could be used to determine if damage propagation is any different with the different layups or if they are similar but occurring at the different depths inside the samples. Another point of interest would be to determine if pre-impregnated material could be used with traditional VARTM methods seen here. The unique quality of it was that damage propagation did not occur a great deal inside the samples, compared the VARTM samples. If it could be used so that it was used between each ply of fabric infusion fabric, then infused with resin in a traditional VARTM process, the problem of cracks going from ply to ply and causing separation could be reduced. There are many fabric architecture combinations that can be explored for the purposes of determining the failure and damage a composite material may undergo. This work can be expanded upon as manufacturing of composites continue to grow in popularity and new methods are developed. The potential of AE testing is in its ability to determine how they can improve manufacturing and what is best for each individual consumer. The use of AE equipment to estimate damage that has occurred and the life left of a structure has been well established, but its use as a tool for how it will perform throughout its life before it is put into commission will be invaluable moving forward.

REFERENCES CITED

1. American Wind Energy Association. (2013). *2012 U.S. Wind Industry Annual Market Report.* Washington, DC.

2. Arumugam V, Kumar CS, Santulli C, Sarasini E, Stanley AJ. (2011). A Global Method for the Identification of Failure Modes in Fiberglass Using Acoustic Emission. *Journal of Testing and Evaluation, 39,* 954-966.

3. Aramid Fiber. (2015). Retrieved February 2, 2016, from http://www.netcomposites.com/guide-tools/guide/reinforcements/aramid-fibrefiber/

4. Bailie, A., Clemmer, S., & Deyette, J. (2015). Analysis of a 30 Percent by 2030 National Renewable Electricity Standard [Powerpoint Slides]. Retrieved from http://www.ucsusa.org/sites/default/files/attach/2015/05/UCS_National-30-Percent-by-2030-RES-Analysis.pdf

5. Barbero, E. J. (2011). *Introduction to Composite Materials Design* (2 ed.). Boca Raton, FL: CRC Press.

6. Bauer, M. (2014). *Manufacturing Reliability for C-Channel Composite Beams*. Industrial and Mechanical Engineering, Montana State University Composites Group. Bozeman: Montana State University.

7. Baxter MG, Pullin R, Holford KM, Evans SL. (2007). Delta T source location for acoustic emission. *Mechanical Systems and Signal Processing, 21,* 1512-1520.

8. Bohse J. (2000). Acoustic emission characteristics of micro-failure processes in polymer blends and composites. *Composites Science and Technology, 60, 1213-1226*.

9. Bourchak M, Farrow IR, Bond IP, Rowland CW, Menan F. (2007). Acoustic emission energy as a fatigue damage parameter for CFRP composites. *International Journal of Fatigue*, *29*, 457-470.

10. Braid Basics. (2016). Retrieved December 4, 2016, from http://www.braider.com/Braid-Basics/

11. Campbell, F. C. (2010). *Structural Composite Materials* [1]. Materials Park, OH: ASM International. Retrieved January 15, 2016, from http://www.asminternational.org/documents/10192/3449376/05287G_Frontmatter.pdf/99be6880-dfa9-41d3-89b6-bfd96d63b878

12. Cantwell WJ, Morton J. (1992). THE SIGNIFICANCE OF DAMAGE AND DEFECTS AND THEIR DETECTION IN COMPOSITE-MATERIALS - A REVIEW. *Journal of Strain Analysis for Engineering Design, 27*, 29-42.

13. Cervenka, A. (1999). Advantages and Disadvantages of Thermoset and Thermoplastic Matrices for Continuous Fibre Composites. *Mechanics of Composite Materials and Structures, 361*, 289-298. Retrieved December 29, 2015, from http://link.springer.com/chapter/10.1007/978-94-011-4489-6_16

14. ChemViews (2012, February). How Wind Turbines Work. *ChemViews Magazine*. Retrieved from http://www.chemistryviews.org/details/ezine/1444481/How_Wind_Turbines_Work.html

15. Chopped Strand Mat. (2014, June 16). Retrieved December 25, 2015, from http://www.amtcomposites.co.za/products/carbon-glass-aramidreinforcements/chopped-strand-mat

16. deGroot PJ, Wijnen PAM, Janssen RBF (1995). Real-time frequency determination of acoustic emission for different fracture mechanisms in carbon epoxy composites. *Composites Science and Technology, 55*, 405-412.

17. Gandelsman, M. (1999). Strain Energy Project. Retrieved January 8, 2016, from http://emweb.unl.edu/Mechanics-Pages/Marina-Gandelsman/strain.html

18. Gorman MR. (1991). PLATE WAVE ACOUSTIC-EMISSION. *Journal of the Acoustical Society of America*, *90*, 358-364.

19. Gutkin R, Green CJ, Vangrattanachai S, Pinho ST, Robinson P, Curtis PT. (2011). On acoustic emission for failure investigation in CFRP: Pattern recognition and peak frequency analyses. *Mechanical Systems and Signal Processing*, *25*, 1393-1407.

20. Hsu NN, Breckenridge FR. (1981). CHARACTERIZATION AND CALIBRATION OF ACOUSTIC-EMISSION SENSORS. *Materials Evaluation, 8*, 39-60.

21. Prosser WH, Seale MD, Smith BT. (1999). Time-frequency analysis of the dispersion of Lamb modes. *The Journal of the Acoustical Society of America*, *105*, 2669-2676.

22. Hybrid Fabrics. (2015, November 16). Retrieved January 2, 2016, from http://www.netcomposites.com/guide-tools/guide/reinforcements/hybrid-fabrics/

23. Fabric Types. (2015). Retrieved January 2, 2016, from http://www.netcomposites.com/guide-tools/guide/reinforcements/fabric-types/

24. KEVLAR®/ Carbon Hybrid. (2010). Retrieved February 7, 2016, from http://www.fibreglast.com/product/kevlar-carbon-hybrid-yellow-1065/carbon-kevlar-hybrid-fabric

25. Kim BW, Nairn JA. (2002). Observations of fiber fracture and interfacial debonding phenomena using the fragmentation test in single fiber composites. *Journal of Composite Materials, 36*, 1825-1858.

26. Knowles, K. M. (2002, October 1). *Micrograph 548* [Photograph]. Ceramics, University of Cambridge, Cambridge.

27. Lamb H. (1917) On waves in an elastic plate. *Proceedings of the Royal Society of London Series a-Containing Papers of a Mathematical and Physical Character, 93*, 114-28.

28. Laminating System for RTM Injection and Wound Composites. (2011). Retrieved January 4, 2016, from http://www.havel-composites.com/shop/74-Ostatni-pro-PREPREGY/3593-Laminacni-system-pro-RTM-injektaz-a-navijene-kompozity.html?pls=0

29. Leão, M. A., Tinô, S. R., Fontes, R. S., & Aquino, E. M. (2011). Bending in Laminas of NFPR: Type of Reinforcement, Fracture and Properties. *Mat. Res. Materials Research, 14*(1), 67-72. Retrieved December 29, 2015, from http://www.scielo.br/scielo.php?pid=S1516-14392011000100013&script=sci_arttext

30. Loutas TH, Kostopouios V, Ramirez-Jimenez C, Pharaoh M. (2006). Damage evolution in center-holed glass/polyester composites under quasi-static loading using time/frequency analysis of acoustic emission monitored waveforms. *Composites Science and Technology, 66*, 1366-1375.

31. Mar-Bal. (2013). History of Composites. Retrieved from http://www.mar-bal.com/language/en/applications/history-of-composites/

32. Multiaxial Fabrics. (2015). Retrieved January 2, 2016, from http://www.netcomposites.com/guide-tools/guide/reinforcements/multiaxial-fabrics/

33. Nelson, J. (2013). *A Comparison of Continuum and Discrete Modeling Techniques of the Effects of Manufacturing Defects Common to Composite Structures.* Industrial and Mechanical Engineering, Montana State University Composites Group. Bozeman: Montana State University.

34. Ni QQ, Iwamoto M. (2002). Wavelet transform of acoustic emission signals in failure of model composites. *Engineering Fracture Mechanics, 69*, 717-728.

35. Ni QQ, Kurashiki K, Iwamoto M. (2001). AE technique for identification of micro failure modes in CFRP composites. *Materials Science Research International, 7*, 67-71.

36. Other Fabrics. (2015). Retrieved January 2, 2016, from http://www.netcomposites.com/guide-tools/guide/reinforcements/other-fabrics/

37. Qui, Y. (2008) *Composite Manufacturing Processes* [PowerPoint Slides]. Retrieved from composites.dhu.edu.cn/download/Composite_Manufacturing_ Processes.ppt

38. Ramirez-Jimenez CR, Papadakis N, Reynolds N, Gan TH, Purnell P, Pharaoh M. (2004). Identification of failure modes in glass/polypropylene composites by means of the primary frequency content of the acoustic emission event. *Composites Science and Technology, 64*, 1819-1827.

39. Riddle, W. (2013). *Development of Reliability Program for Risk Assessment of Composite Structures Treating Defects as Uncertainty Variables.* Industrial and Mechanical Engineering, Montana State University Composites Group. Bozeman: Montana State University.

40. Rumsey MA, Paquette JA. (2008). Structural health monitoring of wind turbine blades - art. no. 69330E. Conference on Smart Sensor, Phenomena, Technology, Networks, and Systems, San Diego, CA.

41. Rusmee, P. (2005, September). Composite Materials. Retrieved February 1, 2016, from http://www.mech.utah.edu/~rusmeeha/labNotes/composites.html

42. Sandia National Laboraties. (2014). *Blade Reliability Collaborative*. Retrieved from Sandia National Laboratories Energy and Climate: http://energy.sandia.gov/energy/renewable-energy/wind-power/materials-reliability-standards/blade-reliability-collaborative/

43. Sause MGR, Muller T, Horoschenkoff A, Horn S. (2012). Quantification of failure mechanisms in mode-I loading of fiber reinforced plastics utilizing acoustic emission analysis. *Composites Science and Technology, 72*, 167-174.

44. Scholey JJ, Wilcox PD, Wisnom MR, Friswell MI. (2010). Quantitative experimental measurements of matrix cracking and delamination using acoustic emission. *Composites Part a-Applied Science and Manufacturing, 41*, 612-23.

45. Schuster, M. (2014). *CHARACTERIZATION AND ENERGY ANALYSIS OF FIBER REINFORCED POLYMER COMPOSITES BY ACOUSTIC EMISSION ANALYSIS*. Industrial and Mechanical Engineering, Montana State University Composites Group. Bozeman: Montana State University.

46. Sedlak P, Hirose Y, Enoki M. (2013). Acoustic emission localization in thin multi-layer plates using first-arrival determination. *Mechanical Systems and Signal Processing, 36*, 636-649.

47. Selcom. (2014). Retrieved January 6, 2016, from http://www.multiaxialfabricselcom.com/en/Products/unidirectional-fabrics-eg-carbon-aramid-and-unidirectional-fiberglass-cloths.html

48. Siemens. (2012, August). *B75 Rotor Blade Fact Sheet*. Retrieved from Siemens: http://www.siemens.com/press/pool/de/feature/2012/energy/factsheet-b75-rotor-blade-e.pdf

49. SNL/MSU/DOE Composite Materials Fatigue Database Version 23. (2016) Bozeman, MT: Montana State University Composites Group.

50. Summerscales, J. (2015, August 26). Composites Design and Manufacture. Retrieved December 30, 2015, from https://www.fose1.plymouth.ac.uk/sme/MATS347/MATS347A4 fracture.htm

51. Surgeon M, Wevers M. (1999). Modal analysis of acoustic emission signals from CFRP laminates. *Ndt & E International*, *32*, 311-22.

52. Suzuki M, Nakanishi H, Iwamoto M, Jinen E. (1988). Application of Static Fracture Mechanisms to Fatigue Fracture Behavior of Class A-SMC Composite. *Proc 4th Japan-US Conf on Composite Materials*, 297-306.

53. Swolfs, Y., Gorbatikh, L., & Verpoest, I. (2013). Stress concentrations in hybrid unidirectional fibre-reinforced composites with random fibre packings. *Composites Science and Technology*, *85*, 10-16. Retrieved December 13, 2015.

54. Unidirectional Fabric. (2015, November 16). Retrieved January 2, 2016, from http://www.netcomposites.com/guide-tools/guide/reinforcements/unidirectional-fabric/

55. United States Department of Transportation, Federal Aviation Administration, Airman Testing Standards Branch. (2012). Advanced Composite Materials. (pp. 4-23) *Aviation Maintenance Technician Handbook-Airframe, Vol. 1. (FAA-H-8083-31)* Retrieved from https://www.faa.gov/regulations_policies/handbooks_manuals/aircraft/amt_airframe_handbook/media/amt_airframe_vol1.pdf

56. United States Energy Information Administration. (2013). *ANNUAL ENERGY OUTLOOK 2013: with Projections to 2040*. (DOE/EIA -0383(2013)) Retrieved from https://www.eia.gov/forecasts/archive/aeo13/pdf/0383(2013).pdf

57. VARTM Infusion. (2006). Retrieved January 3, 2016, from http://www.futuremediacreations.com/technoire/vartm.htm

58. Vallen, H. (2002, September). AE Testing Fundamentals,Equipment, Applications. Retrieved January 21, 2016, from http://www.ndt.net/article/v07n09/05/05.htm

59. Waller JM, Nichols CT, Wentzel DJ, Saulsberry RL. (2010). USE OF MODAL ACOUSTIC EMISSION TO MONITOR DAMAGE PROGRESSION IN CARBON FIBER/EPOXY COMPOSITES. 37th Annual Review of Progress in Quantitative Nondestructive Evaluation (QNDE). San Diego, CA.

60. Wang L, Yuan FG. (Wang) Group velocity and characteristic wave curves of Lamb waves in composites: Modeling and experiments. *Composites Science and Technology, 67*, 1370-1384.

61. Woven Fabrics. (2015). Retrieved January 2, 2016, from http://www.netcomposites.com/guide-tools/guide/reinforcements/woven-fabrics/

62. Yousefi J, Ahmadi M, Shahri MN, Oskouei AR, Moghadas FJ. (2014). Damage Categorization of Glass/Epoxy Composite Material Under Mode II Delamination Using Acoustic Emission Data: A Clustering Approach to Elucidate Wavelet Transformation Analysis. *Arabian Journal for Science and Engineering, 39*, 1325-1335.

63. Zarouchas DS, Van Hemelrijck D. (2013). Monitoring the Structural Integrity of Wind Turbine Blades Subcomponents using Advanced Signal Processing Techniques. *Structural Health Monitoring, 2*, 2448-2455.

64. Zhang, J., Chaisombat, K., He, S., & Wang, C. H. (2012). Hybrid composite laminates reinforced with glass/carbon woven fabrics for lightweight load bearing structures. *Materials & Design, 36*, 75-80. Retrieved January 6, 2016.

APPENDICES

APPENDIX A

COUPON DATA

Coupon Data

Plate No.	Fabric	Company	Layup	Dimensions (mm)	Feature	Test Machine
2434-1	NCT30-D1-E300	Newport	$[0/90]_S$	302x32x1.0	Prepreg	Instron 8562
2434-2	NCT30-D1-E300	Newport	$[0/90]_S$	305x32x1.0	Prepreg	Instron 8562
2434-3	NCT30-D1-E300	Newport	$[0/90]_S$	304x32x1.0	Prepreg	Instron 8562
2434-4	NCT30-D1-E300	Newport	$[0/90]_S$	302x32x1.0	Prepreg	Instron 8562
2434-5	NCT30-D1-E300	Newport	$[0/90]_S$	303x32x1.0	Prepreg	Instron 8562
2434-6	NCT30-D1-E300	Newport	$[0/90]_S$	303x32x1.0	Prepreg	Instron 8562
2434-7	NCT30-D1-E300	Newport	$[0/90]_S$	302x32x1.0	Prepreg	Instron 8562
2434-8	NCT30-D1-E300	Newport	$[0/90]_S$	303x32x1.0	Prepreg	Instron 8562
2434-9	NCT30-D1-E300	Newport	$[0/90]_S$	302x32x1.1	Prepreg	Instron 8562
2434-10	NCT30-D1-E300	Newport	$[0/90]_S$	302x31x1.0	Prepreg	Instron 8562
2434-11	NCT30-D1-E300	Newport	$[0/90]_S$	304x32x1.0	Prepreg	Instron 8562
2434-12	NCT30-D1-E300	Newport	$[0/90]_S$	303x32x1.0	Prepreg	Instron 8562
2434-13	NCT30-D1-E300	Newport	$[0/90]_S$	302x33x1.0	Prepreg	Instron 8562
2434-14	NCT30-D1-E300	Newport	$[0/90]_S$	303x32x1.0	Prepreg	Instron 8562
2434-15	NCT30-D1-E300	Newport	$[0/90]_S$	302x32x1.0	Prepreg	Instron 8562
2435-1	NCT30-D1-E300	Newport	$[0/90_2]_S$	305x34x1.6	Prepreg	Instron 8562
2435-2	NCT30-D1-E300	Newport	$[0/90_2]_S$	304x35x1.6	Prepreg	Instron 8562
2435-3	NCT30-D1-E300	Newport	$[0/90_2]_S$	304x34x1.6	Prepreg	Instron 8562
2435-4	NCT30-D1-E300	Newport	$[0/90_2]_S$	305x35x1.6	Prepreg	Instron 8562
2435-5	NCT30-D1-E300	Newport	$[0/90_2]_S$	304x34x1.6	Prepreg	Instron 8562

2435-6	NCT30-D1-E300	Newport	$[0/90_2]_S$	304x34x1.6	Prepreg	Instron 8562
2435-7	NCT30-D1-E300	Newport	$[0/90_2]_S$	304x34x1.6	Prepreg	Instron 8562
2435-8	NCT30-D1-E300	Newport	$[0/90_2]_S$	305x34x1.6	Prepreg	Instron 8562
2435-9	NCT30-D1-E300	Newport	$[0/90_2]_S$	304x34x1.6	Prepreg	Instron 8562
2435-10	NCT30-D1-E300	Newport	$[0/90_2]_S$	304x34x1.6	Prepreg	Instron 8562
2435-11	NCT30-D1-E300	Newport	$[0/90_2]_S$	303x34x1.6	Prepreg	Instron 8562
2435-12	NCT30-D1-E300	Newport	$[0/90_2]_S$	304x35x1.7	Prepreg	Instron 8562
2435-13	NCT30-D1-E300	Newport	$[0/90_2]_S$	304x34x1.6	Prepreg	Instron 8562
2435-14	NCT30-D1-E300	Newport	$[0/90_2]_S$	305x35x1.6	Prepreg	Instron 8562
2435-15	NCT30-D1-E300	Newport	$[0/90_2]_S$	304x34x1.6	Prepreg	Instron 8562
2439-1	E-LT-3900	Vectorply	[0]	254x26x0.9	w/o stitching	Instron 8562
2439-2	E-LT-3900	Vectorply	[0]	254x26x0.8	w/o stitching	Instron 8562
2439-3	E-LT-3900	Vectorply	[0]	255x26x0.8	w/o stitching	Instron 8562
2439-4	E-LT-3900	Vectorply	[0]	254x26x0.8	w/o stitching	Instron 8562
2439-5	E-LT-3900	Vectorply	[0]	254x26x0.8	w/o stitching	Instron 8562
2439-6	E-LT-3900	Vectorply	[0]	254x26x0.8	w/o stitching	Instron 8562
2439-7	E-LT-3900	Vectorply	[0]	254x26x0.8	w/o stitching	Instron 8562
2439-8	E-LT-3900	Vectorply	[0]	255x26x0.8	w/o stitching	Instron 8562
2439-9	E-LT-3900	Vectorply	[0]	254x26x0.8	w/o stitching	Instron 8562
2439-10	E-LT-3900	Vectorply	[0]	254x26x0.8	w/o stitching	Instron 8562
2439-11	E-LT-3900	Vectorply	[0]	254x26x0.8	w/o stitching	Instron 8562
2439-12	E-LT-3900	Vectorply	[0]	254x26x0.8	w/o stitching	Instron 8562

2439-13	E-LT-3900	Vectorply	[0]	253x27x0.8	w/o stitching	Instron 8562
2439-14	E-LT-3900	Vectorply	[0]	254x26x0.8	w/o stitching	Instron 8562
2439-15	E-LT-3900	Vectorply	[0]	254x26x0.8	w/o stitching	Instron 8562
2439-16	E-LT-3900	Vectorply	[0]	254x26x0.8	w/o stitching	Instron 8562
2439-17	E-LT-3900	Vectorply	[0]	254x25x0.8	w/o stitching	Instron 8562
2439-18	E-LT-3900	Vectorply	[0]	254x26x0.8	w/o stitching	Instron 8562
2439-19	E-LT-3900	Vectorply	[0]	255x26x0.8	w/o stitching	Instron 8562
2439-20	E-LT-3900	Vectorply	[0]	254x26x0.9	w/o stitching	Instron 8562
2439-21	E-LT-3900	Vectorply	[0]	254x26x0.8	w/o stitching	Instron 8562
2439-22	E-LT-3900	Vectorply	[0]	254x26x0.8	w/o stitching	Instron 8562
2439-23	E-LT-3900	Vectorply	[0]	254x26x0.8	w/o stitching	Instron 8562
2439-24	E-LT-3900	Vectorply	[0]	254x26x0.8	w/o stitching	Instron 8562
2439-25	E-LT-3900	Vectorply	[0]	254x26x0.8	w/o stitching	Instron 8562
2439-26	E-LT-3900	Vectorply	[0]	254x26x0.8	w/o stitching	Instron 8562
2439-27	E-LT-3900	Vectorply	[0]	254x26x0.8	w/o stitching	Instron 8562
2439-28	E-LT-3900	Vectorply	[0]	254x26x0.8	w/o stitching	Instron 8562
2439-29	E-LT-3900	Vectorply	[0]	255x26x0.8	w/o stitching	Instron 8562
2439-30	E-LT-3900	Vectorply	[0]	254x29x0.8	w/o stitching	Instron 8562
2440-1	E-LT-3900	Vectorply	[0]	255x29x0.9	w/ stitching	Instron 8562
2440-2	E-LT-3900	Vectorply	[0]	254x28x0.9	w/ stitching	Instron 8562
2440-3	E-LT-3900	Vectorply	[0]	260x28x0.9	w/ stitching	Instron 8562
2440-4	E-LT-3900	Vectorply	[0]	254x28x0.9	w/ stitching	Instron 8562

2440-5	E-LT-3900	Vectorply	[0]	254x28x0.9	w/ stitching	Instron 8562
2440-6	E-LT-3900	Vectorply	[0]	257x28x0.9	w/ stitching	Instron 8562
2440-7	E-LT-3900	Vectorply	[0]	255x28x0.8	w/ stitching	Instron 8562
2440-8	E-LT-3900	Vectorply	[0]	255x28x0.9	w/ stitching	Instron 8562
2440-9	E-LT-3900	Vectorply	[0]	254x28x0.8	w/ stitching	Instron 8562
2440-10	E-LT-3900	Vectorply	[0]	256x27x0.9	w/ stitching	Instron 8562
2440-11	E-LT-3900	Vectorply	[0]	254x28x0.9	w/ stitching	Instron 8562
2440-12	E-LT-3900	Vectorply	[0]	257x28x0.9	w/ stitching	Instron 8562
2440-13	E-LT-3900	Vectorply	[0]	254x28x0.9	w/ stitching	Instron 8562
2440-14	E-LT-3900	Vectorply	[0]	257x27x0.9	w/ stitching	Instron 8562
2440-15	E-LT-3900	Vectorply	[0]	254x28x0.9	w/ stitching	Instron 8562
2440-16	E-LT-3900	Vectorply	[0]	256x28x0.9	w/ stitching	Instron 8562
2440-17	E-LT-3900	Vectorply	[0]	257x29x0.9	w/ stitching	Instron 8562
2440-18	E-LT-3900	Vectorply	[0]	257x28x0.9	w/ stitching	Instron 8562
2440-19	E-LT-3900	Vectorply	[0]	257x28x0.9	w/ stitching	Instron 8562
2440-20	E-LT-3900	Vectorply	[0]	254x28x0.8	w/ stitching	Instron 8562
2440-21	E-LT-3900	Vectorply	[0]	255x28x0.9	w/ stitching	Instron 8562
2440-22	E-LT-3900	Vectorply	[0]	254x28x0.9	w/ stitching	Instron 8562
2440-23	E-LT-3900	Vectorply	[0]	254x28x0.9	w/ stitching	Instron 8562
2440-24	E-LT-3900	Vectorply	[0]	254x28x0.8	w/ stitching	Instron 8562
2440-25	E-LT-3900	Vectorply	[0]	257x28x0.9	w/ stitching	Instron 8562
2440-26	E-LT-3900	Vectorply	[0]	257x27x0.9	w/ stitching	Instron 8562

2440-27	E-LT-3900	Vectorply	[0]	255x28x0.9	w/ stitching	Instron 8562
2440-28	E-LT-3900	Vectorply	[0]	254x28x0.9	w/ stitching	Instron 8562
2440-29	E-LT-3900	Vectorply	[0]	254x28x0.9	w/ stitching	Instron 8562
2440-30	E-LT-3900	Vectorply	[0]	255x28x0.9	w/ stitching	Instron 8562
2441-1	E-LT-3900	Vectorply	[0/90]	251x27x2.0	w/ stitching	Instron 8562
2441-2	E-LT-3900	Vectorply	[0/90]	242x27x2.0	w/ stitching	Instron 8562
2441-3	E-LT-3900	Vectorply	[0/90]	248x27x2.0	w/ stitching	Instron 8562
2441-4	E-LT-3900	Vectorply	[0/90]	252x26x2.0	w/ stitching	Instron 8562
2441-5	E-LT-3900	Vectorply	[0/90]	253x27x2.0	w/ stitching	Instron 8562
2441-6	E-LT-3900	Vectorply	[0/90]	251x26x2.0	w/ stitching	Instron 8562
2441-7	E-LT-3900	Vectorply	[0/90]	253x26x2.0	w/ stitching	Instron 8562
2441-8	E-LT-3900	Vectorply	[0/90]	249x26x2.0	w/ stitching	Instron 8562
2441-9	E-LT-3900	Vectorply	[0/90]	250x27x2.0	w/ stitching	Instron 8562
2441-10	E-LT-3900	Vectorply	[0/90]	253x27x2.0	w/ stitching	Instron 8562
2441-11	E-LT-3900	Vectorply	[0/90]	251x26x2.0	w/ stitching	Instron 8562
2441-12	E-LT-3900	Vectorply	[0/90]	252x26x2.0	w/ stitching	Instron 8562
2441-13	E-LT-3900	Vectorply	[0/90]	248x25x2.0	w/ stitching	Instron 8562
2441-14	E-LT-3900	Vectorply	[0/90]	251x26x2.0	w/ stitching	Instron 8562
2441-15	E-LT-3900	Vectorply	[0/90]	253x25x2.0	w/ stitching	Instron 8562
2441-16	E-LT-3900	Vectorply	[0/90]	252x27x2.0	w/ stitching	Instron 8562
2441-17	E-LT-3900	Vectorply	[0/90]	248x26x2.0	w/ stitching	Instron 8562
2441-18	E-LT-3900	Vectorply	[0/90]	250x26x2.0	w/ stitching	Instron 8562

2441-19	E-LT-3900	Vectorply	[0/90]	252x26x2.0	w/ stitching	Instron 8562
2441-20	E-LT-3900	Vectorply	[0/90]	250x26x2.0	w/ stitching	Instron 8562
2441-21	E-LT-3900	Vectorply	[0/90]	253x26x2.0	w/ stitching	Instron 8562
2441-22	E-LT-3900	Vectorply	[0/90]	249x27x2.0	w/ stitching	Instron 8562
2441-23	E-LT-3900	Vectorply	[0/90]	250x26x2.0	w/ stitching	Instron 8562
2441-24	E-LT-3900	Vectorply	[0/90]	252x26x2.0	w/ stitching	Instron 8562
2441-25	E-LT-3900	Vectorply	[0/90]	251x25x2.0	w/ stitching	Instron 8562
2443-1	E-LT-3900	Vectorply	[0/90]	285x29x1.5	w/o stitching	Instron 8562
2443-2	E-LT-3900	Vectorply	[0/90]	287x29x1.3	w/o stitching	Instron 8562
2443-3	E-LT-3900	Vectorply	[0/90]	288x29x1.4	w/o stitching	Instron 8562
2443-4	E-LT-3900	Vectorply	[0/90]	287x29x1.4	w/o stitching	Instron 8562
2443-5	E-LT-3900	Vectorply	[0/90]	287x29x1.4	w/o stitching	Instron 8562
2443-6	E-LT-3900	Vectorply	[0/90]	287x29x1.4	w/o stitching	Instron 8562
2443-7	E-LT-3900	Vectorply	[0/90]	287x29x1.4	w/o stitching	Instron 8562
2443-8	E-LT-3900	Vectorply	[0/90]	286x28x1.4	w/o stitching	Instron 8562
2443-9	E-LT-3900	Vectorply	[0/90]	287x29x1.3	w/o stitching	Instron 8562
2443-10	E-LT-3900	Vectorply	[0/90]	286x29x1.5	w/o stitching	Instron 8562
2443-11	E-LT-3900	Vectorply	[0/90]	288x29x1.4	w/o stitching	Instron 8562
2443-12	E-LT-3900	Vectorply	[0/90]	287x28x1.4	w/o stitching	Instron 8562
2443-13	E-LT-3900	Vectorply	[0/90]	287x29x1.3	w/o stitching	Instron 8562
2443-14	E-LT-3900	Vectorply	[0/90]	287x29x1.4	w/o stitching	Instron 8562
2443-15	E-LT-3900	Vectorply	[0/90]	286x29x1.4	w/o stitching	Instron 8562

2443-16	E-LT-3900	Vectorply	[0/90]	287x28x1.4	w/o stitching	Instron 8562
2443-17	E-LT-3900	Vectorply	[0/90]	287x29x1.3	w/o stitching	Instron 8562
2443-18	E-LT-3900	Vectorply	[0/90]	287x29x1.5	w/o stitching	Instron 8562
2443-19	E-LT-3900	Vectorply	[0/90]	286x29x1.4	w/o stitching	Instron 8562
2443-20	E-LT-3900	Vectorply	[0/90]	285x29x1.4	w/o stitching	Instron 8562
2443-21	E-LT-3900	Vectorply	[0/90]	287x28x1.4	w/o stitching	Instron 8562
2443-22	E-LT-3900	Vectorply	[0/90]	287x29x1.4	w/o stitching	Instron 8562
2443-23	E-LT-3900	Vectorply	[0/90]	287x29x1.5	w/o stitching	Instron 8562
2443-24	E-LT-3900	Vectorply	[0/90]	286x29x1.4	w/o stitching	Instron 8562
2443-25	E-LT-3900	Vectorply	[0/90]	287x29x1.3	w/o stitching	Instron 8562
2446-1	L1200/G50	PPG-Devold LLC	[0/B_2/90]	285x26x1.9	N/A	Instron 5882
2446-2	L1200/G50	PPG-Devold LLC	[0/B_2/90]	283x26x1.9	N/A	Instron 5882
2446-3	L1200/G50	PPG-Devold LLC	[0/B_2/90]	284x26x1.9	N/A	Instron 5882
2446-4	L1200/G50	PPG-Devold LLC	[0/B_2/90]	287x26x2.0	N/A	Instron 5882
2446-5	L1200/G50	PPG-Devold LLC	[0/B_2/90]	287x26x2.0	N/A	Instron 5882
2446-6	L1200/G50	PPG-Devold LLC	[0/B_2/90]	285x26x1.9	N/A	Instron 5882
2446-7	L1200/G50	PPG-Devold LLC	[0/B_2/90]	284x26x1.9	N/A	Instron 5882
2446-8	L1200/G50	PPG-Devold LLC	[0/B_2/90]	285x26x1.9	N/A	Instron 5882

2446-9	L1200/G50	PPG-Devold LLC	[0/B_2/90]	281x26x1.9	N/A	Instron 5882
2446-10	L1200/G50	PPG-Devold LLC	[0/B_2/90]	284x26x1.9	N/A	Instron 5882
2446-11	L1200/G50	PPG-Devold LLC	[0/B_2/90]	285x26x1.9	N/A	Instron 5882
2446-12	L1200/G50	PPG-Devold LLC	[0/B_2/90]	281x26x1.9	N/A	Instron 5882
2446-13	L1200/G50	PPG-Devold LLC	[0/B_2/90]	285x26x1.9	N/A	Instron 5882
2446-14	L1200/G50	PPG-Devold LLC	[0/B_2/90]	287x26x2.0	N/A	Instron 5882
2446-15	L1200/G50	PPG-Devold LLC	[0/B_2/90]	284x25x2.0	N/A	Instron 5882
2446-16	L1200/G50	PPG-Devold LLC	[0/B_2/90]	288x26x1.8	N/A	Instron 5882
2446-17	L1200/G50	PPG-Devold LLC	[0/B_2/90]	283x26x2.0	N/A	Instron 5882
2446-18	L1200/G50	PPG-Devold LLC	[0/B_2/90]	285x26x1.8	N/A	Instron 5882
2446-19	L1200/G50	PPG-Devold LLC	[0/B_2/90]	286x26x1.9	N/A	Instron 5882
2446-20	L1200/G50	PPG-Devold LLC	[0/B_2/90]	283x26x1.9	N/A	Instron 5882
2446-21	L1200/G50	PPG-Devold LLC	[0/B_2/90]	286x26x1.9	N/A	Instron 8562
2446-22	L1200/G50	PPG-Devold LLC	[0/B_2/90]	286x26x2.0	N/A	Instron 8562

2446-23	L1200/G50	PPG-Devold LLC	[0/B_2/90]	286x26x1.9	N/A	Instron 8562
2446-24	L1200/G50	PPG-Devold LLC	[0/B_2/90]	283x25x1.9	N/A	Instron 8562
2446-25	L1200/G50	PPG-Devold LLC	[0/B_2/90]	285x26x1.8	N/A	Instron 8562
2446-26	L1200/G50	PPG-Devold LLC	[0/B_2/90]	281x25x1.9	N/A	Instron 8562
2446-27	L1200/G50	PPG-Devold LLC	[0/B_2/90]	286x26x1.9	N/A	Instron 8562
2446-28	L1200/G50	PPG-Devold LLC	[0/B_2/90]	286x26x1.9	N/A	Instron 8562
2446-29	L1200/G50	PPG-Devold LLC	[0/B_2/90]	284x26x1.9	N/A	Instron 8562
2446-30	L1200/G50	PPG-Devold LLC	[0/B_2/90]	285x26x1.8	N/A	Instron 8562
2449-1	L1200/G50	PPG-Devold LLC	[0/B]	274x27x1.1	N/A	Instron 5882
2449-2	L1200/G50	PPG-Devold LLC	[0/B]	274x27x1.1	N/A	Instron 5882
2449-3	L1200/G50	PPG-Devold LLC	[0/B]	275x27x1.0	N/A	Instron 5882
2449-4	L1200/G50	PPG-Devold LLC	[0/B]	276x27x1.0	N/A	Instron 5882
2449-5	L1200/G50	PPG-Devold LLC	[0/B]	276x27x1.1	N/A	Instron 5882
2449-6	L1200/G50	PPG-Devold LLC	[0/B]	276x27x1.0	N/A	Instron 5882

2449-7	L1200/G50	PPG-Devold LLC	[0/B]	276x27x1.0	N/A	Instron 5882
2449-8	L1200/G50	PPG-Devold LLC	[0/B]	275x27x1.1	N/A	Instron 5882
2449-9	L1200/G50	PPG-Devold LLC	[0/B]	275x27x1.1	N/A	Instron 5882
2449-10	L1200/G50	PPG-Devold LLC	[0/B]	275x27x1.0	N/A	Instron 5882
2449-11	L1200/G50	PPG-Devold LLC	[0/B]	274x27x1.0	N/A	Instron 5882
2449-12	L1200/G50	PPG-Devold LLC	[0/B]	275x27x1.0	N/A	Instron 5882
2449-13	L1200/G50	PPG-Devold LLC	[0/B]	274x27x1.1	N/A	Instron 5882
2449-14	L1200/G50	PPG-Devold LLC	[0/B]	275x27x1.1	N/A	Instron 5882
2449-15	L1200/G50	PPG-Devold LLC	[0/B]	274x27x1.0	N/A	Instron 5882
2449-16	L1200/G50	PPG-Devold LLC	[0/B]	276x27x1.1	N/A	Instron 5882
2449-17	L1200/G50	PPG-Devold LLC	[0/B]	276x27x1.0	N/A	Instron 5882
2449-18	L1200/G50	PPG-Devold LLC	[0/B]	276x27x1.1	N/A	Instron 5882
2449-19	L1200/G50	PPG-Devold LLC	[0/B]	275x27x1.1	N/A	Instron 5882
2449-20	L1200/G50	PPG-Devold LLC	[0/B]	275x27x1.0	N/A	Instron 5882

2449-21	L1200/G50	PPG-Devold LLC	[0/B]	276x27x1.1	N/A	Instron 8562
2449-22	L1200/G50	PPG-Devold LLC	[0/B]	276x27x1.1	N/A	Instron 8562
2449-23	L1200/G50	PPG-Devold LLC	[0/B]	276x27x1.1	N/A	Instron 8562
2449-24	L1200/G50	PPG-Devold LLC	[0/B]	274x27x1.1	N/A	Instron 8562
2449-25	L1200/G50	PPG-Devold LLC	[0/B]	276x27x1.1	N/A	Instron 8562
2450-1	L1200/G50	PPG-Devold LLC	[90/B]	283x29x1.0	N/A	Instron 5882
2450-2	L1200/G50	PPG-Devold LLC	[90/B]	282x29x0.9	N/A	Instron 5882
2450-3	L1200/G50	PPG-Devold LLC	[90/B]	283x29x1.0	N/A	Instron 5882
2450-4	L1200/G50	PPG-Devold LLC	[90/B]	276x29x0.9	N/A	Instron 5882
2450-5	L1200/G50	PPG-Devold LLC	[90/B]	281x29x0.9	N/A	Instron 5882
2450-6	L1200/G50	PPG-Devold LLC	[90/B]	283x29x1.0	N/A	Instron 5882
2450-7	L1200/G50	PPG-Devold LLC	[90/B]	282x29x1.0	N/A	Instron 5882
2450-8	L1200/G50	PPG-Devold LLC	[90/B]	281x29x0.9	N/A	Instron 5882
2450-9	L1200/G50	PPG-Devold LLC	[90/B]	282x29x0.9	N/A	Instron 5882

2450-10	L1200/G50	PPG-Devold LLC	[90/B]	280x29x1.0	N/A	Instron 5882
2450-11	L1200/G50	PPG-Devold LLC	[90/B]	283x29x1.0	N/A	Instron 5882
2450-12	L1200/G50	PPG-Devold LLC	[90/B]	284x29x1.0	N/A	Instron 5882
2450-13	L1200/G50	PPG-Devold LLC	[90/B]	280x29x0.9	N/A	Instron 5882
2450-14	L1200/G50	PPG-Devold LLC	[90/B]	279x29x1.0	N/A	Instron 5882
2450-15	L1200/G50	PPG-Devold LLC	[90/B]	284x29x1.0	N/A	Instron 5882
2450-16	L1200/G50	PPG-Devold LLC	[90/B]	280x29x0.9	N/A	Instron 5882
2450-17	L1200/G50	PPG-Devold LLC	[90/B]	277x29x0.9	N/A	Instron 5882
2450-18	L1200/G50	PPG-Devold LLC	[90/B]	281x29x1.0	N/A	Instron 5882
2450-19	L1200/G50	PPG-Devold LLC	[90/B]	277x29x1.0	N/A	Instron 5882
2450-20	L1200/G50	PPG-Devold LLC	[90/B]	279x29x1.0	N/A	Instron 5882
2450-21	L1200/G50	PPG-Devold LLC	[90/B]	279x29x0.9	N/A	Instron 8562
2450-22	L1200/G50	PPG-Devold LLC	[90/B]	277x29x0.9	N/A	Instron 8562
2450-23	L1200/G50	PPG-Devold LLC	[90/B]	281x29x1.0	N/A	Instron 8562

2450-24	L1200/G50	PPG-Devold LLC	[90/B]	281x29x0.9	N/A	Instron 8562
2450-25	L1200/G50	PPG-Devold LLC	[90/B]	281x29x1.0	N/A	Instron 8562
2451-1	E-LT-3900	Vectorply	[90]	272x28x1.5	w/ stitching	Instron 5882
2451-2	E-LT-3900	Vectorply	[90]	274x27x1.5	w/ stitching	Instron 5882
2451-3	E-LT-3900	Vectorply	[90]	272x27x1.4	w/ stitching	Instron 5882
2451-4	E-LT-3900	Vectorply	[90]	273x27x1.3	w/ stitching	Instron 5882
2451-5	E-LT-3900	Vectorply	[90]	273x27x1.4	w/ stitching	Instron 5882
2451-6	E-LT-3900	Vectorply	[90]	274x27x1.3	w/ stitching	Instron 5882
2451-7	E-LT-3900	Vectorply	[90]	273x28x1.4	w/ stitching	Instron 5882
2451-8	E-LT-3900	Vectorply	[90]	273x28x1.4	w/ stitching	Instron 5882
2451-9	E-LT-3900	Vectorply	[90]	272x28x1.3	w/ stitching	Instron 5882
2451-10	E-LT-3900	Vectorply	[90]	273x27x1.4	w/ stitching	Instron 5882
2451-11	E-LT-3900	Vectorply	[90]	273x27x1.3	w/ stitching	Instron 5882
2451-12	E-LT-3900	Vectorply	[90]	273x27x1.5	w/ stitching	Instron 5882
2451-13	E-LT-3900	Vectorply	[90]	274x28x1.4	w/ stitching	Instron 5882
2451-14	E-LT-3900	Vectorply	[90]	273x27x1.3	w/ stitching	Instron 5882
2451-15	E-LT-3900	Vectorply	[90]	272x28x1.4	w/ stitching	Instron 5882
2451-16	E-LT-3900	Vectorply	[90]	272x28x1.4	w/ stitching	Instron 5882
2451-17	E-LT-3900	Vectorply	[90]	272x27x1.5	w/ stitching	Instron 5882
2451-18	E-LT-3900	Vectorply	[90]	272x28x1.5	w/ stitching	Instron 5882
2451-19	E-LT-3900	Vectorply	[90]	274x28x1.5	w/ stitching	Instron 5882

2451-20	E-LT-3900	Vectorply	[90]	274x27x1.5	w/ stitching	Instron 5882
2451-21	E-LT-3900	Vectorply	[90]	274x28x1.5	w/ stitching	Instron 8562
2451-22	E-LT-3900	Vectorply	[90]	274x28x1.4	w/ stitching	Instron 8562
2451-23	E-LT-3900	Vectorply	[90]	273x27x1.4	w/ stitching	Instron 8562
2451-24	E-LT-3900	Vectorply	[90]	272x27x1.4	w/ stitching	Instron 8562
2451-25	E-LT-3900	Vectorply	[90]	274x27x1.5	w/ stitching	Instron 8562
2451-26	E-LT-3900	Vectorply	[90]	272x27x1.5	w/ stitching	Instron 8562
2451-27	E-LT-3900	Vectorply	[90]	273x28x1.4	w/ stitching	Instron 8562
2451-28	E-LT-3900	Vectorply	[90]	273x27x1.4	w/ stitching	Instron 8562
2451-29	E-LT-3900	Vectorply	[90]	272x28x1.4	w/ stitching	Instron 8562
2451-30	E-LT-3900	Vectorply	[90]	272x27x1.5	w/ stitching	Instron 8562
2452-1	E-LT-3900	Vectorply	[90]	272x27x1.1	w/o stitching	Instron 5882
2452-2	E-LT-3900	Vectorply	[90]	273x27x1.0	w/o stitching	Instron 5882
2452-3	E-LT-3900	Vectorply	[90]	273x28x1.2	w/o stitching	Instron 5882
2452-4	E-LT-3900	Vectorply	[90]	273x27x1.2	w/o stitching	Instron 5882
2452-5	E-LT-3900	Vectorply	[90]	272x27x1.2	w/o stitching	Instron 5882
2452-6	E-LT-3900	Vectorply	[90]	271x27x1.3	w/o stitching	Instron 5882
2452-7	E-LT-3900	Vectorply	[90]	272x28x1.3	w/o stitching	Instron 5882
2452-8	E-LT-3900	Vectorply	[90]	271x28x1.3	w/o stitching	Instron 5882
2452-9	E-LT-3900	Vectorply	[90]	271x28x1.2	w/o stitching	Instron 5882
2452-10	E-LT-3900	Vectorply	[90]	270x27x1.3	w/o stitching	Instron 5882
2452-11	E-LT-3900	Vectorply	[90]	272x28x1.2	w/o stitching	Instron 5882

2452-12	E-LT-3900	Vectorply	[90]	273x28x1.0	w/o stitching	Instron 5882
2452-13	E-LT-3900	Vectorply	[90]	271x27x1.1	w/o stitching	Instron 5882
2452-14	E-LT-3900	Vectorply	[90]	271x27x1.3	w/o stitching	Instron 5882
2452-15	E-LT-3900	Vectorply	[90]	272x27x1.0	w/o stitching	Instron 5882
2452-16	E-LT-3900	Vectorply	[90]	272x28x1.1	w/o stitching	Instron 5882
2452-17	E-LT-3900	Vectorply	[90]	270x27x1.2	w/o stitching	Instron 5882
2452-18	E-LT-3900	Vectorply	[90]	272x27x1.2	w/o stitching	Instron 5882
2452-19	E-LT-3900	Vectorply	[90]	272x28x1.1	w/o stitching	Instron 5882
2452-20	E-LT-3900	Vectorply	[90]	272x27x1.3	w/o stitching	Instron 5882
2452-21	E-LT-3900	Vectorply	[90]	271x27x1.2	w/o stitching	Instron 8562
2452-22	E-LT-3900	Vectorply	[90]	271x27x1.3	w/o stitching	Instron 8562
2452-23	E-LT-3900	Vectorply	[90]	270x27x1.2	w/o stitching	Instron 8562
2452-24	E-LT-3900	Vectorply	[90]	270x27x1.3	w/o stitching	Instron 8562
2452-25	E-LT-3900	Vectorply	[90]	271x27x1.3	w/o stitching	Instron 8562
2452-26	E-LT-3900	Vectorply	[90]	272x27x1.2	w/o stitching	Instron 8562
2452-27	E-LT-3900	Vectorply	[90]	270x28x1.3	w/o stitching	Instron 8562
2452-28	E-LT-3900	Vectorply	[90]	270x27x1.2	w/o stitching	Instron 8562
2452-29	E-LT-3900	Vectorply	[90]	272x27x1.3	w/o stitching	Instron 8562
2452-30	E-LT-3900	Vectorply	[90]	270x26x1.3	w/o stitching	Instron 8562

APPENDIX B

MANUFACTURING AND MATERIAL INFO

Laminate Global Number	2434
Laminate Project Descript	Prepreg Epoxy/Glass Plate 1
Technician:	Daniel Samborsky
Date:	5/28/2015
Layup (top to bottom):	[0/90/90/0]
Fabric Type #1:	NCT307-D1-E300
Fabric Type #2:	
Fabric Type #3:	
Resin System:	
Resin Quantity; ml, g:	
Process:	Prepreg
Vacuum Pressure (V.P.):	
Peel Ply (P.P.):	
Flow Media (F.M.):	
Initial Cure Temperature:	
Post Cure Temp:	
Plate Size:	20in x 10in
Mix and Degas:	
Caul Plate:	No
Notes:	Manufactured March of 2006. Recently taken out of storage to be tested, produced using methods recommended by Gurit.

Laminate Global Number	2435
Laminate Project Descript	Prepreg Epoxy/Glass Plate 2
Technician:	Daniel Samborsky
Date:	5/28/2015
Layup (top to bottom):	[0/90/90/90/90/0]
Fabric Type #1:	NCT307-D1-E300
Fabric Type #2:	
Fabric Type #3:	
Resin System:	
Resin Quantity; ml, g:	
Process:	Prepreg
Vacuum Pressure (V.P.):	
Peel Ply (P.P.):	
Flow Media (F.M.):	
Initial Cure Temperature:	
Post Cure Temp:	
Plate Size:	20in x 10in
Mix and Degas:	
Caul Plate:	No
Notes:	Manufactured March of 2006. Recently taken out of storage to be tested, produced using methods recommended by Gurit.

Laminate Global Number	2439
Laminate Project Descript	UD Test Plate w/o Stitching
Technician:	Austin Lolatte
Date:	7/21/2015
Layup (top to bottom):	[0]
Fabric Type #1:	Vectorply E-LT-3900
Fabric Type #2:	
Fabric Type #3:	
Resin System:	Hexion Epikote MGS® RIMR 135, RIMH 1366
Resin Quantity; ml, g:	Totals: 531.38ml/ 582.78g Part A: 389.82ml/ 448.29g Part B: 141.57ml/ 134.49g
Process:	Vacuum Bag
Vacuum Pressure (V.P.):	25.2
Peel Ply (P.P.):	Airtech Release Ply Super F (Polyester)
Flow Media (F.M.):	Airtech Greenflow 75
Initial Cure Temperature:	25°C (77°F) -- 48 hrs
Post Cure Temp:	70°C (158°F) -- 12 hrs -- Oven
Plate Size:	15in x 10in
Mix and Degas:	Mixed for 10 min @ 220 RPM
Caul Plate:	No
Notes:	Stitching has been removed.

Laminate Global Number	2440
Laminate Project Descript	UD Test Plate w/ Stitching
Technician:	Austin Lolatte
Date:	7/29/2015
Layup (top to bottom):	[0]
Fabric Type #1:	Vectorply E-LT-3900
Fabric Type #2:	
Fabric Type #3:	
Resin System:	Hexion Epikote MGS® RIMR 135, RIMH 1366
Resin Quantity; ml, g:	Totals: 531.38ml/ 582.78g Part A: 389.82ml/ 448.29g Part B: 141.57ml/ 134.49g
Process:	Vacuum Bag
Vacuum Pressure (V.P.):	25.2
Peel Ply (P.P.):	Airtech Release Ply Super F (Polyester)
Flow Media (F.M.):	Airtech Greenflow 75
Initial Cure Temperature:	25°C (77°F) -- 48 hrs
Post Cure Temp:	70°C (158°F) -- 12 hrs -- Oven
Plate Size:	15in x 10in
Mix and Degas:	Mixed for 10 min @ 220 RPM
Caul Plate:	No
Notes:	

Laminate Global Number	2441
Laminate Project Descript	2-Ply Test Plate w/ Stitching
Technician:	Austin Lolatte
Date:	8/5/2015
Layup (top to bottom):	[0/90]
Fabric Type #1:	Vectorply E-LT-3900
Fabric Type #2:	
Fabric Type #3:	
Resin System:	Hexion Epikote MGS® RIMR 135, RIMH 1366
Resin Quantity; ml, g:	Totals: 586.34ml/ 643.05g Part A: 430.13ml/ 494.65g Part B: 156.21ml/ 148.4g
Process:	Vacuum Bag
Vacuum Pressure (V.P.):	25.2
Peel Ply (P.P.):	Airtech Release Ply Super F (Polyester)
Flow Media (F.M.):	Airtech Greenflow 75
Initial Cure Temperature:	25°C (77°F) -- 48 hrs
Post Cure Temp:	70°C (158°F) -- 12 hrs -- Oven
Plate Size:	15in x 10in
Mix and Degas:	Mixed for 10 min @ 220 RPM
Caul Plate:	No
Notes:	

Laminate Global Number	2443
Laminate Project Descript	2-Ply w/o Stitching
Technician:	Austin Lolatte
Date:	8/27/2015
Layup (top to bottom):	[0/90]
Fabric Type #1:	Vectorply E-LT-3900
Fabric Type #2:	
Fabric Type #3:	
Resin System:	Hexion Epikote MGS® RIMR 135, RIMH 1366
Resin Quantity; ml, g:	Totals: 586.34ml/ 643.05g Part A: 430.13ml/ 494.65g Part B: 156.21ml/ 148.4g
Process:	Vacuum Bag
Vacuum Pressure (V.P.):	25.2
Peel Ply (P.P.):	Airtech Release Ply Super F (Polyester)
Flow Media (F.M.):	Airtech Greenflow 75
Initial Cure Temperature:	25°C (77°F) -- 48 hrs
Post Cure Temp:	70°C (158°F) -- 12 hrs -- Oven
Plate Size:	15in x 10in
Mix and Degas:	Mixed for 10 min @ 220 RPM
Caul Plate:	No
Notes:	Stitching has been removed.

Laminate Global Number	2446
Laminate Project Descript	2-Ply PPG Random Strand Mat Plate
Technician:	Austin Lolatte
Date:	11/29/2015
Layup (top to bottom):	[(0/B)/(B/90)]
Fabric Type #1:	PPG 1250 UD 2026
Fabric Type #2:	
Fabric Type #3:	
Resin System:	Hexion Epikote MGS® RIMR 135, RIMH 1366
Resin Quantity; ml, g:	Totals: 933.64ml/ 1023.94g Part A: 684.91ml/ 787.64g Part B: 248.73ml/ 236.29g
Process:	Vacuum Bag
Vacuum Pressure (V.P.):	25.2
Peel Ply (P.P.):	Airtech Release Ply Super F (Polyester)
Flow Media (F.M.):	Airtech Greenflow 75
Initial Cure Temperature:	25°C (77°F) -- 48 hrs
Post Cure Temp:	60°C (140°F) -- 12 hrs -- Oven
Plate Size:	24in x 20in
Mix and Degas:	Mixed for 10 min @ 220 RPM; degassed for 10 min @ 25.2 in Hg
Caul Plate:	No
Notes:	

Laminate Global Number	2446
Laminate Project Descript	2-Ply PPG Random Strand Mat Plate
Technician:	Austin Lolatte
Date:	11/29/2015
Layup (top to bottom):	[(0/B)/(B/90)]
Fabric Type #1:	PPG 1250 UD 2026
Fabric Type #2:	
Fabric Type #3:	
Resin System:	Hexion Epikote MGS® RIMR 135, RIMH 1366
Resin Quantity; ml, g:	Totals: 933.64ml/ 1023.94g Part A: 684.91ml/ 787.64g Part B: 248.73ml/ 236.29g
Process:	Vacuum Bag
Vacuum Pressure (V.P.):	25.2
Peel Ply (P.P.):	Airtech Release Ply Super F (Polyester)
Flow Media (F.M.):	Airtech Greenflow 75
Initial Cure Temperature:	25°C (77°F) -- 48 hrs
Post Cure Temp:	60°C (140°F) -- 12 hrs -- Oven
Plate Size:	24in x 20in
Mix and Degas:	Mixed for 10 min @ 220 RPM; degassed for 10 min @ 25.2 in Hg
Caul Plate:	No
Notes:	

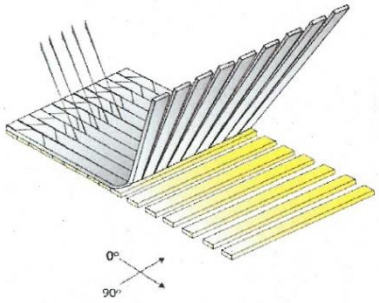
Laminate Global Number	2449
Laminate Project Descript	1-Ply PPG UD Plate
Technician:	Austin Lolatte
Date:	12/7/2015
Layup (top to bottom):	[(0/B)]
Fabric Type #1:	PPG 1250 UD 2002
Fabric Type #2:	
Fabric Type #3:	
Resin System:	Hexion Epikote MGS® RIMR 135, RIMH 1366
Resin Quantity; ml, g:	Totals: 834.13ml/ 914.8g Part A: 611.91ml/ 703.69g Part B: 222.22ml/ 211.11g
Process:	Vacuum Bag
Vacuum Pressure (V.P.):	25.2
Peel Ply (P.P.):	Airtech Release Ply Super F (Polyester)
Flow Media (F.M.):	Airtech Greenflow 75
Initial Cure Temperature:	25°C (77°F) -- 48 hrs
Post Cure Temp:	60°C (140°F) -- 12 hrs -- Oven
Plate Size:	24in x 20in
Mix and Degas:	Mixed for 10 min @ 220 RPM; degassed for 10 min @ 25.2 in Hg
Caul Plate:	No
Notes:	

Laminate Global Number	2450
Laminate Project Descript	Single Ply PPG Transverse UD Plate
Technician:	Austin Lolatte
Date:	12/27/2015
Layup (top to bottom):	[(90/B)]
Fabric Type #1:	PPG 1250 UD 2026
Fabric Type #2:	
Fabric Type #3:	
Resin System:	Hexion Epikote MGS® RIMR 135, RIMH 1366
Resin Quantity; ml, g:	Totals: 815.37ml/ 894.23g Part A: 598.14ml/ 687.87g Part B: 217.22ml/ 206.36g
Process:	Vacuum Bag
Vacuum Pressure (V.P.):	25.2
Peel Ply (P.P.):	Airtech Release Ply Super F (Polyester)
Flow Media (F.M.):	Airtech Greenflow 75
Initial Cure Temperature:	25°C (77°F) -- 48 hrs
Post Cure Temp:	60°C (140°F) -- 12 hrs -- Oven
Plate Size:	24in x 20in
Mix and Degas:	Mixed for 10 min @ 220 RPM; degassed for 10 min @ 25.2 in Hg
Caul Plate:	No
Notes:	

Laminate Global Number	2451
Laminate Project Descript	Single Ply UD 90 Plate w/ Stitching
Technician:	Austin Lolatte
Date:	12/29/2015
Layup (top to bottom):	[90]
Fabric Type #1:	Vectorply E-LT-3900
Fabric Type #2:	
Fabric Type #3:	
Resin System:	Hexion Epikote MGS® RIMR 135, RIMH 1366
Resin Quantity; ml, g:	Totals: 872.95ml/ 957.38g Part A: 640.39ml/ 736.45g Part B: 232.56ml/ 220.93g
Process:	Vacuum Bag
Vacuum Pressure (V.P.):	25.2
Peel Ply (P.P.):	Airtech Release Ply Super F (Polyester)
Flow Media (F.M.):	Airtech Greenflow 75
Initial Cure Temperature:	25°C (77°F) -- 48 hrs
Post Cure Temp:	70°C (158°F) -- 12 hrs -- Oven
Plate Size:	24in x 20in
Mix and Degas:	Mixed for 10 min @ 220 RPM
Caul Plate:	No
Notes:	

Laminate Global Number	2452
Laminate Project Descript	Sinlge Ply UD 90 Plate w/o Stitching
Technician:	Austin Lolatte
Date:	12/29/2015
Layup (top to bottom):	[90]
Fabric Type #1:	Vectorply E-LT-3900
Fabric Type #2:	
Fabric Type #3:	
Resin System:	Hexion Epikote MGS® RIMR 135, RIMH 1366
Resin Quantity; ml, g:	Totals: 997.16ml/ 1093.61g Part A: 731.51ml/ 841.23g Part B: 265.65ml/ 252.37g
Process:	Vacuum Bag
Vacuum Pressure (V.P.):	25.2
Peel Ply (P.P.):	Airtech Release Ply Super F (Polyester)
Flow Media (F.M.):	Airtech Greenflow 75
Initial Cure Temperature:	25°C (77°F) -- 48 hrs
Post Cure Temp:	70°C (158°F) -- 12 hrs -- Oven
Plate Size:	30in x 20in
Mix and Degas:	Mixed for 10 min @ 220 RPM
Caul Plate:	No
Notes:	Stiching removed.

VECTORPLY®
Performance Composite Reinforcements



E-LT 3900

Fiber Type: E-Glass
Architecture: 0º/90º Biaxial
Dry Thickness: 0.042 in. / 1.07 mm
Total Weight: 39.70 oz/sq.yd / 1346 g/sq.m

Layer Number	Fiber Type	Fiber Orientation	Linear Density	Fiber Diameter	Sizing	Ends per Inch	Areal Wt.	
			Yield	µm	Weight		oz/yd²	g/m²
1*	E-Glass	0 Degree	113	24	0.55%	7.00	35.68	1210
2**	E-Glass	90 Degree	1800	13	0.55%	10.50	3.36	114
Stitch Yarn	Stitch Type		Fiber Type		Gauge	Fiber Areal Weight:	39.04	1324
	Mod. Tricot 1-0/0-1/2-1/1-2		100% Polyester		7 per inch	Fabric Areal Weight:	39.70	1346

* PPG Hybon 2026
**PPG Hybon 2022 or Hybon 2026

Vectorply Corporation
3500 Lakewood Drive Phenix City, AL 36867
tel. 334-291-7704 fax. 334-291-7743

NEWPORT
ADHESIVES AND COMPOSITES, INC.
A subsidiary of MITSUBISHI RAYON CO., LTD.

CUSTOMER: [redacted]
PRODUCT: NCT307-D1 E300 1M 36+/-2%
NAC/PART # 801710
BATCH#: **23909**
SOR#: **37262**
MFG DATE: 04/15/2005

SPECIFICATIONS:
FAW: 300+/-5
RC%: 36+/-2%
WIDTH(IN): 39.37

*(Not Certified, for Reference Only)

ROLL#	OAD(G/SQ.M)	AFD(G/SQ.M)	RC(%)	Gross wt	NET WT(LBS)	Total YARDS*	Net YARDS*	Allowance Yards
1	480	300	37.5	100.1	82.4	85.0	85.0	-
2	468	300	35.9	100.8	83.1	85.0	85.0	-

$(0)_4$	Ply Properties, Single ply =0.26 mm thick			
	V_F	E_L	E_T	G
		GPa	GPa	GPa
Avg.	0.47	35.5	8.33	8.55
S.D.		1.11	0.34	0.18
	Longitudinal direction			
	UTS_L	$E_L$max	UCS_L	$E_L$min
	MPa	%	MPa	%
Avg.	1005	2.83	-788	-2.22
S.D.	37.3	0.11	11	0.03
$(0)_{11}$	Transverse direction			
	UTS_T	$E_T$max	UCS_T	$E_T$min
	MPa	%	MPa	%
Avg.	51.2	0.739	-168	-2.02
S.D.	2.59	0.03	2.52	0.03
Shear Strength				
	MPa			
Avg.	112			
S.D.	1.53			

Oven cure – 0.83 °C/minute ramp to 121 °C, hold for 3 hours

MSU Database Properties

SPECIFICATION

Product: L 1200/G50-E07

Rev.data:

Layers

Layer	Material 1								Area Weight [g/m²]
	Tex	Material Type							
0°	2400	E-Glass							1152
90°	200	E-Glass							52
CS	2400	E-Glass							50
Stitch	7.6	Polyester/							7

Nominal area weight:	1251
Theoretical width [mm]:	3280 mm
Average area weight:	1250

Resin Compatibility *
UP, EP, VE

Processing and Controll

Binding/ Stitch Information	
Stitch type:	Tricot
Stitch length:	5mm / Stitch
Space between needles:	3.57mm
Pilot yarn colour:	Violet

Quality Assurance / Test		
Weight:	ISO 4605	
Loss of ignition:	ISO 1887	
Moisture content:	ISO 3344	

Logistics

Roll length:	180m
Roll width:	Various widths
Roll weight:	
Roll direction:	Matt facing roll
Max fringe length:	- 10mm

Tube size:	76mm
Pallet size:	120x130
Rolls per pallet:	
Stacking:	Pyramide

Devold AMT Acceptance Criteria

1. Area weight should be within ±3% of average value
2. Fibre orientation should be within ±2° of nominal value
3. There should be no dirt or oil spots
4. Gap wider than 5mm will be considered as a defect (measured 90° on roving)
5. No damage on outer roving or stitch yarn due to cutting edges

** UP:Polyester; EP: Epoxy; VE: Vinylester; ac: Anhydride cure*

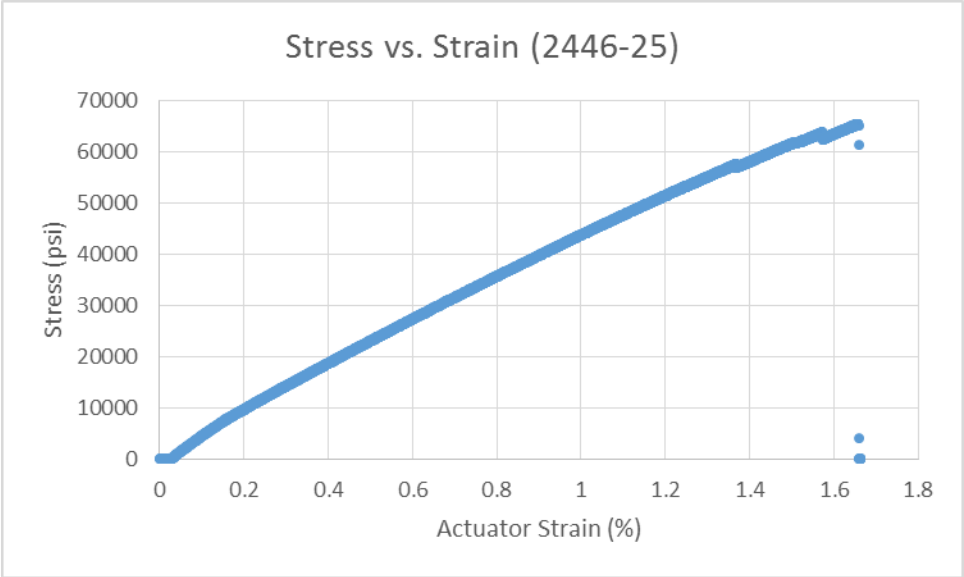
*** CpE: Counts per ends, yarns/cm*

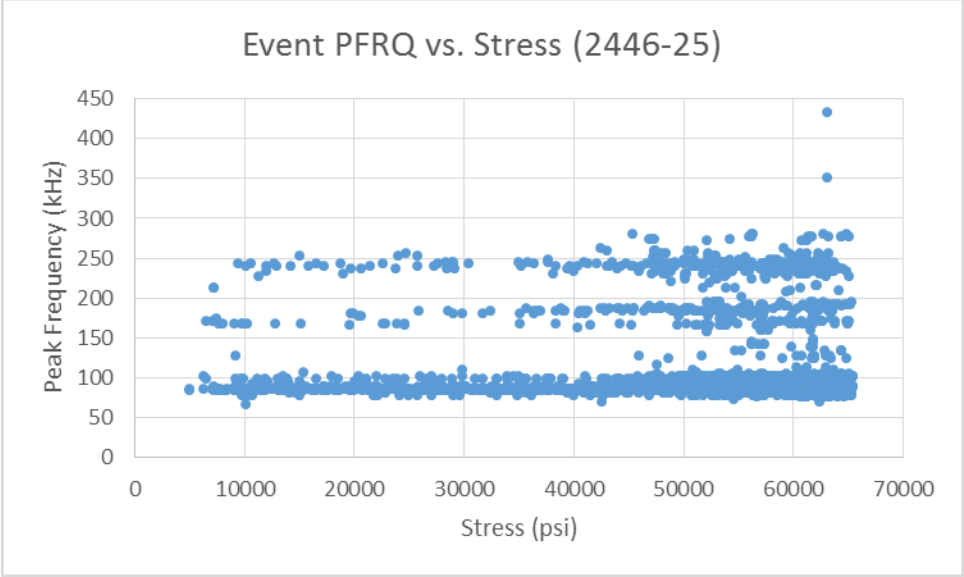
Comment
0° kjglk 90° ±45°

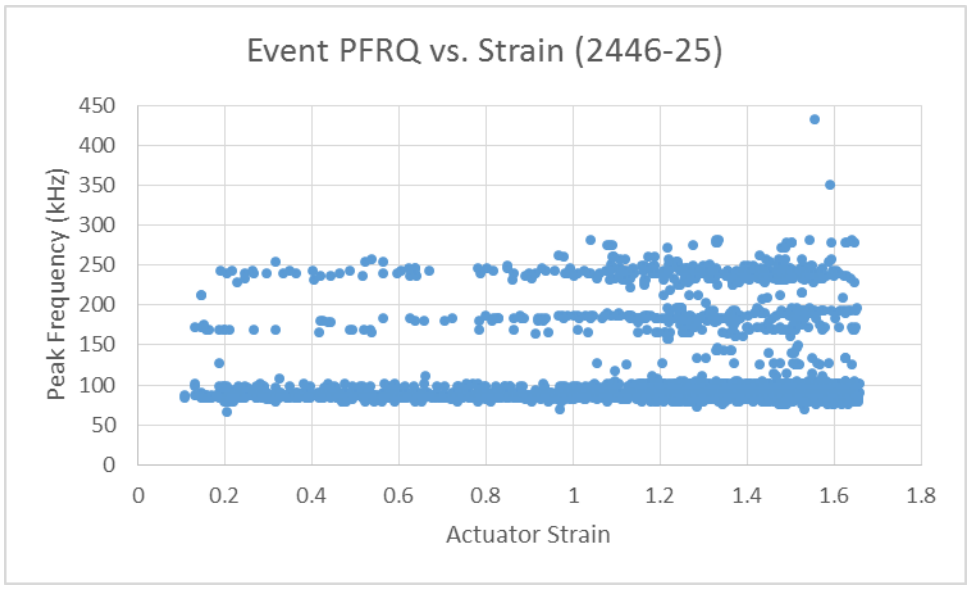
APPENDIX C

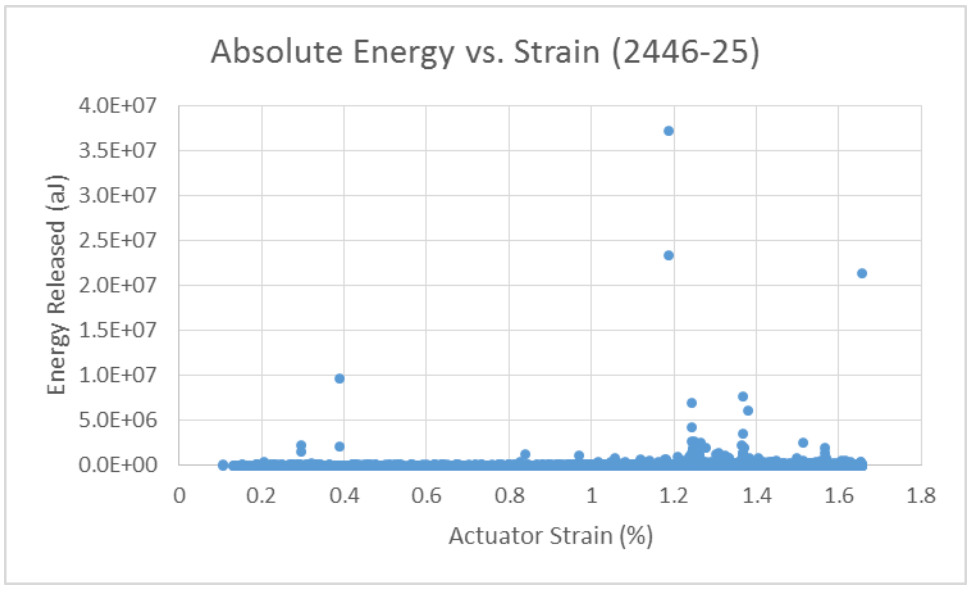
COUPON TEST DATA

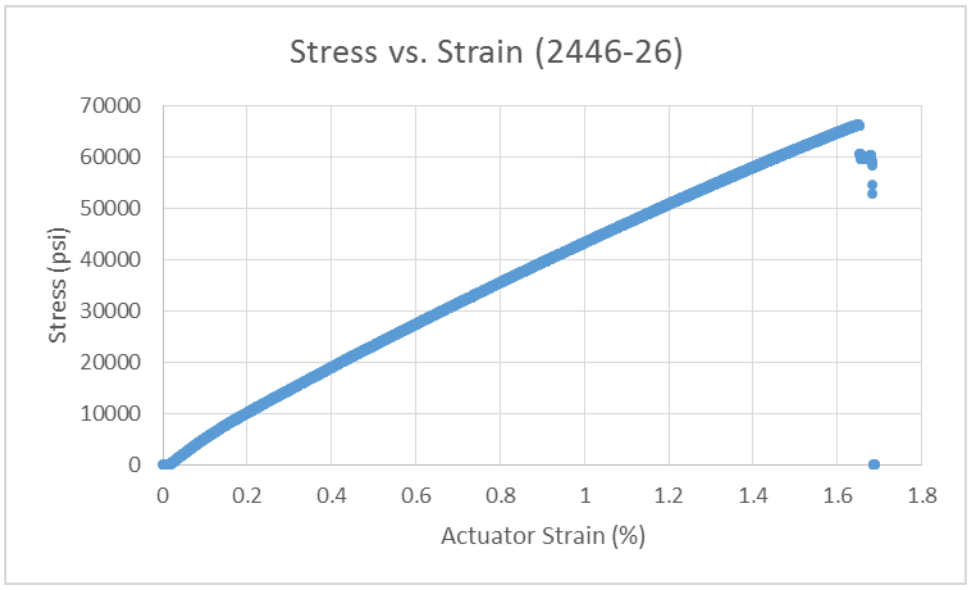
GLASS- C3

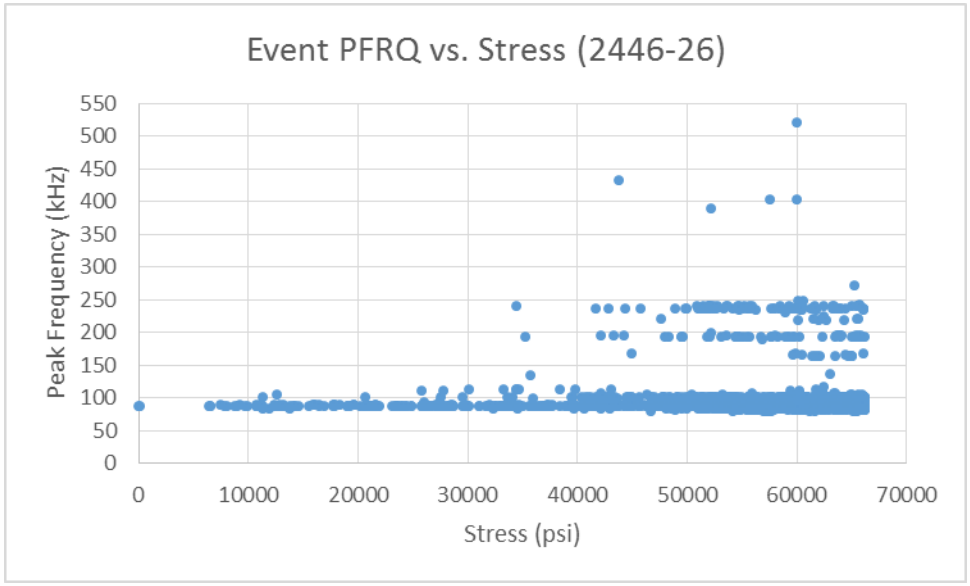

Stress vs. Strain (2446-25)
Stress (psi)
70000
60000
50000
40000
30000
20000
10000
0
0
0.2
0.4
0.6
0.8
1
1.2
1.4
1.6
1.8
Actuator Strain (%)

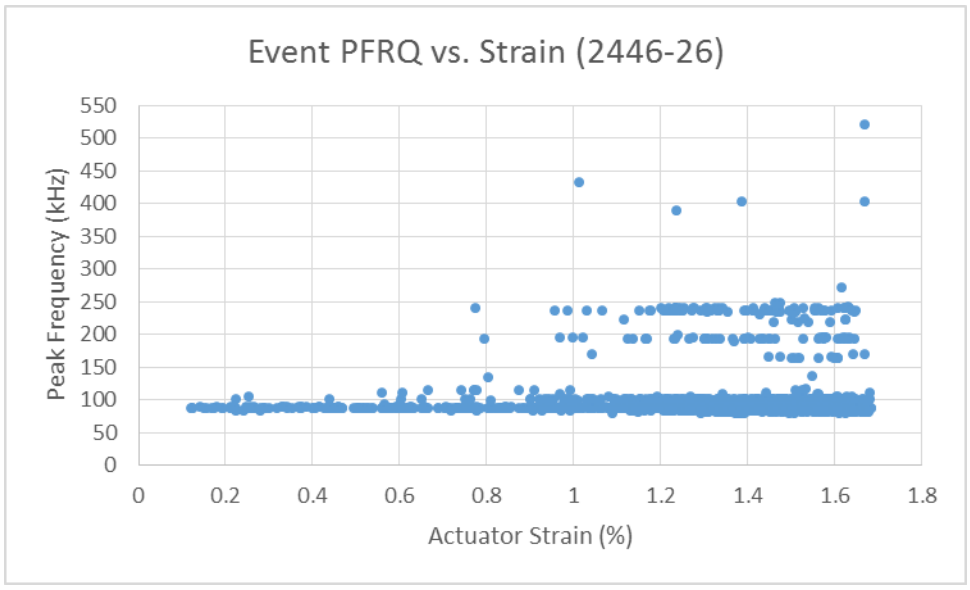

Event PFRQ vs. Stress (2446-25)
Peak Frequency (kHz)
450
400
350
300
250
200
150
100
50
0
0
10000
20000
30000
40000
50000
60000
70000
Stress (psi)

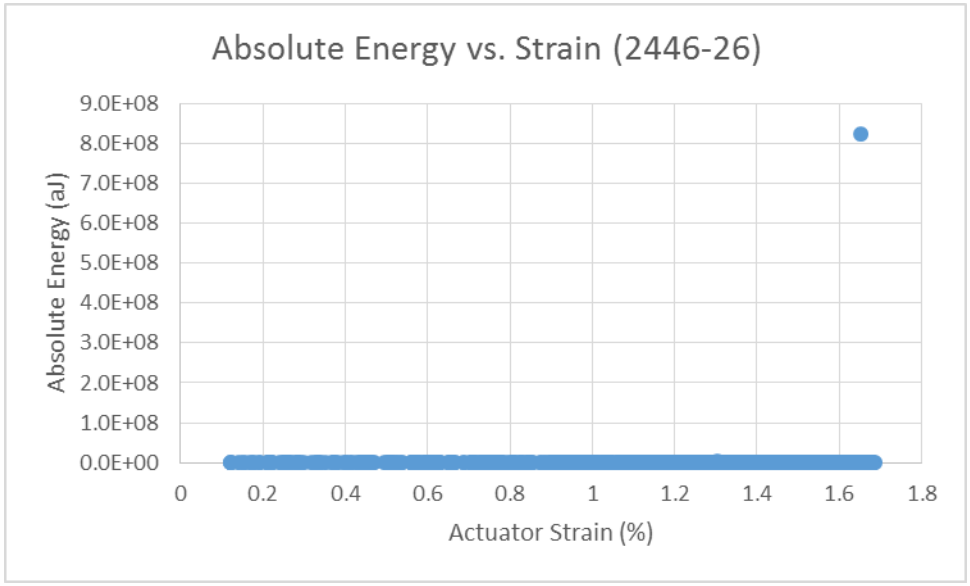

Event PFRQ vs. Strain (2446-25)
Peak Frequency (kHz)
450
400
350
300
250
200
150
100
50
0
0
0.2
0.4
0.6
0.8
1
1.2
1.4
1.6
1.8
Actuator Strain

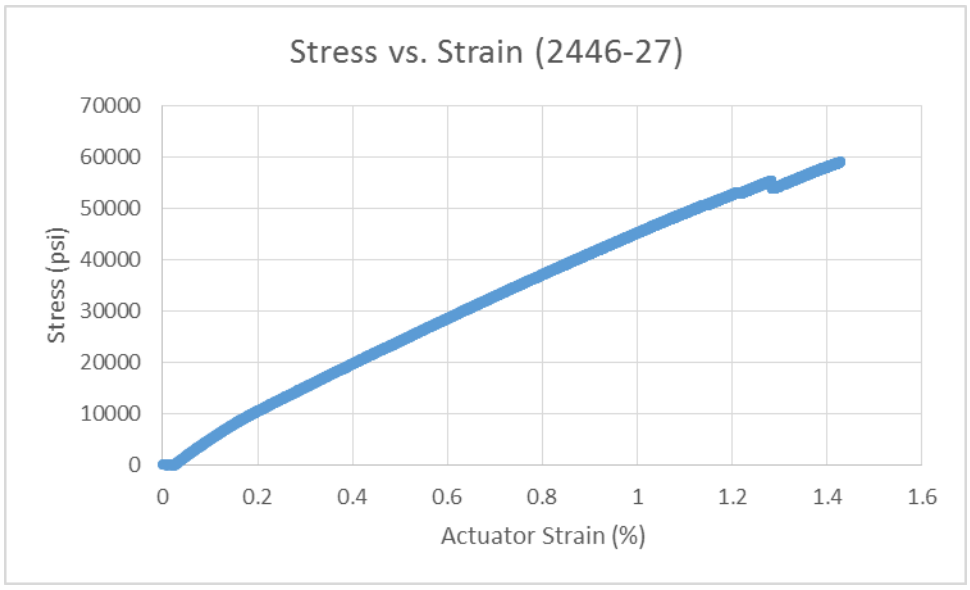

Absolute Energy vs. Strain (2446-25)
Energy Released (aJ)
4.0E+07
3.5E+07
3.0E+07
2.5E+07
2.0E+07
1.5E+07
1.0E+07
5.0E+06
0.0E+00
0
0.2
0.4
0.6
0.8
1
1.2
1.4
1.6
1.8
Actuator Strain (%)

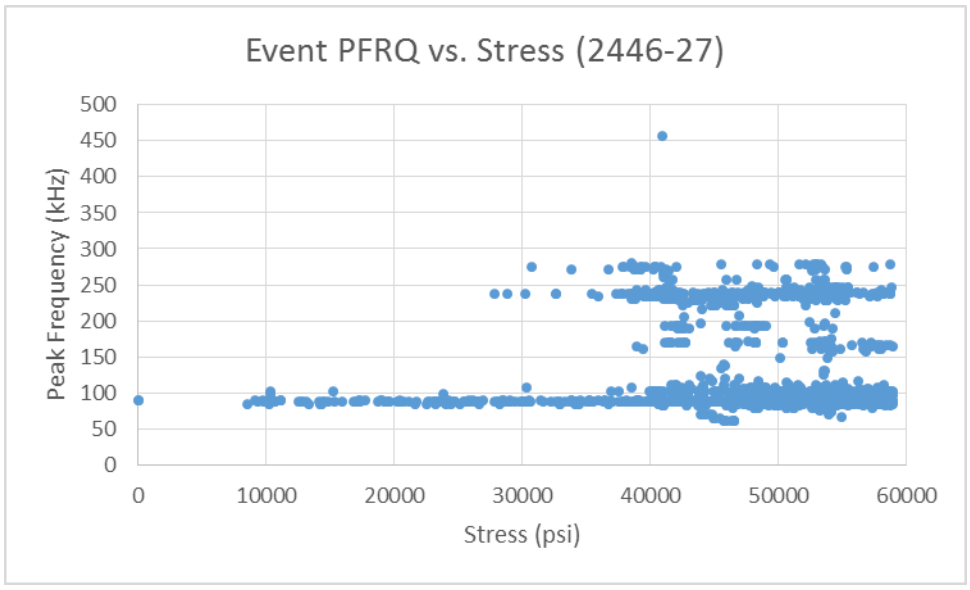

Stress vs. Strain (2446-26)
Stress (psi)
70000
60000
50000
40000
30000
20000
10000
0
0
0.2
0.4
0.6
0.8
1
1.2
1.4
1.6
1.8
Actuator Strain (%)

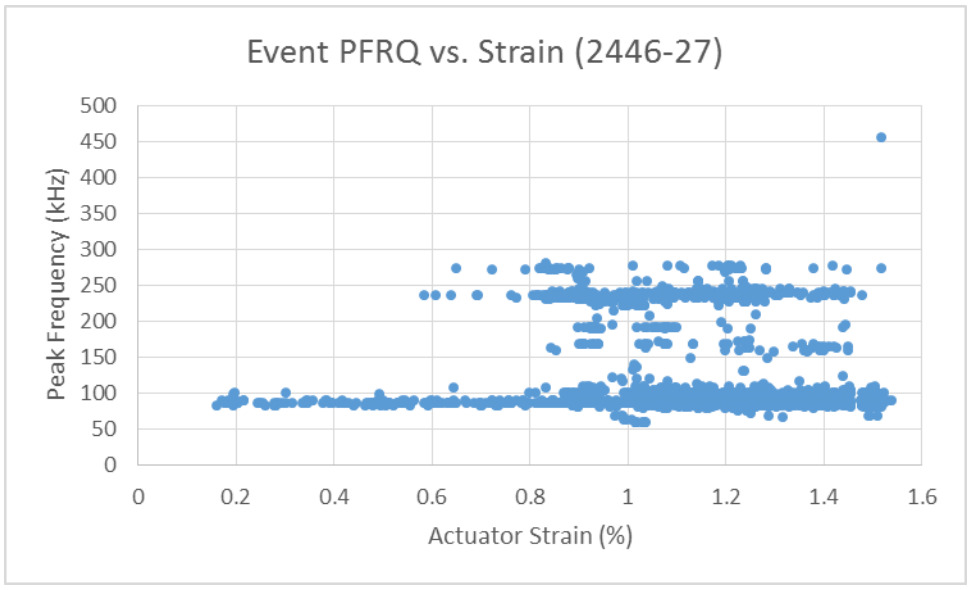

Event PFRQ vs. Stress (2446-26)
Peak Frequency (kHz)
550
500
450
400
350
300
250
200
150
100
50
0
0
10000
20000
30000
40000
50000
60000
70000
Stress (psi)

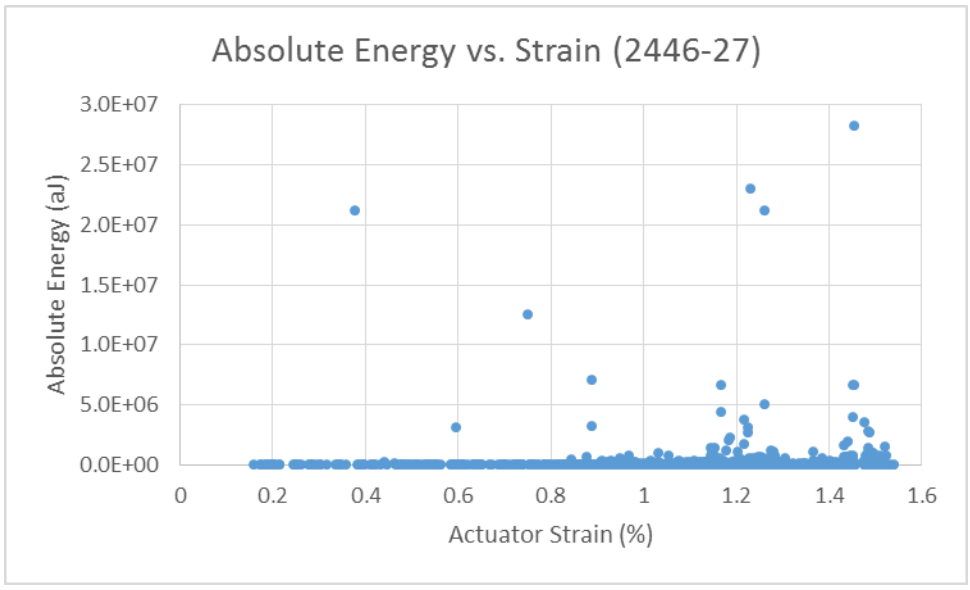

Event PFRQ vs. Strain (2446-26)
Peak Frequency (kHz)
550
500
450
400
350
300
250
200
150
100
50
0
0
0.2
0.4
0.6
0.8
1
1.2
1.4
1.6
1.8
Actuator Strain (%)

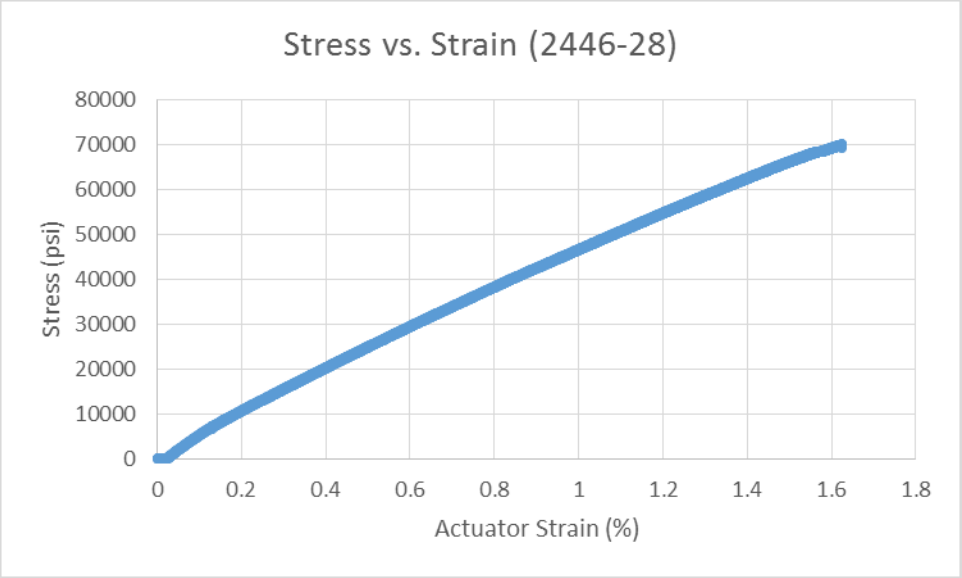

Absolute Energy vs. Strain (2446-26)
Absolute Energy (aJ)
9.0E+08
8.0E+08
7.0E+08
6.0E+08
5.0E+08
4.0E+08
3.0E+08
2.0E+08
1.0E+08
0.0E+00
0
0.2
0.4
0.6
0.8
1
1.2
1.4
1.6
1.8
Actuator Strain (%)

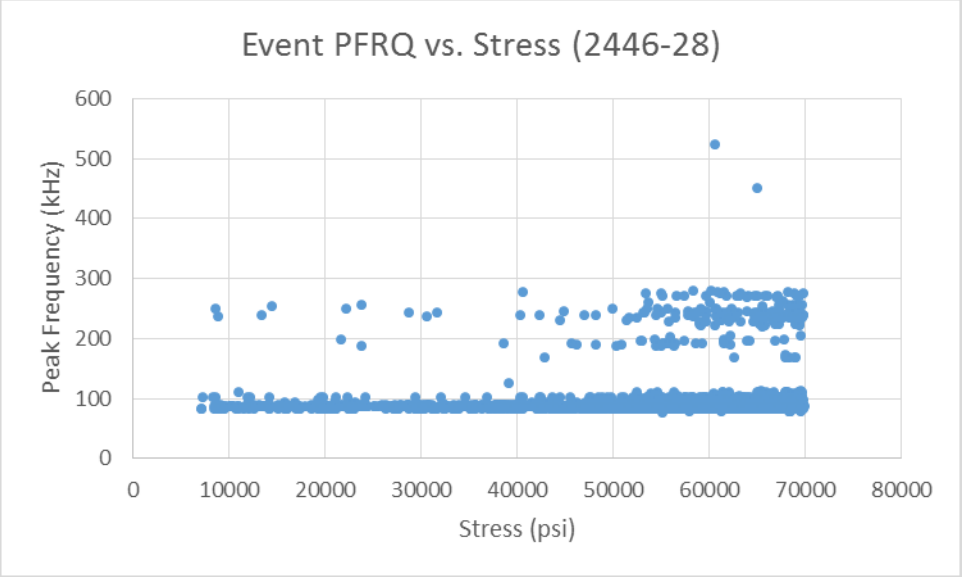

Stress vs. Strain (2446-27)
Stress (psi)
70000
60000
50000
40000
30000
20000
10000
0
0
0.2
0.4
0.6
0.8
1
1.2
1.4
1.6
Actuator Strain (%)

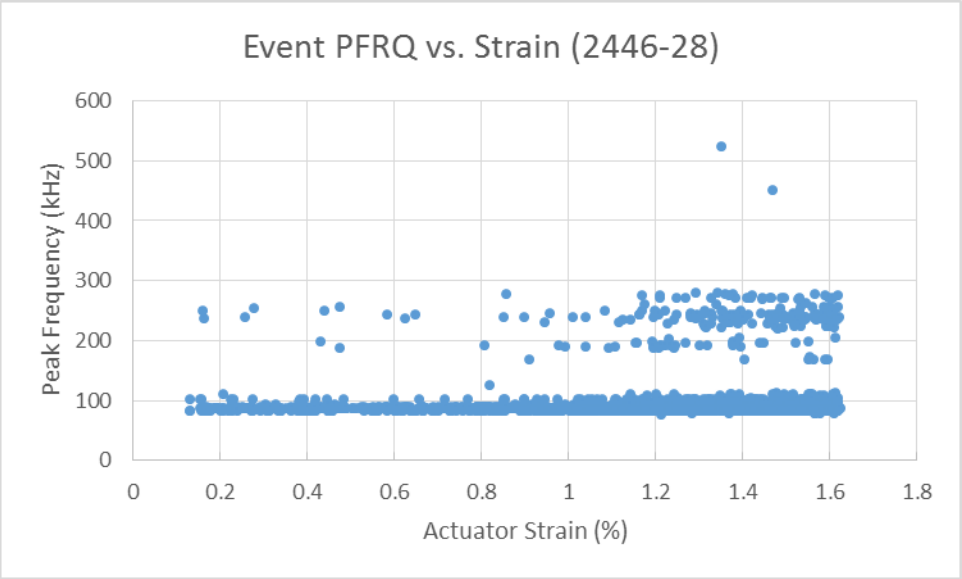

Event PFRQ vs. Stress (2446-27)
Peak Frequency (kHz)
500
450
400
350
300
250
200
150
100
50
0
0
10000
20000
30000
40000
50000
60000
Stress (psi)

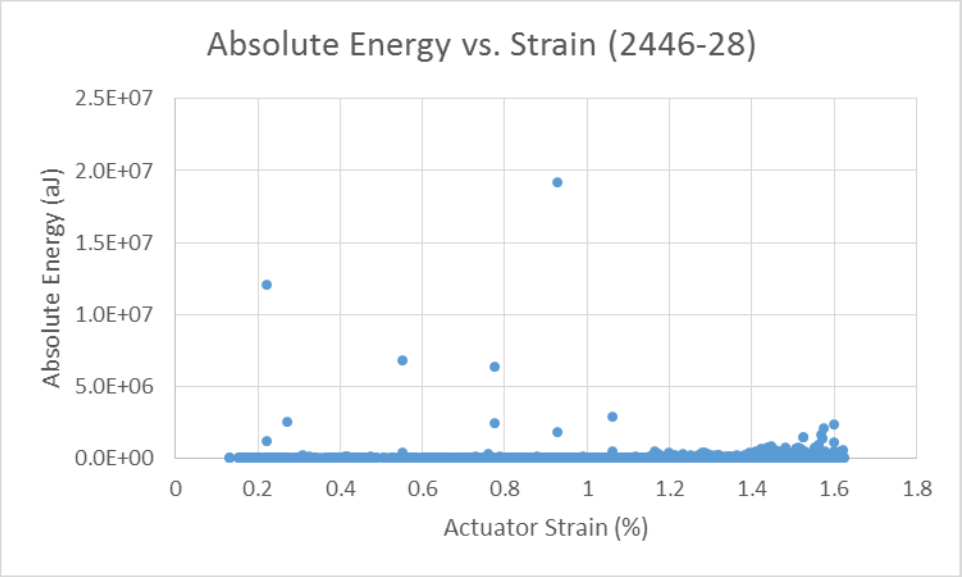

Event PFRQ vs. Strain (2446-27)
Peak Frequency (kHz)
500
450
400
350
300
250
200
150
100
50
0
0
0.2
0.4
0.6
0.8
1
1.2
1.4
1.6
Actuator Strain (%)


Absolute Energy vs. Strain (2446-27)
Absolute Energy (aJ)
3.0E+07
2.5E+07
2.0E+07
1.5E+07
1.0E+07
5.0E+06
0.0E+00
0
0.2
0.4
0.6
0.8
1
1.2
1.4
1.6
Actuator Strain (%)

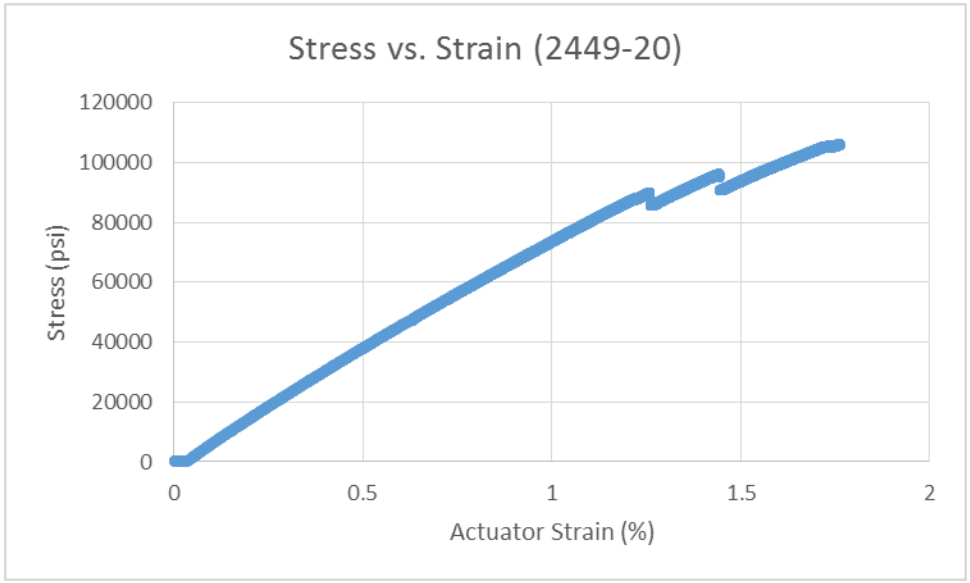

Stress vs. Strain (2446-28)
Stress (psi)
80000
70000
60000
50000
40000
30000
20000
10000
0
0
0.2
0.4
0.6
0.8
1
1.2
1.4
1.6
1.8
Actuator Strain (%)

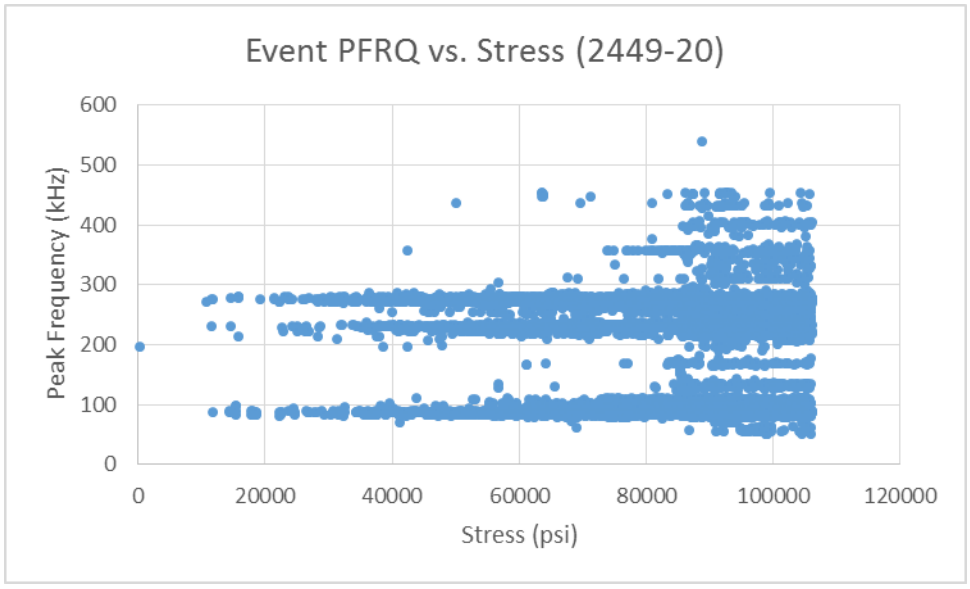

Event PFRQ vs. Stress (2446-28)
Peak Frequency (kHz)
600
500
400
300
200
100
0
0
10000
20000
30000
40000
50000
60000
70000
80000
Stress (psi)

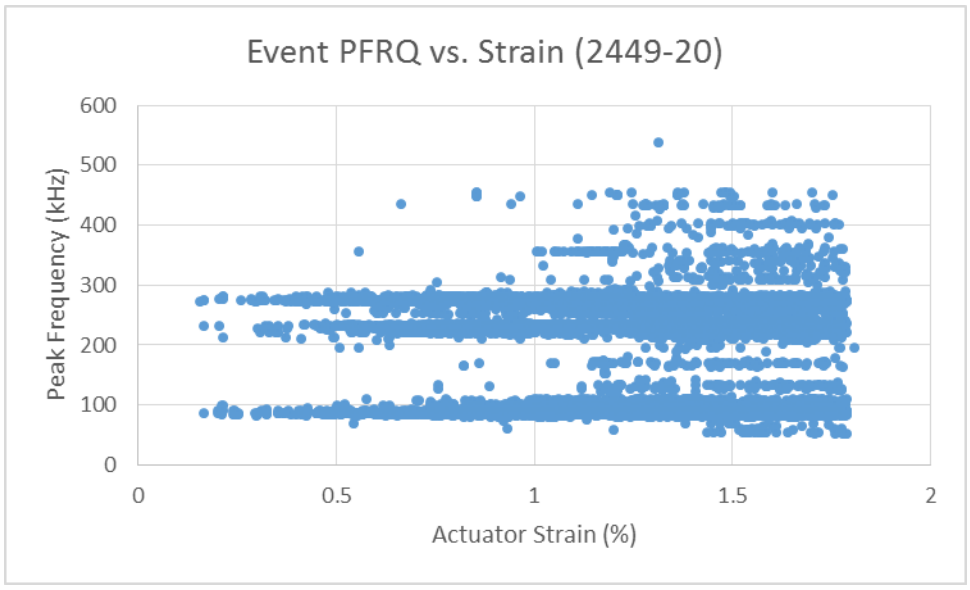

Event PFRQ vs. Strain (2446-28)
Peak Frequency (kHz)
600
500
400
300
200
100
0
0
0.2
0.4
0.6
0.8
1
1.2
1.4
1.6
1.8
Actuator Strain (%)

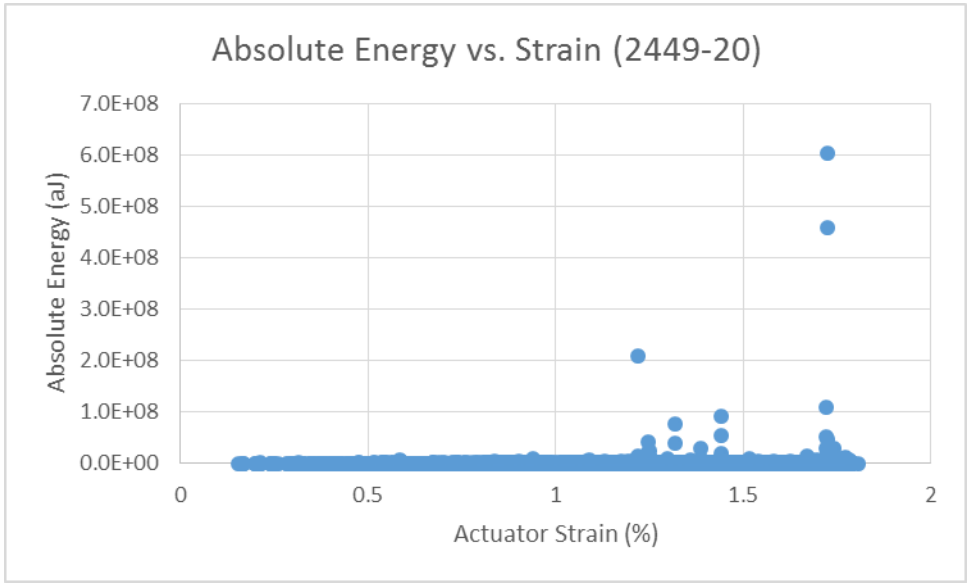

Absolute Energy vs. Strain (2446-28)
Absolute Energy (aJ)
2.5E+07
2.0E+07
1.5E+07
1.0E+07
5.0E+06
0.0E+00
0
0.2
0.4
0.6
0.8
1
1.2
1.4
1.6
1.8
Actuator Strain (%)

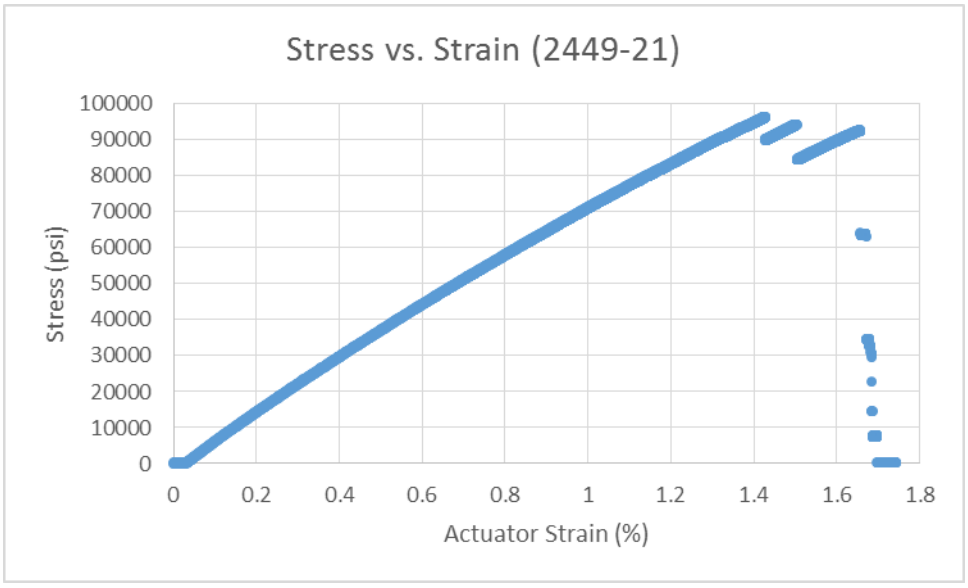
GLASS- C1

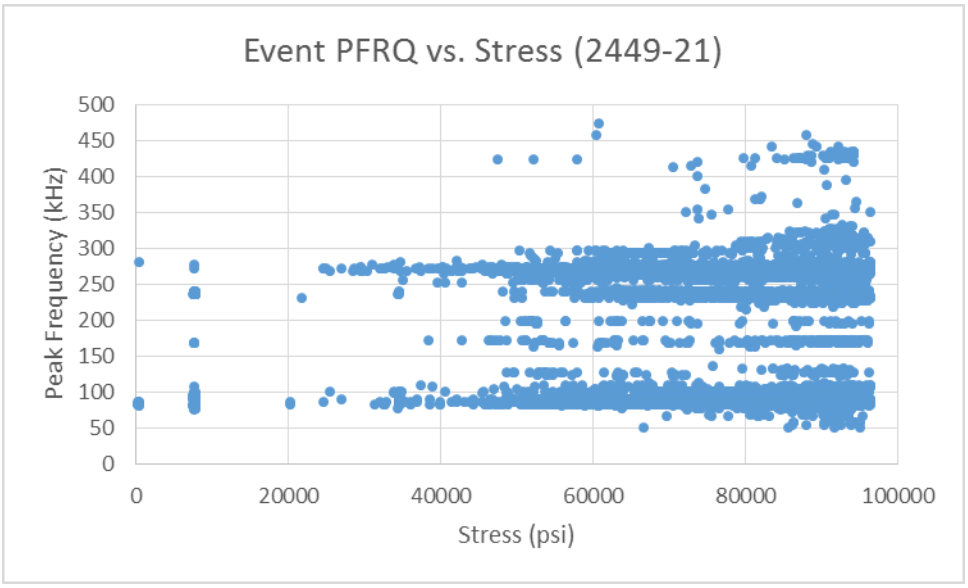

Stress vs. Strain (2449-20)
Stress (psi)
120000
100000
80000
60000
40000
20000
0
0
0.5
1
1.5
2
Actuator Strain (%)

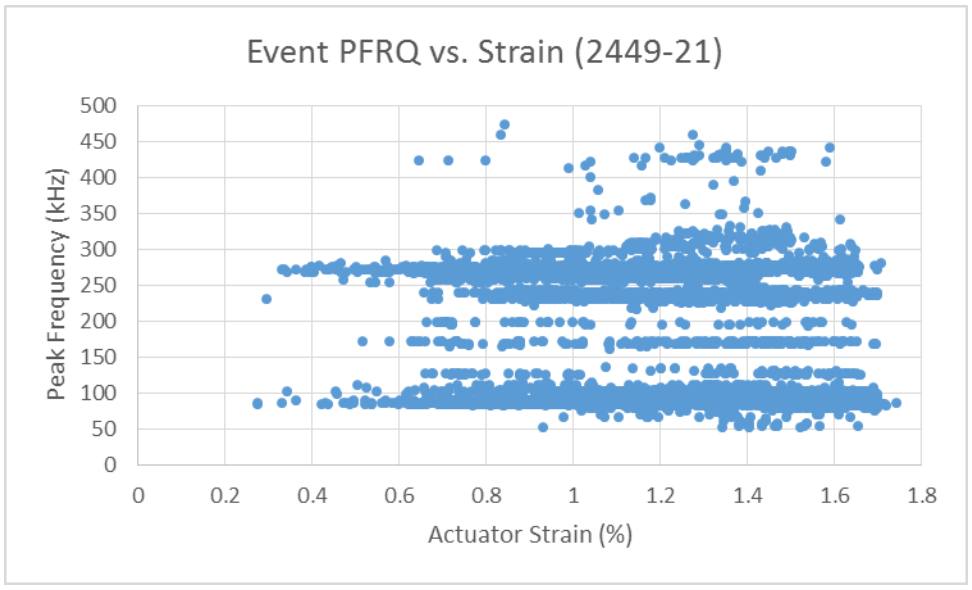

Event PFRQ vs. Stress (2449-20)
Peak Frequency (kHz)
600
500
400
300
200
100
0
0
20000
40000
60000
80000
100000
120000
Stress (psi)

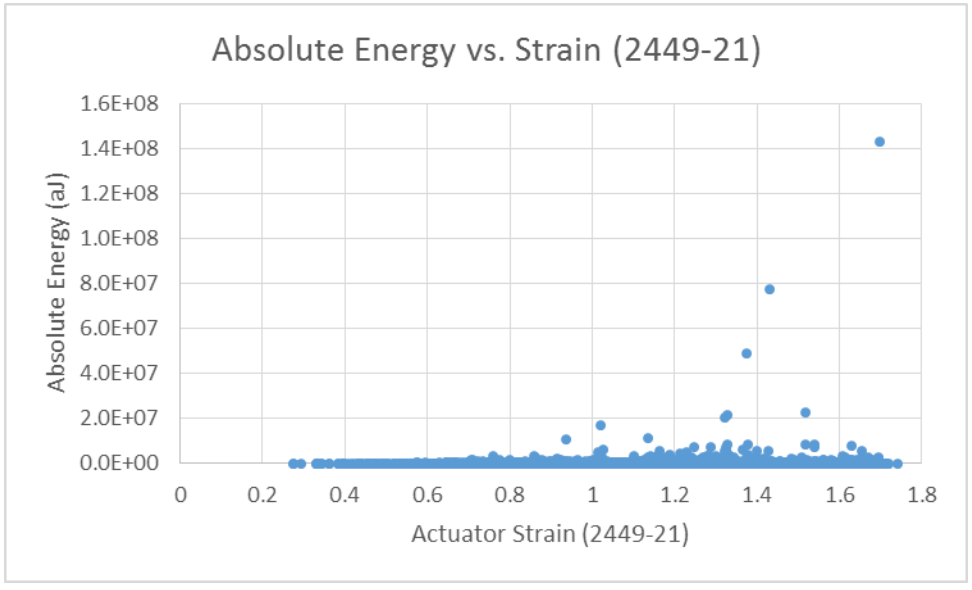

Event PFRQ vs. Strain (2449-20)
Peak Frequency (kHz)
600
500
400
300
200
100
0
0
0.5
1
1.5
2
Actuator Strain (%)

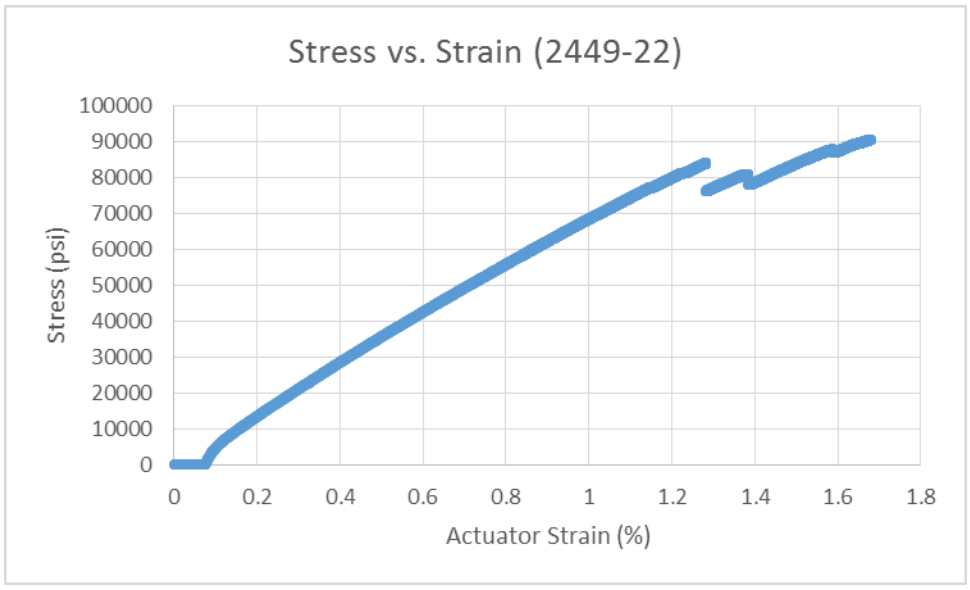

Absolute Energy vs. Strain (2449-20)
Absolute Energy (aJ)
7.0E+08
6.0E+08
5.0E+08
4.0E+08
3.0E+08
2.0E+08
1.0E+08
0.0E+00
0
0.5
1
1.5
2
Actuator Strain (%)

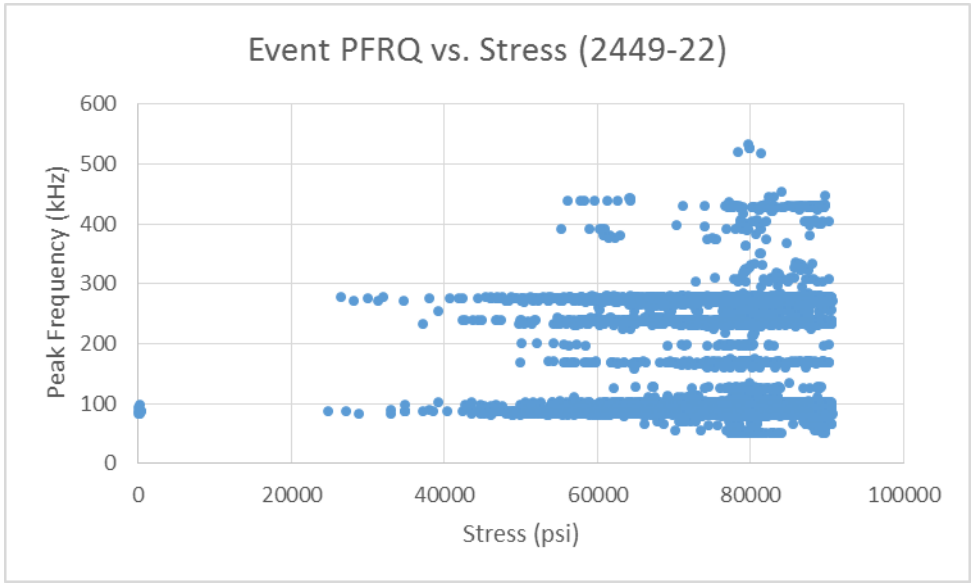

Stress vs. Strain (2449-21)
Stress (psi)
100000
90000
80000
70000
60000
50000
40000
30000
20000
10000
0
0
0.2
0.4
0.6
0.8
1
1.2
1.4
1.6
1.8
Actuator Strain (%)

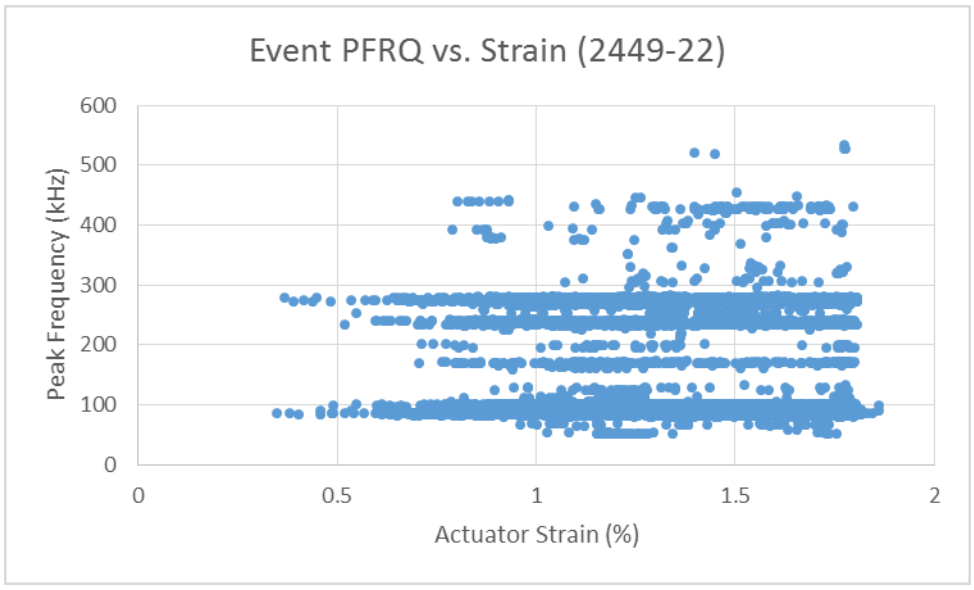

Event PFRQ vs. Stress (2449-21)
Peak Frequency (kHz)
500
450
400
350
300
250
200
150
100
50
0
0
20000
40000
60000
80000
100000
Stress (psi)

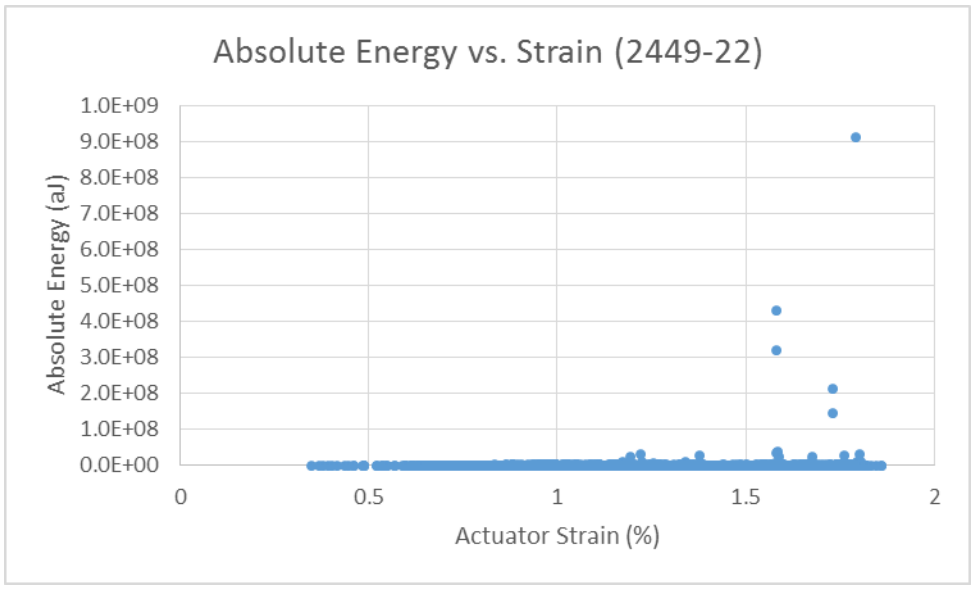

Event PFRQ vs. Strain (2449-21)
Peak Frequency (kHz)
500
450
400
350
300
250
200
150
100
50
0
0
0.2
0.4
0.6
0.8
1
1.2
1.4
1.6
1.8
Actuator Strain (%)

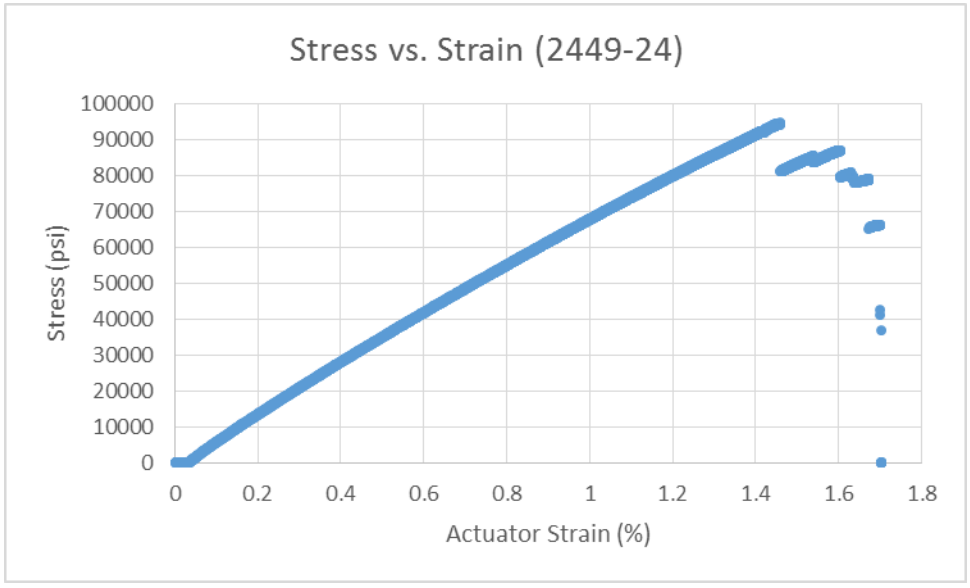

Absolute Energy vs. Strain (2449-21)
Absolute Energy (aJ)
1.6E+08
1.4E+08
1.2E+08
1.0E+08
8.0E+07
6.0E+07
4.0E+07
2.0E+07
0.0E+00
0
0.2
0.4
0.6
0.8
1
1.2
1.4
1.6
1.8
Actuator Strain (2449-21)

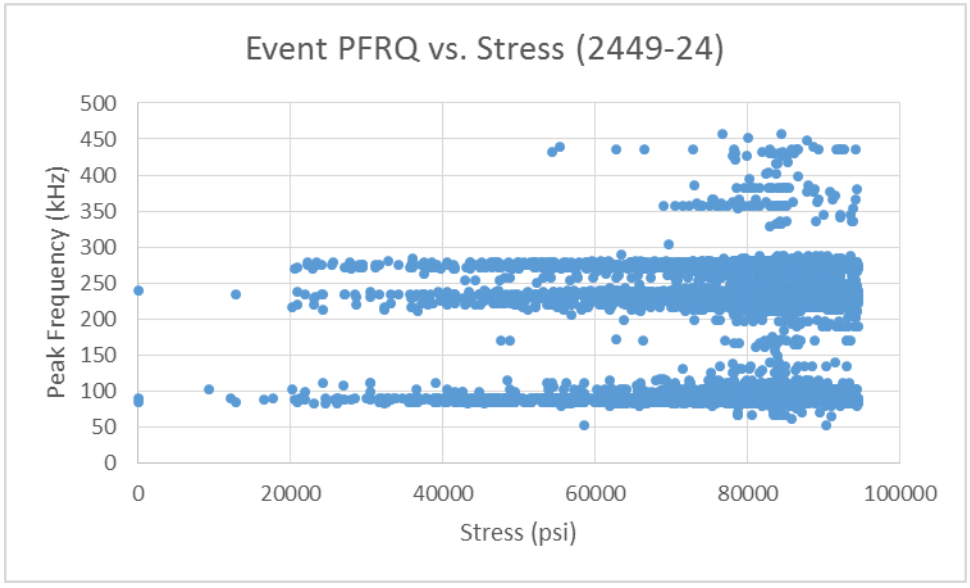

Stress vs. Strain (2449-22)
Stress (psi)
100000
90000
80000
70000
60000
50000
40000
30000
20000
10000
0
0
0.2
0.4
0.6
0.8
1
1.2
1.4
1.6
1.8
Actuator Strain (%)

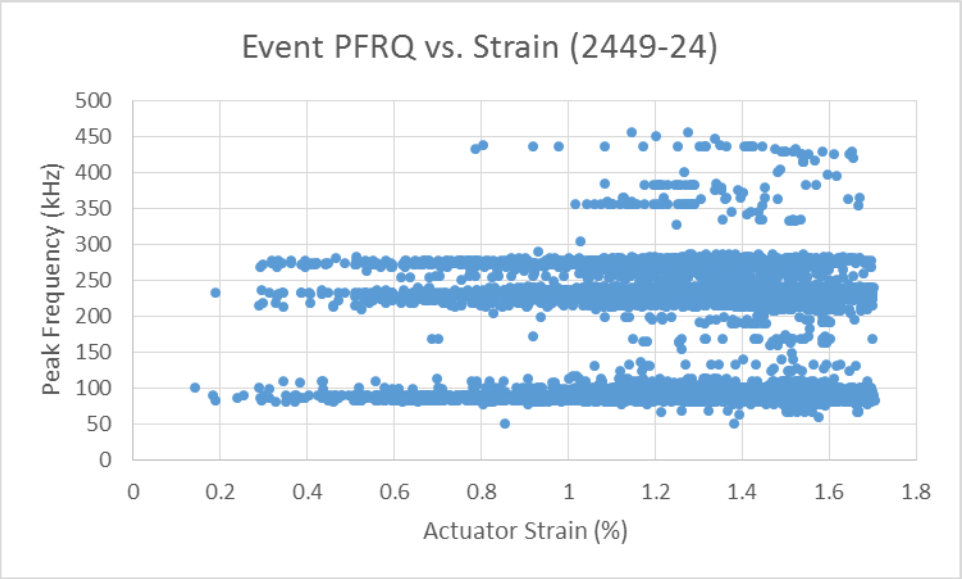

Event PFRQ vs. Stress (2449-22)
Peak Frequency (kHz)
600
500
400
300
200
100
0
0
20000
40000
60000
80000
100000
Stress (psi)

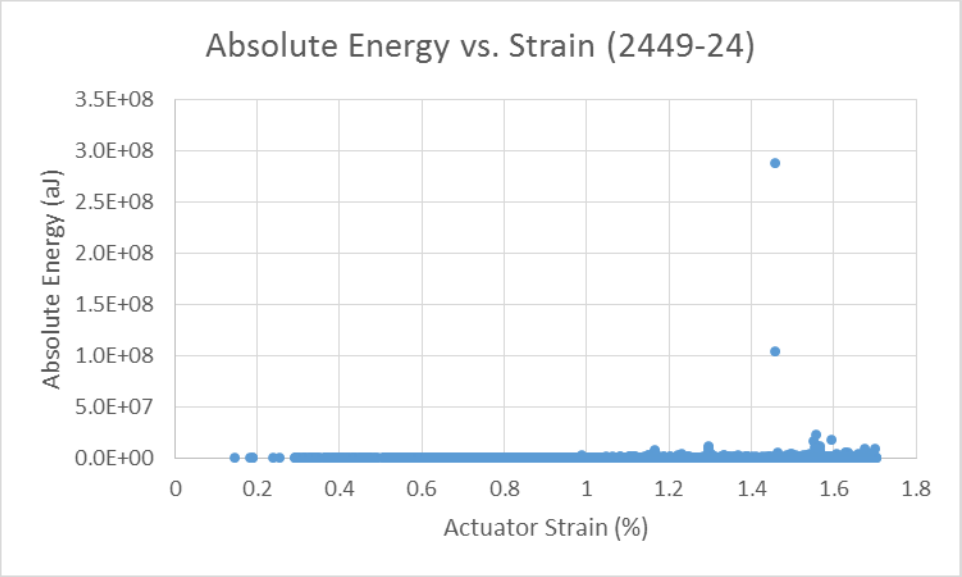

Event PFRQ vs. Strain (2449-22)
Peak Frequency (kHz)
600
500
400
300
200
100
0
0
0.5
1
1.5
2
Actuator Strain (%)


Absolute Energy vs. Strain (2449-22)
Absolute Energy (aJ)
1.0E+09
9.0E+08
8.0E+08
7.0E+08
6.0E+08
5.0E+08
4.0E+08
3.0E+08
2.0E+08
1.0E+08
0.0E+00
0
0.5
1
1.5
2
Actuator Strain (%)

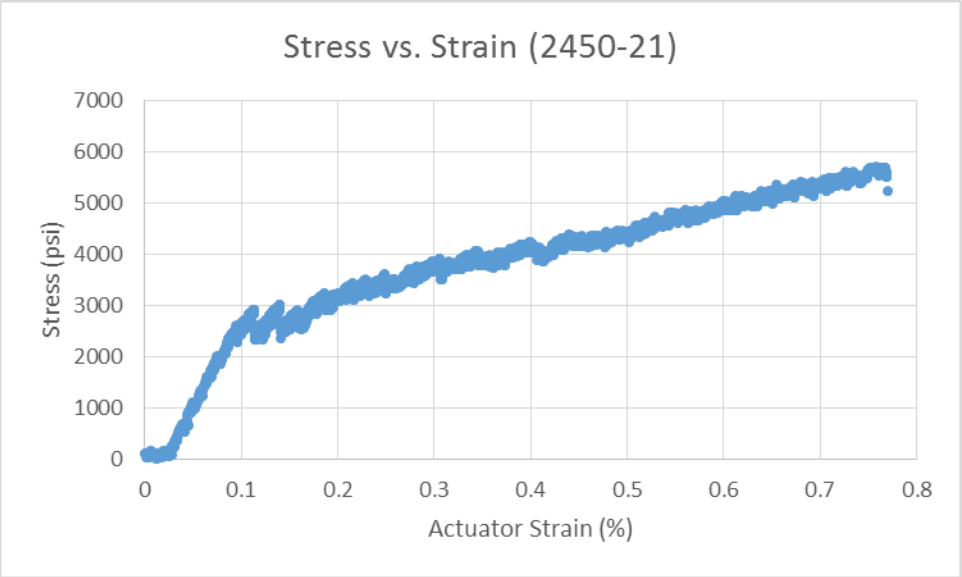

Stress vs. Strain (2449-24)
Stress (psi)
100000
90000
80000
70000
60000
50000
40000
30000
20000
10000
0
0
0.2
0.4
0.6
0.8
1
1.2
1.4
1.6
1.8
Actuator Strain (%)

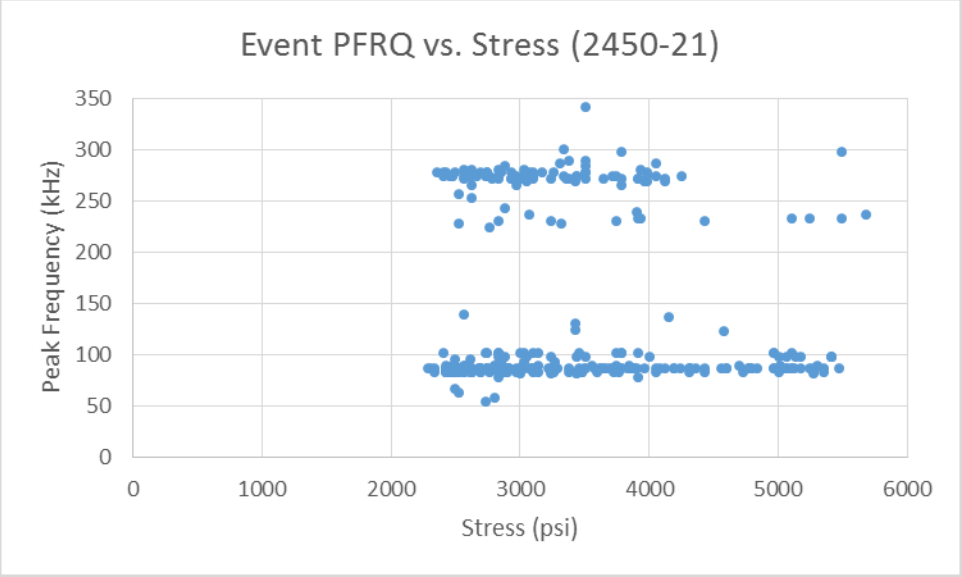

Event PFRQ vs. Stress (2449-24)
Peak Frequency (kHz)
500
450
400
350
300
250
200
150
100
50
0
0
20000
40000
60000
80000
100000
Stress (psi)

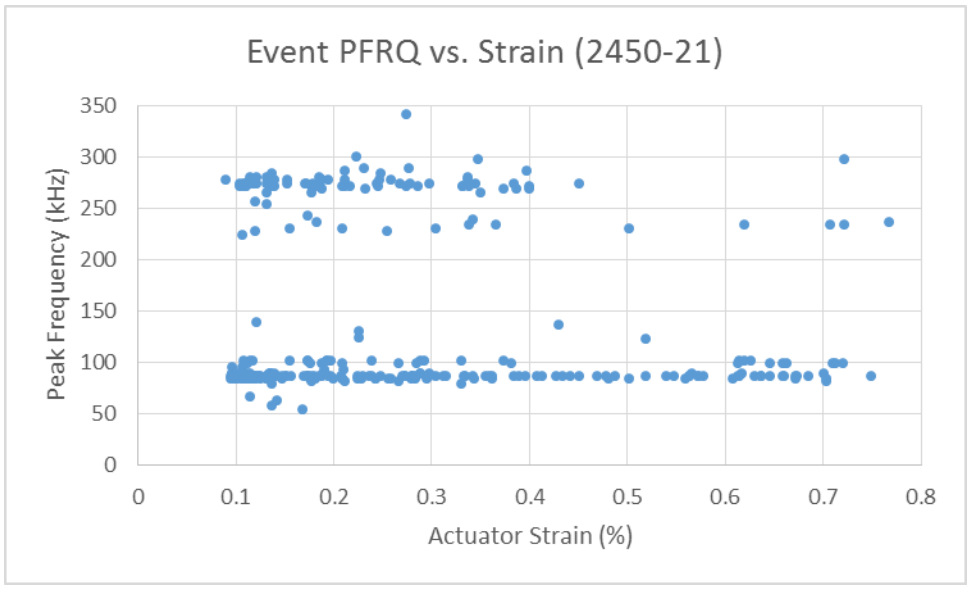

Event PFRQ vs. Strain (2449-24)
Peak Frequency (kHz)
500
450
400
350
300
250
200
150
100
50
0
0
0.2
0.4
0.6
0.8
1
1.2
1.4
1.6
1.8
Actuator Strain (%)

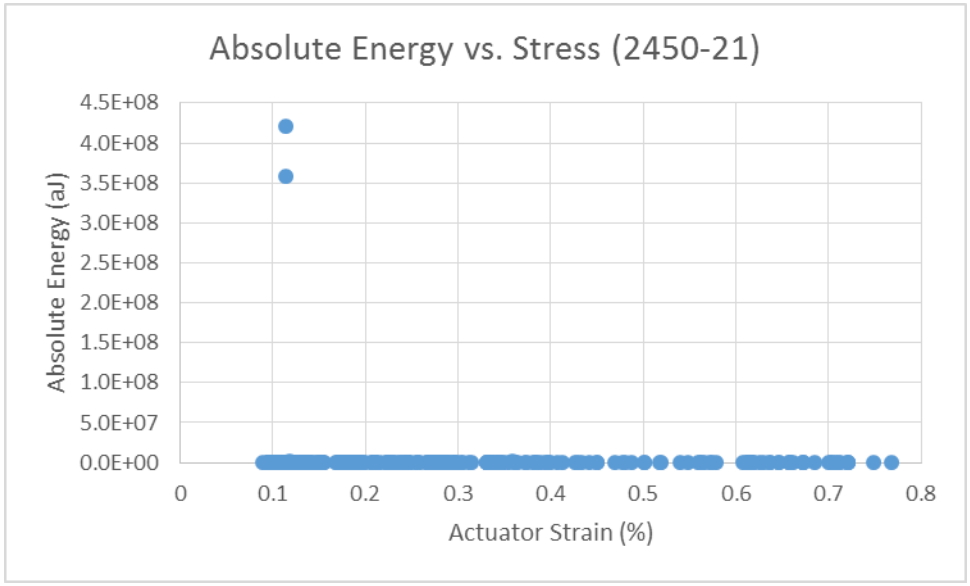

Absolute Energy vs. Strain (2449-24)
Absolute Energy (aJ)
3.5E+08
3.0E+08
2.5E+08
2.0E+08
1.5E+08
1.0E+08
5.0E+07
0.0E+00
0
0.2
0.4
0.6
0.8
1
1.2
1.4
1.6
1.8
Actuator Strain (%)

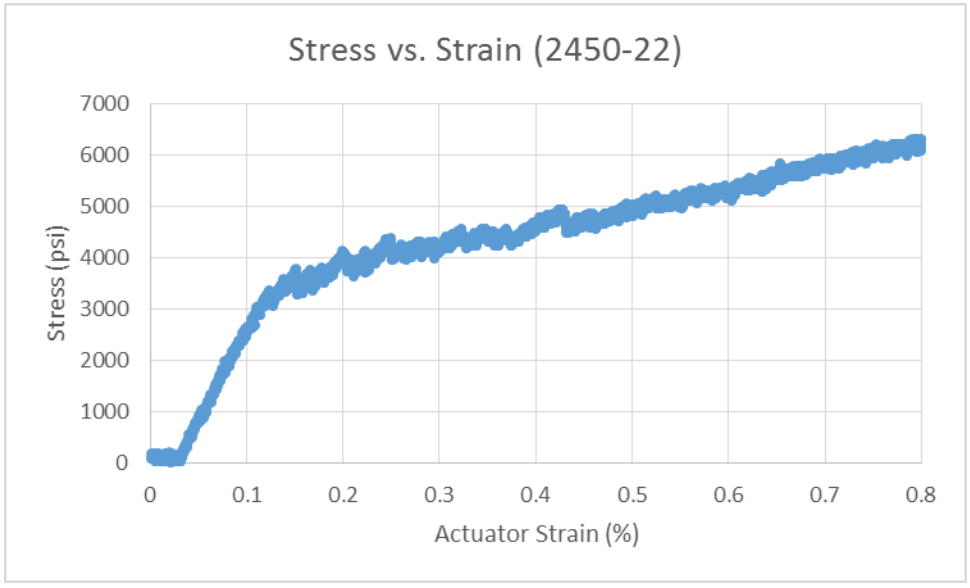
GLASS- C2

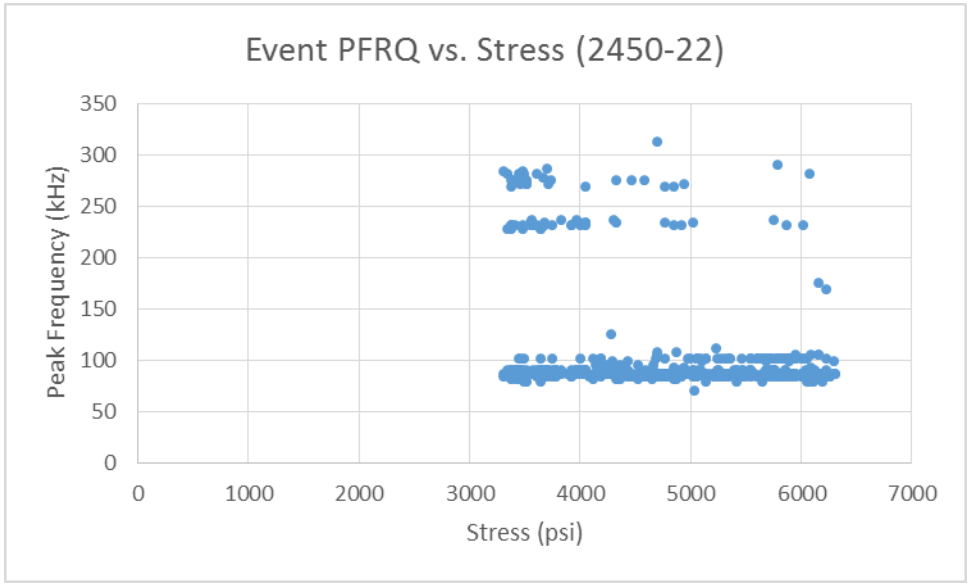

Stress vs. Strain (2450-21)
Stress (psi)
7000
6000
5000
4000
3000
2000
1000
0
0
0.1
0.2
0.3
0.4
0.5
0.6
0.7
0.8
Actuator Strain (%)

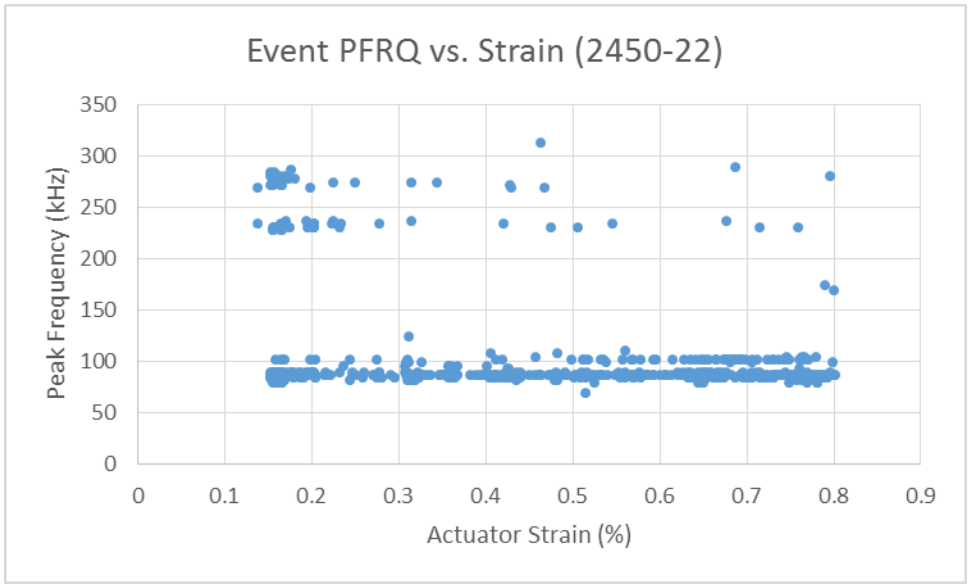

Event PFRQ vs. Stress (2450-21)
Peak Frequency (kHz)
350
300
250
200
150
100
50
0
0
1000
2000
3000
4000
5000
6000
Stress (psi)

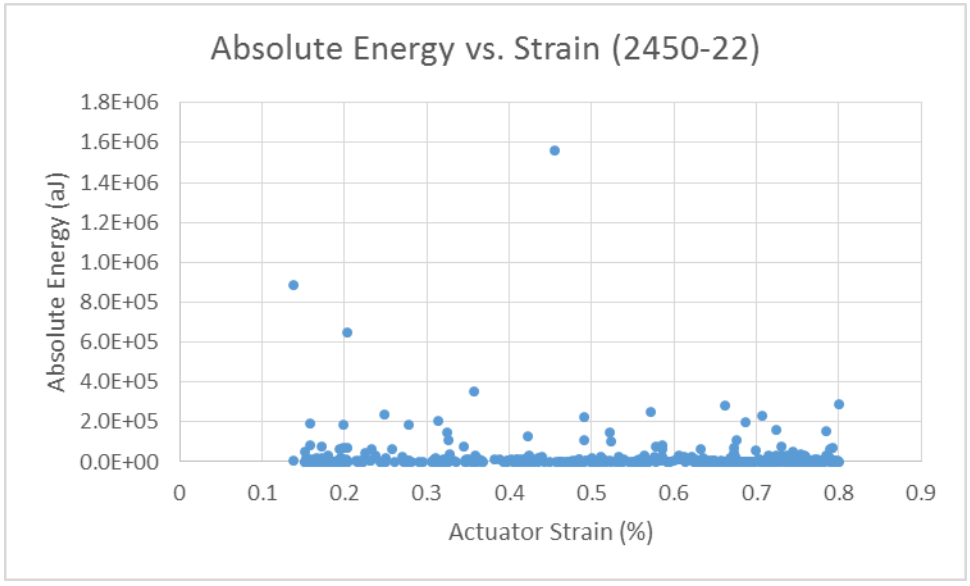

Event PFRQ vs. Strain (2450-21)
Peak Frequency (kHz)
350
300
250
200
150
100
50
0
0
0.1
0.2
0.3
0.4
0.5
0.6
0.7
0.8
Actuator Strain (%)

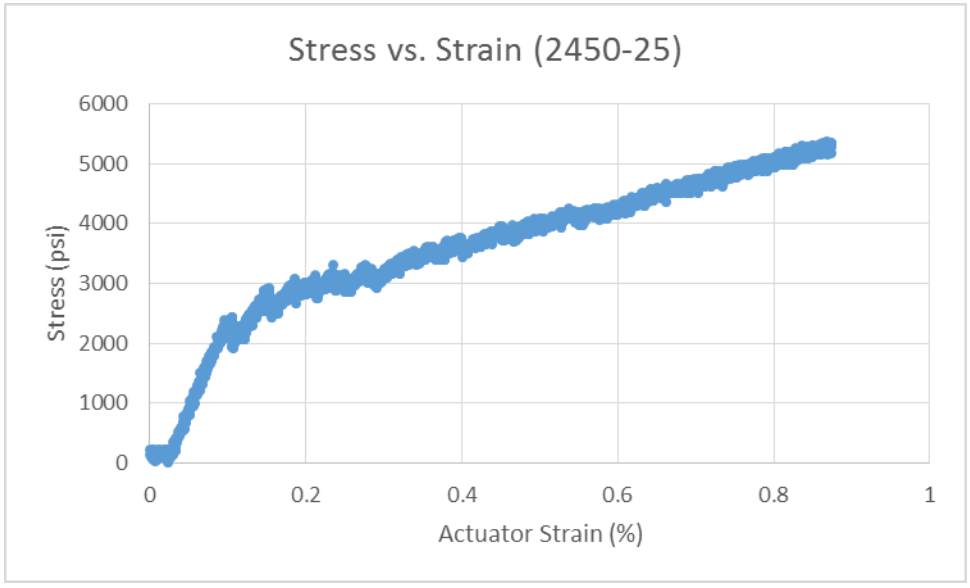

Absolute Energy vs. Stress (2450-21)
Absolute Energy (aJ)
4.5E+08
4.0E+08
3.5E+08
3.0E+08
2.5E+08
2.0E+08
1.5E+08
1.0E+08
5.0E+07
0.0E+00
0
0.1
0.2
0.3
0.4
0.5
0.6
0.7
0.8
Actuator Strain (%)

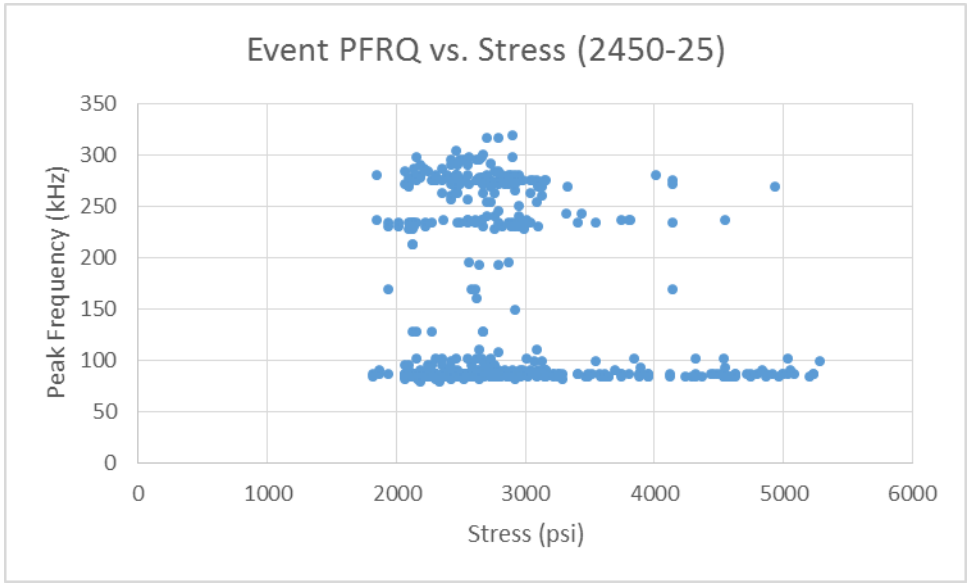

Stress vs. Strain (2450-22)
Stress (psi)
7000
6000
5000
4000
3000
2000
1000
0
0
0.1
0.2
0.3
0.4
0.5
0.6
0.7
0.8
Actuator Strain (%)

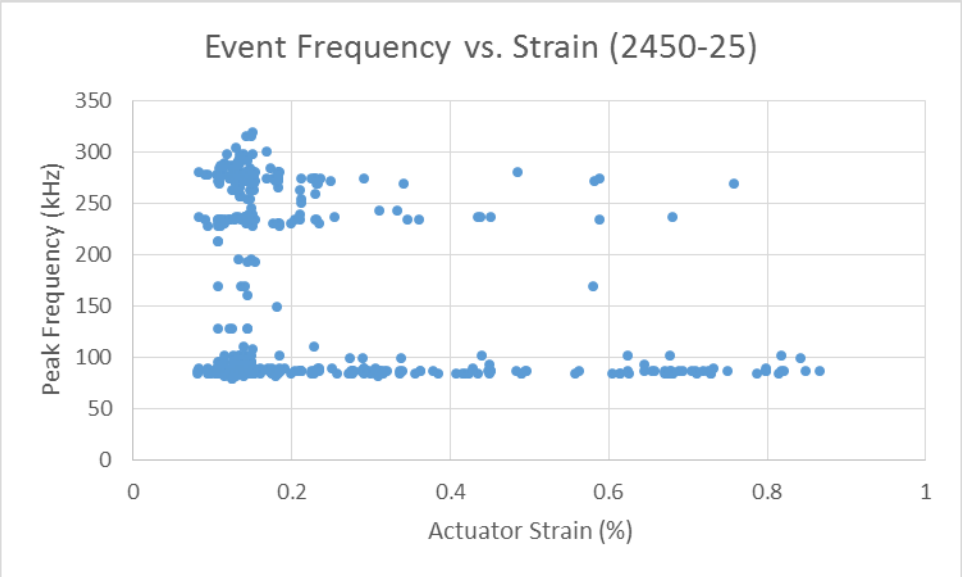

Event PFRQ vs. Stress (2450-22)
Peak Frequency (kHz)
350
300
250
200
150
100
50
0
0
1000
2000
3000
4000
5000
6000
7000
Stress (psi)

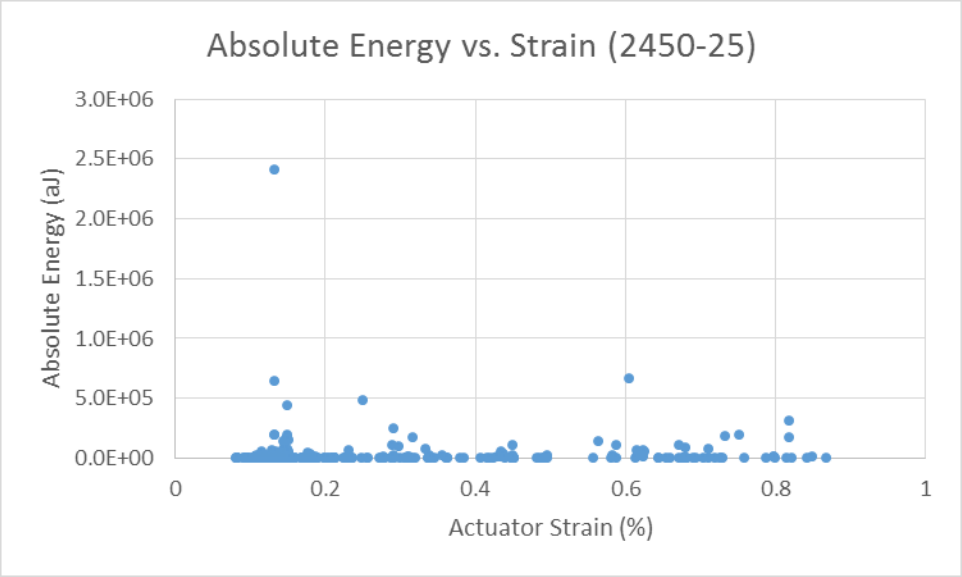

Event PFRQ vs. Strain (2450-22)
Peak Frequency (kHz)
350
300
250
200
150
100
50
0
0
0.1
0.2
0.3
0.4
0.5
0.6
0.7
0.8
0.9
Actuator Strain (%)


Absolute Energy vs. Strain (2450-22)
Absolute Energy (aJ)
1.8E+06
1.6E+06
1.4E+06
1.2E+06
1.0E+06
8.0E+05
6.0E+05
4.0E+05
2.0E+05
0.0E+00
0
0.1
0.2
0.3
0.4
0.5
0.6
0.7
0.8
0.9
Actuator Strain (%)

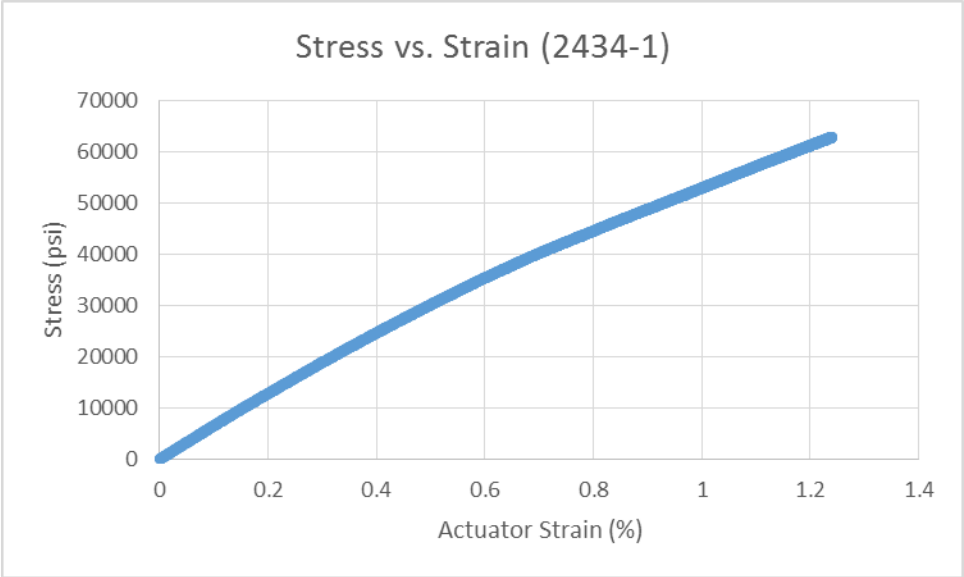

Stress vs. Strain (2450-25)
Stress (psi)
6000
5000
4000
3000
2000
1000
0
0
0.2
0.4
0.6
0.8
1
Actuator Strain (%)

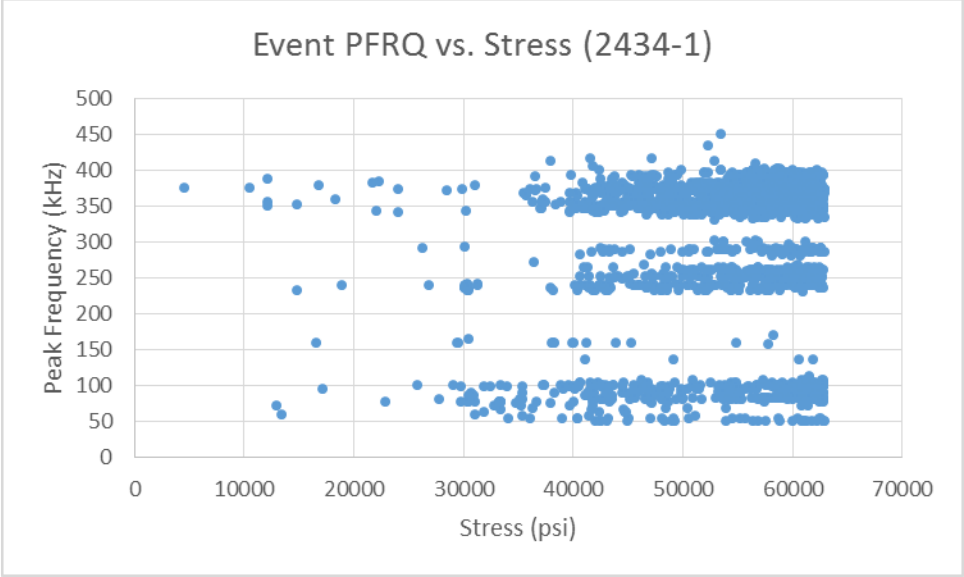

Event PFRQ vs. Stress (2450-25)
Peak Frequency (kHz)
350
300
250
200
150
100
50
0
0
1000
2000
3000
4000
5000
6000
Stress (psi)

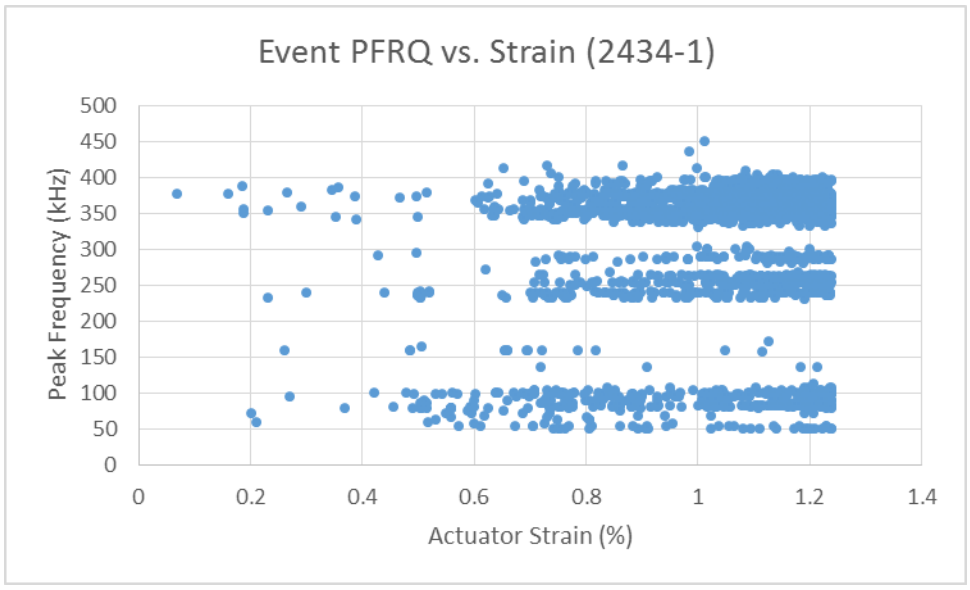

Event Frequency vs. Strain (2450-25)
Peak Frequency (kHz)
350
300
250
200
150
100
50
0
0
0.2
0.4
0.6
0.8
1
Actuator Strain (%)

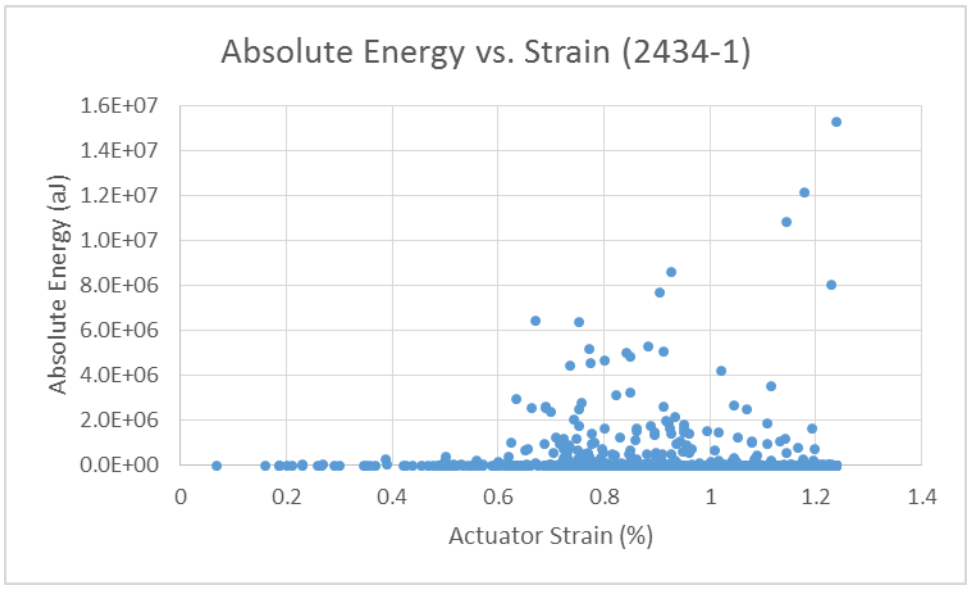

Absolute Energy vs. Strain (2450-25)
Absolute Energy (aJ)
3.0E+06
2.5E+06
2.0E+06
1.5E+06
1.0E+06
5.0E+05
0.0E+00
0
0.2
0.4
0.6
0.8
1
Actuator Strain (%)

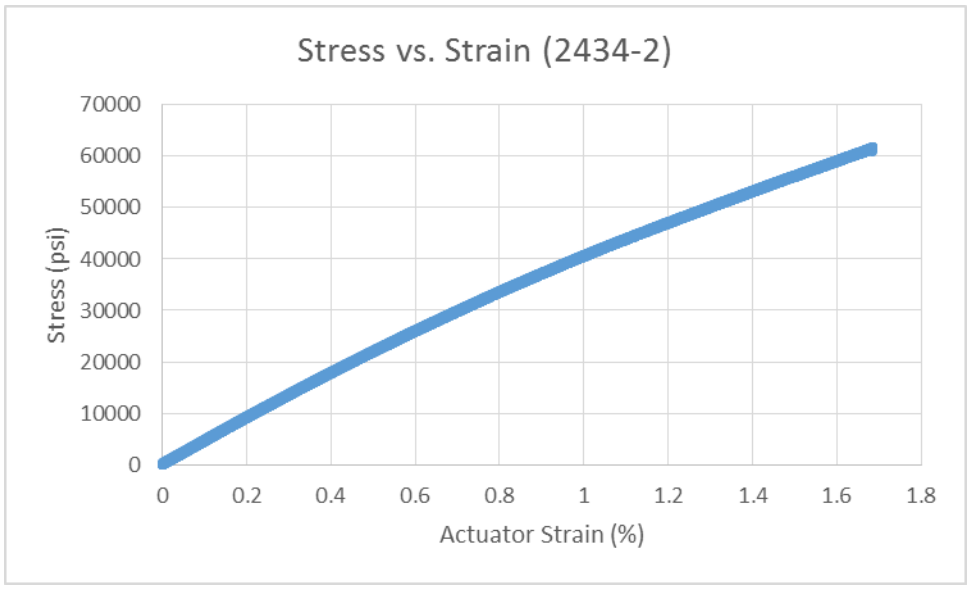
GLASS- B1

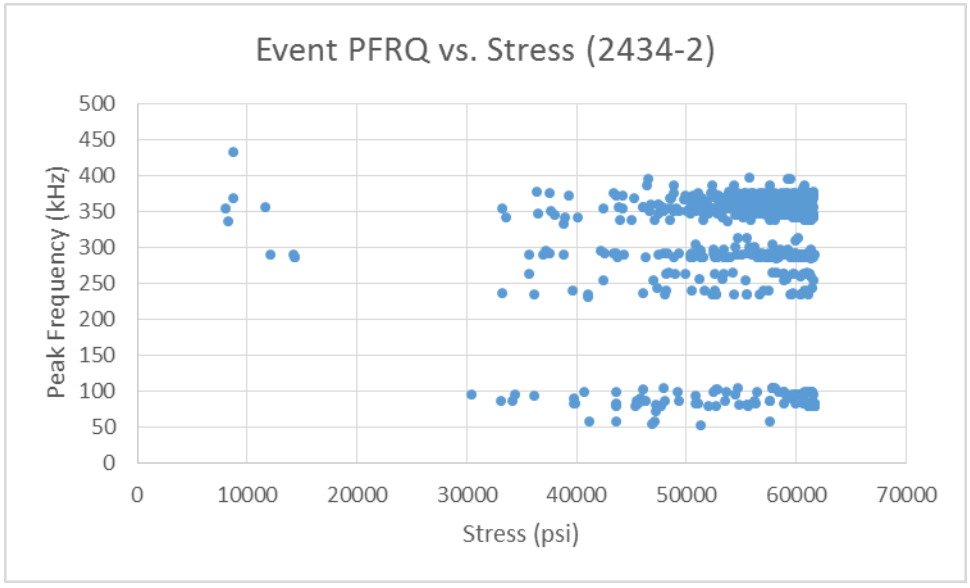

Stress vs. Strain (2434-1)
Stress (psi)
70000
60000
50000
40000
30000
20000
10000
0
0
0.2
0.4
0.6
0.8
1
1.2
1.4
Actuator Strain (%)

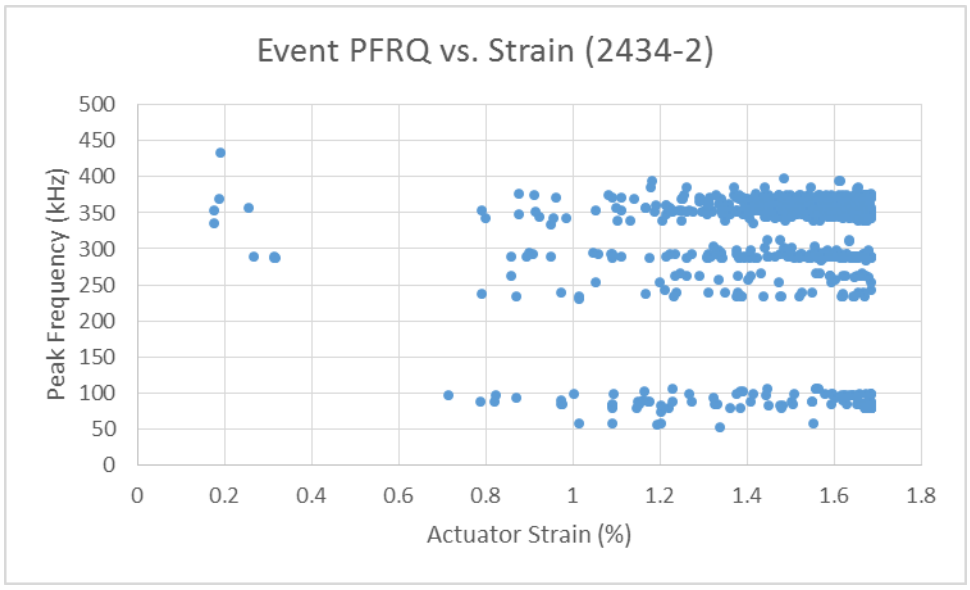

Event PFRQ vs. Stress (2434-1)
Peak Frequency (kHz)
500
450
400
350
300
250
200
150
100
50
0
0
10000
20000
30000
40000
50000
60000
70000
Stress (psi)

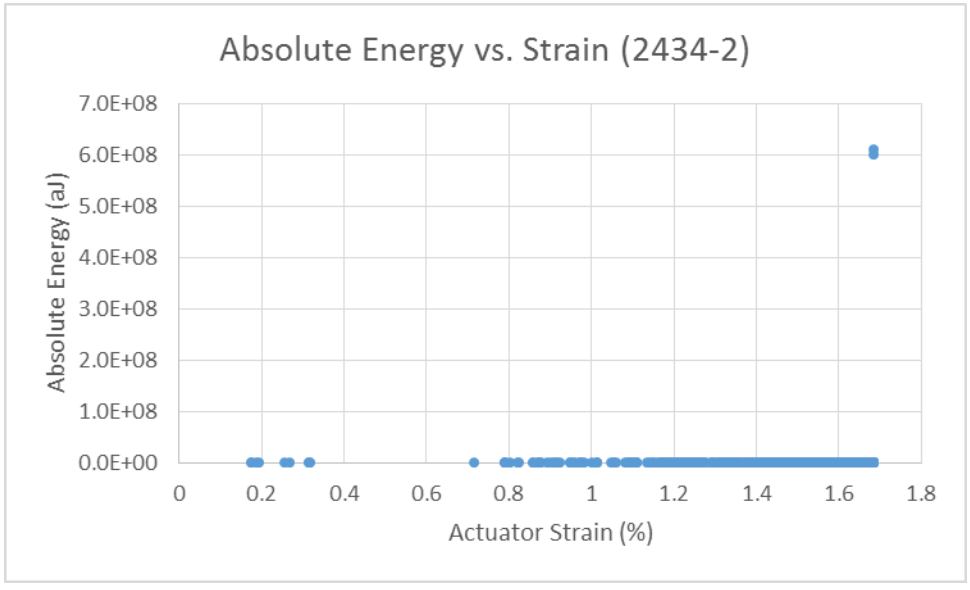

Event PFRQ vs. Strain (2434-1)
Peak Frequency (kHz)
500
450
400
350
300
250
200
150
100
50
0
0
0.2
0.4
0.6
0.8
1
1.2
1.4
Actuator Strain (%)

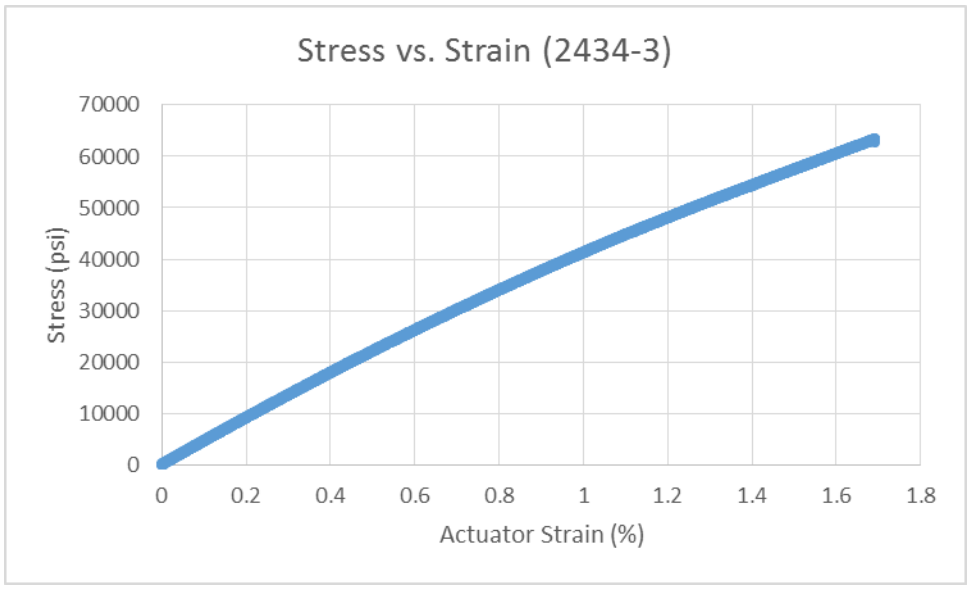

Absolute Energy vs. Strain (2434-1)
Absolute Energy (aJ)
1.6E+07
1.4E+07
1.2E+07
1.0E+07
8.0E+06
6.0E+06
4.0E+06
2.0E+06
0.0E+00
0
0.2
0.4
0.6
0.8
1
1.2
1.4
Actuator Strain (%)

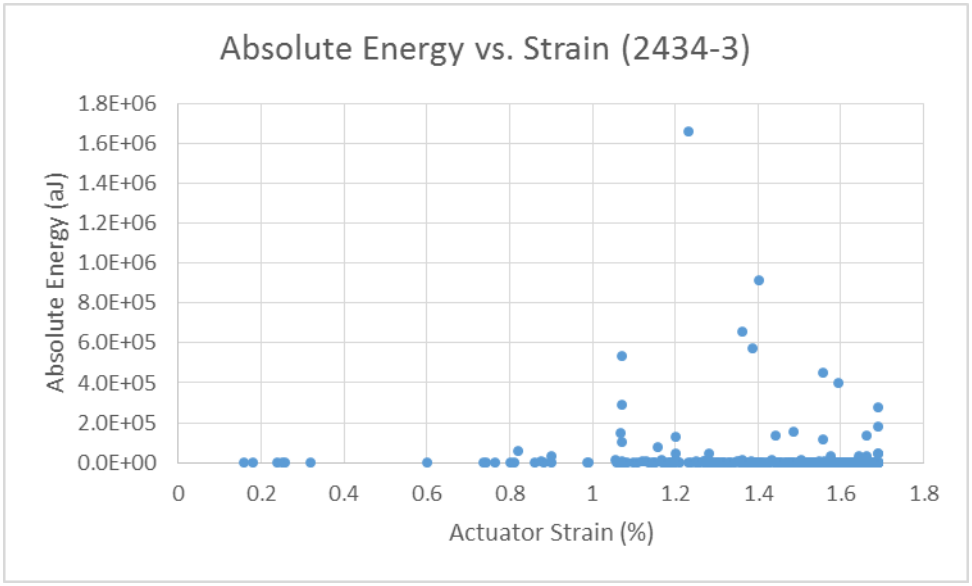

Stress vs. Strain (2434-2)
Stress (psi)
70000
60000
50000
40000
30000
20000
10000
0
0
0.2
0.4
0.6
0.8
1
1.2
1.4
1.6
1.8
Actuator Strain (%)

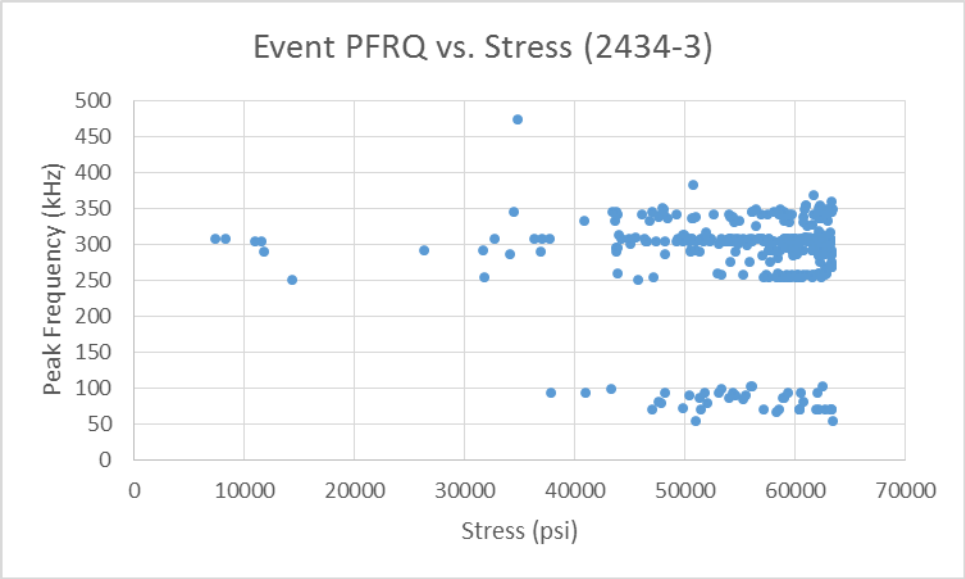

Event PFRQ vs. Stress (2434-2)
Peak Frequency (kHz)
500
450
400
350
300
250
200
150
100
50
0
0
10000
20000
30000
40000
50000
60000
70000
Stress (psi)

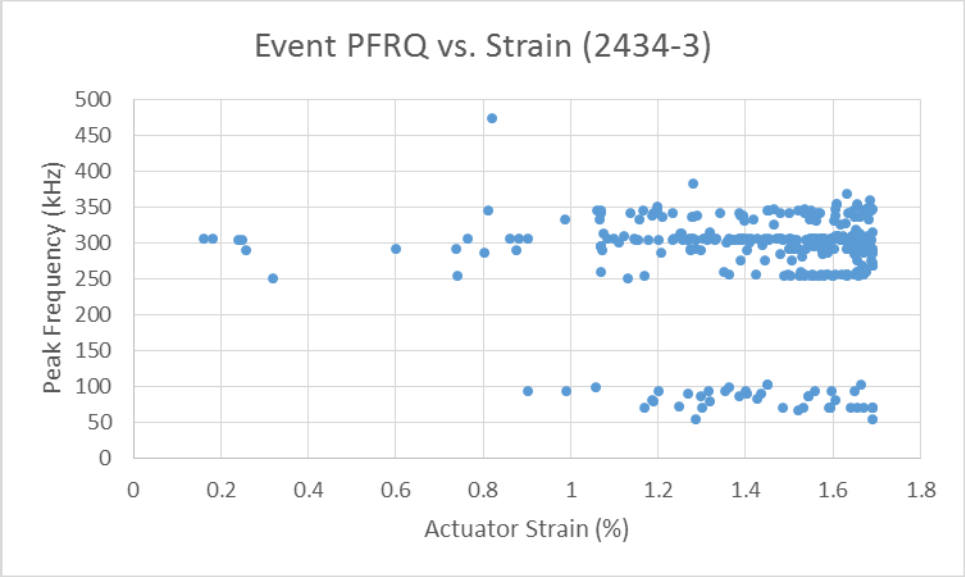

Event PFRQ vs. Strain (2434-2)
Peak Frequency (kHz)
500
450
400
350
300
250
200
150
100
50
0
0
0.2
0.4
0.6
0.8
1
1.2
1.4
1.6
1.8
Actuator Strain (%)


Absolute Energy vs. Strain (2434-2)
Absolute Energy (aJ)
7.0E+08
6.0E+08
5.0E+08
4.0E+08
3.0E+08
2.0E+08
1.0E+08
0.0E+00
0
0.2
0.4
0.6
0.8
1
1.2
1.4
1.6
1.8
Actuator Strain (%)

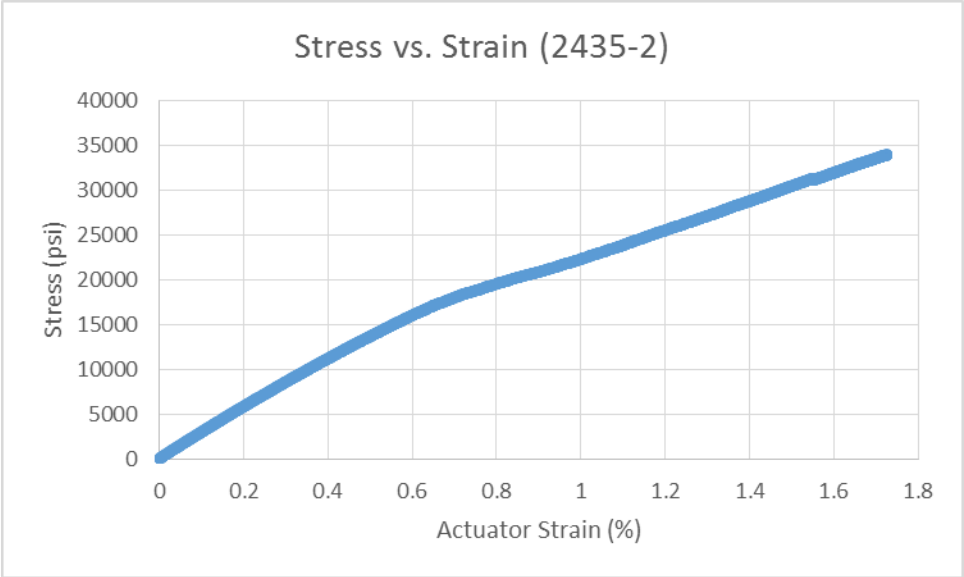

Stress vs. Strain (2434-3)
Stress (psi)
70000
60000
50000
40000
30000
20000
10000
0
0
0.2
0.4
0.6
0.8
1
1.2
1.4
1.6
1.8
Actuator Strain (%)

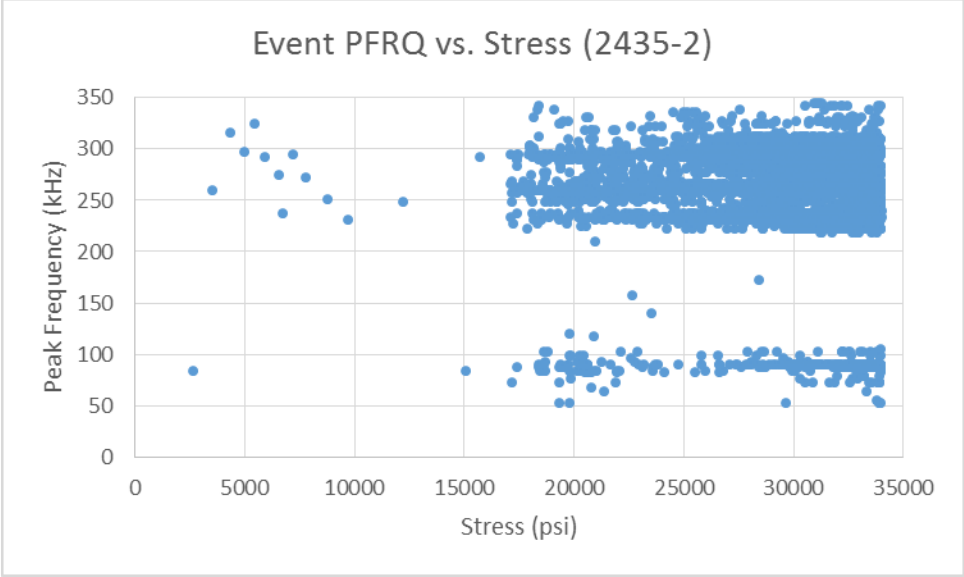

Absolute Energy vs. Strain (2434-3)
Absolute Energy (aJ)
1.8E+06
1.6E+06
1.4E+06
1.2E+06
1.0E+06
8.0E+05
6.0E+05
4.0E+05
2.0E+05
0.0E+00
0
0.2
0.4
0.6
0.8
1
1.2
1.4
1.6
1.8
Actuator Strain (%)

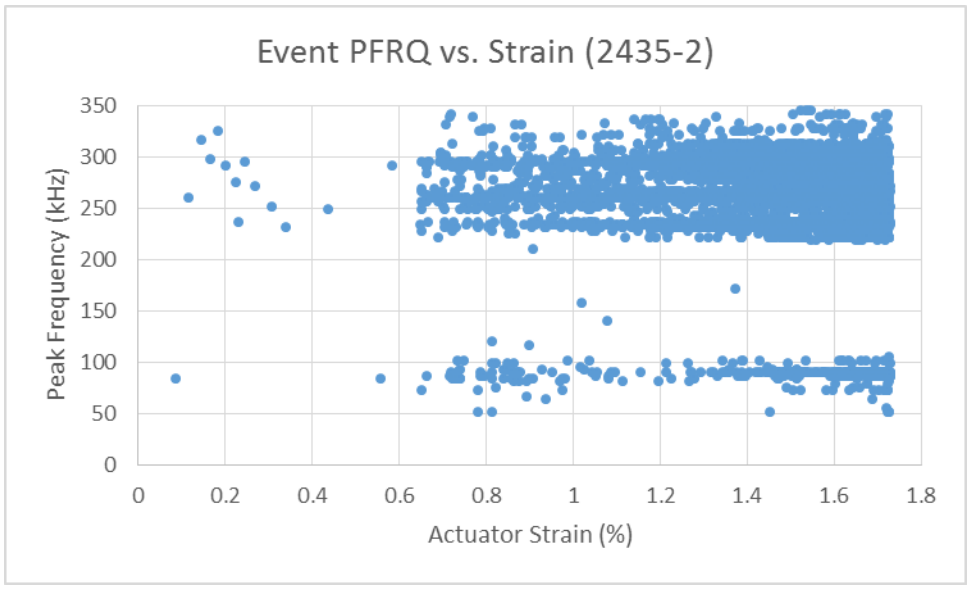

Event PFRQ vs. Stress (2434-3)
Peak Frequency (kHz)
500
450
400
350
300
250
200
150
100
50
0
0
10000
20000
30000
40000
50000
60000
70000
Stress (psi)

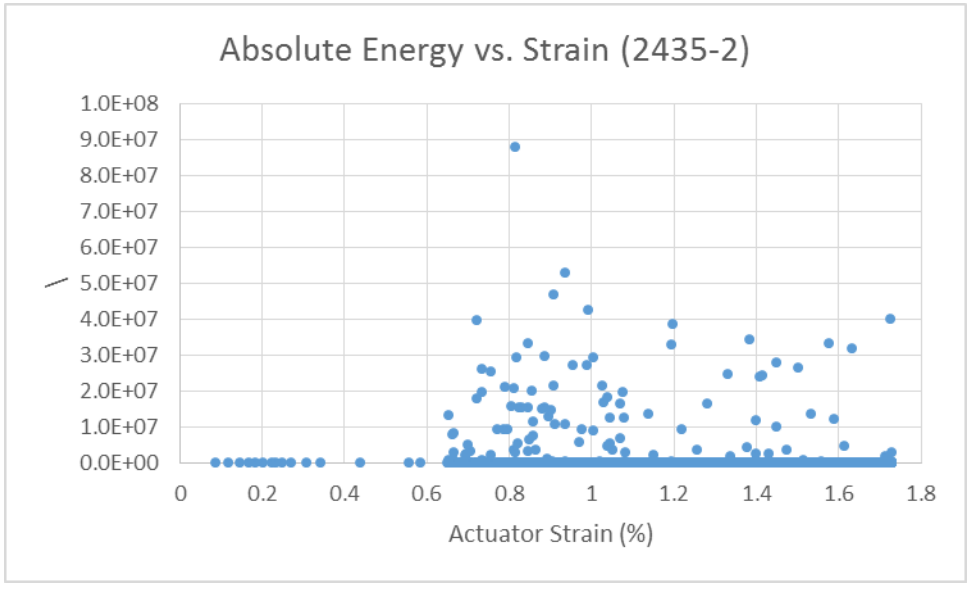

Event PFRQ vs. Strain (2434-3)
Peak Frequency (kHz)
500
450
400
350
300
250
200
150
100
50
0
0
0.2
0.4
0.6
0.8
1
1.2
1.4
1.6
1.8
Actuator Strain (%)

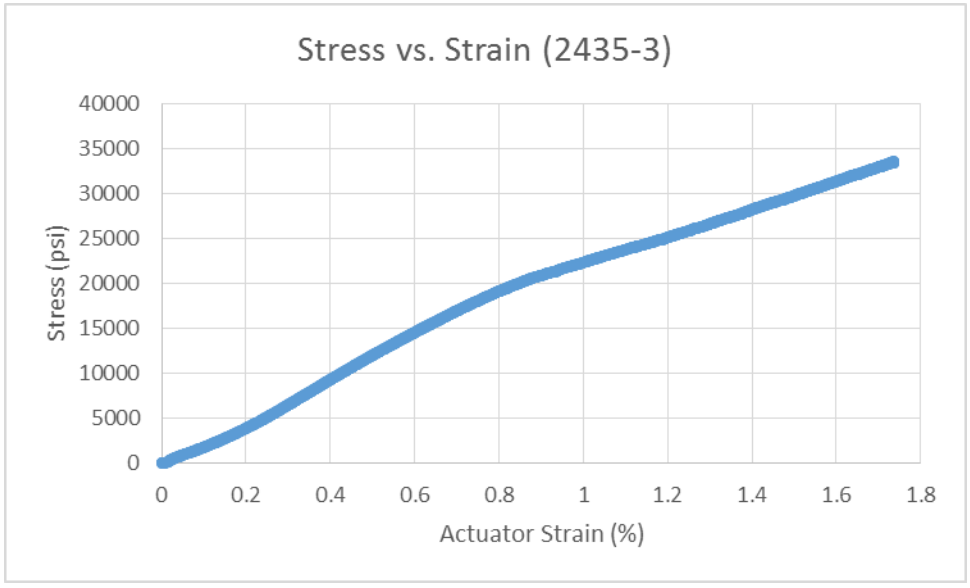
GLASS- B2

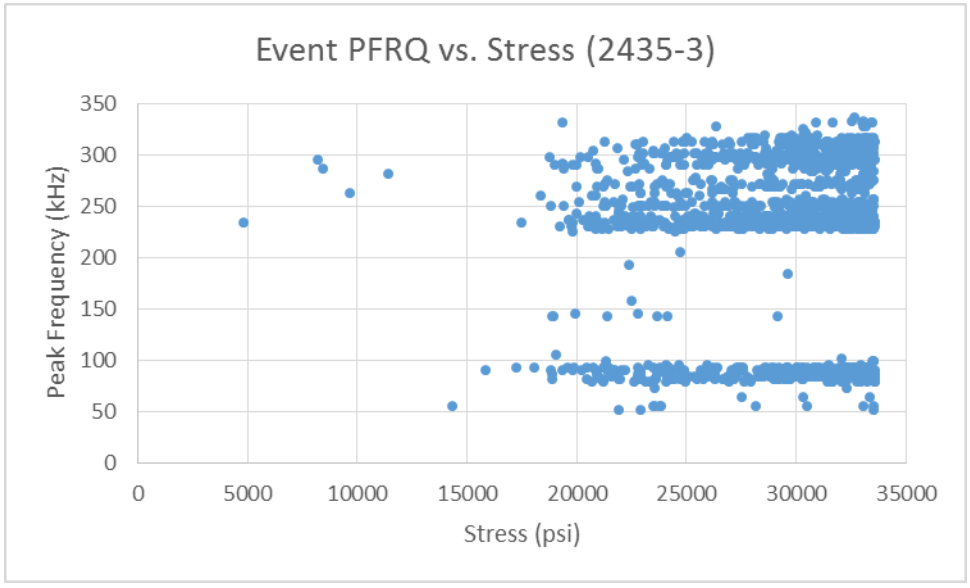

Stress vs. Strain (2435-2)
Stress (psi)
40000
35000
30000
25000
20000
15000
10000
5000
0
0
0.2
0.4
0.6
0.8
1
1.2
1.4
1.6
1.8
Actuator Strain (%)

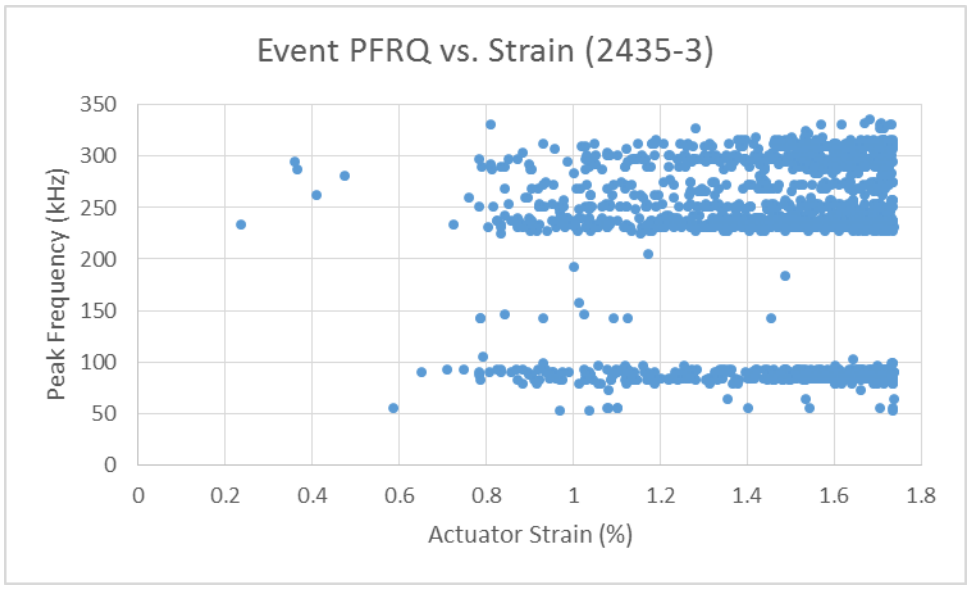

Event PFRQ vs. Stress (2435-2)
Peak Frequency (kHz)
350
300
250
200
150
100
50
0
0
5000
10000
15000
20000
25000
30000
35000
Stress (psi)

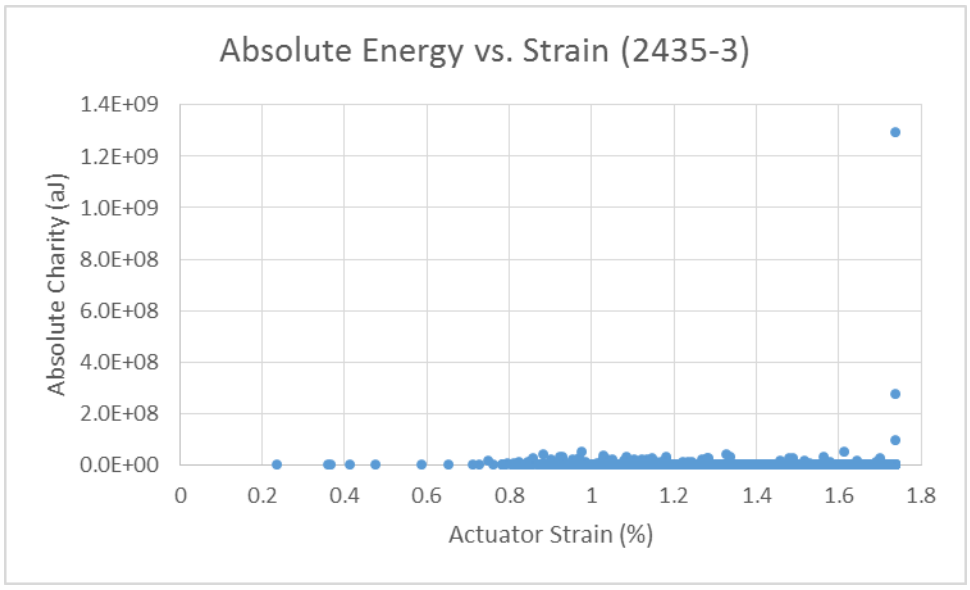

Event PFRQ vs. Strain (2435-2)
Peak Frequency (kHz)
350
300
250
200
150
100
50
0
0
0.2
0.4
0.6
0.8
1
1.2
1.4
1.6
1.8
Actuator Strain (%)

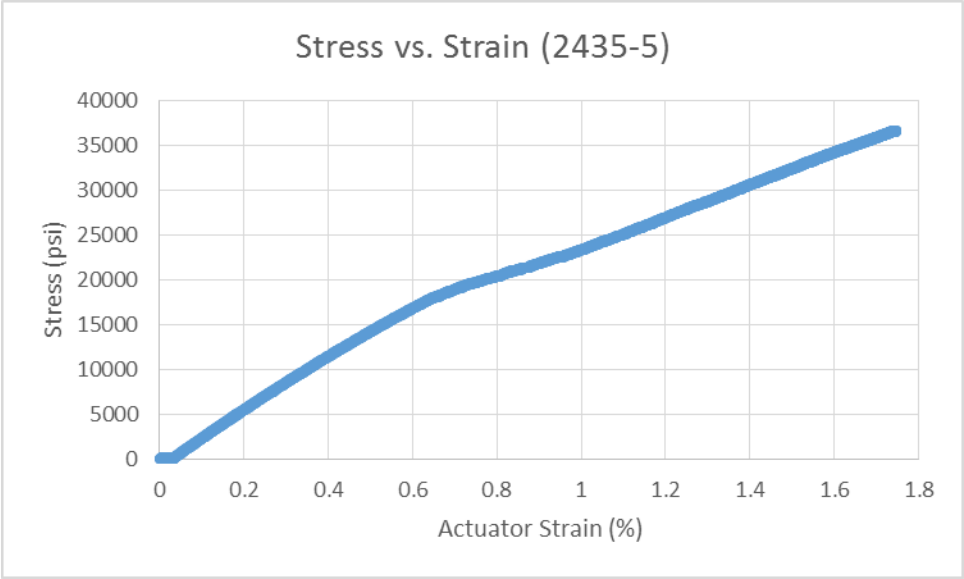

Absolute Energy vs. Strain (2435-2)
1.0E+08
9.0E+07
8.0E+07
7.0E+07
6.0E+07
5.0E+07
4.0E+07
3.0E+07
2.0E+07
1.0E+07
0.0E+00
0
0.2
0.4
0.6
0.8
1
1.2
1.4
1.6
1.8
Actuator Strain (%)

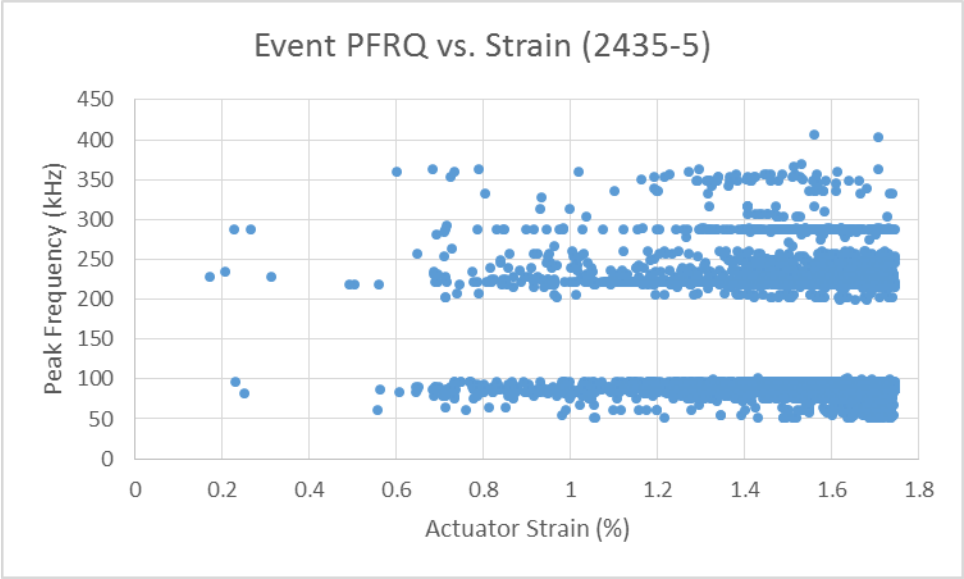

Stress vs. Strain (2435-3)
Stress (psi)
40000
35000
30000
25000
20000
15000
10000
5000
0
0
0.2
0.4
0.6
0.8
1
1.2
1.4
1.6
1.8
Actuator Strain (%)

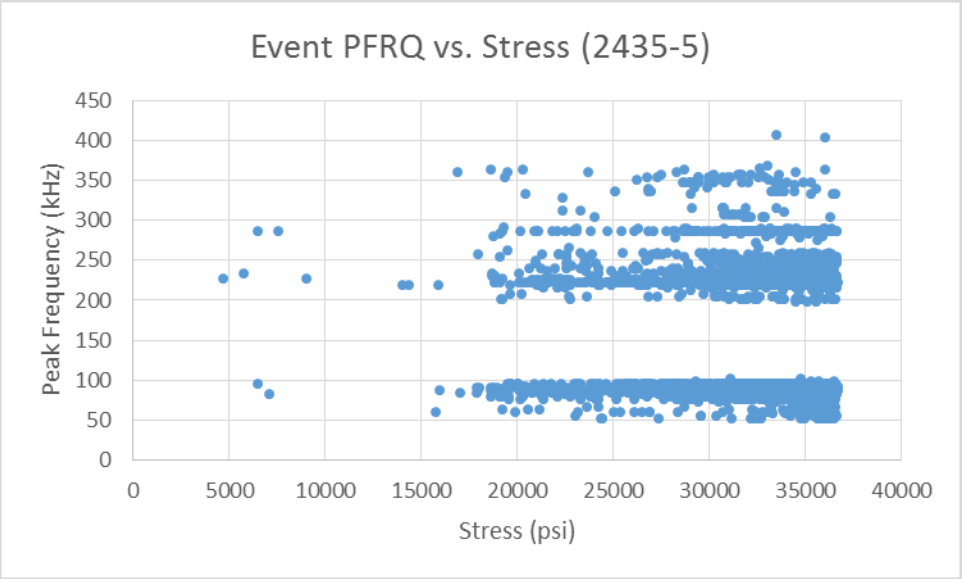

Event PFRQ vs. Stress (2435-3)
Peak Frequency (kHz)
350
300
250
200
150
100
50
0
0
5000
10000
15000
20000
25000
30000
35000
Stress (psi)

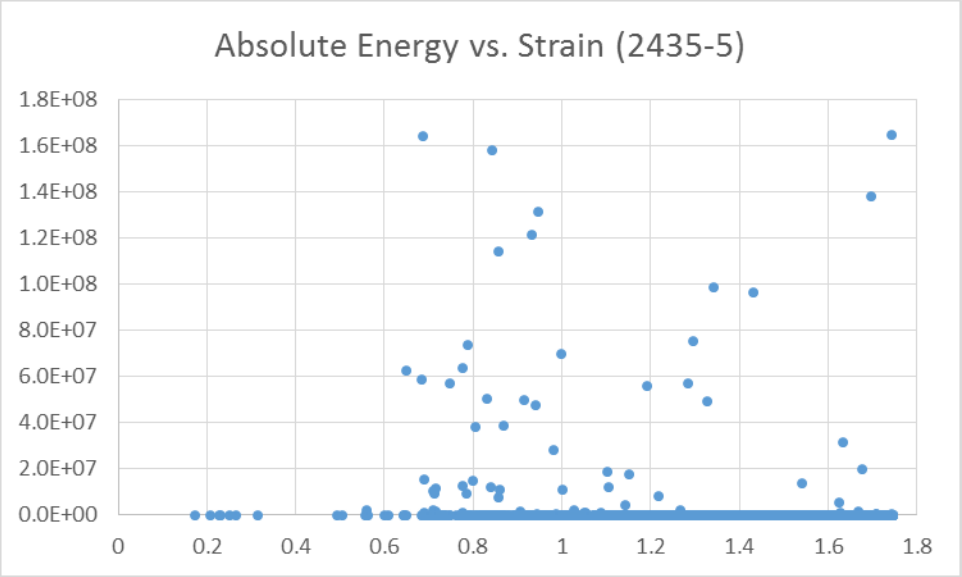

Event PFRQ vs. Strain (2435-3)
Peak Frequency (kHz)
350
300
250
200
150
100
50
0
0
0.2
0.4
0.6
0.8
1
1.2
1.4
1.6
1.8
Actuator Strain (%)


Absolute Energy vs. Strain (2435-3)
Absolute Charity (aJ)
1.4E+09
1.2E+09
1.0E+09
8.0E+08
6.0E+08
4.0E+08
2.0E+08
0.0E+00
0
0.2
0.4
0.6
0.8
1
1.2
1.4
1.6
1.8
Actuator Strain (%)

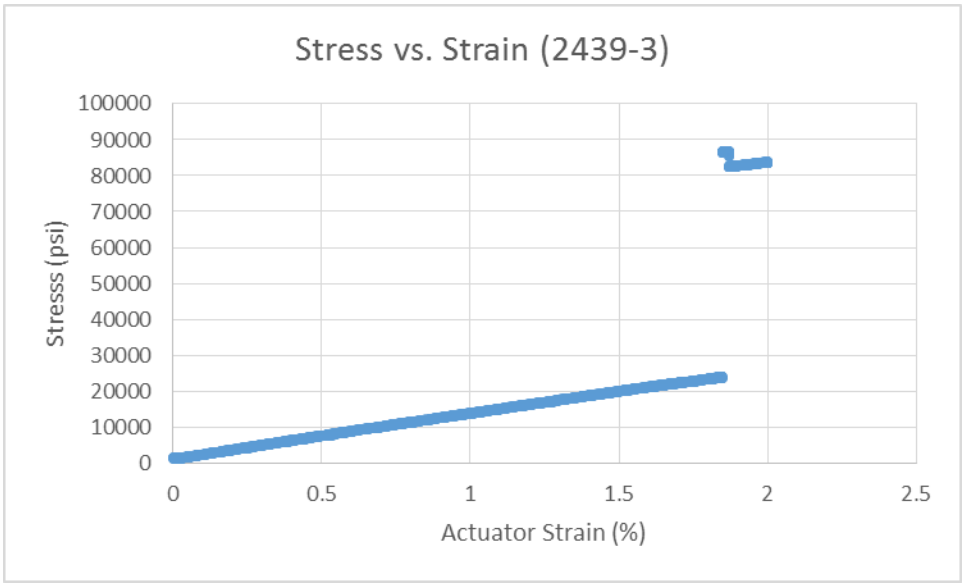

Stress vs. Strain (2435-5)
Stress (psi)
40000
35000
30000
25000
20000
15000
10000
5000
0
0
0.2
0.4
0.6
0.8
1
1.2
1.4
1.6
1.8
Actuator Strain (%)

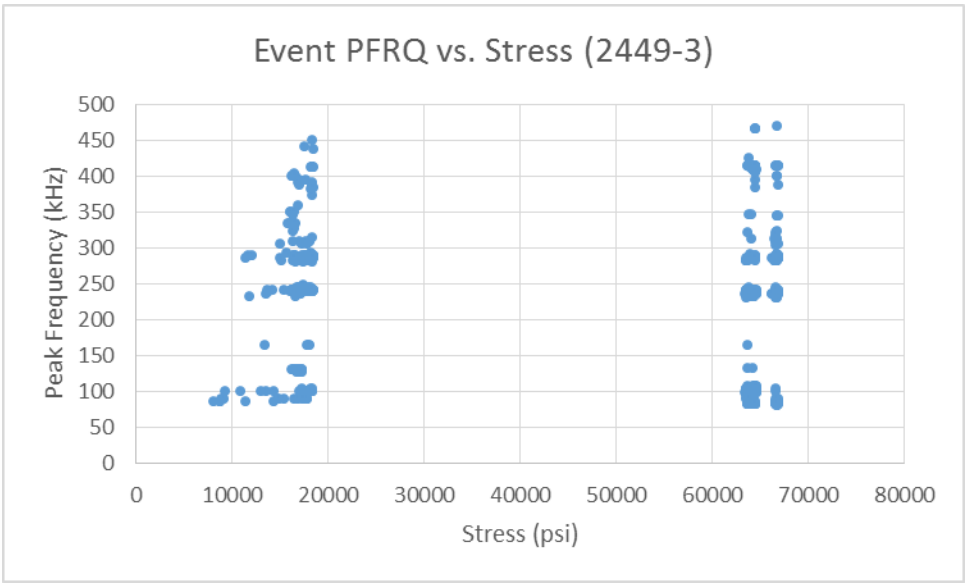

Event PFRQ vs. Strain (2435-5)
Peak Frequency (kHz)
450
400
350
300
250
200
150
100
50
0
0
0.2
0.4
0.6
0.8
1
1.2
1.4
1.6
1.8
Actuator Strain (%)

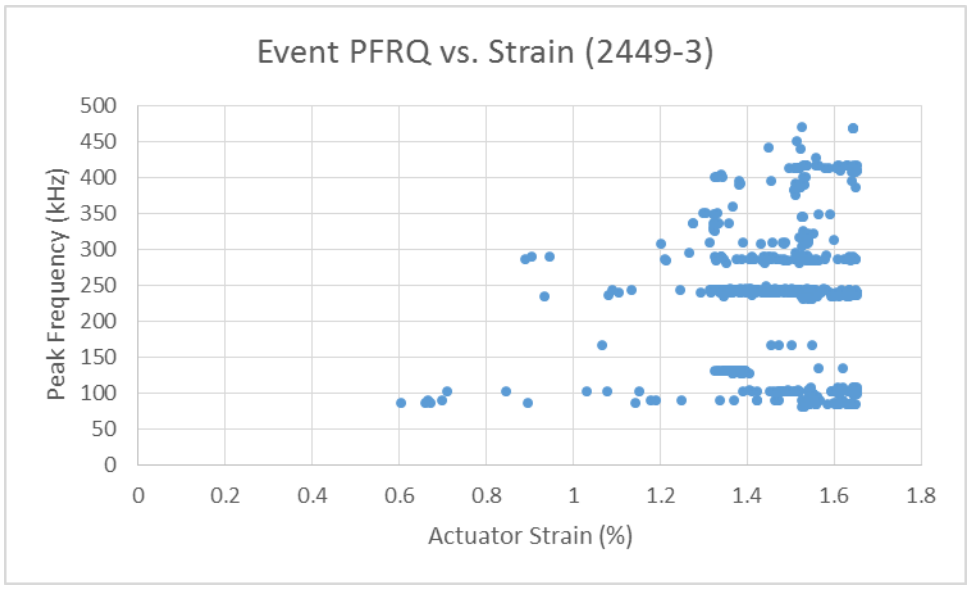

Event PFRQ vs. Stress (2435-5)
Peak Frequency (kHz)
450
400
350
300
250
200
150
100
50
0
0
5000
10000
15000
20000
25000
30000
35000
40000
Stress (psi)

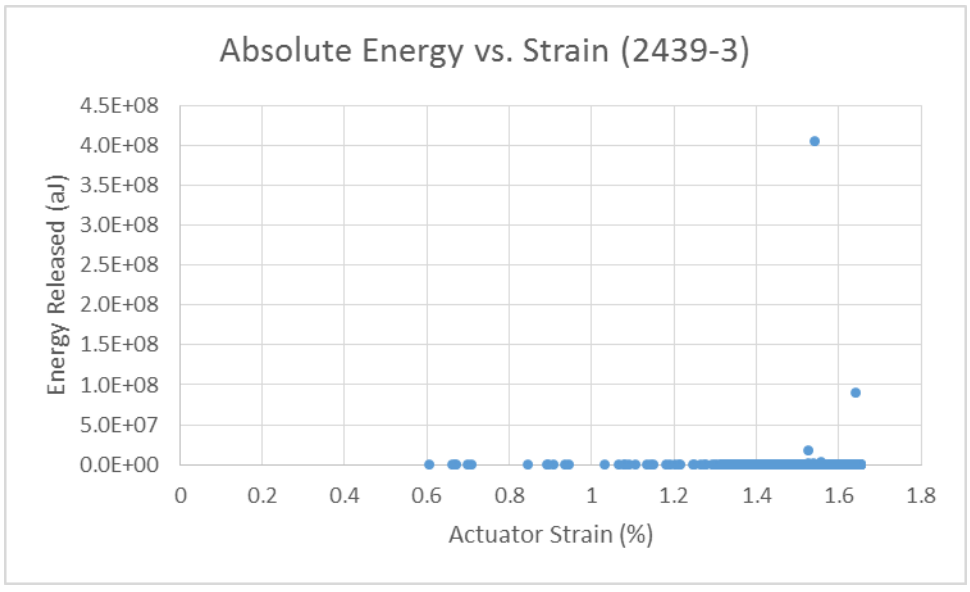

Absolute Energy vs. Strain (2435-5)
1.8E+08
1.6E+08
1.4E+08
1.2E+08
1.0E+08
8.0E+07
6.0E+07
4.0E+07
2.0E+07
0.0E+00
0
0.2
0.4
0.6
0.8
1
1.2
1.4
1.6
1.8

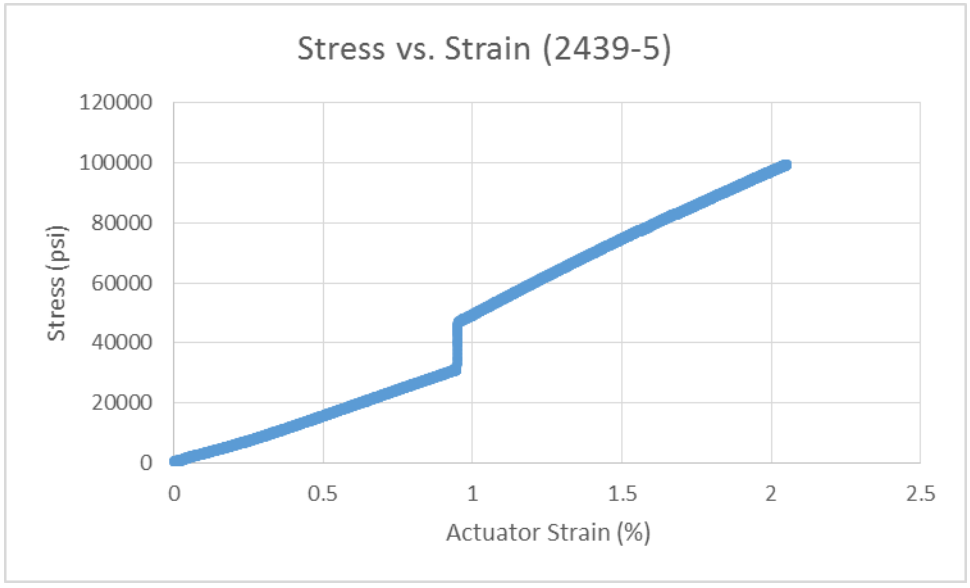
GLASS- A1*

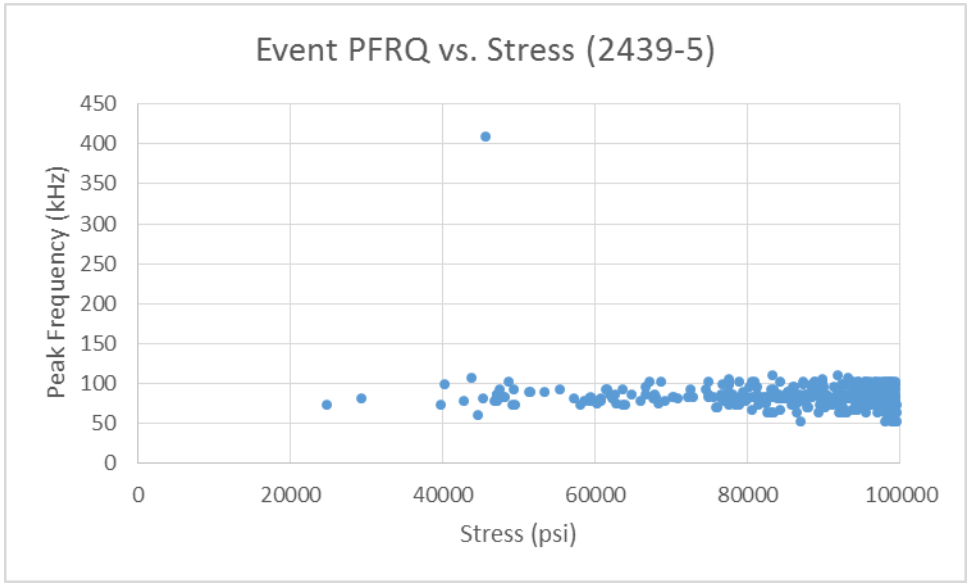

Stress vs. Strain (2439-3)
Stresss (psi)
100000
90000
80000
70000
60000
50000
40000
30000
20000
10000
0
0
0.5
1
1.5
2
2.5
Actuator Strain (%)

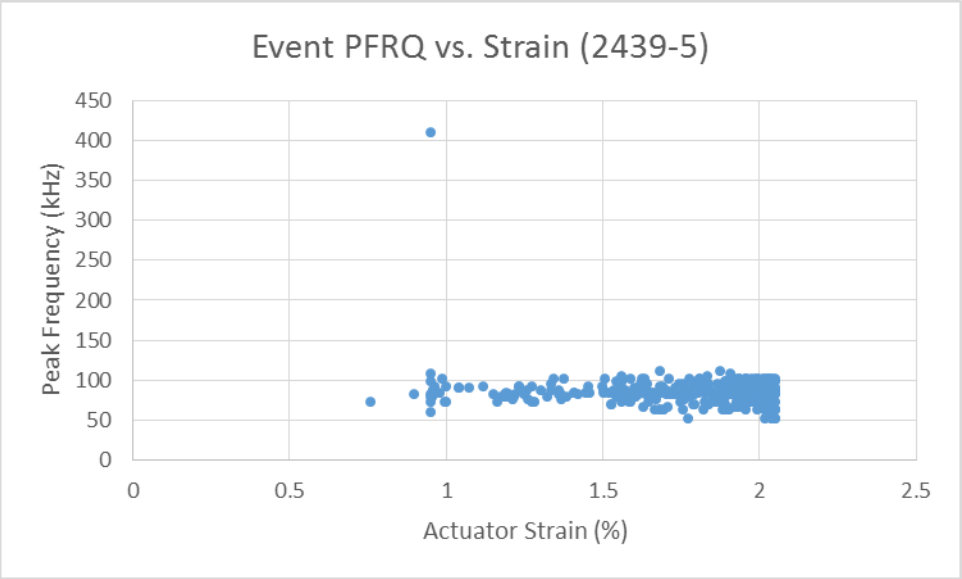

Event PFRQ vs. Stress (2449-3)
Peak Frequency (kHz)
500
450
400
350
300
250
200
150
100
50
0
0
10000
20000
30000
40000
50000
60000
70000
80000
Stress (psi)

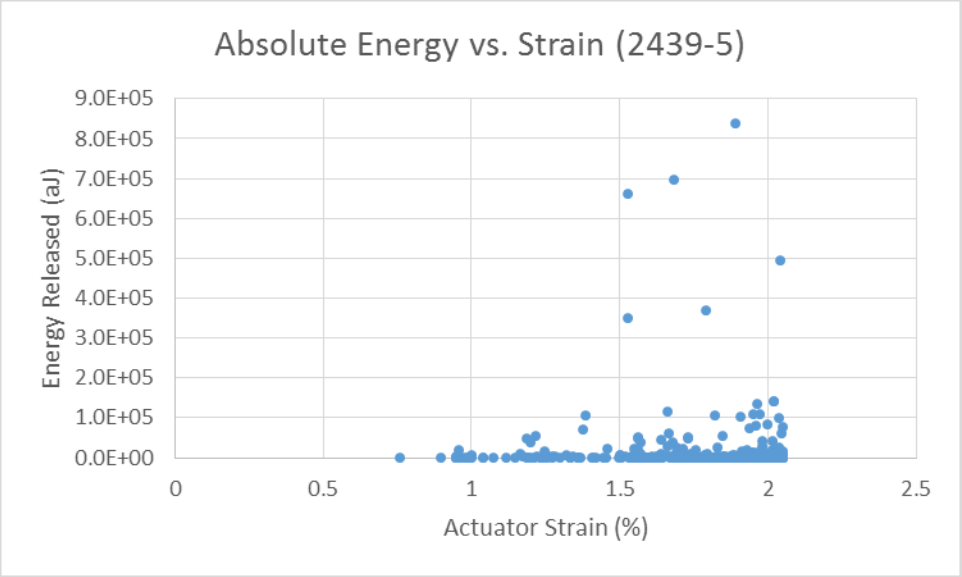

Event PFRQ vs. Strain (2449-3)
Peak Frequency (kHz)
500
450
400
350
300
250
200
150
100
50
0
0
0.2
0.4
0.6
0.8
1
1.2
1.4
1.6
1.8
Actuator Strain (%)


Absolute Energy vs. Strain (2439-3)
Energy Released (aJ)
4.5E+08
4.0E+08
3.5E+08
3.0E+08
2.5E+08
2.0E+08
1.5E+08
1.0E+08
5.0E+07
0.0E+00
0
0.2
0.4
0.6
0.8
1
1.2
1.4
1.6
1.8
Actuator Strain (%)

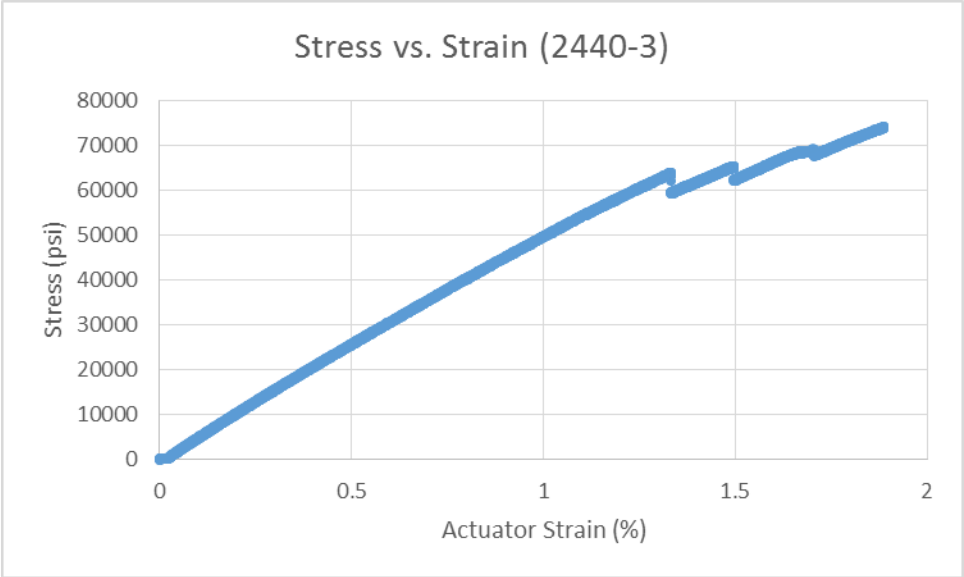

Stress vs. Strain (2439-5)
120000
100000
80000
60000
40000
20000
0
Stress (psi)
0
0.5
1
1.5
2
2.5
Actuator Strain (%)

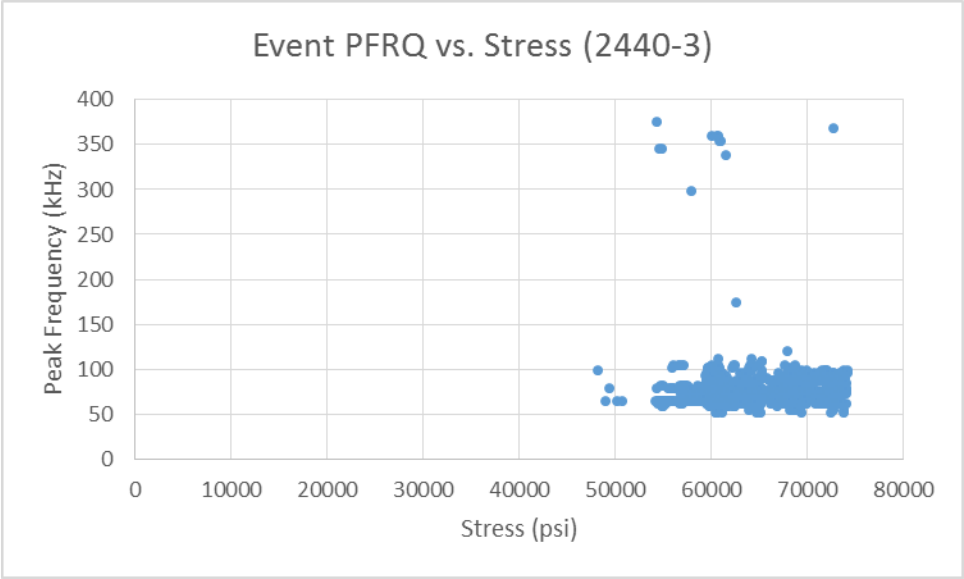

Event PFRQ vs. Stress (2439-5)
450
400
350
300
250
200
150
100
50
0
Peak Frequency (kHz)
0
20000
40000
60000
80000
100000
Stress (psi)

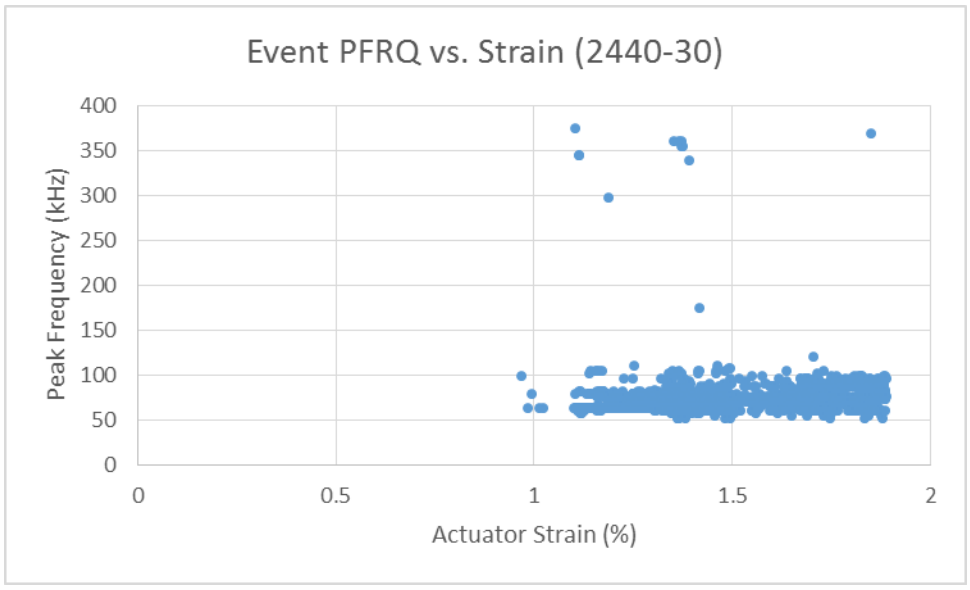

Event PFRQ vs. Strain (2439-5)
Peak Frequency (kHz)
450
400
350
300
250
200
150
100
50
0
0
0.5
1
1.5
2
2.5
Actuator Strain (%)

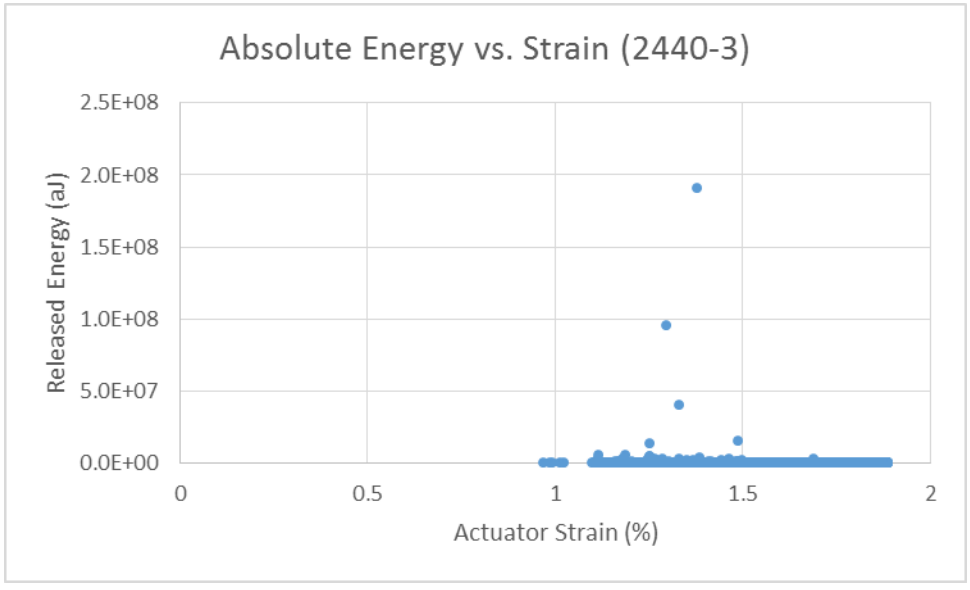

Absolute Energy vs. Strain (2439-5)
Energy Released (aJ)
9.0E+05
8.0E+05
7.0E+05
6.0E+05
5.0E+05
4.0E+05
3.0E+05
2.0E+05
1.0E+05
0.0E+00
0
0.5
1
1.5
2
2.5
Actuator Strain (%)

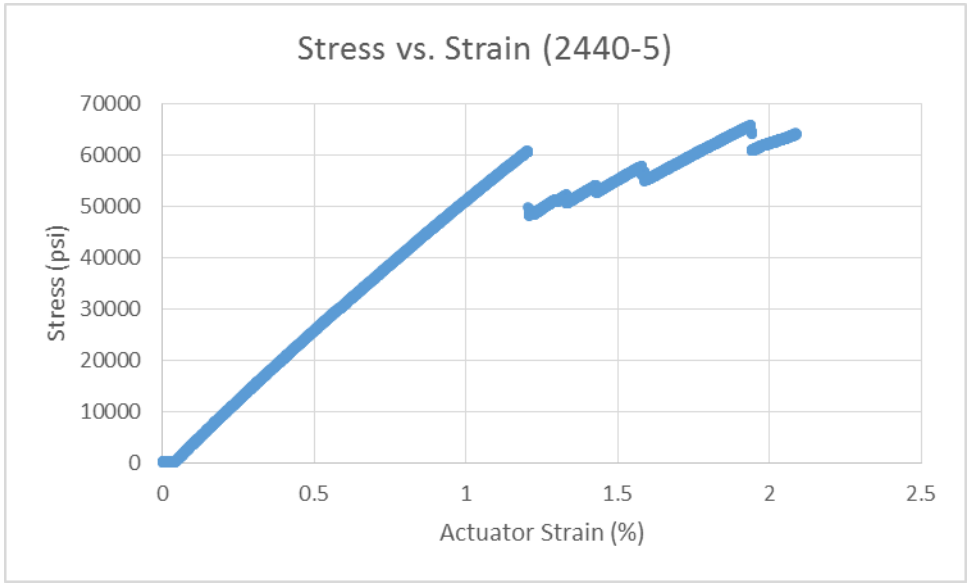
GLASS- A1

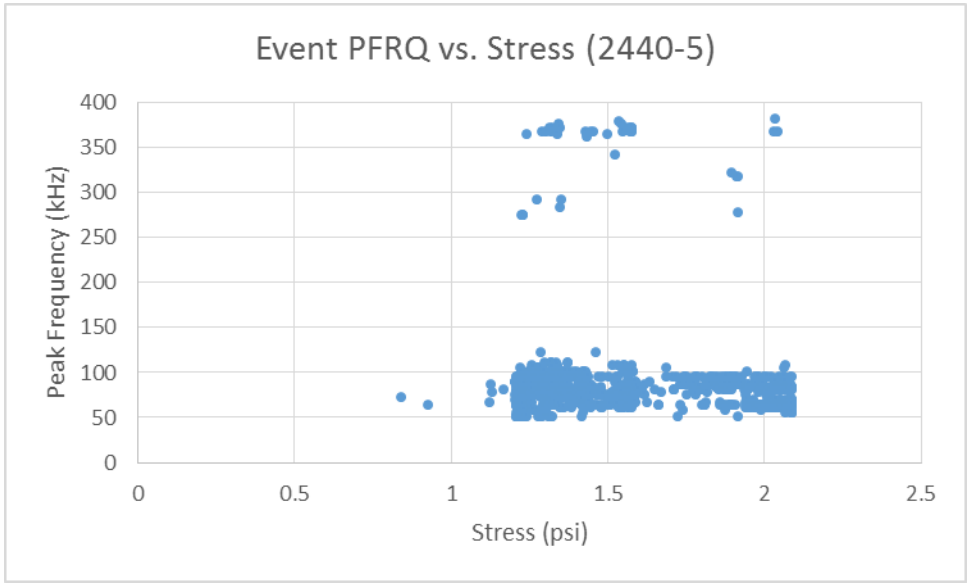

Stress vs. Strain (2440-3)
Stress (psi)
80000
70000
60000
50000
40000
30000
20000
10000
0
0
0.5
1
1.5
2
Actuator Strain (%)

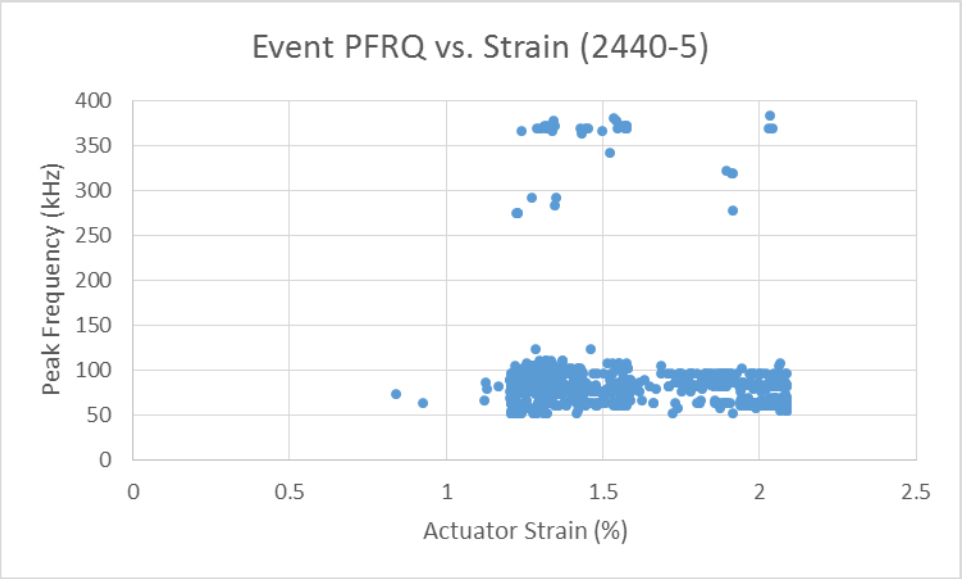

Event PFRQ vs. Stress (2440-3)
Peak Frequency (kHz)
400
350
300
250
200
150
100
50
0
0
10000
20000
30000
40000
50000
60000
70000
80000
Stress (psi)

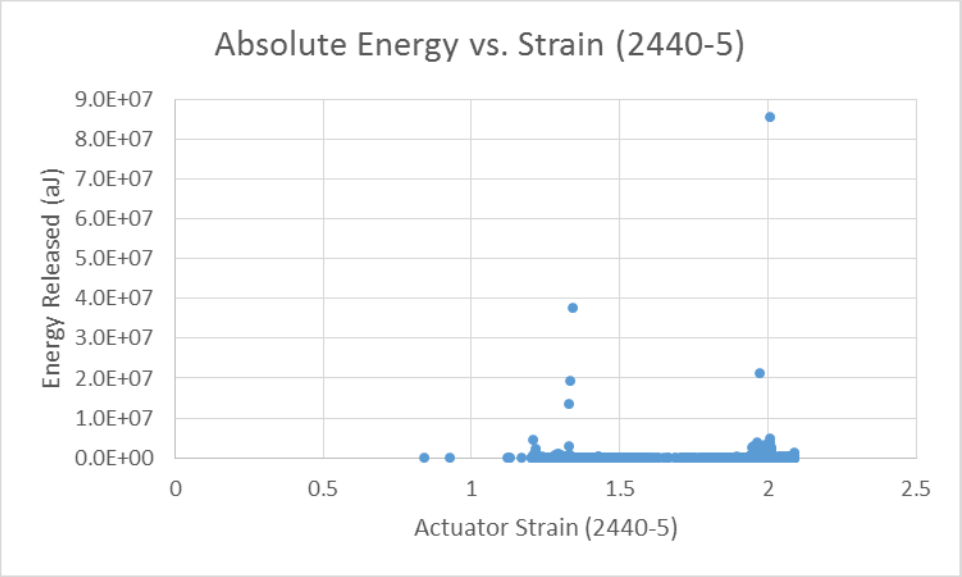

Event PFRQ vs. Strain (2440-30)
Peak Frequency (kHz)
400
350
300
250
200
150
100
50
0
0
0.5
1
1.5
2
Actuator Strain (%)


Absolute Energy vs. Strain (2440-3)
Released Energy (aJ)
2.5E+08
2.0E+08
1.5E+08
1.0E+08
5.0E+07
0.0E+00
0
0.5
1
1.5
2
Actuator Strain (%)

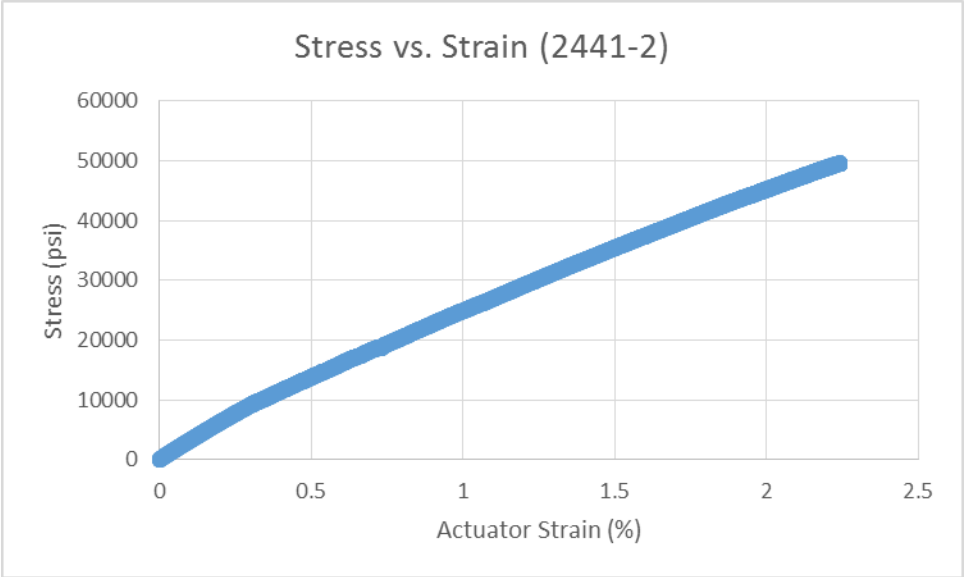

Stress vs. Strain (2440-5)
Stress (psi)
70000
60000
50000
40000
30000
20000
10000
0
0
0.5
1
1.5
2
2.5
Actuator Strain (%)

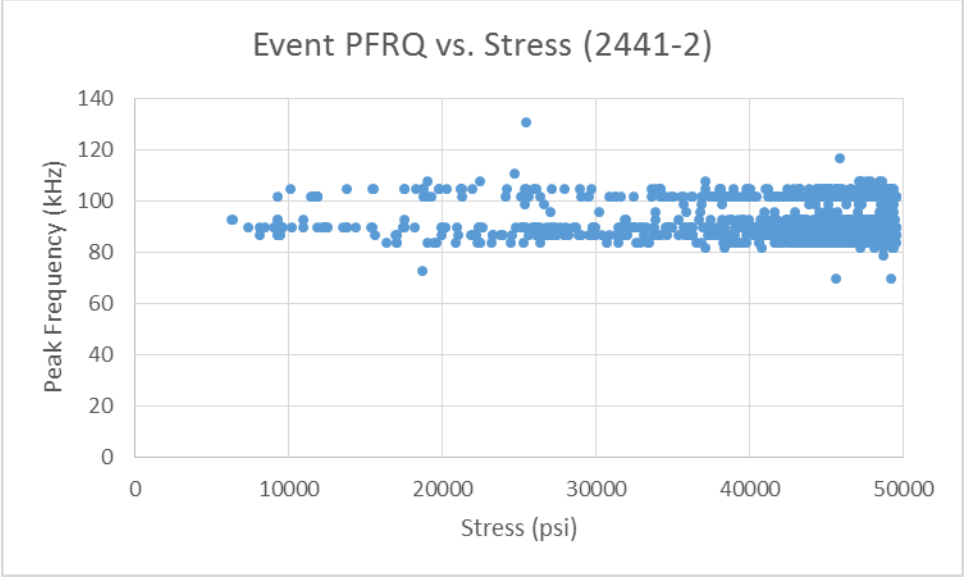

Event PFRQ vs. Stress (2440-5)
Peak Frequency (kHz)
400
350
300
250
200
150
100
50
0
0
0.5
1
1.5
2
2.5
Stress (psi)

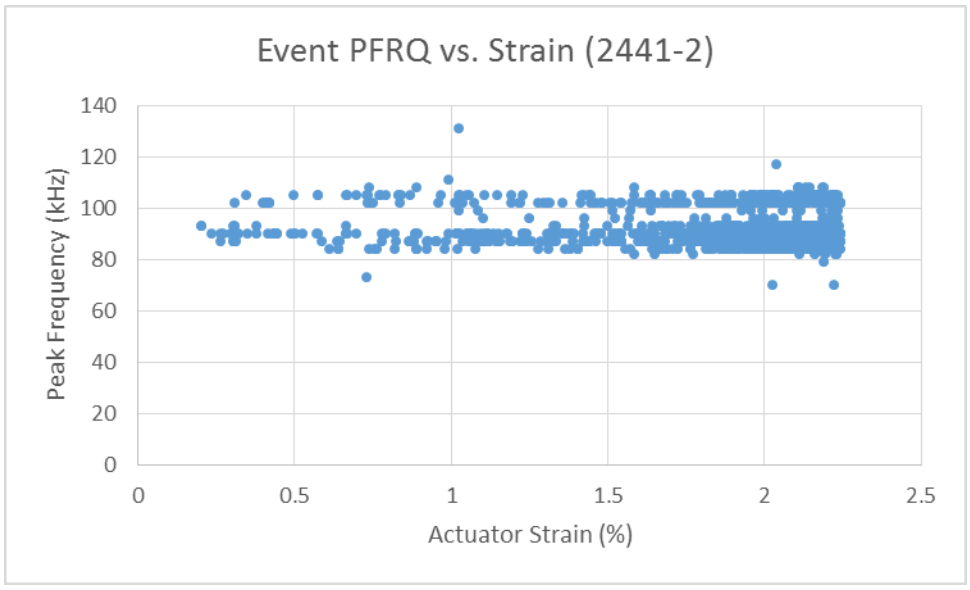

Event PFRQ vs. Strain (2440-5)
Peak Frequency (kHz)
400
350
300
250
200
150
100
50
0
0
0.5
1
1.5
2
2.5
Actuator Strain (%)

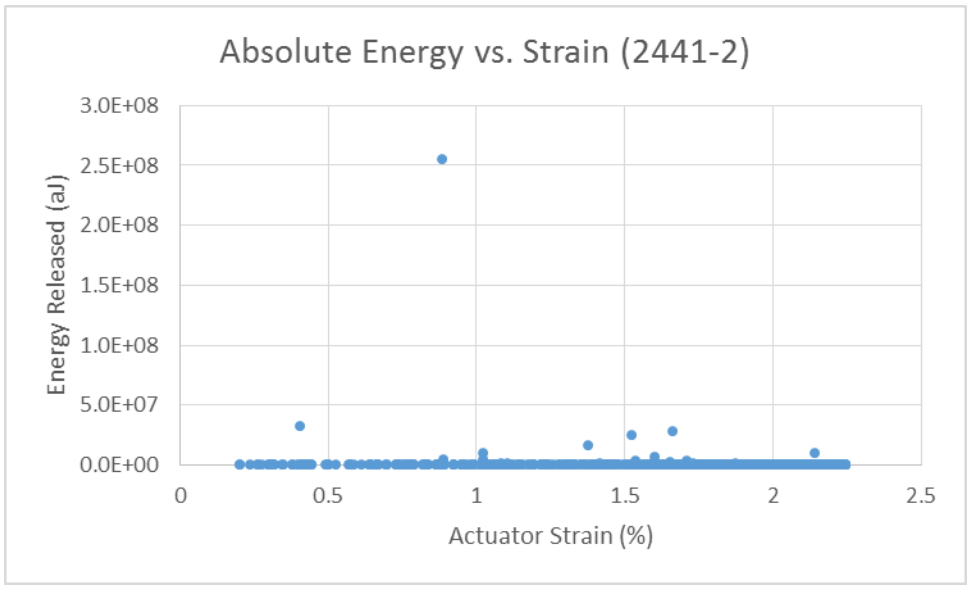

Absolute Energy vs. Strain (2440-5)
Energy Released (aJ)
9.0E+07
8.0E+07
7.0E+07
6.0E+07
5.0E+07
4.0E+07
3.0E+07
2.0E+07
1.0E+07
0.0E+00
0
0.5
1
1.5
2
2.5
Actuator Strain (2440-5)

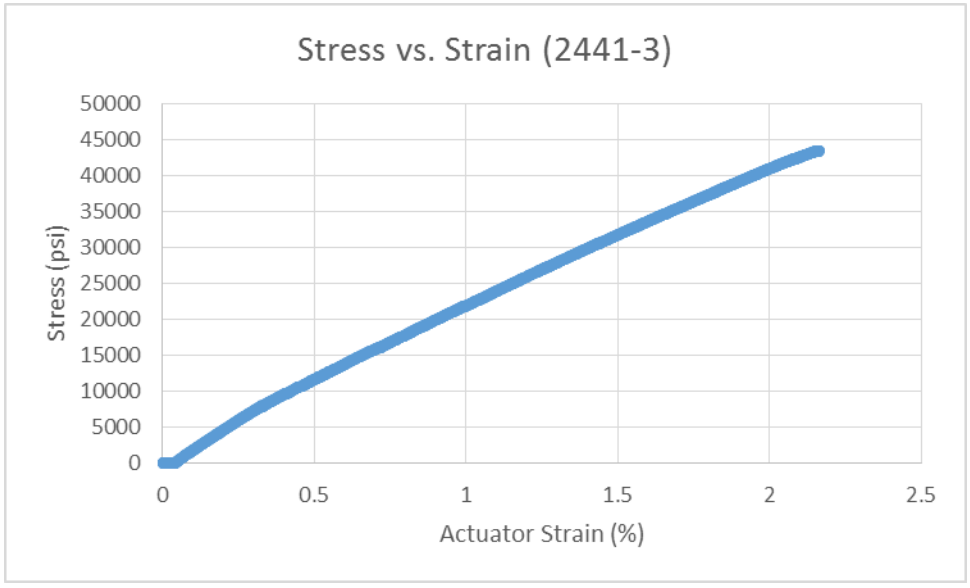
GLASS- A3

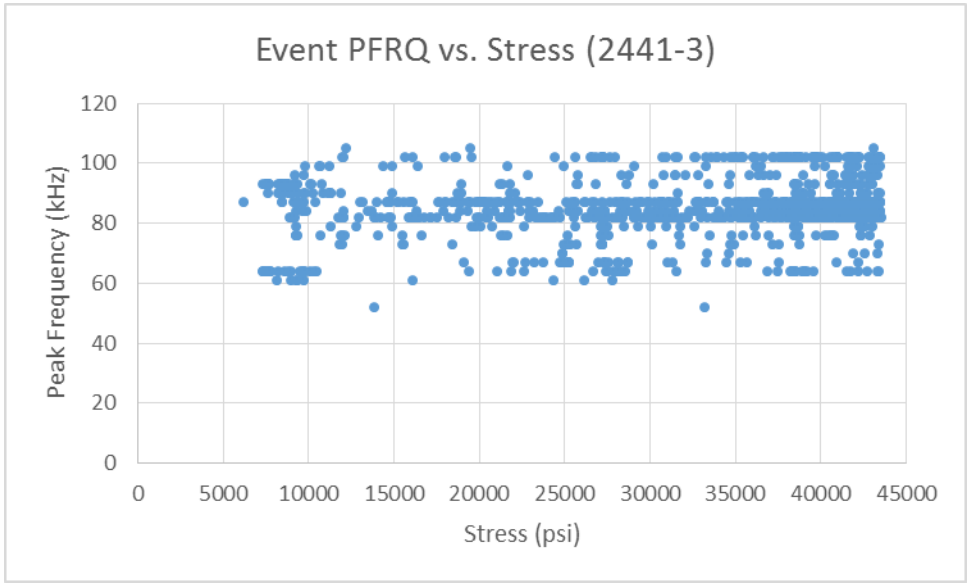

Stress vs. Strain (2441-2)
Stress (psi)
60000
50000
40000
30000
20000
10000
0
0
0.5
1
1.5
2
2.5
Actuator Strain (%)

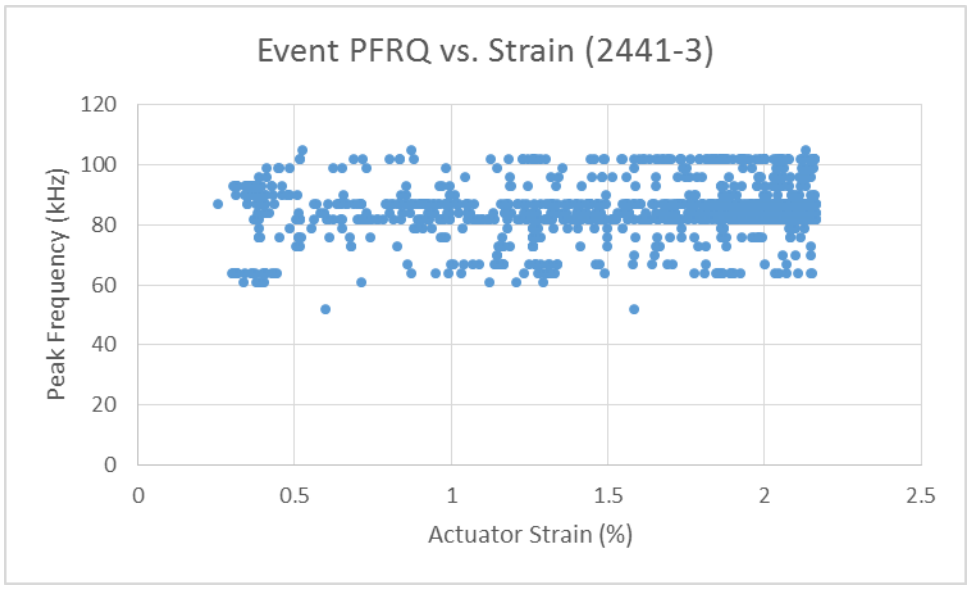

Event PFRQ vs. Stress (2441-2)
Peak Frequency (kHz)
140
120
100
80
60
40
20
0
0
10000
20000
30000
40000
50000
Stress (psi)

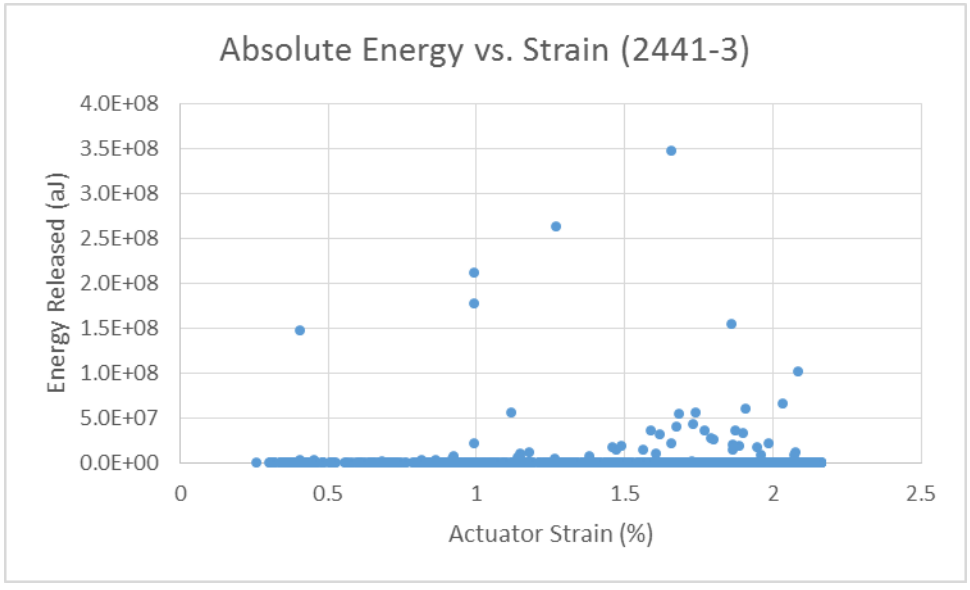

Event PFRQ vs. Strain (2441-2)
Peak Frequency (kHz)
140
120
100
80
60
40
20
0
0
0.5
1
1.5
2
2.5
Actuator Strain (%)

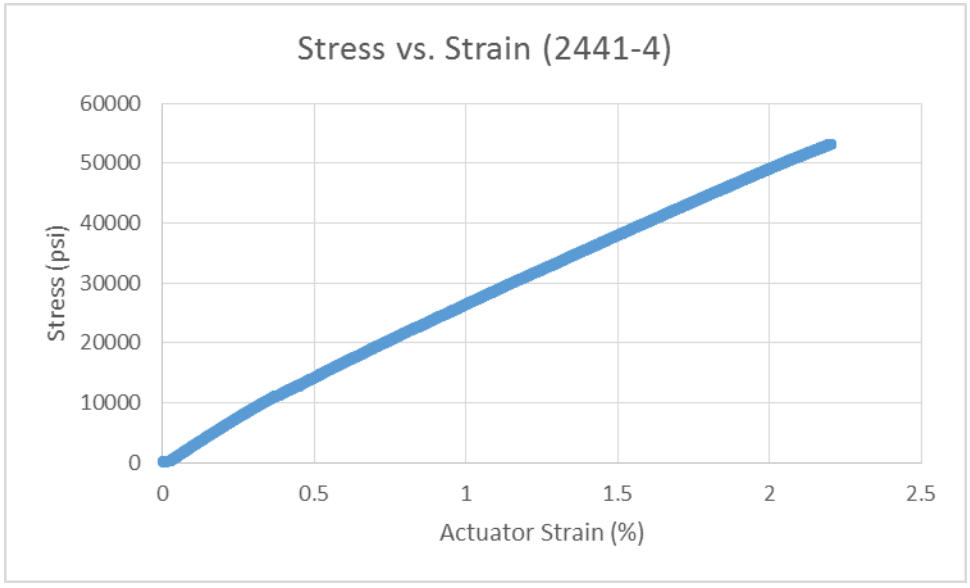

Absolute Energy vs. Strain (2441-2)
Energy Released (aJ)
3.0E+08
2.5E+08
2.0E+08
1.5E+08
1.0E+08
5.0E+07
0.0E+00
0
0.5
1
1.5
2
2.5
Actuator Strain (%)

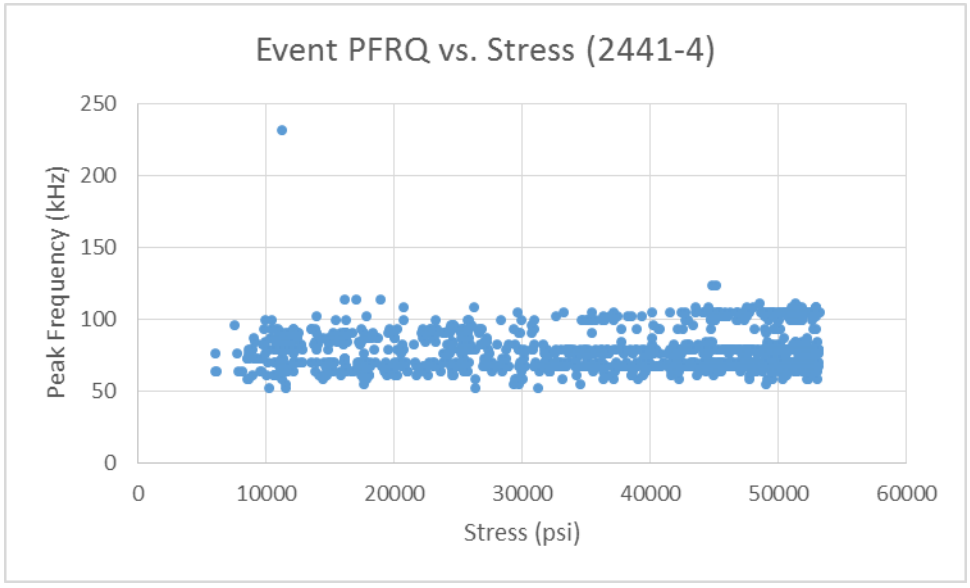

Stress vs. Strain (2441-3)
Stress (psi)
50000
45000
40000
35000
30000
25000
20000
15000
10000
5000
0
0
0.5
1
1.5
2
2.5
Actuator Strain (%)

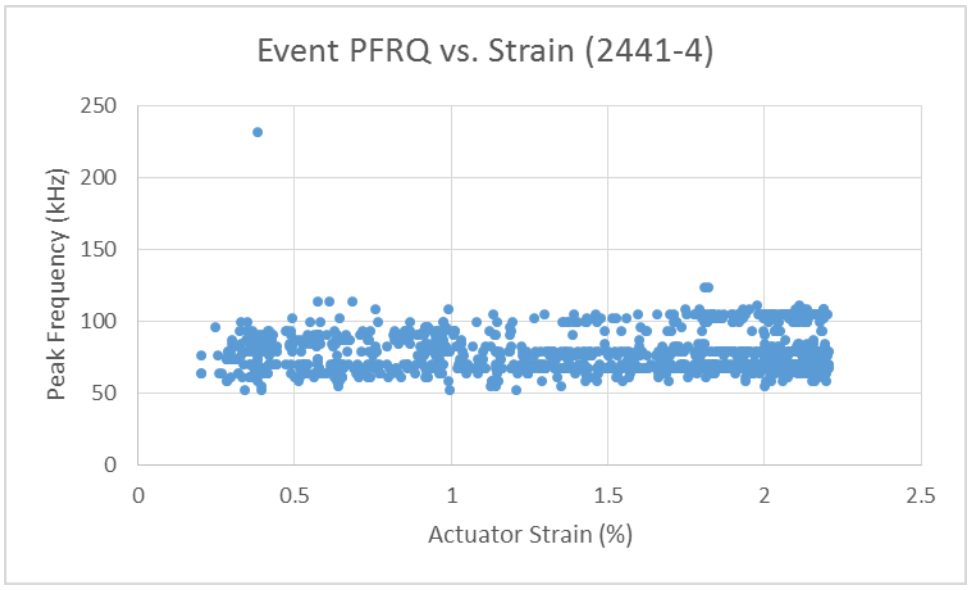

Event PFRQ vs. Stress (2441-3)
Peak Frequency (kHz)
120
100
80
60
40
20
0
0
5000
10000
15000
20000
25000
30000
35000
40000
45000
Stress (psi)

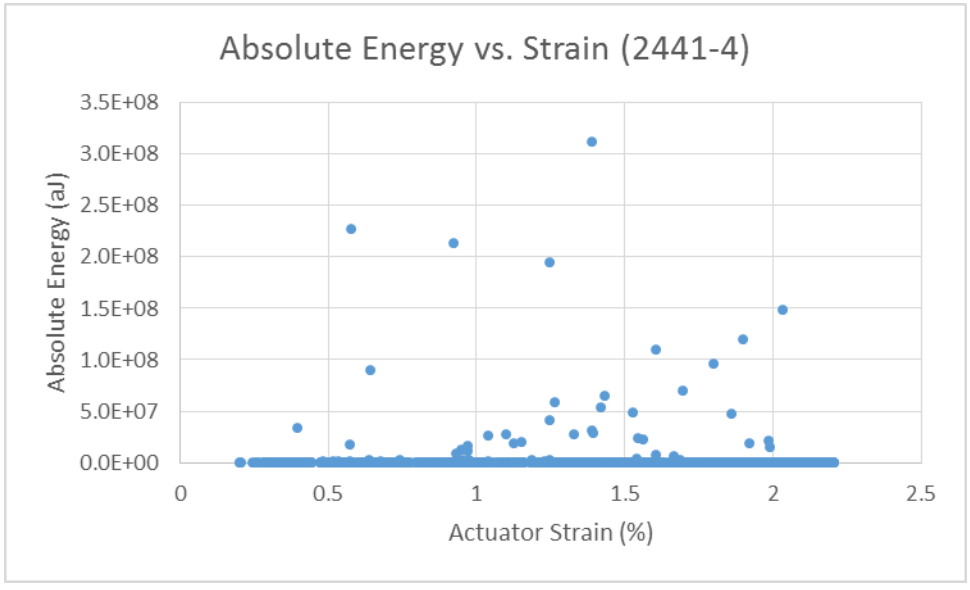

Event PFRQ vs. Strain (2441-3)
Peak Frequency (kHz)
120
100
80
60
40
20
0
0
0.5
1
1.5
2
2.5
Actuator Strain (%)

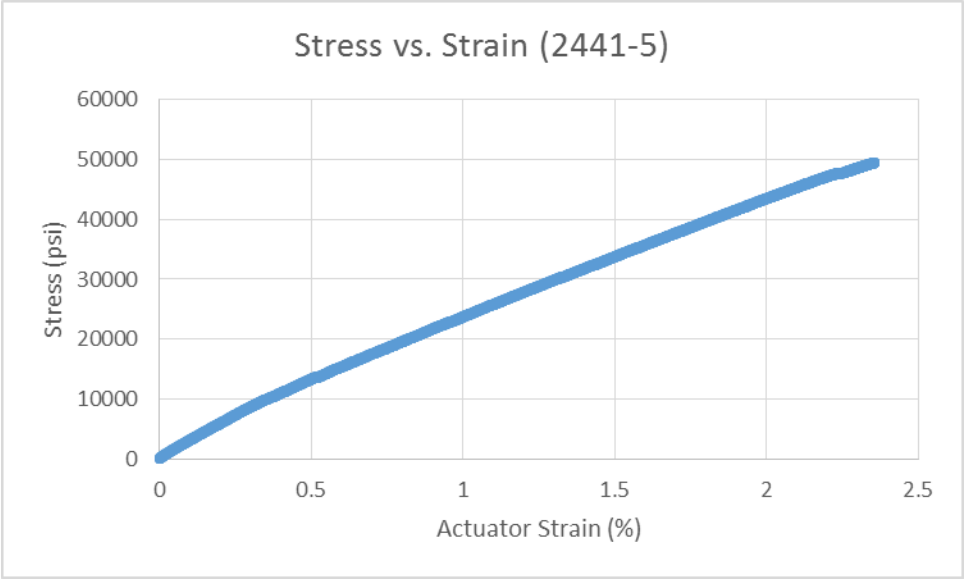

Absolute Energy vs. Strain (2441-3)
Energy Released (aJ)
4.0E+08
3.5E+08
3.0E+08
2.5E+08
2.0E+08
1.5E+08
1.0E+08
5.0E+07
0.0E+00
0
0.5
1
1.5
2
2.5
Actuator Strain (%)

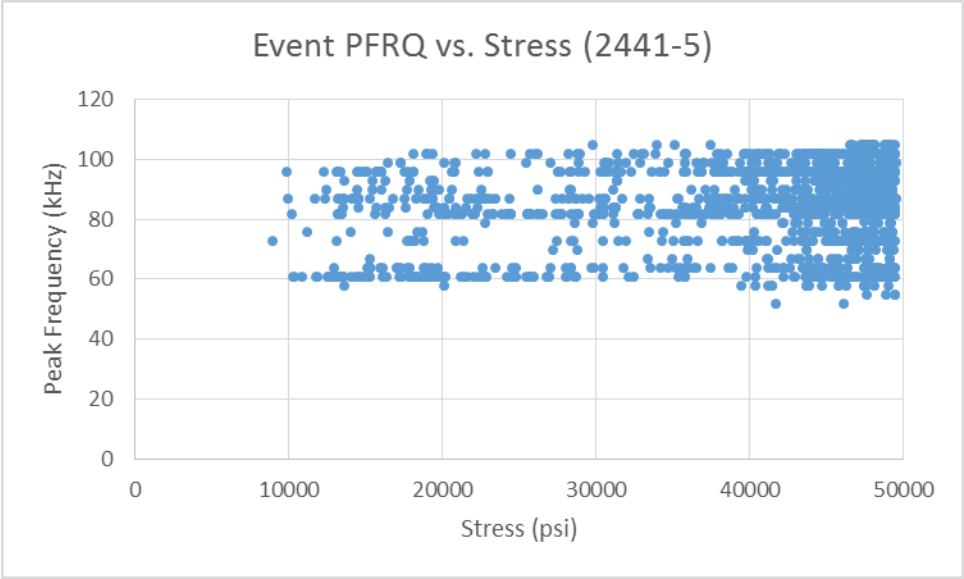

Stress vs. Strain (2441-4)
Stress (psi)
60000
50000
40000
30000
20000
10000
0
0
0.5
1
1.5
2
2.5
Actuator Strain (%)

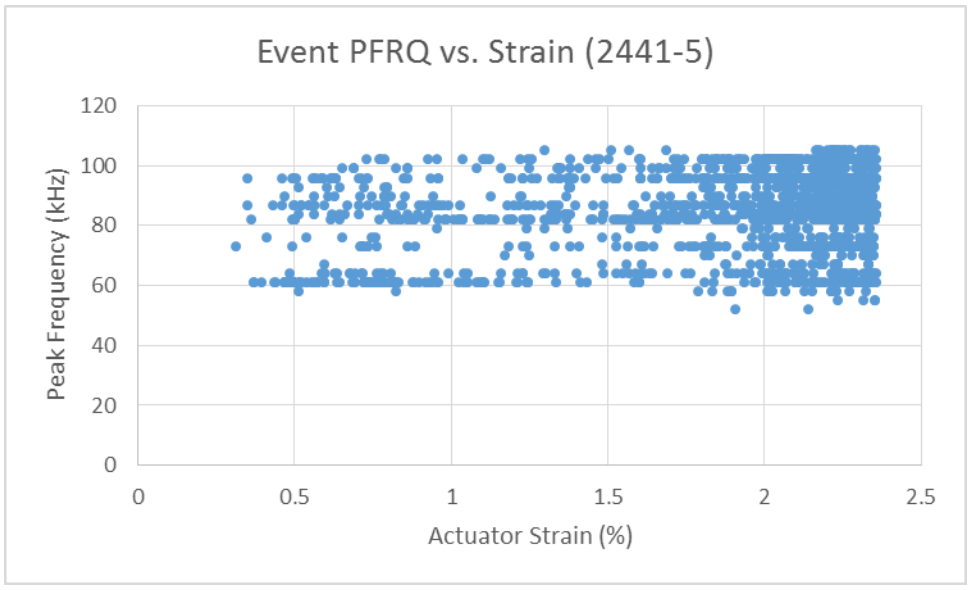

Event PFRQ vs. Stress (2441-4)
Peak Frequency (kHz)
250
200
150
100
50
0
0
10000
20000
30000
40000
50000
60000
Stress (psi)

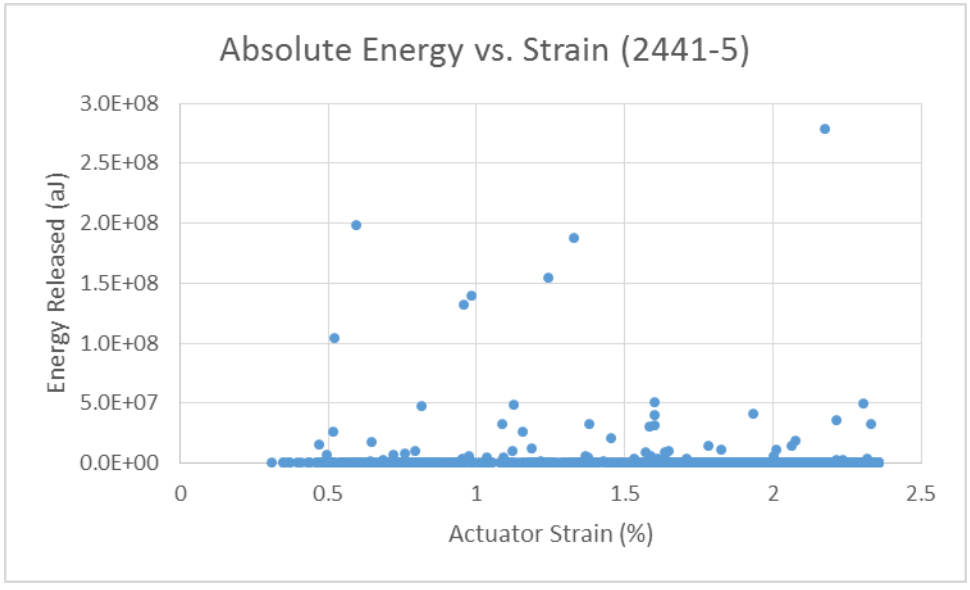

Event PFRQ vs. Strain (2441-4)
Peak Frequency (kHz)
250
200
150
100
50
0
0
0.5
1
1.5
2
2.5
Actuator Strain (%)

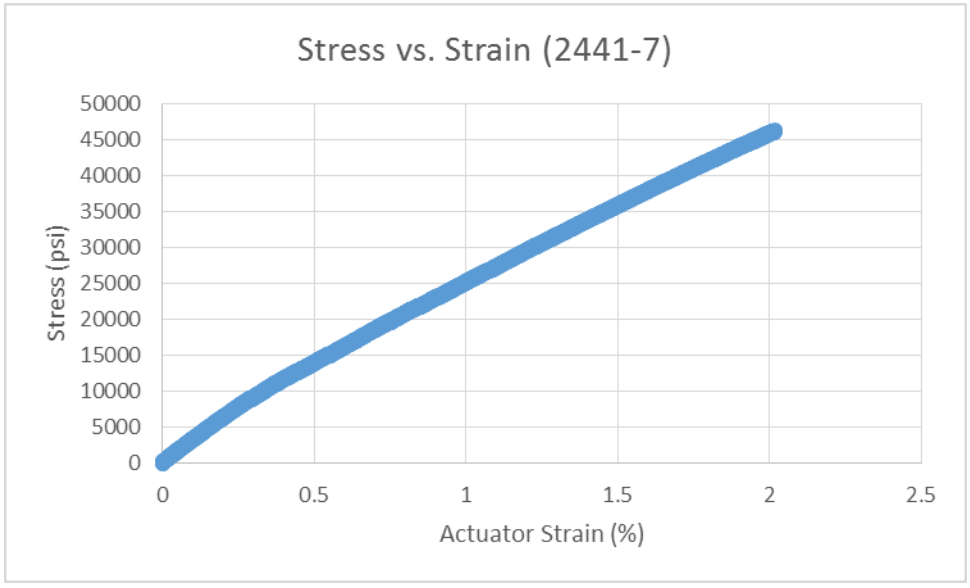

Absolute Energy vs. Strain (2441-4)
Absolute Energy (aJ)
3.5E+08
3.0E+08
2.5E+08
2.0E+08
1.5E+08
1.0E+08
5.0E+07
0.0E+00
0
0.5
1
1.5
2
2.5
Actuator Strain (%)

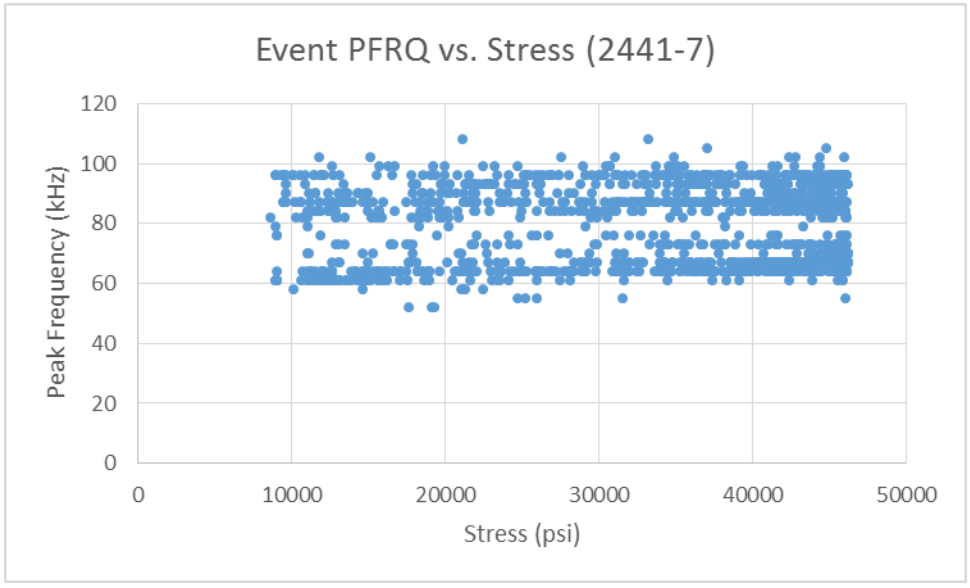

Stress vs. Strain (2441-5)
Stress (psi)
60000
50000
40000
30000
20000
10000
0
0
0.5
1
1.5
2
2.5
Actuator Strain (%)

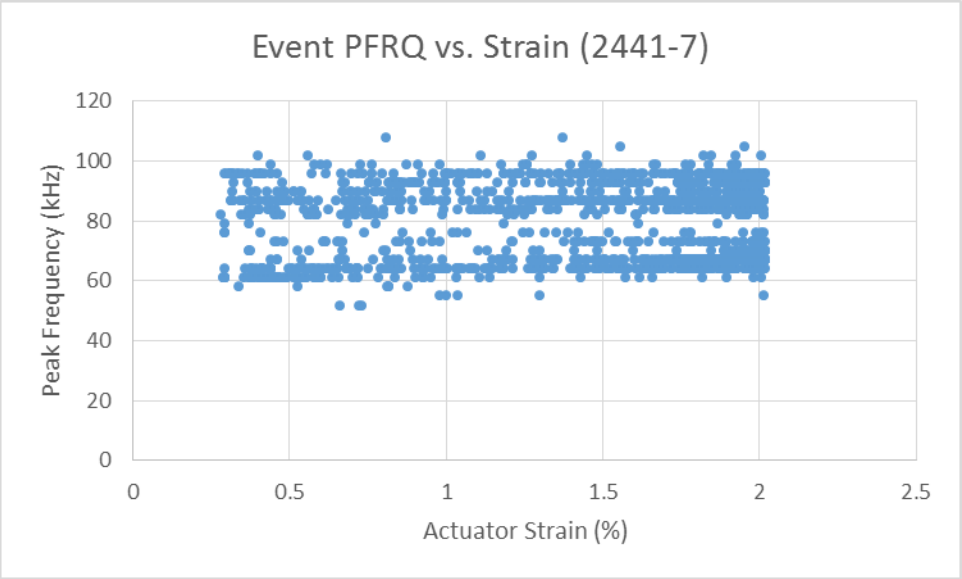

Event PFRQ vs. Stress (2441-5)
Peak Frequency (kHz)
120
100
80
60
40
20
0
0
10000
20000
30000
40000
50000
Stress (psi)

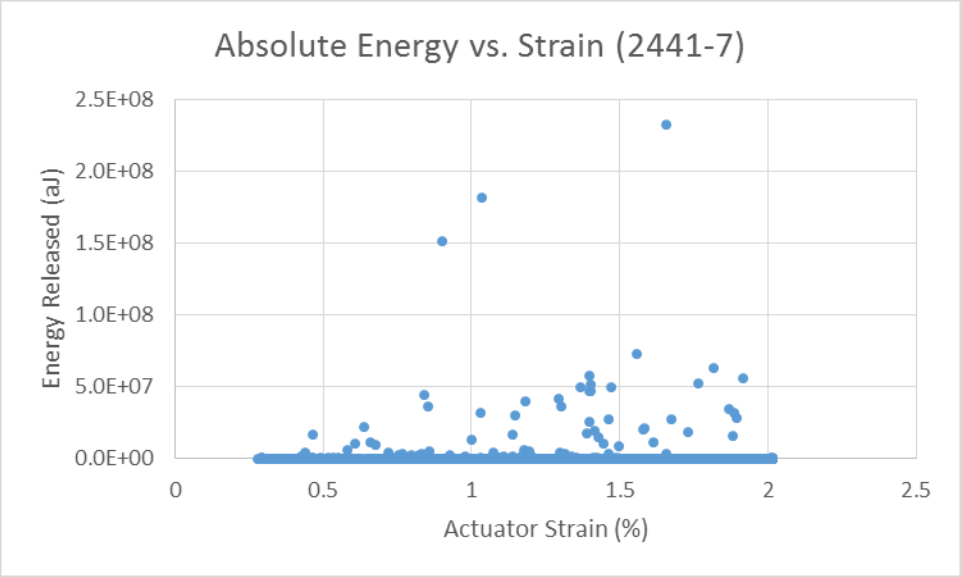

Event PFRQ vs. Strain (2441-5)
Peak Frequency (kHz)
120
100
80
60
40
20
0
0
0.5
1
1.5
2
2.5
Actuator Strain (%)


Absolute Energy vs. Strain (2441-5)
Energy Released (aJ)
3.0E+08
2.5E+08
2.0E+08
1.5E+08
1.0E+08
5.0E+07
0.0E+00
0
0.5
1
1.5
2
2.5
Actuator Strain (%)

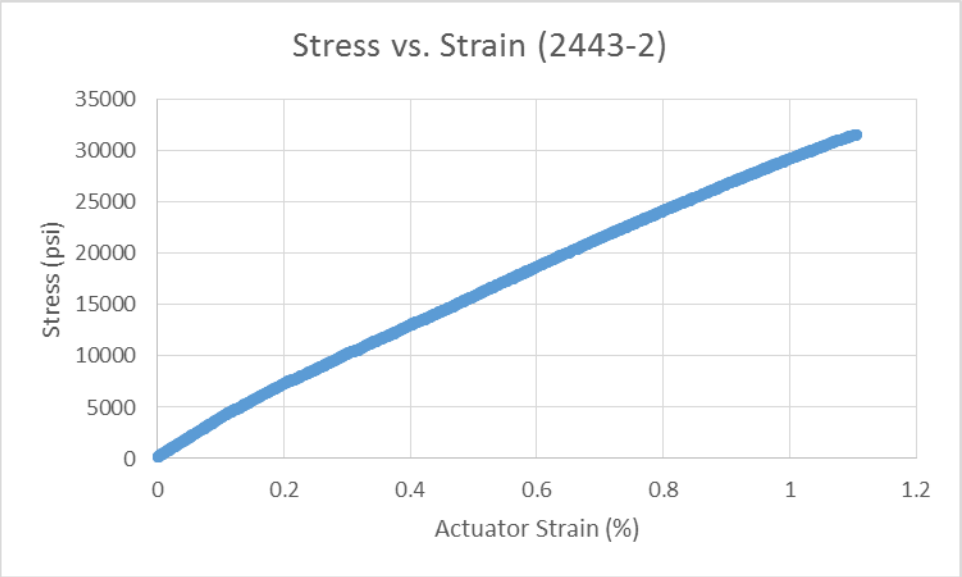

Stress vs. Strain (2441-7)
Stress (psi)
50000
45000
40000
35000
30000
25000
20000
15000
10000
5000
0
0
0.5
1
1.5
2
2.5
Actuator Strain (%)

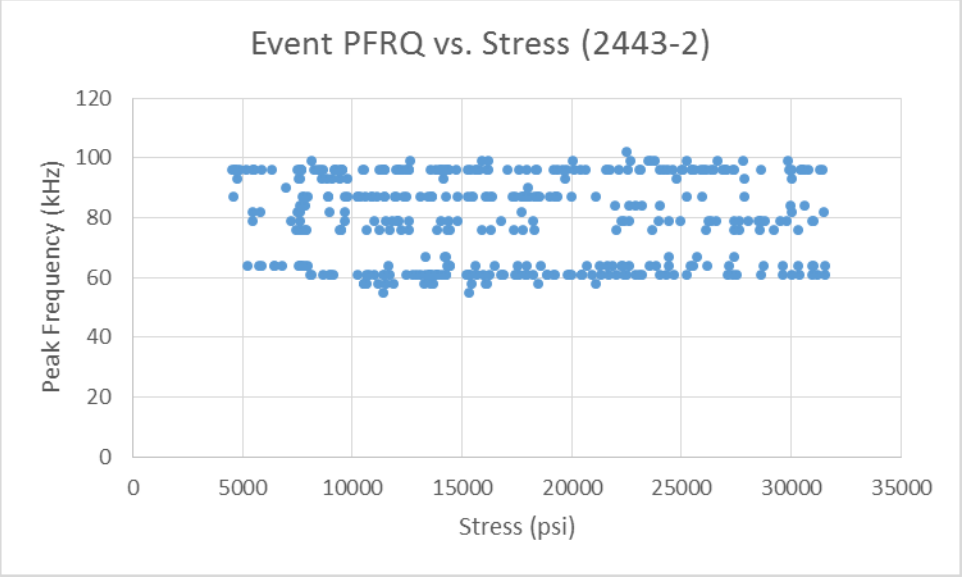

Event PFRQ vs. Stress (2441-7)
Peak Frequency (kHz)
120
100
80
60
40
20
0
0
10000
20000
30000
40000
50000
Stress (psi)

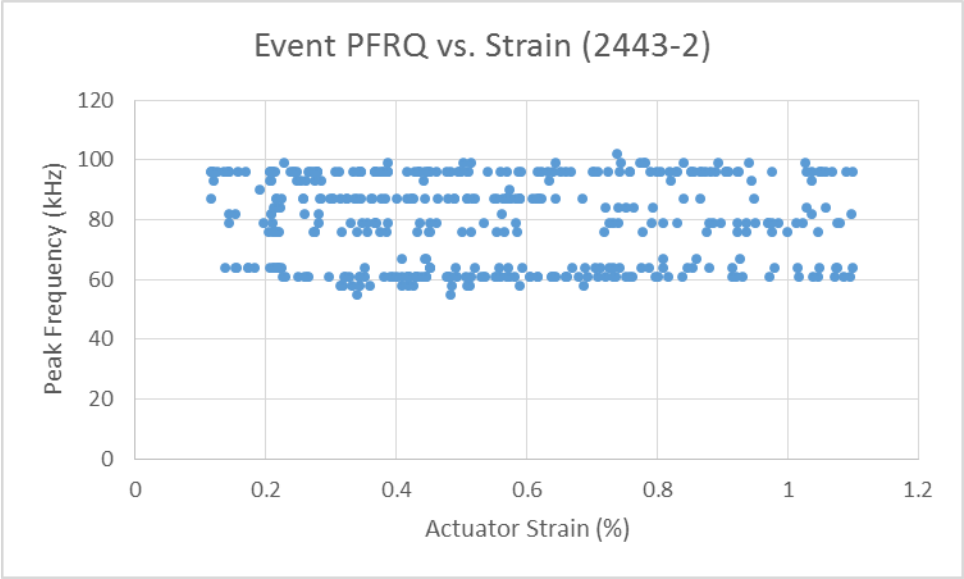

Event PFRQ vs. Strain (2441-7)
Peak Frequency (kHz)
120
100
80
60
40
20
0
0
0.5
1
1.5
2
2.5
Actuator Strain (%)

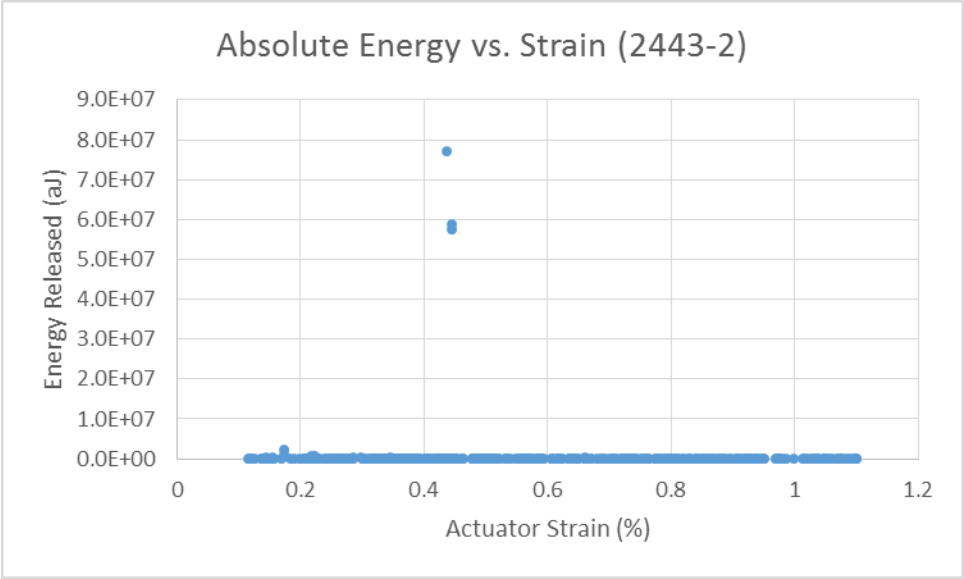

Absolute Energy vs. Strain (2441-7)
Energy Released (aJ)
2.5E+08
2.0E+08
1.5E+08
1.0E+08
5.0E+07
0.0E+00
0
0.5
1
1.5
2
2.5
Actuator Strain (%)

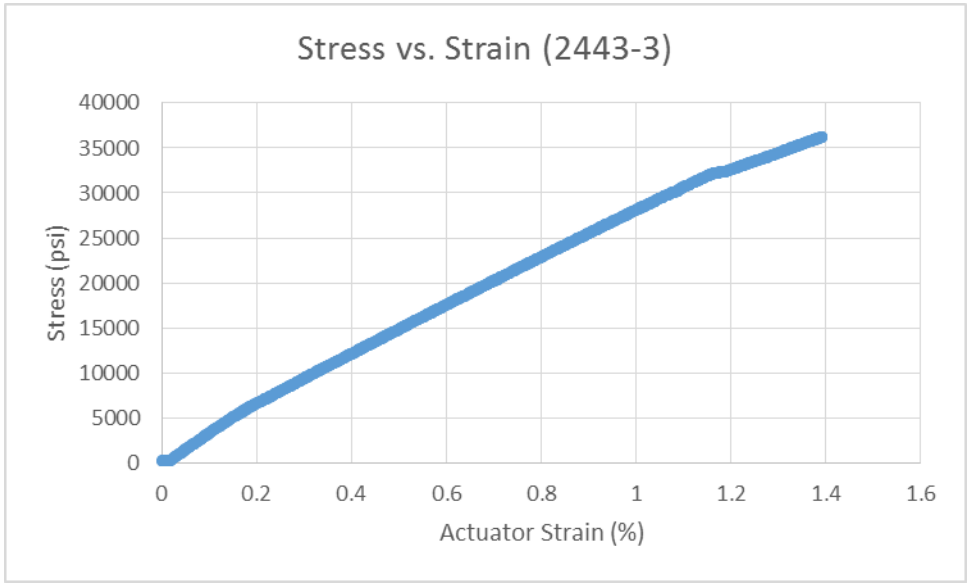
GLASS- A3*

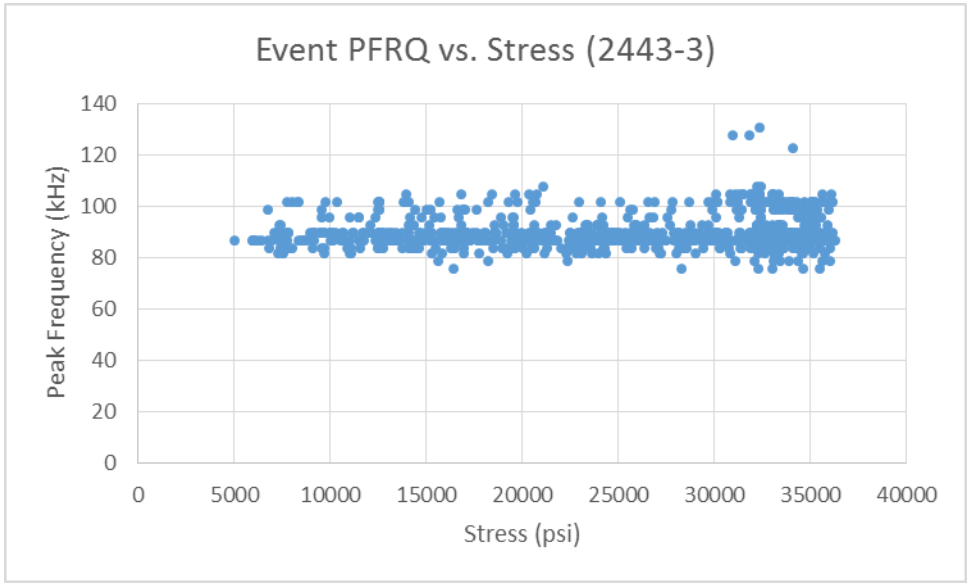

Stress vs. Strain (2443-2)
Stress (psi)
35000
30000
25000
20000
15000
10000
5000
0
0
0.2
0.4
0.6
0.8
1
1.2
Actuator Strain (%)

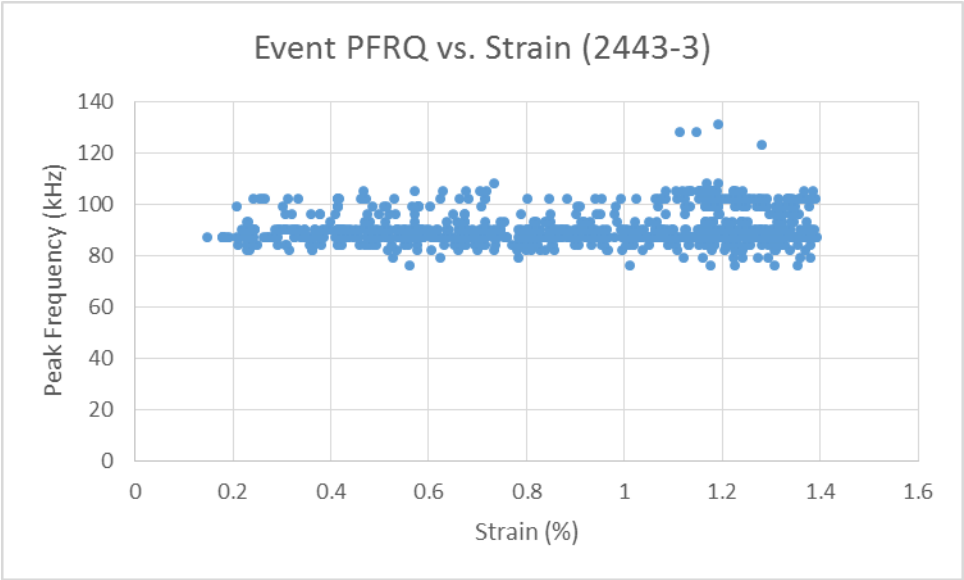

Event PFRQ vs. Stress (2443-2)
Peak Frequency (kHz)
120
100
80
60
40
20
0
0
5000
10000
15000
20000
25000
30000
35000
Stress (psi)

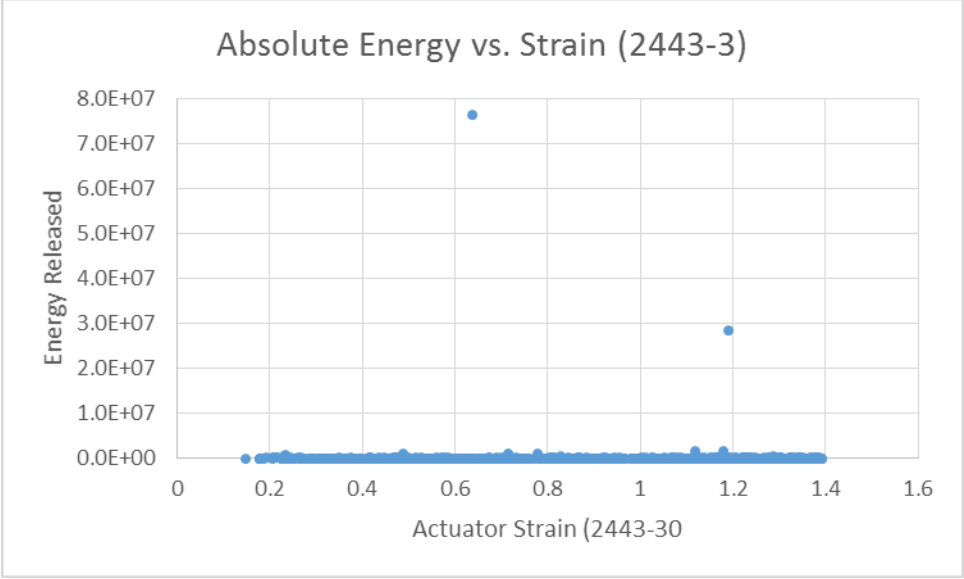

Event PFRQ vs. Strain (2443-2)
Peak Frequency (kHz)
120
100
80
60
40
20
0
0
0.2
0.4
0.6
0.8
1
1.2
Actuator Strain (%)

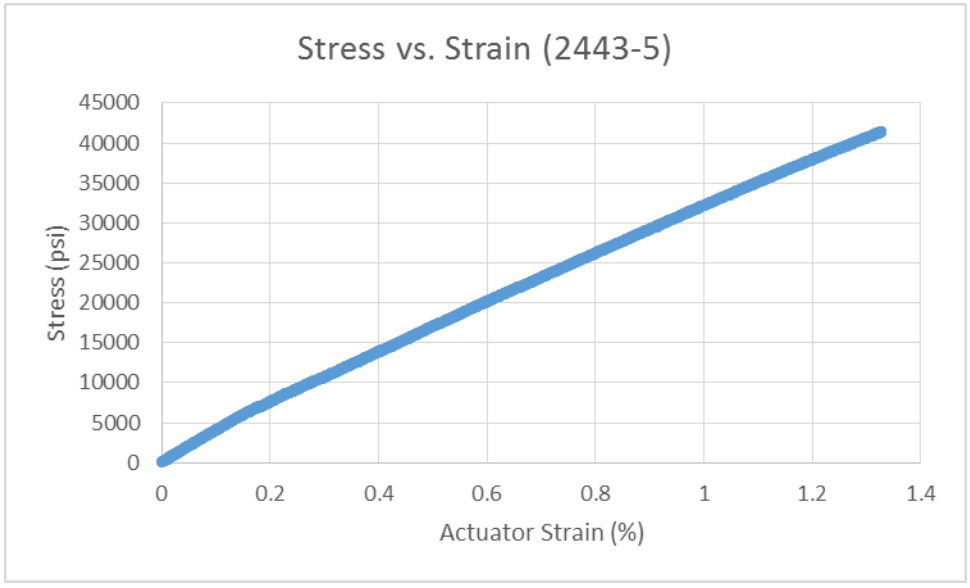

Absolute Energy vs. Strain (2443-2)
Energy Released (aJ)
9.0E+07
8.0E+07
7.0E+07
6.0E+07
5.0E+07
4.0E+07
3.0E+07
2.0E+07
1.0E+07
0.0E+00
0
0.2
0.4
0.6
0.8
1
1.2
Actuator Strain (%)

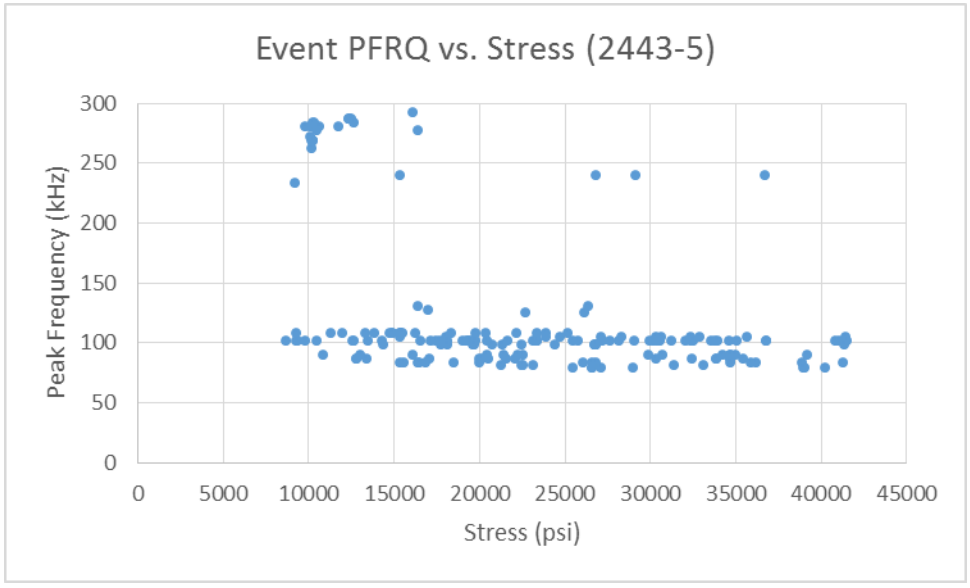

Stress vs. Strain (2443-3)
Stress (psi)
40000
35000
30000
25000
20000
15000
10000
5000
0
0
0.2
0.4
0.6
0.8
1
1.2
1.4
1.6
Actuator Strain (%)

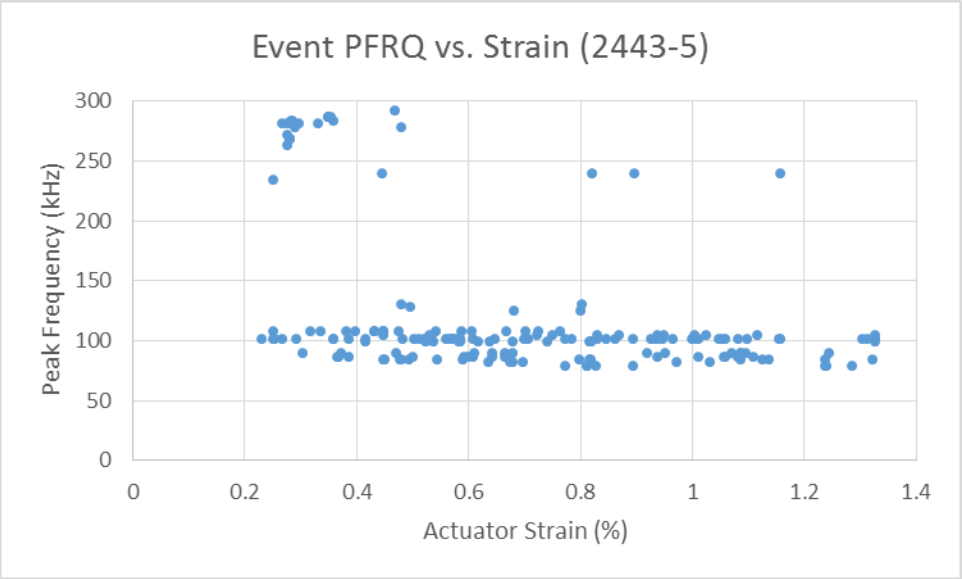

Event PFRQ vs. Stress (2443-3)
Peak Frequency (kHz)
140
120
100
80
60
40
20
0
0
5000
10000
15000
20000
25000
30000
35000
40000
Stress (psi)

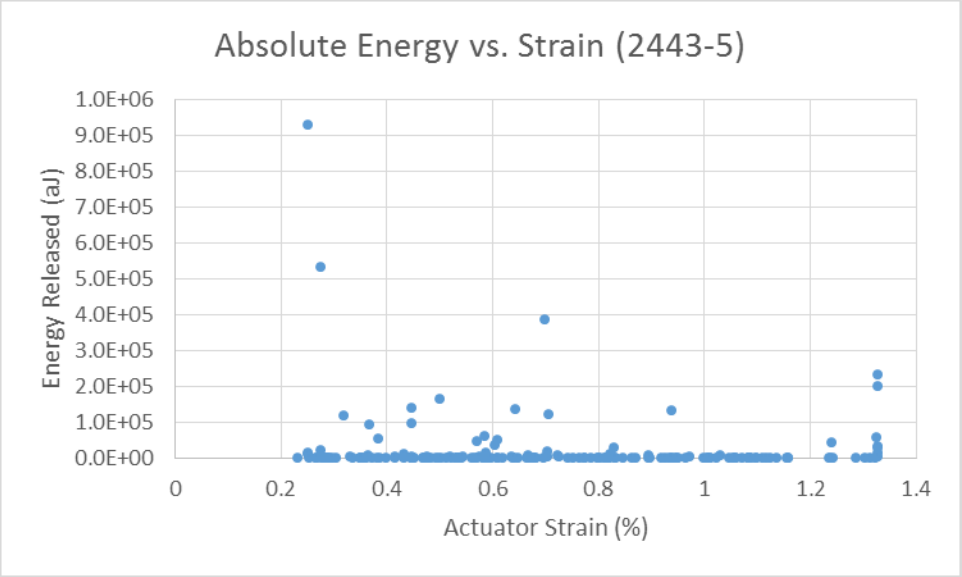

Event PFRQ vs. Strain (2443-3)
Peak Frequency (kHz)
140
120
100
80
60
40
20
0
0
0.2
0.4
0.6
0.8
1
1.2
1.4
1.6
Strain (%)


Absolute Energy vs. Strain (2443-3)
Energy Released
8.0E+07
7.0E+07
6.0E+07
5.0E+07
4.0E+07
3.0E+07
2.0E+07
1.0E+07
0.0E+00
0
0.2
0.4
0.6
0.8
1
1.2
1.4
1.6
Actuator Strain (2443-30

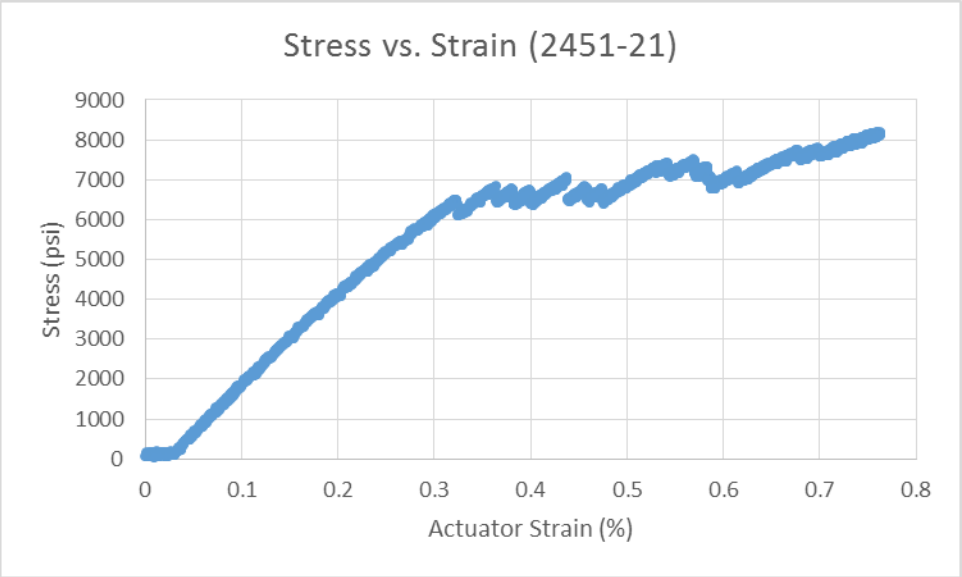

Stress vs. Strain (2443-5)
Stress (psi)
45000
40000
35000
30000
25000
20000
15000
10000
5000
0
0
0.2
0.4
0.6
0.8
1
1.2
1.4
Actuator Strain (%)

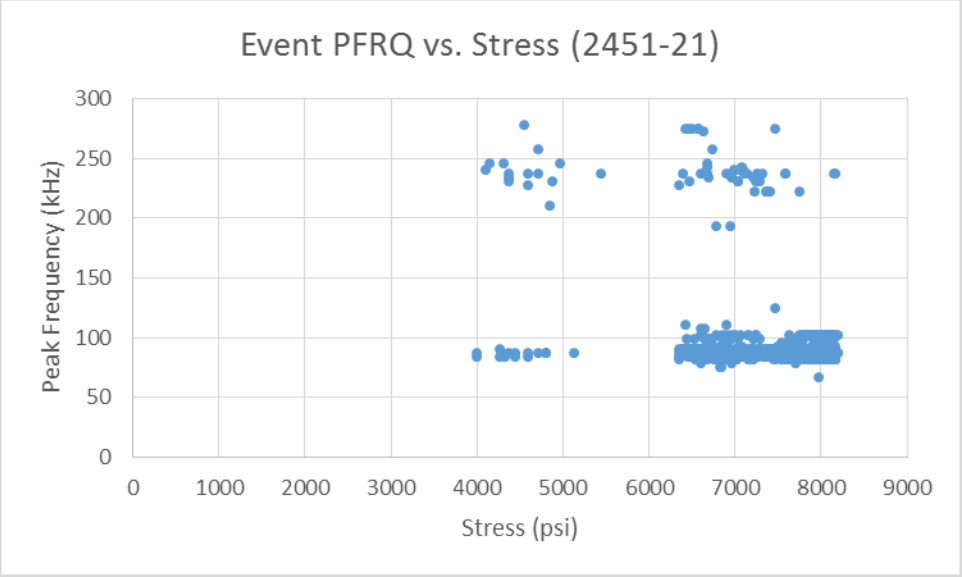

Event PFRQ vs. Stress (2443-5)
Peak Frequency (kHz)
300
250
200
150
100
50
0
0
5000
10000
15000
20000
25000
30000
35000
40000
45000
Stress (psi)

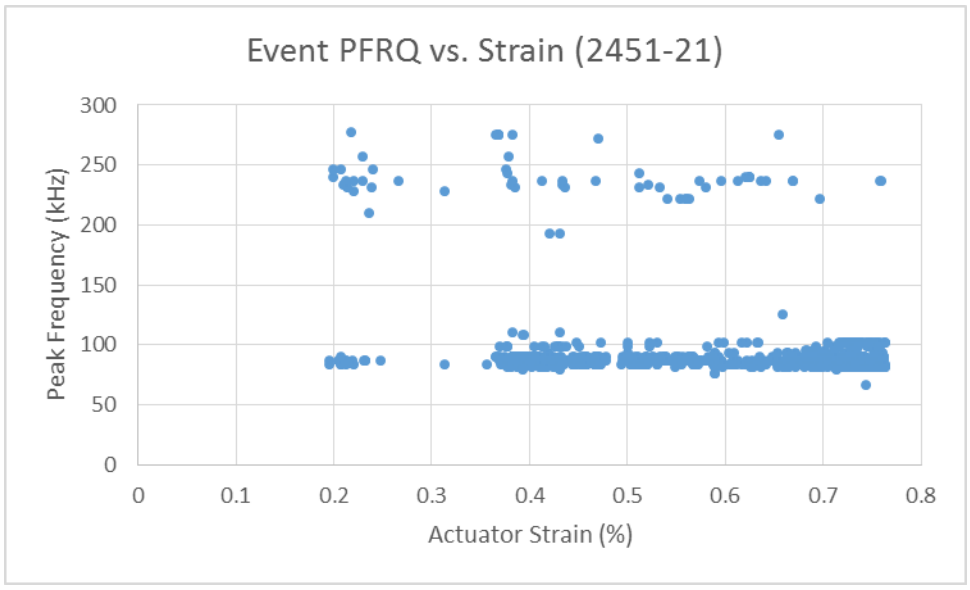

Event PFRQ vs. Strain (2443-5)
Peak Frequency (kHz)
300
250
200
150
100
50
0
0
0.2
0.4
0.6
0.8
1
1.2
1.4
Actuator Strain (%)

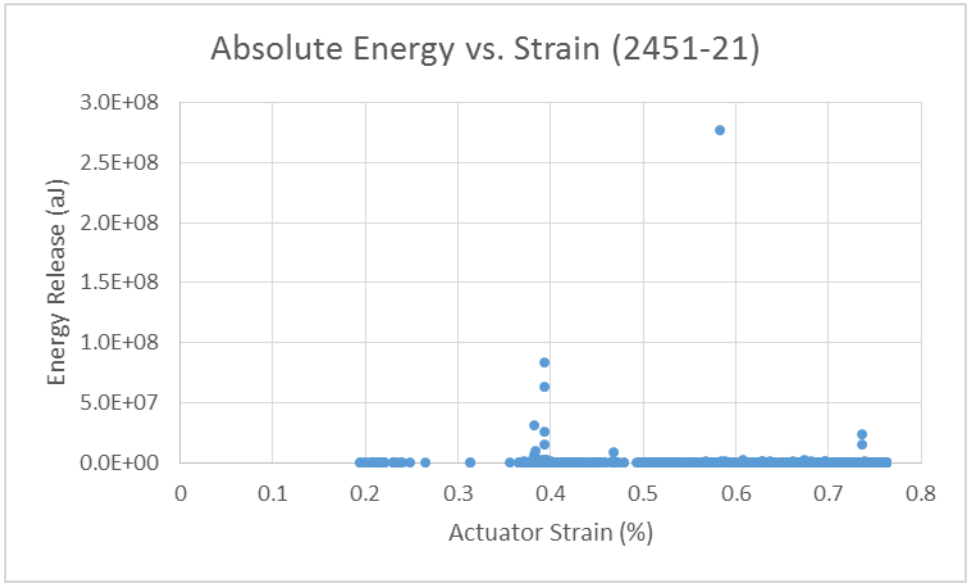

Absolute Energy vs. Strain (2443-5)
Energy Released (aJ)
1.0E+06
9.0E+05
8.0E+05
7.0E+05
6.0E+05
5.0E+05
4.0E+05
3.0E+05
2.0E+05
1.0E+05
0.0E+00
0
0.2
0.4
0.6
0.8
1
1.2
1.4
Actuator Strain (%)

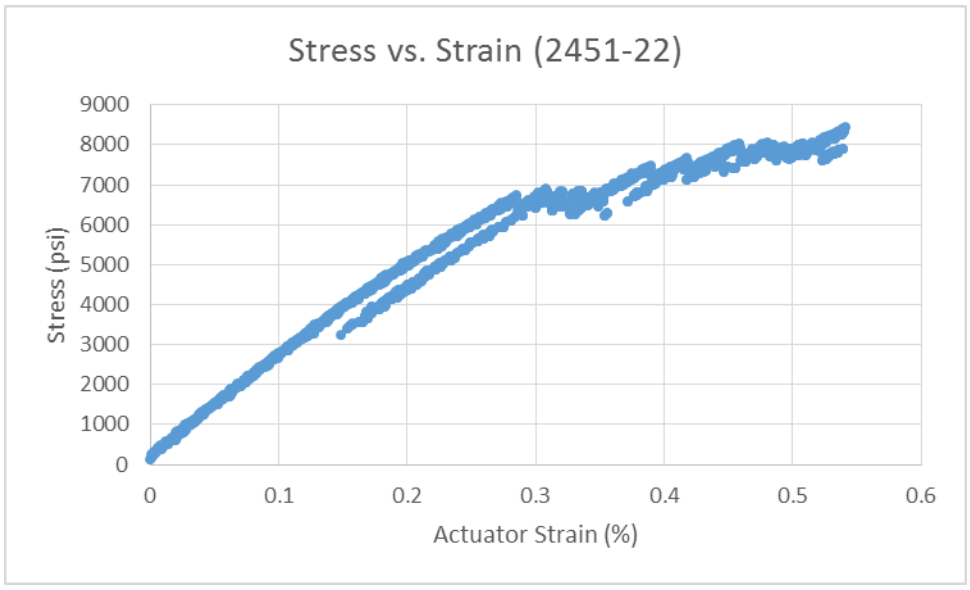
GLASS- A2

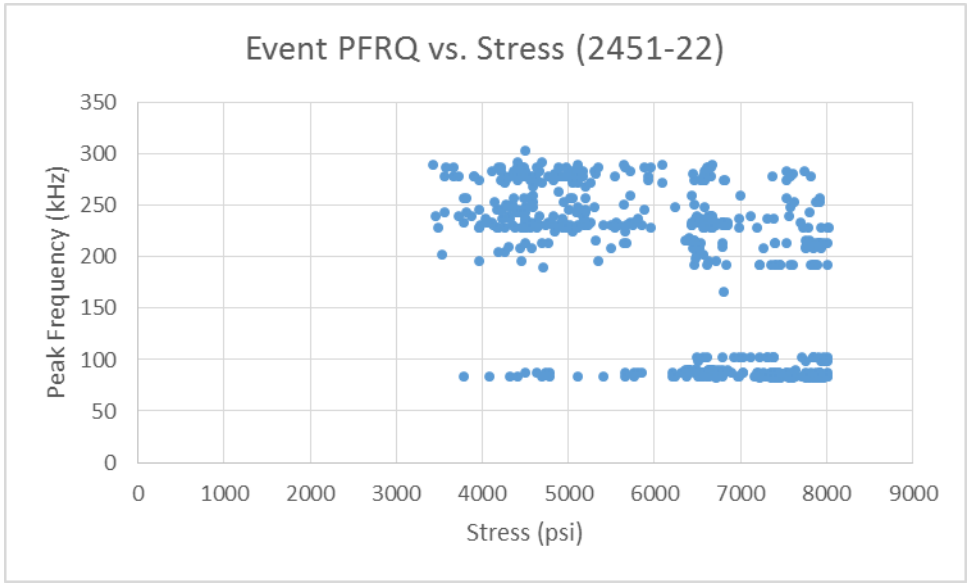

Stress vs. Strain (2451-21)
Stress (psi)
9000
8000
7000
6000
5000
4000
3000
2000
1000
0
0
0.1
0.2
0.3
0.4
0.5
0.6
0.7
0.8
Actuator Strain (%)

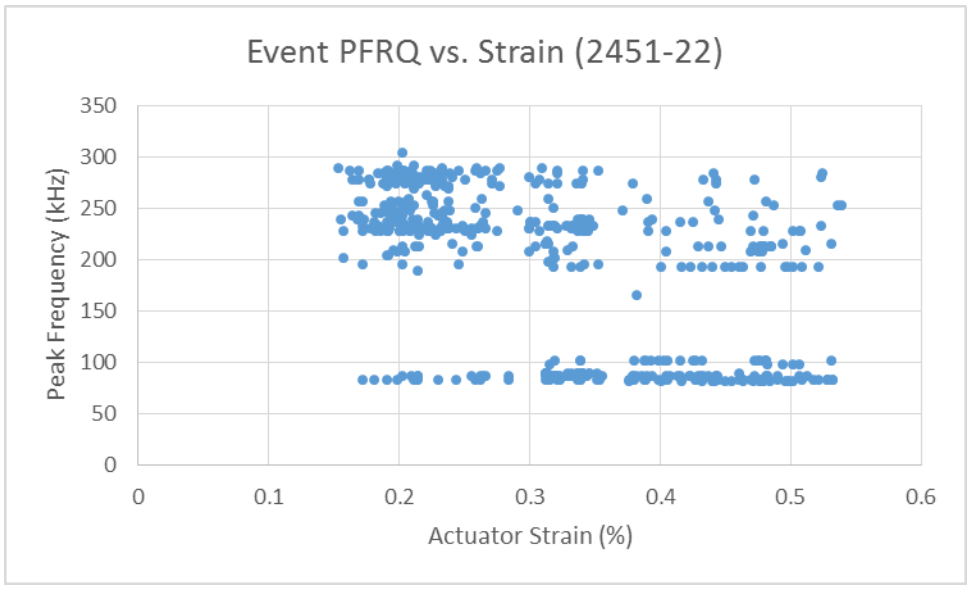

Event PFRQ vs. Stress (2451-21)
Peak Frequency (kHz)
300
250
200
150
100
50
0
0
1000
2000
3000
4000
5000
6000
7000
8000
9000
Stress (psi)

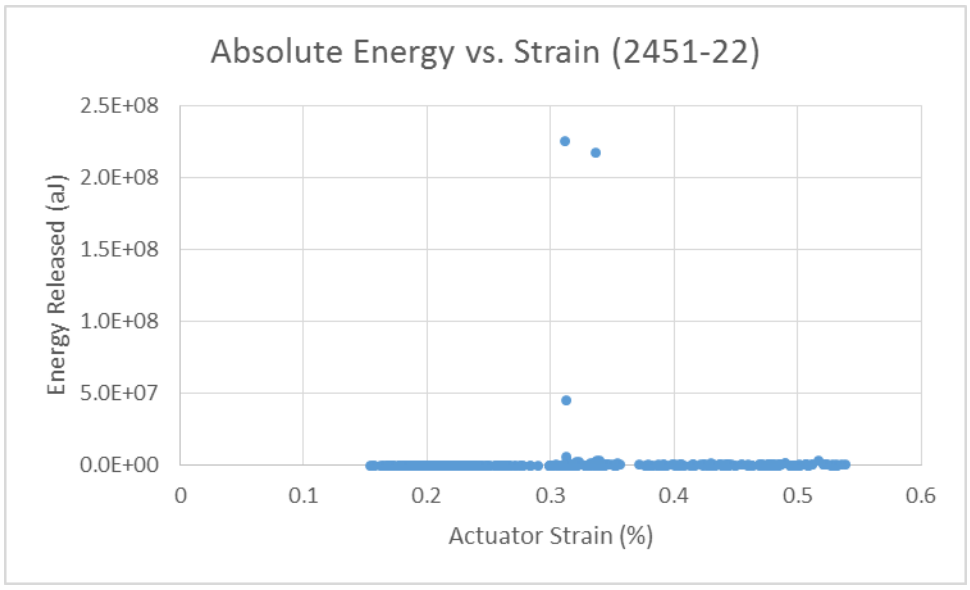

Event PFRQ vs. Strain (2451-21)
Peak Frequency (kHz)
300
250
200
150
100
50
0
0
0.1
0.2
0.3
0.4
0.5
0.6
0.7
0.8
Actuator Strain (%)

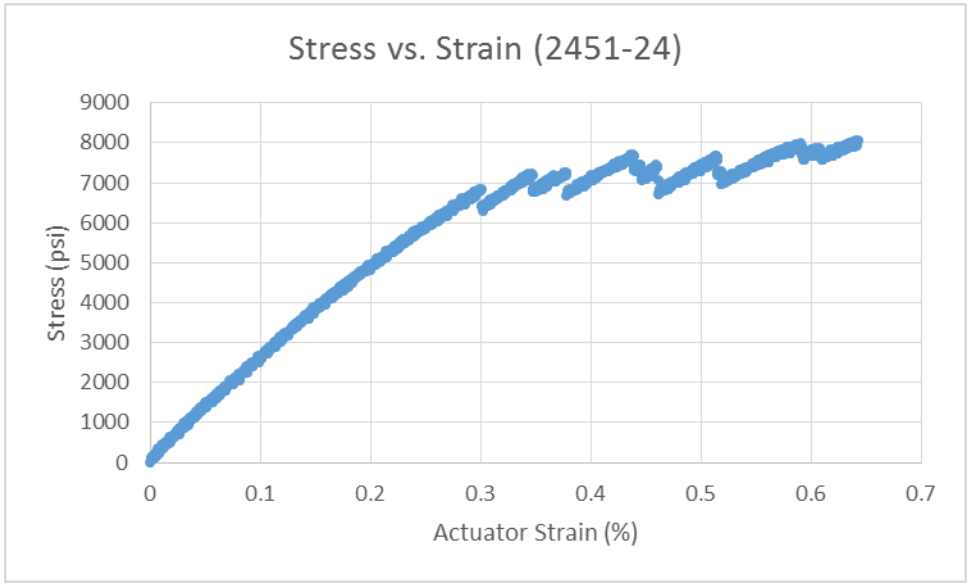

Absolute Energy vs. Strain (2451-21)
Energy Release (aJ)
3.0E+08
2.5E+08
2.0E+08
1.5E+08
1.0E+08
5.0E+07
0.0E+00
0
0.1
0.2
0.3
0.4
0.5
0.6
0.7
0.8
Actuator Strain (%)

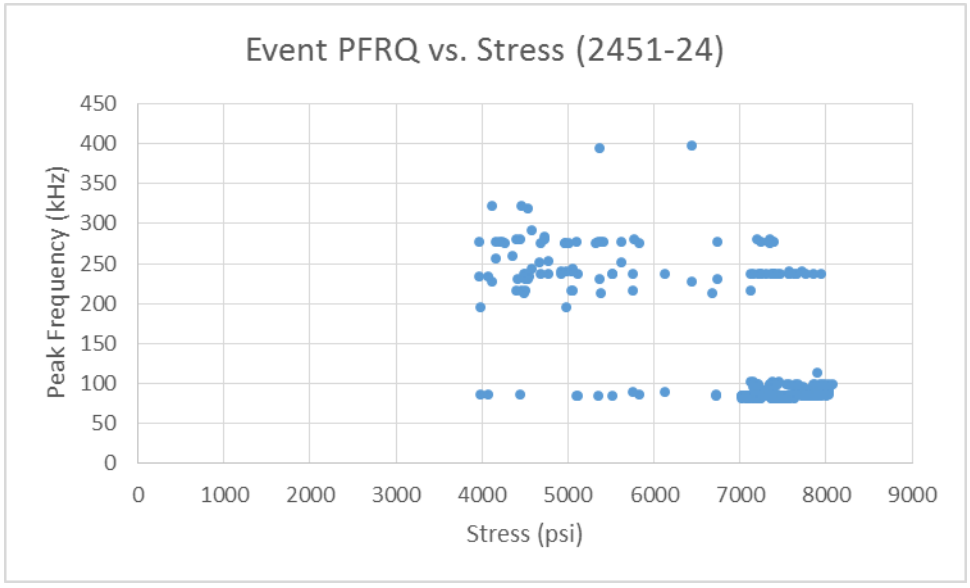

Stress vs. Strain (2451-22)
Stress (psi)
9000
8000
7000
6000
5000
4000
3000
2000
1000
0
0
0.1
0.2
0.3
0.4
0.5
0.6
Actuator Strain (%)

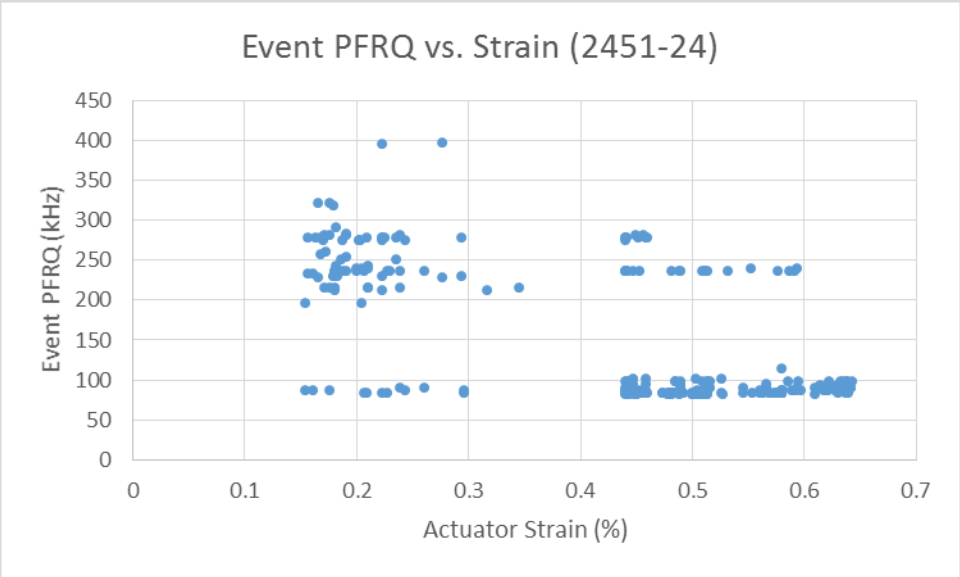

Event PFRQ vs. Stress (2451-22)
Peak Frequency (kHz)
350
300
250
200
150
100
50
0
0
1000
2000
3000
4000
5000
6000
7000
8000
9000
Stress (psi)

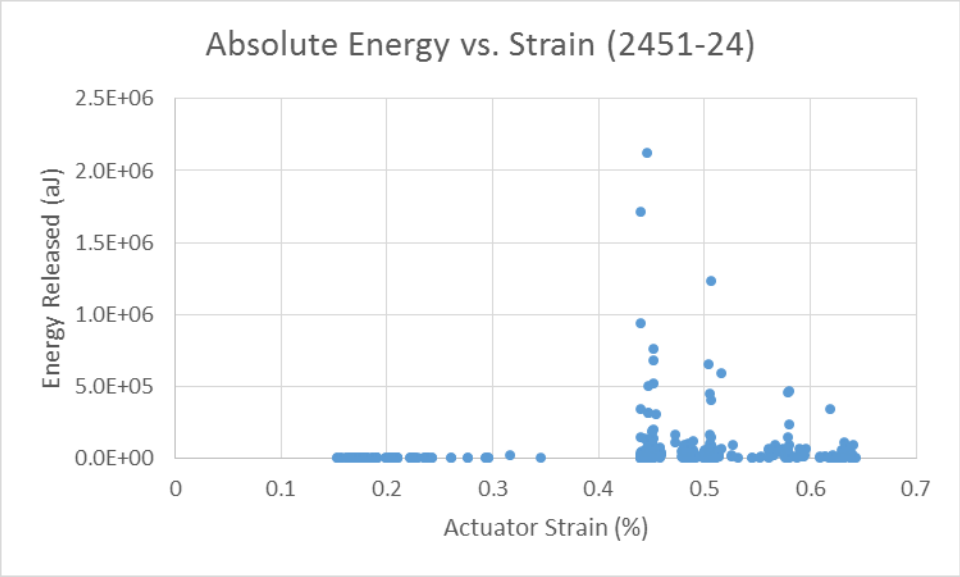

Event PFRQ vs. Strain (2451-22)
Peak Frequency (kHz)
350
300
250
200
150
100
50
0
0
0.1
0.2
0.3
0.4
0.5
0.6
Actuator Strain (%)


Absolute Energy vs. Strain (2451-22)
Energy Released (aJ)
2.5E+08
2.0E+08
1.5E+08
1.0E+08
5.0E+07
0.0E+00
0
0.1
0.2
0.3
0.4
0.5
0.6
Actuator Strain (%)

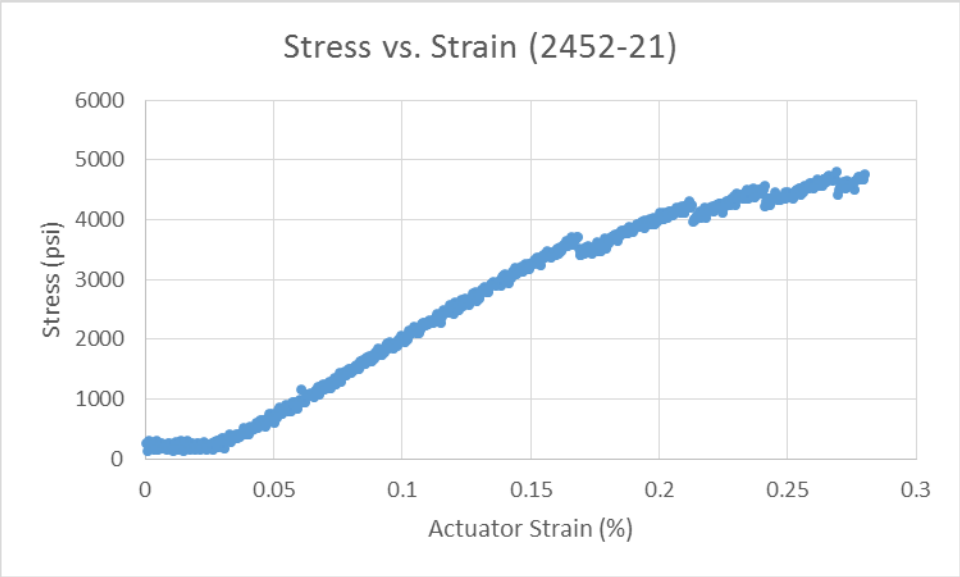

Stress vs. Strain (2451-24)
Stress (psi)
9000
8000
7000
6000
5000
4000
3000
2000
1000
0
0
0.1
0.2
0.3
0.4
0.5
0.6
0.7
Actuator Strain (%)

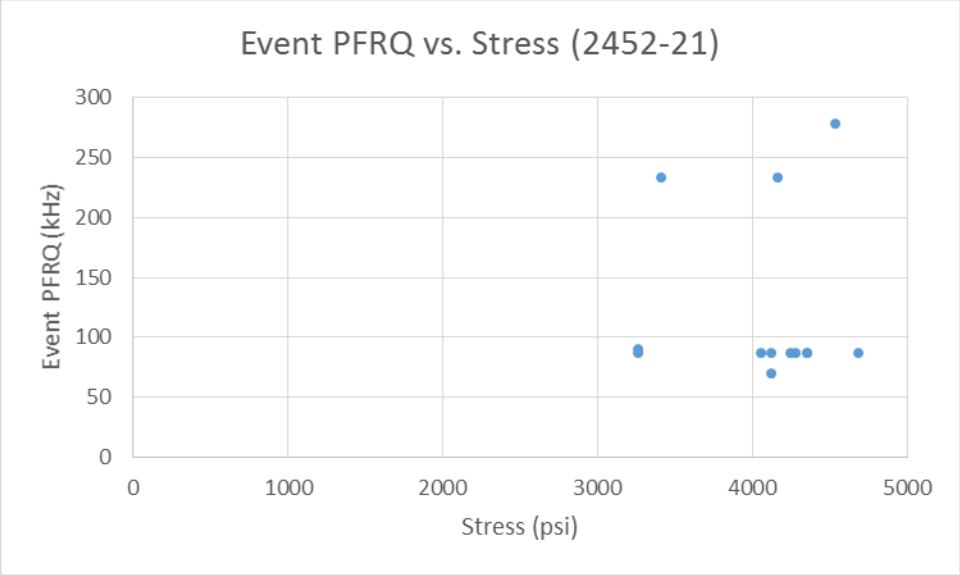

Event PFRQ vs. Stress (2451-24)
Peak Frequency (kHz)
450
400
350
300
250
200
150
100
50
0
0
1000
2000
3000
4000
5000
6000
7000
8000
9000
Stress (psi)

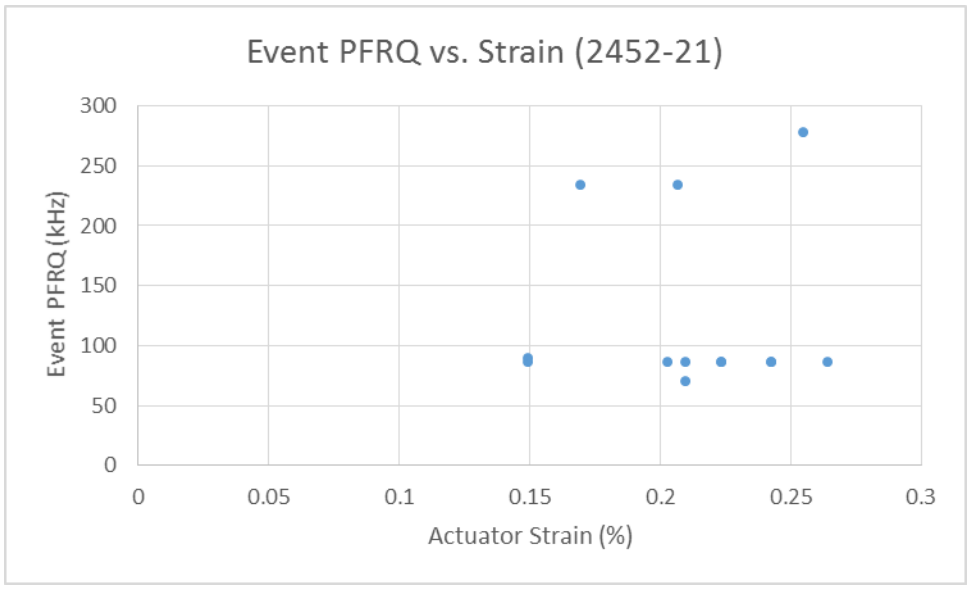

Event PFRQ vs. Strain (2451-24)
Event PFRQ (kHz)
450
400
350
300
250
200
150
100
50
0
0
0.1
0.2
0.3
0.4
0.5
0.6
0.7
Actuator Strain (%)

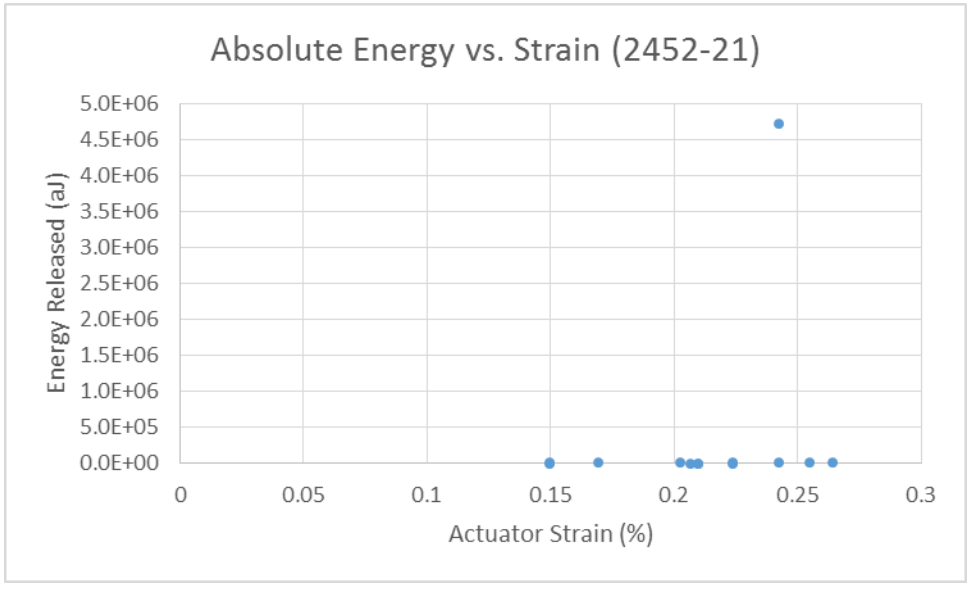

Absolute Energy vs. Strain (2451-24)
Energy Released (aJ)
2.5E+06
2.0E+06
1.5E+06
1.0E+06
5.0E+05
0.0E+00
0
0.1
0.2
0.3
0.4
0.5
0.6
0.7
Actuator Strain (%)

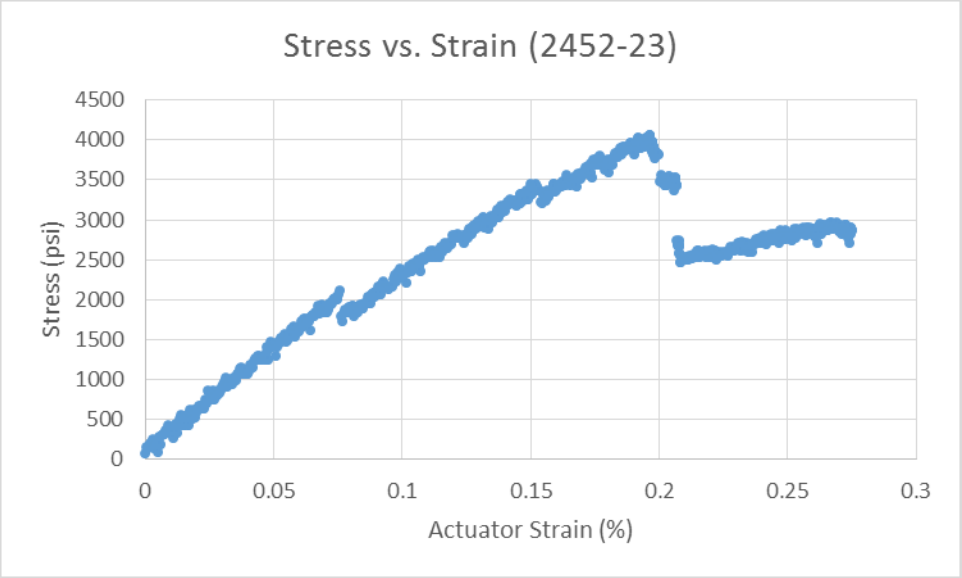
GLASS- A2*

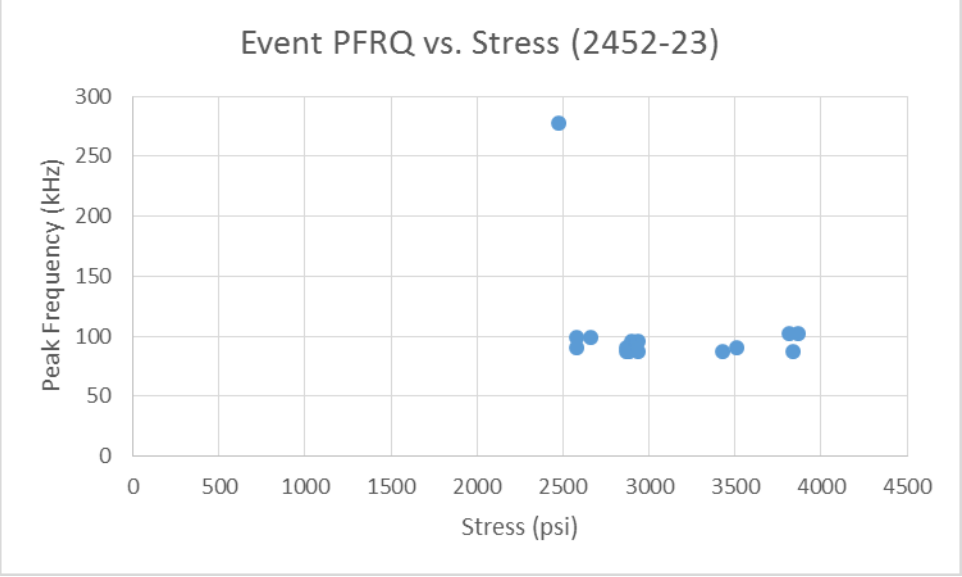

Stress vs. Strain (2452-21)
Stress (psi)
6000
5000
4000
3000
2000
1000
0
0
0.05
0.1
0.15
0.2
0.25
0.3
Actuator Strain (%)

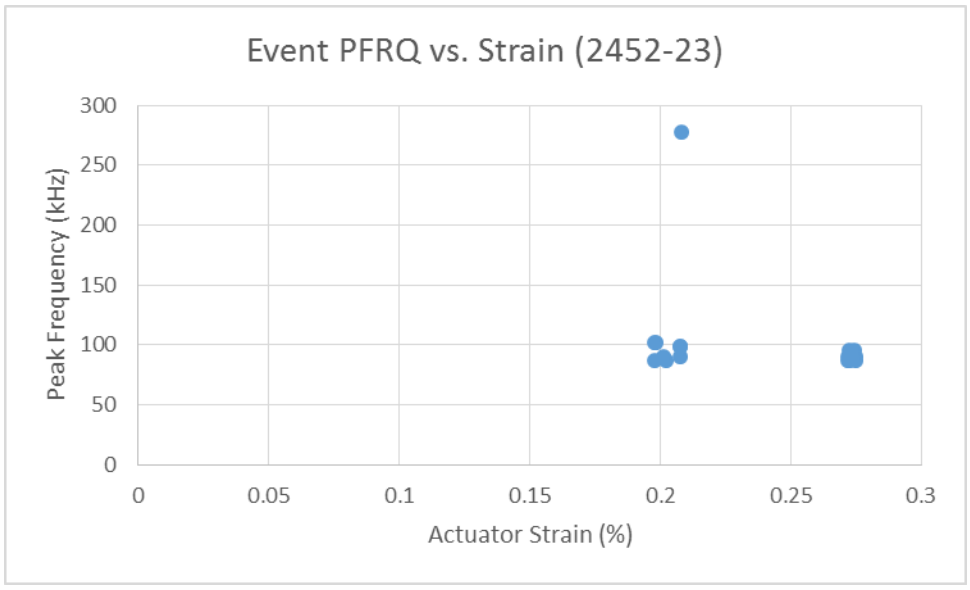

Event PFRQ vs. Stress (2452-21)
Event PFRQ (kHz)
300
250
200
150
100
50
0
0
1000
2000
3000
4000
5000
Stress (psi)

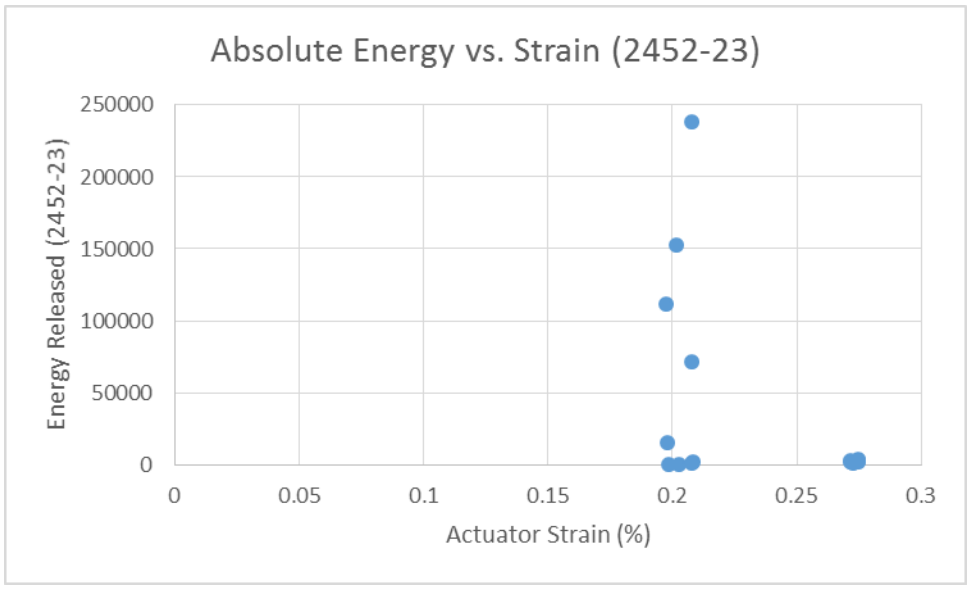

Event PFRQ vs. Strain (2452-21)
Event PFRQ (kHz)
300
250
200
150
100
50
0
0
0.05
0.1
0.15
0.2
0.25
0.3
Actuator Strain (%)

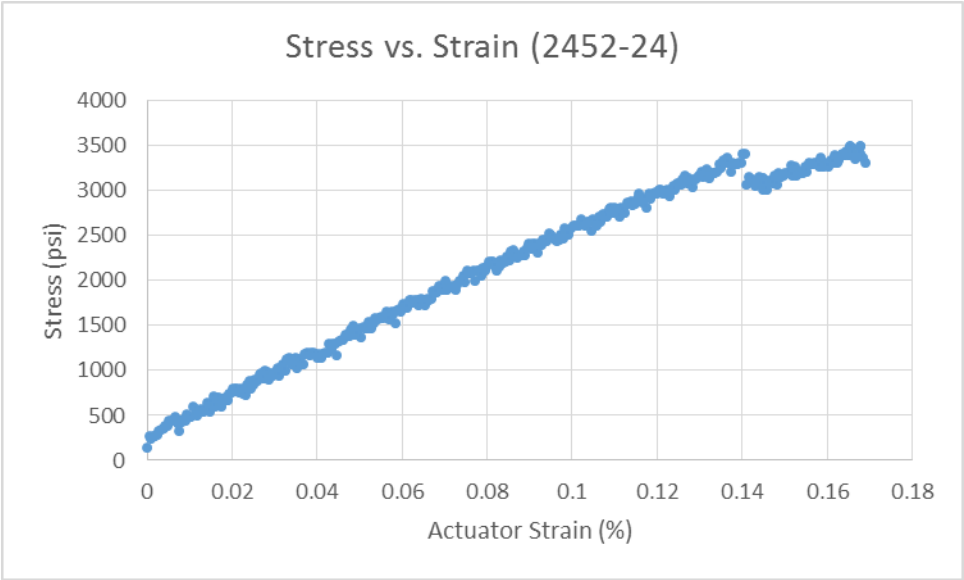

Absolute Energy vs. Strain (2452-21)
Energy Released (aJ)
5.0E+06
4.5E+06
4.0E+06
3.5E+06
3.0E+06
2.5E+06
2.0E+06
1.5E+06
1.0E+06
5.0E+05
0.0E+00
0
0.05
0.1
0.15
0.2
0.25
0.3
Actuator Strain (%)

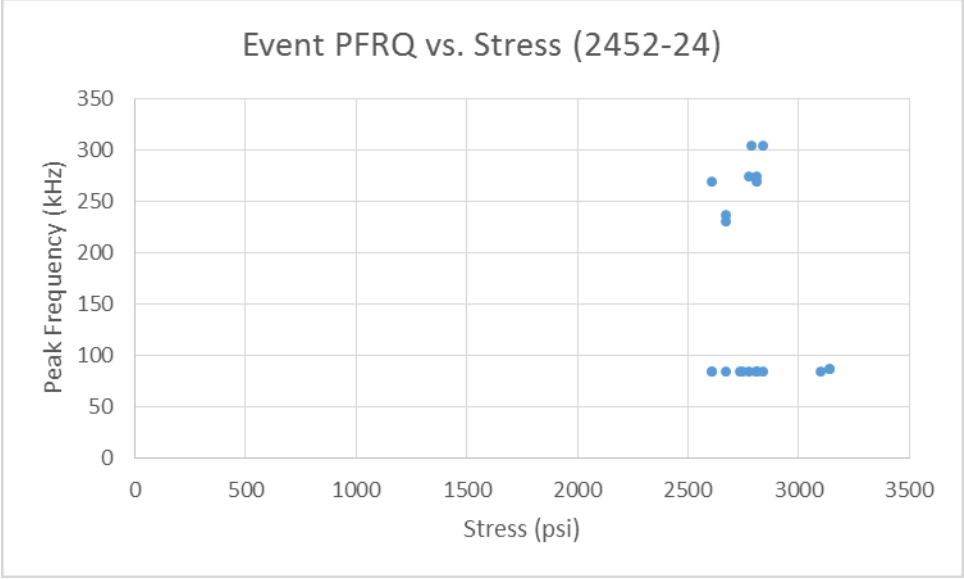

Stress vs. Strain (2452-23)
Stress (psi)
4500
4000
3500
3000
2500
2000
1500
1000
500
0
0
0.05
0.1
0.15
0.2
0.25
0.3
Actuator Strain (%)

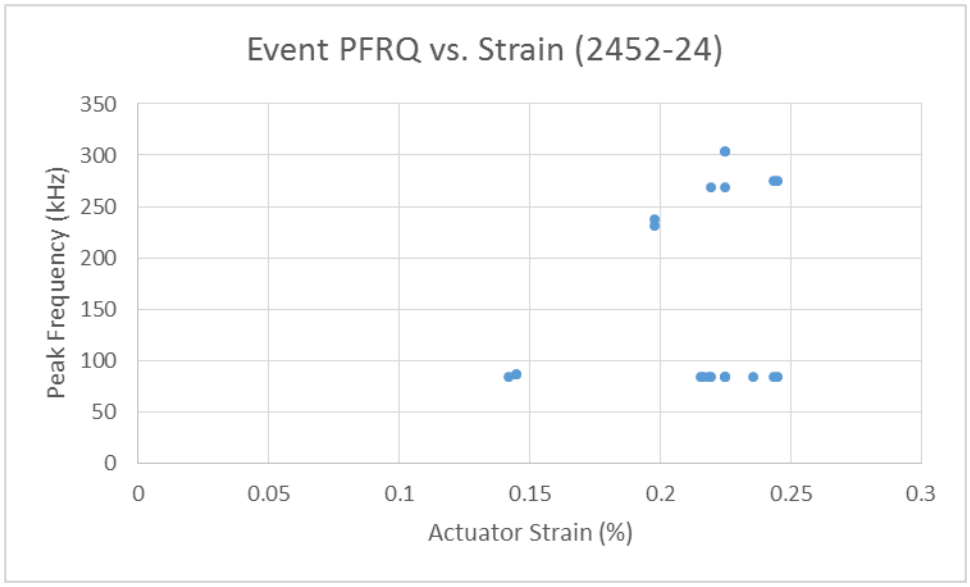

Event PFRQ vs. Stress (2452-23)
Peak Frequency (kHz)
300
250
200
150
100
50
0
0
500
1000
1500
2000
2500
3000
3500
4000
4500
Stress (psi)

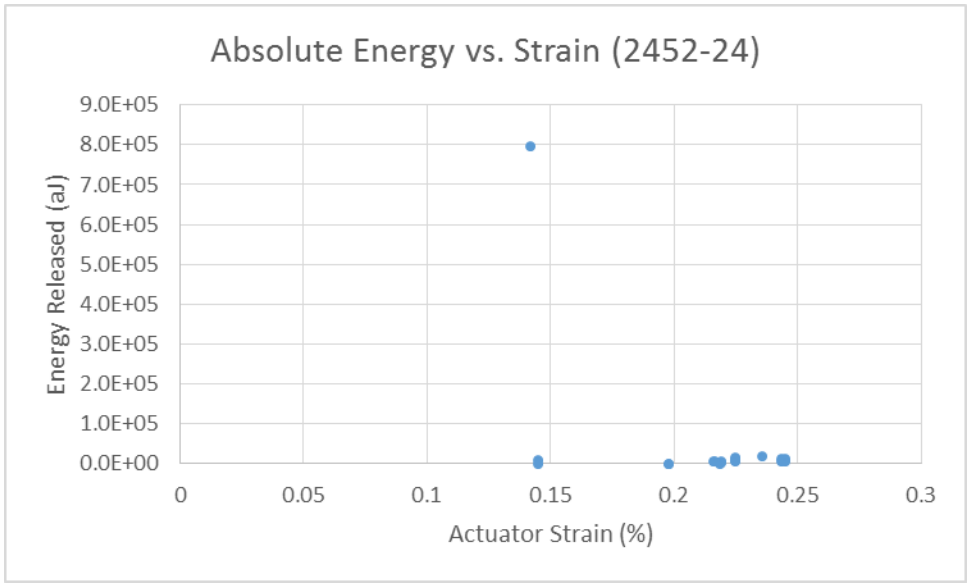

Event PFRQ vs. Strain (2452-23)
Peak Frequency (kHz)
300
250
200
150
100
50
0
0
0.05
0.1
0.15
0.2
0.25
0.3
Actuator Strain (%)


Absolute Energy vs. Strain (2452-23)
Energy Released (2452-23)
250000
200000
150000
100000
50000
0
0
0.05
0.1
0.15
0.2
0.25
0.3
Actuator Strain (%)


Stress vs. Strain (2452-24)
Stress (psi)
4000
3500
3000
2500
2000
1500
1000
500
0
0
0.02
0.04
0.06
0.08
0.1
0.12
0.14
0.16
0.18
Actuator Strain (%)


Event PFRQ vs. Stress (2452-24)
Peak Frequency (kHz)
350
300
250
200
150
100
50
0
0
500
1000
1500
2000
2500
3000
3500
Stress (psi)


Event PFRQ vs. Strain (2452-24)
Peak Frequency (kHz)
350
300
250
200
150
100
50
0
0
0.05
0.1
0.15
0.2
0.25
0.3
Actuator Strain (%)


Absolute Energy vs. Strain (2452-24)
Energy Released (aJ)
9.0E+05
8.0E+05
7.0E+05
6.0E+05
5.0E+05
4.0E+05
3.0E+05
2.0E+05
1.0E+05
0.0E+00
0
0.05
0.1
0.15
0.2
0.25
0.3
Actuator Strain (%)

APPENDIX D

MS EXCEL ANOVA SETUP

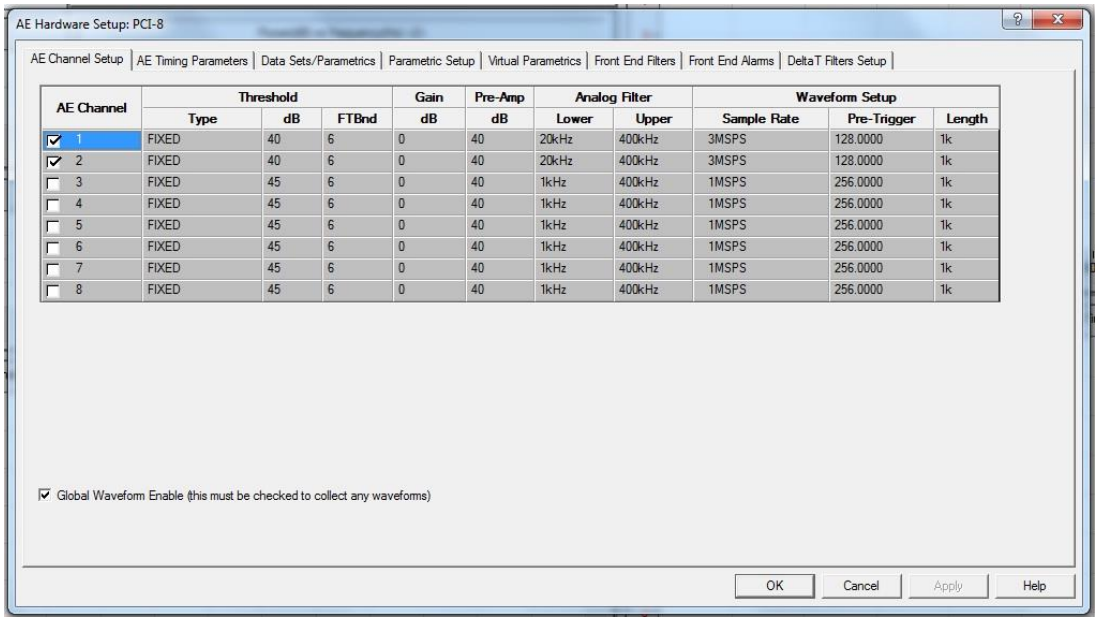
							TOTAL ABSOLUTE ENERGY RELEASED (nJ)				
COUPON #	2440	2439	2451	2452	2441	2443	2434	2435	2449	2450	2446
DESIGNATION	A1	A1*	A2	A2*	A3	A3*	B1	B2	C1	C2	C3
	58.027	53.351	64.586	0.478	236.562	20.309	24.678	153.166	391.817	78.832	127.355
	123.656	0.021	53.865	0.000	293.774	12.010	122.172	290.995	159.441	1.105	29.831
	31.163	0.666	105.936	0.061	235.081	66.743	0.778	137.340	301.792	202.347	91.569
			2.158	0.094	202.556		4.369	235.330	140.980	56.654	30.419
					151.615				110.396	1.090	12.951
					191.515						

DATA SUMMARY

Groups	*Count*	*Sum*	*Average*	*Variance*
A1	3	212.846	70.949	2263.971
A1*	3	54.038	18.013	936.726
A2	4	226.546	56.637	1823.076
A2*	4	0.633	0.158	0.047
A3	6	1311.103	218.517	2344.686
A3*	3	99.061	33.020	870.115
B1	4	151.996	37.999	3259.635
B2	4	816.832	204.208	5192.411
C1	5	1104.427	220.885	14532.946
C2	5	340.027	68.005	6811.774
C3	5	292.125	58.425	2379.950

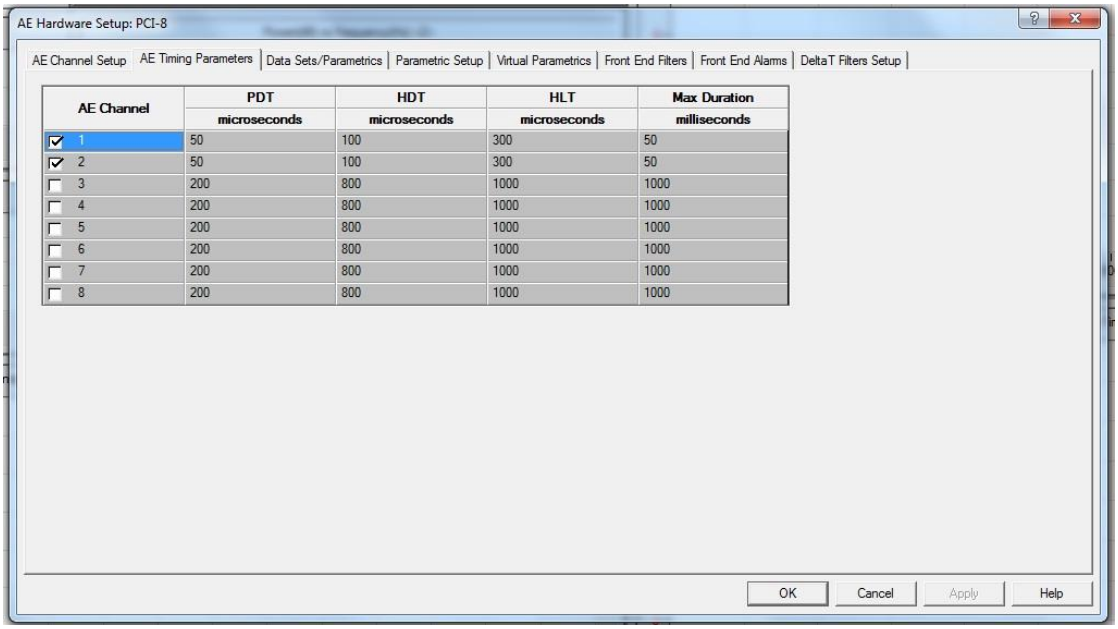
APPENDIX E

AEWIN SOFTWARE SETTINGS



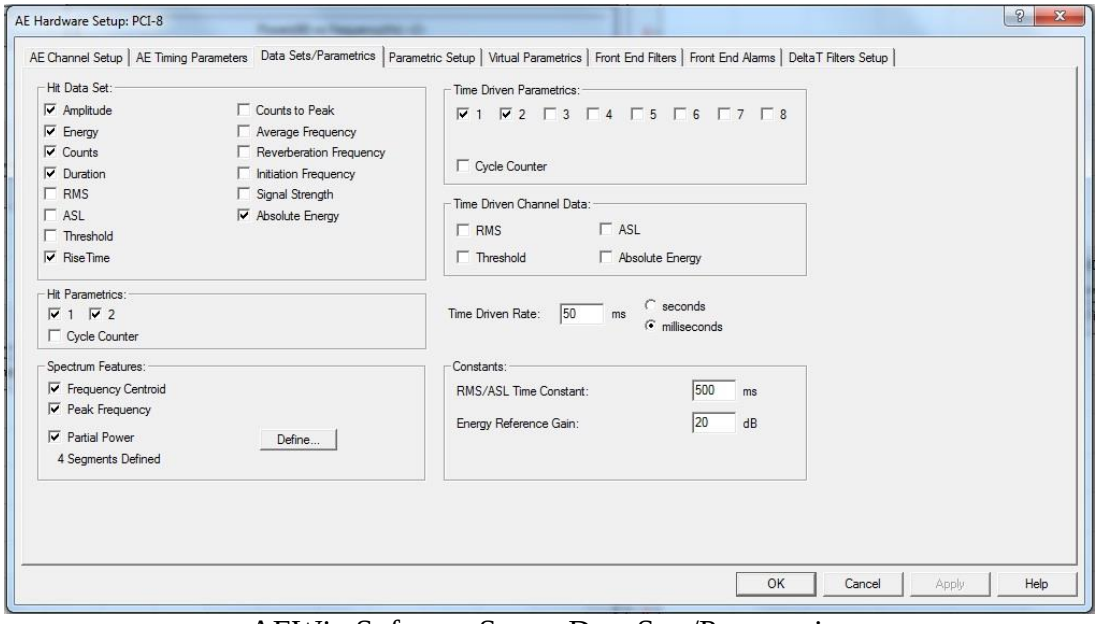
AE Channel	Threshold			Gain	Pre-Amp	Analog Filter		Waveform Setup		
	Type	dB	FTBnd	dB	dB	Lower	Upper	Sample Rate	Pre-Trigger	Length
1	FIXED	40	6	0	40	20kHz	400kHz	3MSPS	128.0000	1k
2	FIXED	40	6	0	40	20kHz	400kHz	3MSPS	128.0000	1k
3	FIXED	45	6	0	40	1kHz	400kHz	1MSPS	256.0000	1k
4	FIXED	45	6	0	40	1kHz	400kHz	1MSPS	256.0000	1k
5	FIXED	45	6	0	40	1kHz	400kHz	1MSPS	256.0000	1k
6	FIXED	45	6	0	40	1kHz	400kHz	1MSPS	256.0000	1k
7	FIXED	45	6	0	40	1kHz	400kHz	1MSPS	256.0000	1k
8	FIXED	45	6	0	40	1kHz	400kHz	1MSPS	256.0000	1k

AEWin Software Setup: AE Channel Setup

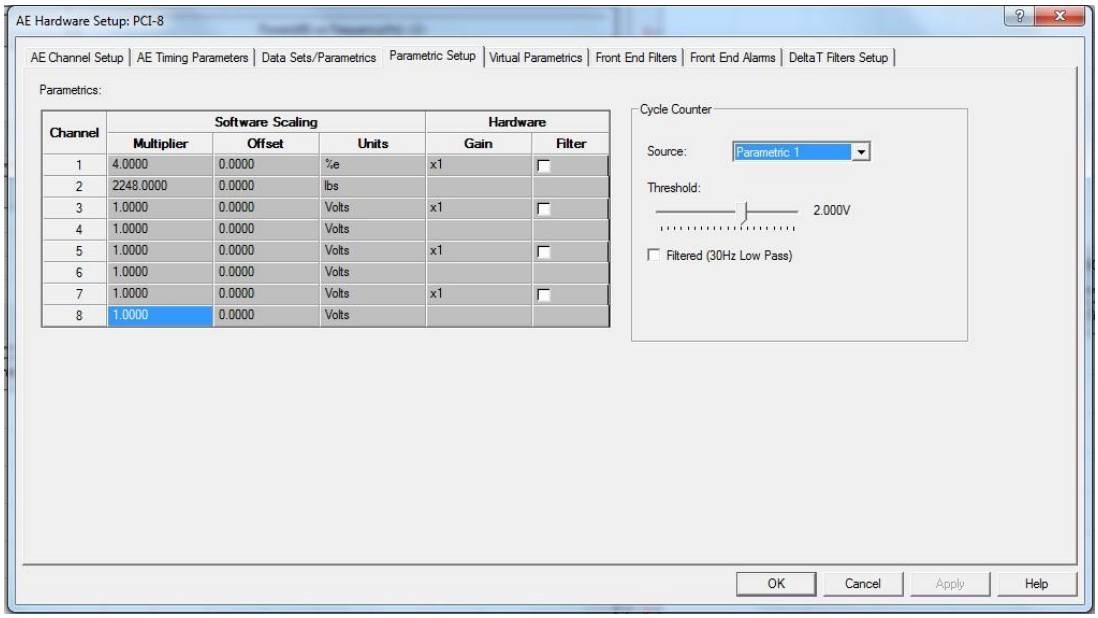


AE Channel	PDT	HDT	HLT	Max Duration
	microseconds	microseconds	microseconds	milliseconds
1	50	100	300	50
2	50	100	300	50
3	200	800	1000	1000
4	200	800	1000	1000
5	200	800	1000	1000
6	200	800	1000	1000
7	200	800	1000	1000
8	200	800	1000	1000

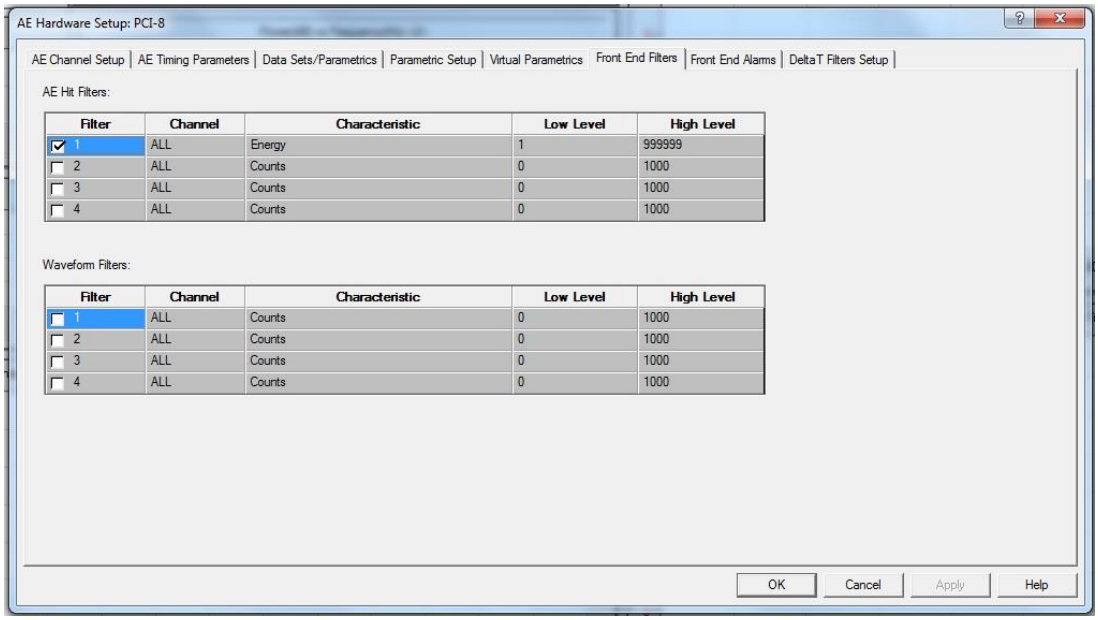
AEWin Software Setup: AE Timing Parameters



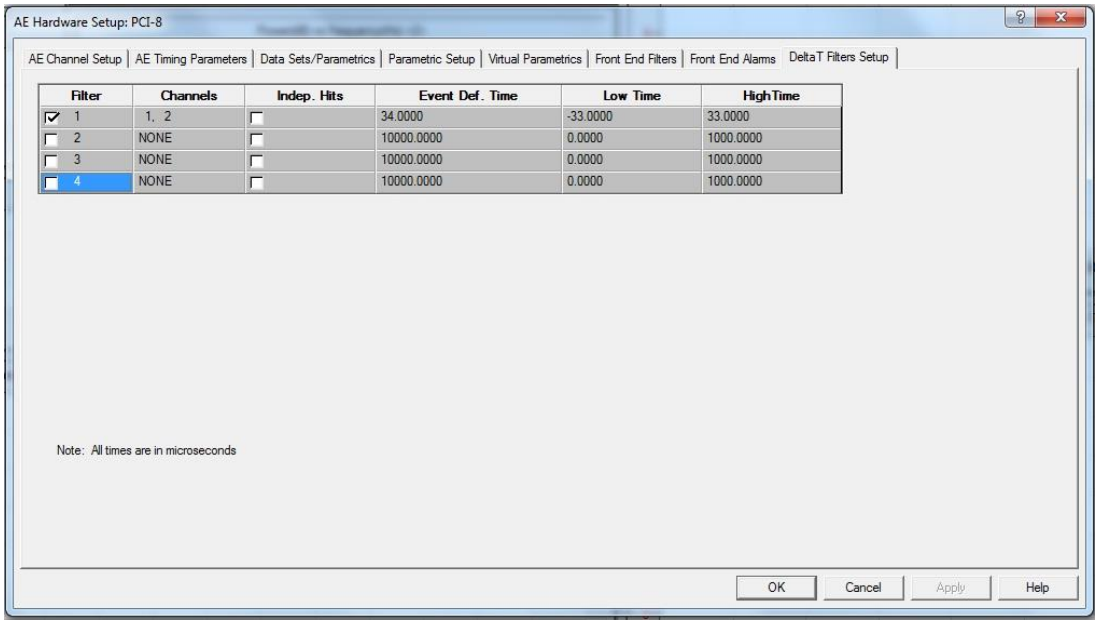
AEWin Software Setup: Data Sets/Parametrics



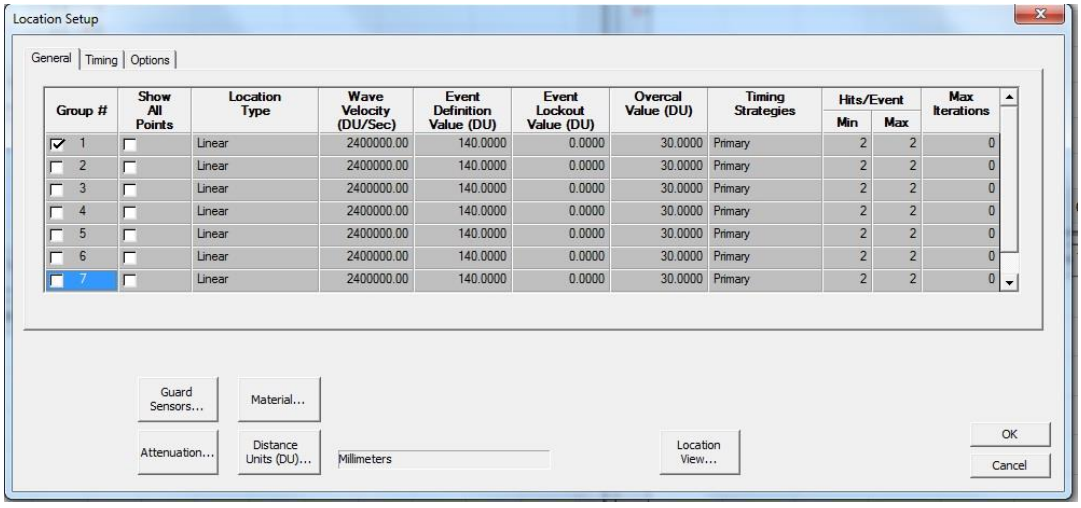
AEWin Software Setup: Parametric Setup



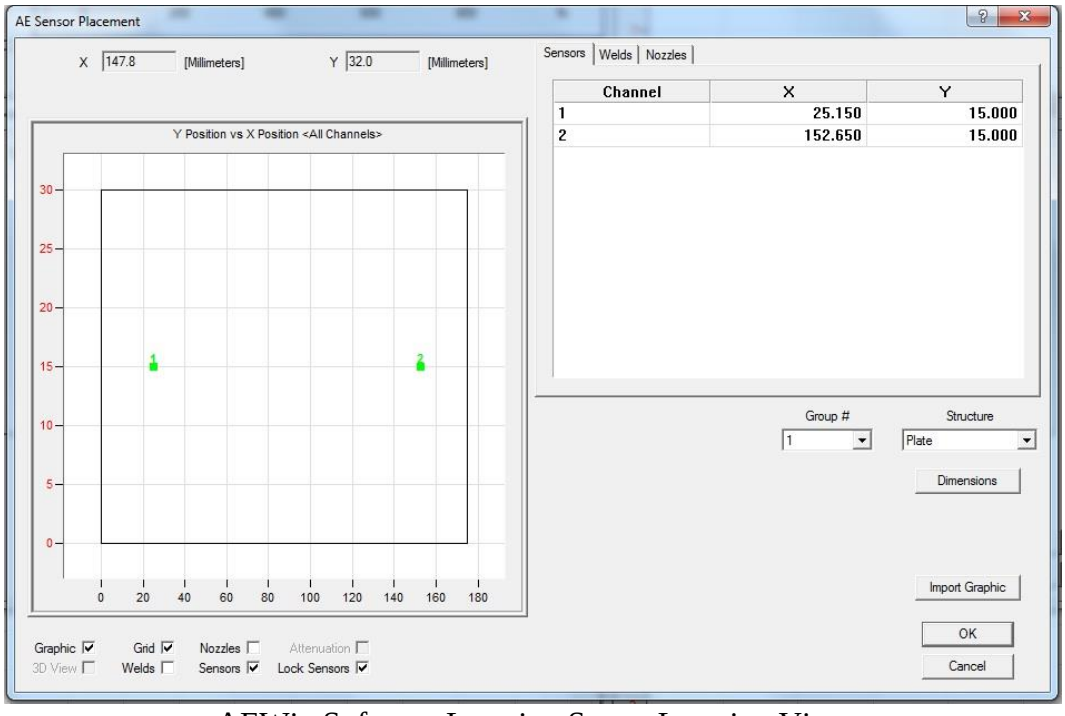
AEWin Software Setup: Front End Filters



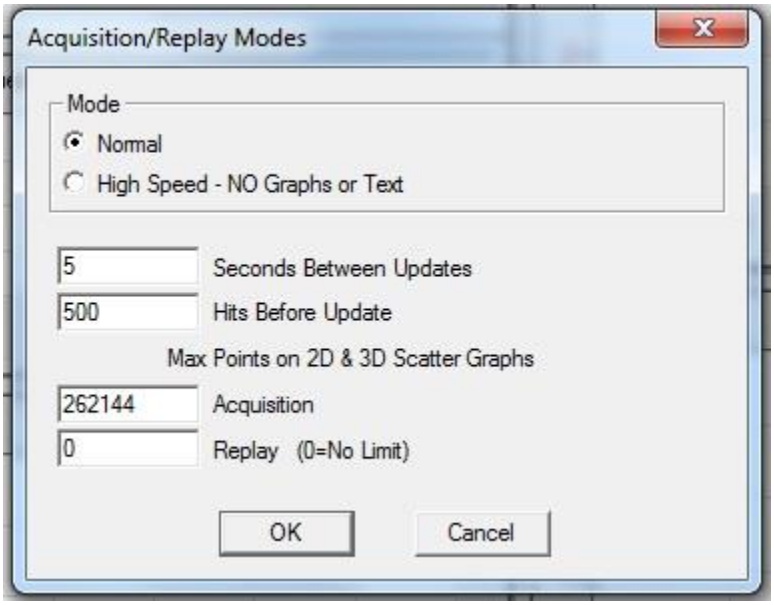
AEWin Software Setup: DeltaT Filters Setup



AEWin Software Location Setup: General



AEWin Software Location Setup: Location View



AEWin Software Acquisition/Replay Mode Settings